

STUDY OF WAVE PROPAGATION AND POTENTIAL STRUCTURES IN AN EXPANDING HELICON PLASMA

By

KSHITISH KUMAR BARADA

PHYS06200704009

Institute for Plasma Research, Gandhinagar

A thesis submitted to the

Board of Studies in Physical Sciences

In partial fulfillment of requirements

For the Degree of

DOCTOR OF PHILOSOPHY

Of

HOMI BHABHA NATIONAL INSTITUTE



August, 2013

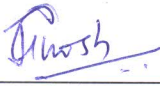
Homi Bhabha National Institute

Recommendations of the Viva Voice Board

As members of the Viva Voice Board, we certify that we have read the dissertation prepared by **Kshitish Kumar Barada** entitled "Study of Wave Propagation and Potential Structures in an Expanding Helicon Plasma" and recommend that it may be accepted as fulfilling the dissertation requirement for the Degree of Doctor of Philosophy.


_____ Date: 10.01.2014
Chairman: Prof. Y. C. Saxena

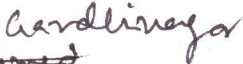

_____ Date: 10.01.2014
Supervisor: Dr. Prabal Kumar Chattopadhyay


_____ Date: 10.01.2014
Member: Dr. Joydeep Ghosh


_____ Date: 10.01.2014
Member: Dr. Devendra Sharma

Final approval and acceptance of this dissertation is contingent upon the candidate's submission of the final copies of the dissertation to HBNI.

I hereby certify that I have read this dissertation prepared under my direction and recommend that it may be accepted as fulfilling the dissertation requirement.

10.01.2014
Date: _____
Place: ~~Almed~~ 


Supervisor: Dr. Prabal Kumar Chattopadhyay

STATEMENT BY AUTHOR

This dissertation has been submitted in partial fulfillment of requirements for an advanced degree at Homi Bhabha National Institute (HBNI) and is deposited in the Library to be made available to borrowers under rules of the HBNI.

Brief quotations from this dissertation are allowable without special permission, provided that accurate acknowledgement of source is made. Requests for permission for extended quotation from or reproduction of this manuscript in whole or in part may be granted by the Competent Authority of HBNI when in his or her judgment the proposed use of the material is in the interests of scholarship. In all other instances, however, permission must be obtained from the author.

Kshitish Kumar Barada
Kshitish Kumar Barada

DECLARATION

I, hereby declare that the investigation presented in the thesis has been carried out by me. The work is original and has not been submitted earlier as a whole or in part for a degree/diploma at this or any other Institution/University.

Kshitish Kumar Barada

Kshitish Kumar Barada

“There is nothing in a caterpillar that tells you it's going to be a butterfly”

..... *Richard Buckminster Fuller*

Architect, systems theorist, author, designer, inventor, and futurist

Dedicated to

My Family

ACKNOWLEDGEMENT

This thesis is complete because of numerous supports I have got from different people. First and foremost I thank my supervisor Dr. Prabal Kumar Chattopadhyay for his guidance and support throughout this thesis work. Though I have done experiments in my university, he introduced me to experimental techniques through the study of electrical noise. I would like to thank him for the freedom and openness he provided me with. Discussions with him always started from experimental techniques and ended in nice physics. I would also like to thank Dr. Joydeep Ghosh for encouragement in the rough periods of my thesis and also for fruitful physics discussions. Thanks are due to Prof. Yogesh Saxena for constant encouragement and constructive criticism which gave favorable direction to this thesis. I would also like to thank Dr. Devendra Sharma for the understanding I have on sheaths and double layers.

I am indebted to Dr. R. Ganesh, Dr. Sudip Sengupta, Dr. Devendra Sharma, Prof. R. Jha and Prof. Amita Das for excellent teaching during the course work which helped me to understand basics of plasma physics. I express my sincere thanks to Academic Dean, Dr. Mukherjee for his timely help. I would like to extend my sincere gratitude to Shравan bhai, Shilpa mam, Smita mam, Pragnya mam, Arundhati mam, Hemant bhai, Shailendra bhai, Sutapa mam and all Library and Computer Centre Staff members for their support on many occasions. I extend my thanks to Atrey Sir, Chamunde ji, Harvey ji, Sourbhan ji, Khanduri ji, Vartak ji, Savai ji, Sirin mam, Silel ji and Hitesh bhai for all the administrative helps.

Staying in a hostel away from home never turned out to be difficult because of my friends, juniors and seniors with whom I discussed my life, my Physics problems. Playing in the weekends was utmost a necessity in these seven years. I would like to thank every one of them for their love and support they have provided me with during this period. I thank you Ujjwal, Gurudatt, Vikram, Sita, Prabal, Ashwin, Deepak for always reminding me that we are the best. I thank Neeraj bheya, Pintuda, Ritudi, Rajneesh bheya, Manas bheya, Bhaskar bheya, Anuraga bheya, Mayadi, Kishor bheya, Vikrant bheya, Sunitadi, Shekhar bhai, Jugal bhai, Satya bhai, Sharad bhai, Sushil, Rameswar, Sanat, Pravesh, Manjeet, Sayak, Soumen, Aditya, Vara, Mangi,

Vidhi, Deepa, Akanksha, Neeraj, Chandrasekhar, Meghraj, Harish, Rupendra, Bibhu, Samir, Arghya, Debu, Bhumika, Anup, Ratan, Amit, Sonu, Umesh, Surabhi and Modhu.

I cannot forget those relaxing moments while trekking in the forests of Gujarat with Govind bhai, Mahesh and Ghate in the frustrating periods of my life in between. Surprisingly, it was awesome to know you three and I hope I have made a lasting impression on you as you have on me. In the lab Sayak, Manjit and Soumen always provided a conducive and joyful atmosphere for physics study. Thank you friends. Arindam bheya, it's you who triggered the interest in diagnostics in me. What a time we had! Thank you very much for being a part of my life even today. I would like to thank Acharya ji, Sadrakhiya ji, Vishnu bhai, Swadesh bhai, Narendra bhai, Madan ji and Variaji for their support in building up my experimental set up and Madan ji for showing the Ahmedabad market. Thanks are due to Jignesh bhai, Praveenlal and all electronics group member for their help in electronics circuits for diagnostics. Jiba's food has always been blended with his love for us which made the hygienic and healthy food tastier. When I used to go home, I always missed his food.

This work would not have completed without the constant support, patience and encouragement from my parents and family members. Dear Daddy, I learnt honesty from you and Mummy, I learnt determination from you. My sweet younger sisters and brother, your love will remain always with me. Finally, I would like to thank all those who have come into my life, putting an unforgettable impression in my life including my classmates and teachers at school, college and University.

Kshitish Kumar Barada

LIST OF PUBLICATIONS

1. **Kshitish K. Barada**, P. K. Chattopadhyay, J. Ghosh, Sunil Kumar, and Y. C. Saxena. "A linear helicon plasma device with controllable magnetic field gradient." **Review of Scientific Instruments** **83**, 063501 (2012).
2. **Kshitish K. Barada**, P. K. Chattopadhyay, J. Ghosh, Sunil Kumar, and Y. C. Saxena. "Observation of low magnetic field density peaks." Under review **Physics of Plasmas** **20**, 042119 (2013)
3. **Kshitish K. Barada**, P. K. Chattopadhyay, J. Ghosh, Sunil Kumar, and Y. C. Saxena. "Experimental Observation of Left Polarized Wave Absorption near Electron Cyclotron Resonance Frequency in Helicon Antenna Produced Plasma." **Physics of Plasmas** **20**, 012123(2013)
4. **Kshitish K. Barada**, P. K. Chattopadhyay, J. Ghosh, D.Sharma, and Y. C. Saxena. "Charging of a plasma filled dielectric glass wall wrapped in a helicon antenna" to be submitted.
5. **Kshitish K. Barada**, P. K. Chattopadhyay, J. Ghosh, D. Sharma, and Y. C. Saxena. "Diverging magnetic field near helicon antenna increases antenna coupling efficiency in low magnetic field operation." To be submitted.
6. **Kshitish K. Barada**, P. K. Chattopadhyay, J. Ghosh, D. Sharma, and Y. C. Saxena. "Transition from a quasi double layer to a multiple double layer containing current free plasma" to be submitted.
7. **Kshitish K. Barada**, P. K. Chattopadhyay, J. Ghosh, D. Sharma, and Y. C. Saxena. "The downstream density peak in low magnetic field helicon discharge" to be submitted.

Contents

Abstract.....	iv
List of Figures.....	v
List of Tables.....	xi

Chapter 1: Introduction

1.1 History of Helicon Sources.....	1
1.2 Review of Relevant Previous Work.....	3
1.3 Motivation and objective	6
1.4 Description of chapters and main findings	7
References.....	11

Chapter 2: Helicon Physics

2.1 Introduction.....	16
2.2 Derivation of dispersion relation	17
2.2.1 Vacuum Waves	17
2.2.2 Plasma Waves	20
2.3 Oblique propagation and Resonance cone.....	32
2.4 Helicon waves in a cylinder.....	34
2.5 Helicon mode structure in non uniform radial density	37
2.6 Models of Helicon Power Deposition.....	38
2.7 Mode Transitions in Helicon Discharge	39
2.8 Summary of the Chapter	41
References.....	42

Chapter 3: Experimental Set up and Diagnostics

3.1 Introduction.....	45
-----------------------	----

3.2 Vacuum Vessel and Vacuum System	45
3.3 Electromagnets.....	47
3.4 Antenna and RF Matching Circuit.....	49
3.4.1 The Antenna	51
3.4.2 Matching Network.....	52
3.5 Diagnostics.....	56
3.5.1 Single Langmuir Probe.....	56
3.5.2 Wall Probe.....	65
3.5.3 RF Compensated Probe	68
3.5.4 Double Langmuir Probe	73
3.5.5 Triple Langmuir Probe	77
3.5.6 Emissive Probe.....	82
3.5.7 B-dot Probe	90
3.5.8 Antenna-Plasma Load Measurements	92
3.6 Summary of Chapter 3	93
References.....	94
 Chapter 4: Helicon Characterization	
4.1 Antenna Efficiency	98
4.2 Discharge mode transitions.....	101
4.3 Mode structure at Low magnetic field	104
4.4 Axial density profile	107
4.5 Observation of Current free double layer	109
4.6 Summary of Chapter 4.....	110
References.....	112

Chapter 5: Low Magnetic Field Helicon Study

5.1 Introduction.....	114
5.2 Multiple Density Peaks.....	117
5.3 Polarization reversal and asymmetric density peaking.....	126
5.4 Downstream Density Peak.....	134
5.5 Efficient Low Field Helicon Source	139
5.6 Conclusions.....	144
References	146

Chapter 6: Current Free Double Layer

6.1 Introduction.....	149
6.2 Boltzmann Plasma Expansion.....	150
6.3 Double Layer	152
6.4 Current Free Double layer	155
6.4.1 Helicon CFDL experiments	155
6.4.2 Helicon CFDL Models	156
6.4.3 Helicon CFDL instabilities	158
6.4.4 Effect of Magnetic field Strength and Gradient.....	159
6.5 Study of Dielectric Wall Charging	160
6.6 Experimental Observations of multiple CFDL.....	165
6.7 Summary of Chapter 6.....	174
References.....	175

Chapter 7: Conclusion and Future Work

7.1 Conclusion	179
7.2 Future Work.....	181

ABSTRACT

Diverging magnetic fields are found naturally in universe including our magnetosphere and in solar coronal funnels. Diverging magnetic fields are used in expanding plasmas to accelerate particles by electric fields produced by localized potential structures, called double layer, formed self consistently inside the plasma. Acceleration of charged particles in low temperature plasmas is of interest to surface function modification as well as to development of electrostatic thrusters. This thesis devotes its study to find the role of diverging magnetic fields in helicon source operation and self consistent potential structure formation in bulk of plasma. A geometrically expanding (small diameter source attached to a bigger diameter expansion chamber) linear helicon device along with various diagnostics is designed and built with a diverging magnetic field. The helicon plasma produced with an $m = +1$ half helical antenna powered by a 2.5 kW RF power source at 13.56 MHz is characterized. Mode transitions are observed and mode structures are studied at low magnetic fields (<100 G). Though a monotonic increase in density with magnetic field is expected for helicon plasma, multiple density peaks are observed for the first time for field variations at low magnetic fields and are explained on the basis of oblique resonance of helicon waves in a bounded geometry for the first time. Characterization on both sides of the antenna at low magnetic fields revealed the role of left circularly polarized waves in electron cyclotron absorption in bounded plasmas. Changing the magnetic field topology at low magnetic fields, it is found that diverging magnetic fields near antenna can increase the efficiency of the source as high as 80 % from the zero field case. With a magnetic field ~ 100 G near the source and ~ 10 G at the end of the expansion chamber, density peaks on axis are observed nearly two wavelengths away from the antenna where the field is ~ 35 G. Helicon wave phase measurements show that the wave does not propagate in the source region owing to the density cut-off of the wave but starts to propagate in the downstream for lower densities and magnetic fields. Finally, diverging magnetic fields and their gradient near the geometrical expansion location are varied to create strong potential structures along the magnetic field direction. The very first direct observation of multiple potential structures of varying strengths in current free plasmas is presented in this thesis.

List of Figures

Figure 2.1 Dispersion of electromagnetic waves parallel to magnetic field showing the range of operation of Helicon waves in $n^2 - \omega$ diagram.

Figure 2.2 Coupling of Helicon and TG modes at low magnetic field for different N_{\parallel} at density $n_e = 10^{17} \text{ m}^{-3}$ for $m = +1$ mode.

Figure 2.3 n-B diagram showing the parameter space of Helicon and TG modes.

Figure 2.4 Resonance cone showing the infinite potential surface of a point source at cone apex.

Figure 2.5 Mode structure of $m=0, +1$ modes in a plasma with cylindrical boundary.

Figure 2.6 Mode transition in a helicon discharge by changing magnetic field.

Figure 3.1 Picture of Helicon experimental Set up.

Figure 3.2 Schematic of the helicon experimental set up.

Figure 3.3 (a) Plot for magnetic field produced by 6 magnets at -47.8, -38.5, -20, -3.5, 13, 30 by passing a positive current of 52 Ampere and (b) additional variable current in the seventh coil at 47 cm to get a variable gradient.

Figure 3.4 Picture of the inside of the match box showing the variable Load and Tune Capacitors with auxiliary inductors.

Figure 3.5 Picture of the half helical $m=+1$ antenna just before installation.

Figure 3.6 Schematic of the matching network attached to RF generator and a load composed of the antenna and plasma.

Figure 3.7 Smith Chart showing operational matching regimes of the current matching network attached to an inductive helicon antenna.

Figure 3.8 Typical IV characteristics of Langmuir probe with sheath ionization.

Figure 3.9 Schematic of SLP measurement circuit.

Figure 3.10 Equivalent electrical circuit of a Langmuir probe for time varying bias and current measurements.

Figure 3.11 Voltage drop across a measuring resistance in the absence of plasma for different bias frequencies applied to Langmuir probe through a RG 58 coaxial cable of 2 meter length showing the limitations of bias frequency.

Figure 3.12. (a) Instantaneous flow of excess electrons to the wall in response to an RF voltage in an RF cycle. (b) Subsequent decrease in the average value of induced voltage i.e. floating potential of the wall.

Figure 3.13 Schematic of the wall probe measurement arrangement.

Figure 3.14 Picture of the wall probe for DC bias measurement.

Figure 3.15 Picture of the RF compensated probe along with an uncompensated probe.

Figure 3.16 Schematic of the RF compensated probe along showing the compensating winding, coupling capacitor and the self resonating RF chokes.

Figure 3.17 Comparison of IV characteristics of compensated and uncompensated Langmuir probe.

Figure 3.18 Schematics of Double Langmuir probe measurement circuit.

Figure 3.19 Determination of temperature from double probe IV characteristics.

Figure 3.20 Double Probe characteristics measured at $z=22$ cm for different RF for powers 50-500 W with 4×10^{-3} mbar pressure and 55 Gauss magnetic field.

Figure 3.21 Schematics of the triple Langmuir probe circuit

Figure 3.22 Potential diagram of TLP.

Figure 3.23 Modified circuit of TLP with optical isolation for instantaneous display of ion saturation current and temperature.

Figure 3.24 IV characteristics of an emissive probe showing the bias dependence contributions from emission current and collection current [35].

Figure 3.25 Plasma potential determination by floating potential method where an emitting probe's floating potential approaches the local plasma potential for strong emission.

Figure 3.26 Plasma potential determination by inflection point method, where the differentiated IV characteristic of a partially emitting hot probe has an inflection point near the plasma potential [35].

Figure 3.27 Plasma potential determination by separation point method where the IV characteristics of cold and hot probes separate from each other.

Figure 3.28 Schematic of the emissive probe for measurement of plasma potential with floating potential method.

Figure 3.29 Floating potential variation of emissive probe with filament heating current in plasma measured at $z=50$ cm for 200 G source magnetic field, 100 W RF power and 2×10^{-4} mbar pressure

Figure 3.30 Picture of the single loop B-dot probe made of a coaxial cable.

Figure 3.31 The graphs showing the inherent electrostatic pick up rejection by use of a single loop b-dot probe. The probe output for 0 deg (red), 180 deg (black) and 360 deg (blue) showing the capacitive pick up is negligible.

Figure 4.1 Variation of antenna RMS current and antenna resistance with RF power in vacuum at 5×10^{-5} mbar.

Figure 4.2 (a) Antenna current and (b) estimated antenna-plasma resistance variation with RF power at 2×10^{-3} mbar Ar and 100 G magnetic field measured at Z=22 cm.

Figure 4.3 Mode transitions observed at 100 Gauss for different Argon pressures. Transitions are observed (a) in density variation with power at $z=20$ cm and (b) in load capacitor values of the matching network.

Figure 4.4 Radial density profile for two different RF powers (50W and 600W) at pressure $\sim 2 \times 10^{-3}$ mbar and magnetic field ~ 100 G measured at Z=22 cm.

Figure 4.5 Radial variation measured B_z (circles) at 30 G, 300W and 2×10^{-3} mbar. The solid lines are theoretical curves of pure $\mathbf{m} = +1$ mode along with mixed modes with 25%, 50%, 75% and 100% additional $\mathbf{m} = 0$ mode content. All values are normalized to 1.

Figure 4.6 Radial variation of B_z amplitude in normalized units for 300W RF power, 30 G and Argon neutral pressure of 2×10^{-3} mbar measured at Z=40 cm.

Figure 4.7 Variation of axial magnetic field of Helicon wave along the axis for 600 W RF power at pressure $\sim 2 \times 10^{-3}$ mbar and magnetic field ~ 100 Gauss.

Figure 4.8 Axial variation of helicon wave phase measured at $r=0$ with a single loop B-dot probe at $\sim 2 \times 10^{-3}$ mbar, 300W and 100 G magnetic field.

Figure 4.9 Axial variation of density measured at $r=0$ for three powers 200W, 300W and 400W, source magnetic field of 100 G and 2×10^{-3} mbar Ar pressure.

Figure 4.10 Axial variations of (a) plasma potential and (b) plasma density at 2×10^{-3} mbar and 1.2×10^{-4} mbar of Argon with RF power of 600W and 280 G magnetic field in source.

Figure 5.2 Density variation with applied magnetic field in the WOMBAT experiment. Degeling et al .

Figure 5.2 Plasma density on axis at $z = 20$ cm versus magnetic field. (a) 300, 400, and 500 W RF power, $p = 2 \times 10^{-3}$ mbar, (b) 300, 400, and 500 W RF power, $p = 0.8 \times 10^{-3}$ mbar, and (c) 100, 200, and 350 W RF power, $p = 0.4 \times 10^{-3}$ mbar.

Figure 5.3 C_L values of the matching network at $z = 20$ cm versus magnetic field. (a) 300, 400, and 500 W RF power, $p = 2 \times 10^{-3}$ mbar, (b) 300, 400, and 500 W RF power, $p = 0.8 \times 10^{-3}$ mbar, and (c) 100, 200, and 350 W RF power, $p = 0.4 \times 10^{-3}$ mbar.

Figure 5.4 Axial profile of the axial component of the wave magnetic field at two different (30 and 50 G) ambient magnetic fields.

Figure 5.5 Variation of phase with distance for $p = 0.4 \times 10^{-3}$ mbar, RF power 350 W. $B = 30$ G (open circle) and $B = 50$ G (open diamond).

Figure 5.6 radial density profile for different powers measured at $z=20$ cm for 30 G magnetic field and 2×10^{-3} mbar

Figure 5.7 Floating potential fluctuation amplitude variation with magnetic field measured for RF powers of 200 W, 300 W and 400 W with argon fill in pressure of 0.8×10^{-3} mbar.

Figure 5.8 $m=|l|$ propagation direction for normal and reverse field directions shown schematically.

Figure 5.9 Variation of electron density (n_e), visible light intensity (I_{vis}) and antenna plasma resistance (R_p) with magnetic field for 500 W at pressure 1.4×10^{-3} mbar. (a) n_e at +18 cm, (b) n_e at -18 cm, (c) I_{vis} at +18 cm, (d) I_{vis} at -18 cm and (e) R_p

Figure 5.10 Variation of electron density (n_e) with magnetic field for 300, 400 and 500 W at pressure 1.4×10^{-3} mbar. (a) n_e at +18 cm and (b) n_e at -18 cm.

Figure 5.11 Variation of electron density (n_e) with magnetic field for 500 W at pressures 8×10^{-4} , 1.4×10^{-3} and 2.4×10^{-3} mbar. (a) n_e at +18 cm, (b) n_e at -18 cm

Figure 5.12 Variation of electron density (n_e) with magnetic field for 500 W at pressure 1.4×10^{-3} mbar. (a) “normal B” and (b) “reverse B”. n_e at +18 cm, (b) n_e at -18 cm. Inset of (a) at +18 cm “normal B” (open triangle) and “reverse B” (+).

Figure 5.13 Radial variations of axial wave field component of helicon waves measured at $z = +18$ cm for both directions of magnetic field at (a) 12 G, “normal B” (open diamond) and “reverse B” (open circle) (b) 30 G, “normal B” (open diamond) and “reverse B” (open circle).) RF power is 500 W and pressure 1.4×10^{-3} mbar.

Figure 5.14: Axial variation of density and magnetic field, $p=4 \times 10^{-4}$ mbar, power=400W, (a) Reverse current in 7th coil & (b) no current in 7th coil.

Figure 5.15 Variation of helicon B_z phase along axis for 88 G source magnetic field, 300W RF power and 8×10^{-4} mbar neutral pressure.

Figure 5.16 Axial variation of density for 200W, 300W and 400W at there argon neutral pressures of (a) 2×10^{-3} mbar, (b) 8×10^{-4} mbar & (c) 4×10^{-4} mbar. Magnetic field at antenna centre is 88 G.

Figure 5.17 Axial variation of magnetic field for Cases A-D when 1 A current is passed in the coil(s).

Figure 5.18 variation of density at $z = +18$ cm with applied magnetic field at antenna centre for Cases A-D. RF power is 300W and pressure 8×10^{-4} mbar.

Figure 5.19 variation of density at $z = -18$ cm with applied magnetic field at antenna centre for Cases A-D. RF power is 300W and pressure 8×10^{-4} mbar.

Figure 5.20 Variation of density at $z = -18$ cm with applied magnetic field at antenna centre for Cases A-D. RF power is 300W and pressure 8×10^{-4} mbar

Figure 5.21 Increase in efficiency from the zero field case to the efficiency at the density peak for the four field topologies shown in Figure 5.20.

Figure 6.1 Ambipolar plasma expansion in diverging magnetic field.

Figure 6.2 Electric potential, electric field and space charge distribution inside a double layer [13].

Figure 6.3 Potential distribution $\Phi(x)$, and the ion and electron phase space distributions across a DL with potential drop Φ_0 (and the corresponding internal electric field \mathbf{E}). The hatched areas indicate accelerated populations. The reflection of ions and electrons within the separatrices (symmetrically placed broken and barred curves) are indicated by the arrows symbolizing velocity reversal. Ions or electrons with energy larger than Φ_0 (with very large initial velocity) are not reflected but can pass through the DL, as indicated.

Figure 6.4 Chi-Kung source, axial applied magnetic field, measured axial plasma potential and density at 250 W RF power, 0.2 mTorr and 130 G at source.

Figure 6.5 Axial variation of DC bias potential for different RF powers at Argon fill- in pressure of 4×10^{-4} mbar. the shaded region are the antenna circular ring positions.

Figure 6.6 Variation of DC bias potential with power near antenna ring at $z = +9$ cm at Argon pressure of 4×10^{-4} mbar.

Figure 6.7 Variation of DC bias potential with neutral pressure of Argon at RF power of 300 W and magnetic field 200 G.

Figure 6.8 Variation of DC bias potential with magnetic field for three different gases: Helium, Argon and Krypton at magnetic field of 200G and neutral gas pressure of 4×10^{-4} mbar.

Figure 6.9 Experimental set up with new coil positions to study the role of magnetic field gradient on CFDL formation.

Figure 6.3 Axial component of dc magnetic field and (c) its gradient for different coil current. 4 coils are placed at -24.5 cm, -6.5 cm, 12.5 cm, and 28 cm with +95 A. 5th coil is placed at 46 cm and given currents are +35 A, 0 A, -35 A, and -95 A.

Figure 6.11 Plasma potential variation on axis measured at $z=18$ cm with source magnetic field for 100 W RF power and 2×10^{-4} mbar Argon pressure.

Figure 6.4 Variation of floating potential near the wall and plasma potential at the axis measured at $z=20$ cm in the source chamber with the last coil negative current. Current in four other coils are 95 A each. RF power 100 W, pressure 2×10^{-4} mbar.

Figure 6.5 Variation of edge and central current density in the source chamber with the last coil negative current. Current in four other coils are 95 A each. Rf power 100 W, pressure 2×10^{-4} mbar.

Figure 6.6 Variation of plasma potential along the axis of the device for different current in the last coil; circle -95 Amp, square -35 Amp, Triangle 0 Amp and star =35 Amp. Current in other four coils placed at 30.5 cm, 18 cm, 10.6 cm, 3cm are +95 Amps each.

Figure 6.15 Radial variation of plasma potential with I_v measured at $z=18$ cm with an L-shaped emissive probe for 100W RF power and 2×10^{-4} mbar Argon pressure.

List of Tables

Table 3.1 Parameter regime, length scales and time scales of the present helicon experiment.

Introduction

This chapter initially reviews history of helicon wave research and its applications in brief. Later, it reviews research on helicon physics relevant to the present thesis work. This will be followed by the motivation and objectives of the thesis work. Finally, the content and important findings of this thesis work will be summarized.

1.1 History of Helicon Sources

Plasma is a complex medium which supports many mechanical and electromagnetic waves. Plasma waves are often classified as electrostatic or electromagnetic waves. Moreover, the direction of propagation and polarization with respect to the magnetic field is often used for detailed classification. Magnetic fields introduce anisotropy in the plasma medium for which magnetized plasmas support a number of waves both in parallel and perpendicular directions. Right circularly polarized electromagnetic waves propagating along the magnetic field are typically referred to as whistler [1]. The name is derived from the whistling audio tones with constant amplitude and declining frequency received in radio receivers during World War I [2] which were mistaken as flying grenades. Barkhausen [3] explained this phenomenon as the highly dispersive broadening of a sharp pulse, initiated by lightning that propagates in the ionosphere. Storey [4] performed measurement on whistling atmospherics and described them as right handed circularly polarized waves that propagate in free space where ion effects and collisions were neglected. Helicon waves are whistler waves in a bounded plasma so that the wavelength is of the order of the plasma dimensions. They are quasi-electromagnetic waves and

are different from classical whistler waves which are purely electromagnetic in nature. Helicons can have both right and left handed polarizations compared to whistlers which have only right hand polarization.

In 1960, Aigrain [5] suggested the possibilities of observing whistler waves in solid state plasmas. Aigrain called the wave a helicon wave because the electric field traces out a helix when the wave propagates along the magnetic field. In an accidental observation, Bowers et al [6] reported experimental finding of helicon wave while measuring the hall resistivity of a pure sodium metal using a static magnetic field parallel to the applied oscillating magnetic fields. They observed a damped oscillation whose frequency was proportional to the applied DC magnetic field instead of an expected decaying signal in the output of the receiver coil. They identified the waves as those proposed by Aigrain. Detailed theory for the propagation and damping of helicon waves was given by Legendy [7] for solid state plasmas and Klossenberg, McNamara and Thonemann (KMT theory) [8] for gaseous plasmas. Following these theories, Harding and Thonemann [9] carried experiment in indium and showed good agreement with the theoretical prediction. Much of the early work on helicon wave was in solid state plasmas because of an immediate use as a diagnostics for measuring Hall coefficients in pure metals. Lehane and Thonemann [10] first observed helicon waves in gaseous plasma and found a very good agreement with wave axial damping rates given by KMT theory. Gallet et al [11] used helicon waves in gaseous plasma in toroidal ZETA fusion device as a diagnostics for measurement of plasma density and static magnetic field by measuring the damping of the helicon waves using magnetic probes.

First use of helicon waves as an efficient source for plasma production was demonstrated by Boswell [12] who using a double loop antenna at 8 MHz produced plasma of $4 \times 10^{18}/\text{m}^3$ density with a magnetic field of 1.5 kilo Gauss and RF power of 600 W. This density was higher by an order from the conventional RF discharges with equal RF input power and magnetic field. This high efficiency plasma production led to increased interest in helicon plasma physics as well as its various potential applications. Today they are considered for many applications like material processing, [13], negative ion production [14], Preionization [15-17] and current drive [18-19] in fusion plasmas and for space propulsion [20-22].

The mechanism responsible for efficient coupling of RF power into helicon source plasmas is still under investigation. Many collisional and collisionless processes are proposed in the last two decades. The prominent models are Landau damping [23-27], parametric turbulence [28-29], helicon to TG mode conversion [30-32], radially localized helicon modes [33-34] and nonlinear trapping of electrons in helicon wave fields [35-36].

1.2 Review of Relevant Previous Work

Diverging magnetic fields in nature are found in our magnetosphere and solar coronal funnels. Diverging magnetic fields are seldom used in helicon sources. Recent observation of efficient helicon plasma production at low diverging magnetic fields [37] invites attention. Diverging magnetic fields are used in low pressure helicon discharges to produce ion beams for space propulsion and surface functionalization of semiconductor materials. Ion beams in helicon discharges are produced when ions get accelerated in an electric field produced self consistently in the bulk of the plasma. In a diverging magnetic field, design of efficient low magnetic field (<100 G) helicon sources and creation of potential structures at high magnetic fields (>100 G) are the topics of study in this thesis.

Helicon wave frequency lies in the frequency range $\omega_{ci} \ll \omega \ll \omega_{ce} \ll \omega_{pe}$ where ω_{ci} , ω , ω_{ce} and ω_{pe} are the ion cyclotron, RF source, electron cyclotron, and plasma frequencies respectively. Most of the helicon source including the one presented in this thesis use 13.56 MHz RF source. This correspond electron cyclotron frequency for axial magnetic field of 5 G. Helicon sources normally operate with magnetic fields in the range of 200 G to 1000 G. This makes electron cyclotron frequency is at least 15 times than applied RF frequency. This we will call as normal magnetic field operation. However, when the magnetic goes down near to the value where cyclotron frequency is few times the applied RF frequency we will call it low magnetic field (“low-B”) operation.

Appearance of helicon mode is generally identified by mode transitions which involves a transition from a capacitive to inductive to wave sustained discharge. The step like transitions can be observed in measured plasma density and antenna-plasma resistance, obtained by either

increasing power at fixed magnetic field (B) of few hundred Gauss or vice versa. At high magnetic fields, it is observed that the density increases with applied magnetic field when the discharge is in helicon mode as per the dispersion relation. However, previous studies have shown that at low magnetic fields of less than 100 Gauss, plasma density peaks at some specific magnetic fields, generally between 20 Gauss to 50 Gauss in different experiments using 13.56 MHz RF system [37-44]. Unlike usual helicon discharge mode transitions at high magnetic fields (few hundred Gauss), the observation of density peaks at low magnetic fields seems to be a resonance phenomenon.

Chen [39] first reported this low magnetic peak in 2 cm diameter helicon discharge using 1600 W RF power where the density peak was observed at ~ 50 G with peak density of $6 \times 10^{18} \text{ m}^{-3}$ an increase of nearly 40% from the no field case. Degeling et al [38] have observed density peak around 50G for RF powers in 500-2000 W in a 18 cm diameter source using single loop antenna at 13.56 MHz. Wang et al [41] have shown that the a higher magnetic field is required for the density peak to occur for a plasma formed using higher ion mass or a higher source frequency. Recently Lafleur et al [37] have done extensive experiments in a diverging magnetic field helicon experiment and have shown that the density can increase by an order from the no field case.

Few explanations are available for the observed density peak at low magnetic fields. Some of them are TG-helicon coupling [45, 47] at low magnetic fields, non-linear wave particle trapping [37-38] and wall reflection [46].

More recently, helicon waves have been considered for space plasma propulsion. They have been considered either as an ionizing source with a secondary stage for acceleration or as a stand-alone propulsion device. Concept such as VASIMIR [20] utilizes helicon as an ionizing source and worry about magnetic field detachment separately. Similarly, annular geometry helicon plasma is being investigated as a primary stage for space propulsion [21] and will have to address detachment and/or acceleration mechanism following the source. Another proposed method to circumvent the problem of detachment is utilizing double layer formation in helicon plasma [22]. The claim for this acceleration mechanism is that a sharp potential drop occurs downstream at lower pressure (<1 mTorr) in helicon plasma which can accelerate ions to supersonic speeds.

Double layer is a localized structure of layers of positive and negative space charges giving rise to a localized electric field much higher than the electric field outside double layer and is formed in the bulk of the plasma away from the boundaries unlike the sheaths which form near the boundary. In general, various groups of trapped electron/ion and passing electron/ion are postulated to maintain DL structure. All groups combinedly decide the net current across DL. A non zero net current corresponds to current driven DL (CDDL) whereas zero net current corresponds to CFDL. A large number of experiments on DL have been carried out in different devices such as, discharge tube, double and triple plasma devices, Q-machines and expanding plasma devices. [48-50]. Following Perkins and Sun's prediction of CFDL in 1981 [51] experimental observations were reported on CFDL by Chan 1981 [52] and Hatakeyama 1983 [53] in a triple plasma device. Subsequently, two new classes of CFDL were reported; one by Hairapetian and Stenzel [54] and the other by Charles and Boswell [55] in expanding plasmas produced by helicon antenna. Hairapetian and Stenzel have explained the existence of CFDL based on two electron population. However, for expanding plasma in helicon devices four prominent models [56-59] have been proposed. These models while not complete have described experimental observation to some extent. All of these models include a thermal ion population in the upstream and a flowing ion population downstream as well as a thermal electron population upstream. They differ in their treatment of an additional electron population on the upstream side of the double layer. Model by Takahashi et al [59] proposes an electron distribution in the downstream as a depleted energetic electron tail to overcome the potential drop of the DL and neutralize the ion beam.

CFDL in a helicon plasma device is forced to be current free due to insulating source tube allowing no net current. Since the reporting of low pressure helicon CFDL in 2003 [55] a lot of work [60-69] has been focused on parametric study like effect of magnetic field, pressure, gas mass, geometry of experimental set up and antenna frequency. Ion beams created by acceleration due to the potential structure are a potential option for space propulsion. The rapid potential change near the expanding magnetic field with an associated acceleration of ions by the DL electric field is now being employed in the development of plasma thrusters. Meige et al [70] have done 1D simulation and found that finite wall charging is necessary for the CFDL formation and it may be noted that this can be a reason that no CFDL formation is reported so far without use of dielectric source tubes. So, it is important to understand the dependence of DL

strength on various plasma parameters as well as magnetic field geometry along with the role of wall charging on CFDL formation.

Charles and Boswell [71] studied the role of magnetic field on CFDL formation. By increasing the magnetic field they have observed ion beam formation in downstream plasma for a critical magnetic field of 50 G in the source. The source potential and density increased simultaneously at 50 G but in the downstream plasma the effect was little. Ion magnetization at 50 G is attributed to this transition from an expanding plasma to a plasma containing a CFDL. When the ion is magnetized the ion loss to the radial wall decreases and amounted to the density rise. Similar results were obtained by Takahashi et al [69] in EMPI source have shown that for two different dielectric source tubes of radii of 3.25 cm and 2.3 cm, the CFDL is formed for 125 G and 195 G respectively the values of these magnetic fields also are the magnetic fields where the ions got magnetized.

Though the observations of the CFDL were reported by many authors, the location and strength of the CFDL dependency on magnetic field gradient and magnetic field topology is not clear. The role of magnetic field gradient and its location was studied by Sutherland et al [67], Byhring et al [63] and Schroder et al [64]. Sutherland et al. [67] showed that the CFDL strength could be scaled by a factor of at least 2 in a bigger system and that the double layer presumably forms in the vicinity of maximal gradient of the magnetic field. Byhring et al [63] changed the magnetic field gradient by using an extra coil in which the current is passed in the same direction as the other coils. So by increasing the current in their last coil they could decrease the magnetic field gradient which location was much inside the source plasma. They have found that CFDL vanished for higher last coil currents which were confirmed by RFEA measurements. A study on independent effects of geometric expansion, magnetic field and field gradient along with its location are studied by Schroder et al [64] in VINETA device. For magnetic field gradient location coinciding with the geometric expansion they have found the CFDL strength is highest.

1.3 Motivation and objective

The primary objective of the work described here in the thesis is to develop a helicon plasma source in geometrically and magnetically diverging configuration. Design, fabricate and operation of each subsystems have been carried out during the thesis work. This thesis aims to

study characterizing discharge modes, investigating the mechanism responsible for low magnetic field density peak, studying double layer and its relation with the wall charging.

1.4 Description of chapters and main findings

The work described in this thesis has two main elements; (1) Development of experimental system and (2) Physics studies in the system. This thesis consists of seven chapters. The first chapter is an introduction to helicon research and also includes the motivation and objective of the thesis. The second chapter describes theory of helicon wave dispersion, wave mode structure, physics of discharge mode transitions and power coupling to plasma. In the third chapter experimental set up and its sub-systems along with various diagnostics used are discussed. After describing the previous studies, experimental set up and diagnostics in chapter 1, 2 and 3, the initial characterization of the RF plasma produced in the linear plasma device is described in Chapter four. Once the system is evacuated to 1×10^{-6} mbar, Argon gas is fed into the system at 5×10^{-3} mbar pressure through the end flange connected to the source chamber. After that RF power is slowly delivered to the antenna through the matching network. Gas breakdown is observed at few W (< 10 W) of RF power with almost no reflected power without magnetic field. We have obtained various plasma discharges in the pressure range of 1×10^{-4} mbar to 1×10^{-2} mbar by applying suitable magnetic field in the span of 0 to 280 Gauss and RF power in the range of few Watts to 1.5 kW. Thus the neutral pressure, magnetic field and RF power are the controlling parameters of our experiment. Mode transitions are studied by measuring density and load capacitance values (a measure of antenna-plasma coupling) for different pressures by varying the RF power. By increasing the pressure, Helicon operation regime is achieved for 112 Gauss magnetic field. The values of RF power at which the transitions occurred are lower for higher neutral pressures. Helicon $m=+1$ modes are characterized by measuring the radial and axial wave profile. The axial wavelength of the helicon waves are measured by measuring the axial phase variation using a single loop B-dot probe with respect to another reference B-dot probe phase fixed at a constant radial and axial location. Axial plasma potential is measured with a floating emissive probe at low pressure, 600 W RF power and 288 Gauss magnetic field. Plasma potential drops of $\sim 8T_e$ are observed over $\sim 1000 \lambda_D$ distance. These above mentioned preliminary results along with the details of the experimental set up and its capabilities are published in **Rev. Sci. Instrum.** **83**, 063501 (2012).

Low field helicon experiments in a diverging magnetic field configuration are discussed in chapter five. Experiments are carried out using argon gas with $m = +1$ right helical antenna operating at 13.56 MHz by varying the magnetic field from 0 Gauss to 100 Gauss (G). The plasma density 18 cm away from antenna centre varies with varying the magnetic field at constant input power and gas pressure and reaches to its peak value at a magnetic field value of ~ 25 G. Another peak of smaller magnitude in density has been observed near 50 G. Measurement of amplitude and phase of the axial component of the wave using magnetic probes for two magnetic field values corresponding to the observed density peaks indicated the existence of radial modes. Measured parallel wave number together with the estimated perpendicular wave number suggests oblique mode propagation of helicon waves along the resonance cone boundary for these magnetic field values. Further, the observations of larger floating potential fluctuations measured with Langmuir probes at those magnetic fields values, indicate that near resonance cone boundary, these electrostatic fluctuations are proposed to take energy from helicon wave and dump power to the plasma causing density peaks. The results are published in **Physics of Plasmas** **20**, 042119 (2013). Asymmetry in density peaks on either side of an $m = +1$ half helical antenna is observed both in terms of peak position and its magnitude with respect to magnetic field variation. However, the density peaks occurred at different critical magnetic fields on both sides of antenna. Depending upon the direction of the magnetic field, in the $m = +1$ propagation side, the main density peak has been observed around 27 Gauss (G) of magnetic field. On this side the density peaks around 5 G, corresponding to electron cyclotron resonance (ECR) is not very pronounced whereas on the $m = -1$ propagation side, very pronounced ECR peak has been observed around 5 G. Another prominent density peak around 13 G has also been observed on $m = -1$ side. However, no peak has been observed around 27 G on the $m = -1$ side. The density peak data is also supported by the light intensity measurements on both sides of the antenna. Reversing the magnetic field direction symmetrically reverses all the density peak observations. Observation of ECR peak around 5 G on $m = -1$ side is explained on the basis of the polarization reversal effect of circularly polarized waves in a bounded plasma while the other peaks on either side are explained with the help of cyclotron resonance for obliquely propagating helicon waves. The measured antenna-plasma resistance, a measure of power coupled to the plasma by the antenna, can only be explained if density variations on both sides of the antenna are taken into account. The results are published in **Physics of Plasmas** **20**, 012123 (2013). Experiments were

further performed by changing the divergence of the magnetic field near the helicon antenna. By increasing the divergence it is observed that the antenna plasma coupling increases. A helicon antenna generally has a k-spectrum but when the antenna is in a uniform magnetic field, the resonance cone propagation is achieved only for a single mode at a certain magnetic field. With a diverging magnetic field, many modes can have resonance cone propagation at a single magnetic field value at the antenna centre. The efficient coupling is explained on the basis of multiple mode absorption near antenna through resonance cone absorption for different magnetic fields available near the antenna. This conjecture is further strengthened by the observed higher values of density maintained for more values of magnetic field of 20 – 60 Gauss i.e. widening of the density peak as the divergence is increased. The manuscript based on these results is ready for submission. The resonance cone absorption is further studied at the downstream of the plasma where the magnetic field reduces to ~10 Gauss from ~100 Gauss at the source. Phase measurements show that helicon waves are stationary near the antenna and propagate only in the diffusion chamber. Density peaks are observed in the downstream where the resonance cone propagation angles are near the wave propagation angles. These results are reproduced for different power and pressure values. Normal ECR absorption at location where magnetic field ~ 5 Gauss, is observed in the downstream by varying the magnetic field configuration using an extra coil and supplying negative current to it w. r. t to other coils. The manuscript based on these results is ready to be submitted for publication.

Chapter six discusses the study of current free double layer near the geometrical expansion region of the plasma and the relation of this potential structure to charging of the dielectric wall and magnetic field gradient. Experiments are carried out to study the role of magnetic field gradient near the geometrical expansion location. The experiments are done at 100 W RF power and 2×10^{-4} mbar with different magnetic field gradients near the geometrical expansion of the chamber. It is observed that the increasing the magnetic field gradient, the CFDL structure evolved from a single weak CFDL to a multiple structure which consists of a strong CFDL and a weak CFDL. The plasma potential in the source dielectric chamber is with respect to the floating glass wall. The wall charges to a higher negative potential and lifts the plasma potential in the source chamber to higher positive values at low pressures. So the parametric dependence of dielectric wall charging caused by RF potential fluctuation induced into the plasma through the capacitance of the glass tube is studied near the antenna for different

RF power, neutral pressure, magnetic field and gas mass. Conclusions and future scopes are presented in the last chapter.

References

- [1] Paul Murray Bellan. *Fundamentals of plasma physics*. Cambridge University Press, 2006.
- [2] R. W. Boswell, *A Study of Wave in Gaseous Plasma*, Ph. D. Thesis, Flinders University, Adelaide, Australia (1974)
- [3] Barkhausen, Heinrich. "Whistling tones from the Earth." *Proceedings of the Institute of Radio Engineers* 18, no. 7 (1930): 1155-1159.
- [4] Storey, L. R. O. "An investigation of whistling atmospherics." *Philosophical Transactions of the Royal Society of London. Series A, Mathematical and Physical Sciences* 246, no. 908 (1953): 113-141.
- [5] Aigrain P, Proc. Int. Conf. on Semiconductor Physics, Prague (London: Butterworths) p 224(1960)
- [6] Bowers, R., C. Legendy, and F. Rose. "Oscillatory galvanomagnetic effect in metallic sodium." *Physical Review Letters* 7, no. 9 (1961): 339-341.
- [7] Legendy, C. R. (1964). Macroscopic theory of helicons. *Physical Review*, 135(6A), A1713.
- [8] Harding, G. N., and P. C. Thonemann. "A study of helicon waves in indium." *Proceedings of the Physical Society* 85, no. 2 (1965): 317.
- [9] Klozenberg, J. P., B. McNamara, and P. C. Thonemann. "The dispersion and attenuation of helicon waves in a uniform cylindrical plasma." *J. Fluid Mech* 21, no. 3 (1965): 545-563.
- [10] Lehane, J. A., and P. C. Thonemann. "An experimental study of helicon wave propagation in a gaseous plasma." *Proceedings of the Physical Society* 85, no. 2 (1965): 301.
- [11] Gallet, R. M., Richardson, J. M., Wieder, B., Ward, G. D., & Harding, G. N. (1960). Microwave whistler mode propagation in a dense laboratory plasma. *Physical Review Letters*, 4(7), 347.
- [12] Boswell, R. W. "Plasma production using a standing helicon wave." *Physics Letters A* 33, no. 7 (1970): 457-458.
- [13] Perry, A. J., D. Vender, and R. W. Boswell. "The application of the helicon source to plasma processing." *Journal of Vacuum Science & Technology B: Microelectronics and Nanometer Structures* 9, no. 2 (1991): 310-317.
- [14] Wang, S. J., et al. "Observation of enhanced negative hydrogen ion production in weakly magnetized RF plasma." *Physics Letters A* 313.4 (2003): 278-283.
- [15] Stubbers, Robert A., et al. "Compact toroid formation using an annular helicon preionization source." AIAA-2007-5307, 43rd Joint Propulsion Conference, Cincinnati, OH, 2007.

- [16] Masters, B. C., et al. "Magnetic and Thermal Characterization of An ELM Simulating Plasma (ESP) With Helicon Pre-Ionization." *Fusion Engineering 2005, Twenty-First IEEE/NPS Symposium on*. IEEE, 2005.
- [17] Jeon, S. J., W. Choe, G. C. Kwon, J. H. Kim, H. S. Yi, S. W. Herr, H. Y. Chang, and D. I. Choi. "Coupling characteristics of a helicon antenna in KAIST-Tokamak plasma." In *SOFT: Symposium on fusion technology*. 1998.
- [18] Loewenhardt, P. K., B. D. Blackwell, R. W. Boswell, G. D. Conway, and S. M. Hamberger. "Plasma production in a toroidal heliac by helicon waves." *Physical review letters* 67, no. 20 (1991): 2792.
- [19] Tripathi, S. K. P., and D. Bora. "Current drive by toroidally bounded whistlers." *Nuclear fusion* 42, no. 10 (2002): L15.
- [20] Diaz, FR Chang. "An overview of the VASIMR engine: High power space propulsion with RF plasma generation and heating." In *AIP Conference Proceedings*, vol. 595, p. 3. 2001.
- [21] Brian Beal, Alec Gallimore, David Morris, Christopher Davis, and Kristina Lemmer "Development of an annular helicon source for electric propulsion applications." Defense Technical Information Center, 2006.
- [22] West, Michael D., Christine Charles, and Rod W. Boswell. "Testing a helicon double layer thruster immersed in a space-simulation chamber." *Journal of Propulsion and Power* 24, no. 1 (2008): 134-141.
- [23] F. F. Chen, "Plasma Ionization by Helicon Waves," *Plasma Physics and Controlled Fusion*, vol. 33, no. 4, pp. 26, 1991.
- [24] Ellingboe, A. R., R. W. Boswell, J. P. Booth, and N. Sadeghi. "Electron beam pulses produced by helicon-wave excitation." *Physics of Plasmas* 2 (1995): 1807.
- [25] Molvik, A. W., A. R. Ellingboe, and T. D. Rognlien. "Hot-electron production and wave structure in a helicon plasma source." *Physical Review Letters* 79.2 (1997): 233.
- [26] Blackwell, David D., and Francis F. Chen. "Time-resolved measurements of the electron energy distribution function in a helicon plasma." *Plasma Sources Science and Technology* 10.2 (2001): 226.
- [27] F. F. Chen, and D. D. Blackwell, "Upper Limit to Landau Damping in Helicon Discharges," *Physical Review Letters*, vol. 82, no. 13, pp. 2677, 1999.
- [28] Krämer, M., Aliev, Y. M., Altukhov, A. B., Gurchenko, A. D., Gusakov, E. Z., and Niemi, K. (2007). Anomalous helicon wave absorption and parametric excitation of electrostatic fluctuations in a helicon-produced plasma. *Plasma Physics and Controlled Fusion*, 49(5A), A167.
- [29] Akhiezer, A. I., Mikhailenko, V. S., and Stepanov, K. N. (1998). Ion-sound parametric turbulence and anomalous electron heating with application to helicon plasma sources. *Physics Letters A*, 245(1), 117-122.

- [30] Borg, G. G., and R. W. Boswell. "Power coupling to helicon and Trivelpiece–Gould modes in helicon sources." *Physics of Plasmas* 5 (1998): 564.
- [31] Arnush, Donald. "The role of Trivelpiece–Gould waves in antenna coupling to helicon waves." *Physics of Plasmas* 7 (2000): 3042.
- [32] Shamrai, Konstantin P., and Vladimir B. Taranov. "Volume and surface rf power absorption in a helicon plasma source." *Plasma Sources Science and Technology* 5.3 (1996): 474.
- [33] B. N. Breizman, and A. V. Arefiev, "Radially Localized Helicon Modes in Nonuniform Plasma," *Physical Review Letters*, vol. 84, no. 17, pp. 4, 2000.
- [34] Chen, Guangye, Alexey V. Arefiev, Roger D. Bengtson, Boris N. Breizman, Charles A. Lee, and Laxminarayan L. Raja. "Resonant power absorption in helicon plasma sources." *Physics of plasmas* 13 (2006): 123507.
- [35] Degeling, A. W., C. O. Jung, R. W. Boswell, and A. R. Ellingboe. "Plasma production from helicon waves." *Physics of Plasmas* 3 (1996): 2788.
- [36] Degeling, A. W., and R. W. Boswell. "Modeling ionization by helicon waves." *Physics of Plasmas* 4 (1997): 2748.
- [37] Lafleur, T., C. Charles, and R. W. Boswell. "Characterization of a helicon plasma source in low diverging magnetic fields." *Journal of Physics D: Applied Physics* 44, no. 5 (2011): 055202.
- [38] Degeling, A. W., C. O. Jung, R. W. Boswell, and A. R. Ellingboe. "Plasma production from helicon waves." *Physics of Plasmas* 3 (1996): 2788.
- [39] Chen, F. F., X. Jiang, J. D. Evans, G. Tynan, and D. Arnush. "Low-field helicon discharges." *Plasma Physics and Controlled Fusion* 39, no. 5A (1997): A411.
- [40] Lho, Taihyeop, Noah Hershkowitz, J. Miller, W. Steer, and Gon-Ho Kim. "Azimuthally symmetric pseudo-surface and helicon wave propagation in an inductively coupled plasma at low magnetic field." *Physics of Plasmas* 5 (1998): 3135.
- [41] Wang, S. J., J. G. Kwak, C. B. Kim, and S. K. Kim. "Observation of enhanced negative hydrogen ion production in weakly magnetized RF plasma." *Physics Letters A* 313, no. 4 (2003): 278-283.
- [42] Sato, G., W. Oohara, and R. Hatakeyama. "Efficient plasma source providing pronounced density peaks in the range of very low magnetic fields." *Applied physics letters* 85, no. 18 (2004): 4007-4009.
- [43] Wang, S. J., Jong-Gu Kwak, S. K. Kim, and Suwon Cho. "Experimental study on the density peaking of an RF plasma at a low magnetic field." *Journal of Korean Physical Society* 51 (2007): 989.
- [44] Sato, G., W. Oohara, and R. Hatakeyama. "Experimental characterization of a density peak at low magnetic fields in a helicon plasma source." *Plasma Sources Science and Technology* 16, no. 4 (2007): 734.

- [45] S. Cho, "The resistance peak of helicon plasmas at low magnetic fields", *Physics of Plasmas* 13, 033504 (2006).
- [46] Chen, Francis F. "The low-field density peak in helicon discharges." *Physics of Plasmas* 10 (2003): 2586.
- [47] Shamrai, Konstantin P., and Vladimir B. Taranov. "Volume and surface rf power absorption in a helicon plasma source." *Plasma Sources Science and Technology* 5, no. 3 (1996): 474.
- [48] Charles, C. "A review of recent laboratory double layer experiments." *Plasma Sources Science and Technology* 16, no. 4 (2007): R1.
- [49] Singh, N. (2011). Current-free double layers: A review. *Physics of Plasmas*, 18(12), 122105-122105.
- [50] Hershkowitz, Noah. "Review of recent laboratory double layer experiments." *Space science reviews* 41, no. 3-4 (1985): 351-391.
- [51] Perkins, Francis W., and Y. C. Sun. "Double layers without current." *Physical Review Letters* 46 (1981): 115-118.
- [52] Chan, Chung, Noah Hershkowitz, and G. L. Payne. "Laboratory double layers with no external fields." *Physics Letters A* 83, no. 7 (1981): 328-330.
- [53] Hatakeyama, R., Y. Suzuki, and N. Sato. "Formation of electrostatic potential barrier between different plasmas." *Physical Review Letters* 50, no. 16 (1983): 1203.
- [54] Hairapetian, G., and R. L. Stenzel. "Observation of a stationary, current-free double layer in a plasma." *Physical review letters* 65, no. 2 (1990): 175.
- [55] Charles, C., & Boswell, R. (2003). Current-free double-layer formation in a high-density helicon discharge. *Applied Physics Letters*, 82(9), 1356-1358.
- [56] Lieberman, M. A., C. Charles, and R. W. Boswell. "A theory for formation of a low pressure, current-free double layer." *Journal of Physics D: Applied Physics* 39, no. 15 (2006): 3294.
- [57] Chen, Francis F. "Physical mechanism of current-free double layers." *Physics of plasmas* 13 (2006): 034502.
- [58] Ahedo, Eduardo, and Manuel Martínez Sánchez. "Theory of a Stationary Current-Free Double Layer in a Collisionless Plasma." *Physical review letters* 103, no. 13 (2009): 135002.
- [59] Takahashi, Kazunori, Christine Charles, Rod W. Boswell, and Tamiya Fujiwara. "Electron Energy Distribution of a Current-Free Double Layer: Druyvesteyn Theory and Experiments." *Physical Review Letters* 107, no. 3 (2011): 035002.
- [60] Charles, Christine, and R. W. Boswell. "Laboratory evidence of a supersonic ion beam generated by a current-free "helicon" double-layer." *Physics of Plasmas* 11 (2004): 1706.

- [61] Sun, Xuan, Amy M. Keesee, Costel Biloiu, Earl E. Scime, Albert Meige, Christine Charles, and Rod W. Boswell. "Observations of ion-beam formation in a current-free double layer." *Physical review letters* 95, no. 2 (2005): 025004.
- [62] Cohen, Samuel Alan, N. S. Siefert, S. Stange, R. F. Boivin, E. E. Scime, and F. M. Levinton. "Ion acceleration in plasmas emerging from a helicon-heated magnetic-mirror device." *Physics of Plasmas* 10 (2003): 2593.
- [63] Byhring, H. S., C. Charles, Å. Fredriksen, and R. W. Boswell. "Double layer in an expanding plasma: Simultaneous upstream and downstream measurements." *Physics of plasmas* 15 (2008): 102113.
- [64] Schröder, T., O. Grulke, and T. Klinger. "The influence of magnetic-field gradients and boundaries on double-layer formation in capacitively coupled plasmas." *EPL (Europhysics Letters)* 97, no. 6 (2012): 65002.
- [65] Wiebold, Matt, Yung-Ta Sung, and John E. Scharer. "Experimental observation of ion beams in the Madison Helicon eXperiment." *Physics of Plasmas* 18 (2011): 063501.
- [66] Saha, S. K., S. Raychaudhuri, S. Chowdhury, M. S. Janaki, and A. K. Hui. "Two-dimensional double layer in plasma in a diverging magnetic field." *Physics of Plasmas* 19 (2012): 092502.
- [67] Sutherland, O., Charles, C., Plihon, N., and Boswell, R. W. (2005). Experimental evidence of a double layer in a large volume helicon reactor. *Physical review letters*, 95(20), 205002.
- [68] Thakur, Saikat Chakraborty, Alex Hansen, and Earl E. Scime. "Threshold for formation of a stable double layer in an expanding helicon plasma." *Plasma Sources Science and Technology* 19, no. 2 (2010): 025008.
- [69] Takahashi, K., Charles, C., Boswell, R. W., and Fujiwara, T. (2010). Double-layer ion acceleration triggered by ion magnetization in expanding radiofrequency plasma sources. *Applied Physics Letters*, 97(14), 141503-141503.
- [70] Albert Meige, Numerical modeling of low-pressure plasmas: applications to electric double layers, Thesis, Australian National University (2006).
- [71] Charles, C., and R. W. Boswell. "The magnetic-field-induced transition from an expanding plasma to a double layer containing expanding plasma." *Applied Physics Letters* 91, no. 20 (2007): 201505-201505.

Helicon Physics

2.1 Introduction

The low frequency right circularly polarized electromagnetic waves in plasma propagating parallel to the magnetic field are known as the whistler waves [1]. Helicon waves are whistler waves in bounded plasmas where the wavelength is of the order of the plasma dimensions. Whistler waves lose their pure electromagnetic character and become quasi-electromagnetic helicon waves when bounded. Helicons can have both the right and left handed polarizations compared to the unbounded medium whistlers which have only right handed polarization. Klozenberg, McNamra and Thonemann [2] first derived the detailed dispersion relation of helicon waves with their mode structure in a gaseous plasma with a vacuum boundary. Blevin and Christiansen [3] obtained the dispersion in a non-uniform plasma. Ferrari and Klozenberg [4] derived the dispersion and attenuation of helicon waves in a plasma with perfectly conducting boundaries.

A brief derivation of the helicon dispersion from cold plasma dielectric tensor is presented. Quasiparallel oblique propagation of right polarized electromagnetic waves is discussed with importance to resonance cone propagation. The mode structure of helicon waves in cylindrical uniform plasmas and the effect of density gradients on these structures are discussed. Another important feature of helicon antenna produced plasma is the mode transitions. RF discharges can be sustained by an electric field of capacitive, inductive or wave origin. An RF inductive plasma is known to support both capacitive and inductive mode. Helicon plasma is a unique discharge in which the discharge can be sustained by all the three modes namely capacitive, inductive and wave or helicon.

2.2 Derivation of dispersion relation

Ordinary fluids such as air or water can support only a few types of oscillations or waves. For example, sound waves in air are due to the propagation of pressure disturbances. Water surface waves are due to the cohesion (surface tension) and inertia of water. The dispersion relation relates the wavelength to the frequency of the wave. This relation can describe the wave motion by providing information about the wavelength and phase velocity for a given frequency. For example, even a vacuum can support a type of wave: electromagnetic radiation.

2.2.1 Vacuum Waves

The dispersion relation for electromagnetic radiation can be found from Maxwell's equations in vacuum (using SI units):

$$\nabla \cdot \mathbf{E} = 0 \quad (2.1)$$

$$\nabla \cdot \mathbf{B} = 0 \quad (2.2)$$

$$\nabla \times \mathbf{E} = -\frac{\partial \mathbf{B}}{\partial t} \quad (2.3)$$

$$\nabla \times \mathbf{B} = \frac{1}{c^2} \frac{\partial \mathbf{E}}{\partial t} \quad (2.4)$$

By combining Equation 2.3 and Equation 2.4, one obtains the differential equation for the electric field:

$$\vec{\nabla} \times \vec{\nabla} \times \vec{E} = -\frac{1}{c^2} \frac{\partial^2 \vec{E}}{\partial t^2} \quad (2.5)$$

Carrying out Fourier analysis while looking for harmonic solutions of type $B, E = B_0, E_0 e^{i(kx - \omega t)}$, Equation 2.5 can transform spatial derivatives into wave vectors and time derivatives into frequencies as

$$\vec{k} \times \vec{k} \times \vec{E} = -\frac{\omega^2}{c^2} \vec{E} \quad (2.6)$$

revealing a relationship between electric field, wave vector, and frequency. Then, using a vector identity and Eq. 2.6 one obtains an equation for the wave electric field:

$$\left(\frac{\omega^2}{c^2} - k^2\right)\vec{E} = \mathbf{0} \quad (2.7)$$

For the non-trivial solution with $\vec{E} \neq 0$, it is necessary that:

$$\frac{\omega^2}{c^2} = k^2, \text{ or } \frac{\omega}{k} = \pm c \quad (2.8)$$

which is the dispersion relation for electromagnetic waves in vacuum. This dispersion relation indicates that the phase velocity $v_{ph} = \omega/k$ is of constant magnitude c . The group velocity (the velocity of energy flow, for a wave packet composed of many different wavenumbers $v_{gr} = c$ is the same for any wave number, so there is no dispersion in the sense that waves of different wavelengths in a wave packet all propagate with the same phase and group velocities. The situation can be very different in plasma, as will be seen later.

Plasma can be considered as a dielectric medium with long range electromagnetic forces leading to collective behavior for which a perturbation at one place in plasma can affect the plasma at other place. The motion of charged particles in the presence of electric and magnetic fields created by the externally applied or self consistently generated sources of charge density and current density makes the dynamics complicated. The dispersion relation relates the wave frequency to the wave number in a medium and the wave phase velocity is defined as $v = \omega/k$. The wave number of an electromagnetic wave in vacuum is related to the frequency by the velocity $c = f\lambda$, so that wavelength can be obtained if frequency is given. But in a complex medium like magnetized plasma with collective behaviour, the medium becomes anisotropic and a detailed derivation of the dispersion relation is tedious. What follows now is the derivation of the cold plasma dielectric tensor.

Cold plasma is one in which the thermal velocities of the particles are much smaller than the phase velocities of the waves ($v_{th} \ll \omega/k$). Magnetized plasma being an anisotropic medium for electromagnetic waves supports various kinds of waves. Since plasma consists of light electrons and heavy ions, characteristic frequencies range from low frequency ion cyclotron frequency to high frequency electron cyclotron frequency. A general fluid description method considering both ions and electrons will be presented for finding normal modes in collisionless, magnetized plasmas. Cold plasma wave equations are derived by the ion and electron equations of motion in the electromagnetic fields and the Maxwell's equation [5]. The momentum equation gives the evolution of current produced in the plasma because of applied (or self generated) electromagnetic fields which in turn evolve following the Maxwell's equations. The solutions of these self consistent equations give out the normal modes.

The seed of theory of helicon wave lies in the theory of whistler wave. Since helicon wave is a bounded whistler the theory becomes more involved and complex. It becomes even more complex when plasma and/or magnetic field are non-uniform. Moreover, at the boundary the very existence of surface wave (Trivelpiece-Gould mode) invites the possibility of coupling between helicon and TG. The basic theory of whistler waves is covered in textbooks such as Stix [5], Swanson [6] and Bellan [1]. In order to interpret and classify the wave experiments considered in the present thesis, plasma waves are introduced theoretically in this chapter. The derivation follows the well established approach of Stix [5], Swanson [6] and Bellan [1] and the waves are classified by their different roots in the cold plasma wave dispersion relation. Starting from Maxwell's equations and the cold plasma particle equations, the cold magnetized plasma dielectric tensor and the dispersion relation are derived in section 2.1.2 for both parallel and perpendicular propagation. For the frequency ranges of interest of this thesis, taking electron mass into consideration, two solutions as a slow and a fast wave are obtained. In section 2.3, resonance cone propagation of an R-wave is discussed when the finite angle of propagation w.r.t magnetic field, coincides with the resonance cone angle. Wave field components are derived in section 2.4 for laboratory experiments where the plasma is bounded in a cylindrical boundary. A brief discussion on the effect of non-uniform radial density profiles on helicon wave propagation is presented in section 2.4. Different mechanisms of helicon power deposition in plasma leading to dense plasmas are described in Section 2.6. Finally the summary of the chapter is presented.

2.2.2 Plasma Waves

The reason plasma waves are so different from vacuum waves is that, in the presence of a plasma, the source terms in Maxwell's equations are non-zero. Charge and current density play a significant role in altering the simple character of vacuum electromagnetic waves. Maxwell's equations become:

$$\nabla \cdot \mathbf{E} = \frac{\rho}{\epsilon_0} \quad (2.9)$$

$$\nabla \cdot \mathbf{B} = 0 \quad (2.10)$$

$$\nabla \times \mathbf{E} = -\frac{\partial \mathbf{B}}{\partial t} \quad (2.11)$$

$$\nabla \times \mathbf{B} = \mu_0 \mathbf{J} + \frac{1}{c^2} \frac{\partial \mathbf{E}}{\partial t} \quad (2.12)$$

In the above equations, ρ and \mathbf{J} (absent in vacuum) are respectively the charge and current density and μ_0, ϵ_0 are permeability and permittivity of free space with c as the speed of light. Taking the curl of Eq. 2.11 and substituting into Eq. 2.12 results in a wave equation:

$$\nabla \times \nabla \times \mathbf{E} = -\frac{1}{c^2} \frac{\partial^2 \mathbf{E}}{\partial t^2} - \mu_0 \frac{\partial \mathbf{J}}{\partial t} \quad (2.13)$$

The plasma current \vec{J} due to a plasma wave is related to the particle velocities. Modelling the plasma as a mix of fluids of several kinds of particles (electrons and different ion species),

$$\vec{J} = \sum_s q_s n_s \vec{v}_s \equiv \vec{\sigma} \cdot \vec{E} \quad (2.14)$$

where the index s in the sum denotes the plasma species (electron & ion), and the conductivity tensor $\vec{\sigma}$ is defined by Eq. 2.14. By substituting the Lorentz force into Newton's second law

(neglecting pressure term as this is a cold plasma model), one obtains the equation of motion for the fluid of different species,

$$\mathbf{m}_s \frac{d\vec{v}_s}{dt} = q_s (\vec{E} + \vec{v}_s \times \vec{B}) \quad (2.15)$$

Where m_s and q_s are the charge and mass of the particle and $v_s(r, t)$ is its velocity. Solving for \vec{v}_s in terms of the components of \vec{E} , and plugging into Eq. 2.14 allows one to determine the conductivity tensor elements.

To proceed to obtain a dispersion relation, again Fourier analyze Eq. 2.11 in time and space with a look out for harmonic solutions like $v, B, E = B_0, E_0 e^{i(kx - \omega t)}$:

$$\vec{k} \times \vec{k} \times \vec{E} = -\frac{\omega^2}{c^2} \vec{E} - i\mu_0 \omega \vec{\sigma} \cdot \vec{E} \quad (2.16)$$

Suppose we consider “cold” plasma, meaning one in which plasma beta $\ll 1$. This corresponds to the limit in which kinetic pressure is negligible. Each species of particle will also have an equation of motion of the form Eq. 2.15. Linearizing this equation assuming zeroth order quantity to be constant we can obtain equations with three components, the sign of charges, ± 1 , is given by ϵ_s ,

$$-i\omega v_{x,s} = \frac{\epsilon_s q}{m_s} E_x + \frac{\epsilon_s q}{m_s} v_y B_0 = \frac{\epsilon_s q}{m_s} E_x + v_y \omega_c \quad (2.17)$$

$$-i\omega v_{y,s} = \frac{\epsilon_s q}{m_s} E_y - \frac{\epsilon_s q}{m_s} v_x B_0 = \frac{\epsilon_s q}{m_s} E_y - v_x \omega_c \quad (2.18)$$

$$-i\omega v_{z,s} = \frac{\epsilon_s q}{m_s} E_z \quad (2.19)$$

Our goal is to obtain an expression for the current \vec{j} in terms of the electric field, from which we can get the components of $\vec{\sigma}$. This relationship can be obtained by finding the velocities of the individual particle species in terms of the electric field from the equations of motion.

Solving the z-component of the equation of motion above for v_z

$$\mathbf{v}_{z,s} = i \frac{\epsilon_s q}{m_s \omega} \mathbf{E}_z \quad (2.20)$$

The current in the z-direction is thus,

$$\mathbf{J}_{z,s} = n \epsilon_s q \mathbf{v}_z \quad (2.21)$$

We can now determine zz component of $\vec{\sigma}$,

$$\mathbf{j}_{z,s} = \sigma_{zz} \mathbf{E}_z = \epsilon_s n q \left(i \frac{\epsilon_s q}{m_s \omega} \mathbf{E}_z \right) = \left(i \frac{n q^2}{m_s \omega} \right) \quad (2.22)$$

$$\text{Therefore, } \sigma_{zz} = i \frac{n q^2}{m_s \omega} \quad (2.23)$$

We can also consider the equation for the \hat{x} and \hat{y} directions. Multiplying the \hat{x} component of the equation of motion by ω ,

$$\omega^2 \mathbf{v}_{x,s} = i \epsilon_s \omega \frac{q}{m_s} \mathbf{E}_x + i \omega \omega_{c,s} \mathbf{v}_{y,s} \quad (2.24)$$

Substituting the \hat{y} components of the equation of motion,

$$-i \omega \mathbf{v}_{y,s} = \frac{\epsilon_s q}{m_s} \mathbf{E}_y - \mathbf{v}_{x,s} \omega_{c,s} \quad (2.25)$$

We get,
$$\omega^2 \mathbf{v}_{x,s} = i \epsilon_s \omega \frac{q}{m_s} \mathbf{E}_x + \omega_{c,s} \left(-\frac{\epsilon_s q}{m_s} \mathbf{E}_y + \mathbf{v}_{x,s} \omega_{c,s} \right)$$

$$= i\epsilon_s \omega \frac{q}{m_s} E_x - \epsilon_s \omega_{c,s} \frac{q}{m_s} E_y + v_{x,s} \omega_{c,s}^2 \quad (2.26)$$

Isolating v_x and dividing by the coefficient,

$$v_{x,s} = i\epsilon_s \frac{q}{m_s} \frac{\omega}{\omega^2 - \omega_{c,s}^2} E_x - \frac{\epsilon_s q}{m_s} \frac{\omega_{c,s}}{\omega^2 - \omega_{c,s}^2} E_y \quad (2.27)$$

With the velocity we can form the current density

$$j_{x,s} = e_s n q v_{x,s} = i \frac{nq^2}{m_s} \frac{\omega}{\omega^2 - \omega_{c,s}^2} E_x - \frac{nq^2}{m_s} \frac{\omega_{c,s}}{\omega^2 - \omega_{c,s}^2} E_y \quad (2.28)$$

The current can also be written using conductivity tensor components,

$$j_{x,s} = \sigma_{xx,s} E_x + \sigma_{xy,s} E_y + \sigma_{xz,s} E_z \quad (2.29)$$

Comparing the above two equations, we get conductivity tensor components as,

$$\sigma_{xx} = i \frac{nq^2}{m_s} \frac{\omega}{\omega^2 - \omega_{c,s}^2}; \text{ and } \sigma_{xy} = -\frac{nq^2}{m_s} \frac{\omega}{\omega^2 - \omega_{c,s}^2} \quad (2.30)$$

The susceptibility tensor is related to conductivity tensor by

$$\vec{\chi} = \left(\vec{I} + \frac{i\vec{\sigma}}{\epsilon_0 \omega} \right) \quad (2.31)$$

And also, we can relate the cross terms as,

$$\chi_{xy} = i \frac{\omega_{c,s}}{\omega} \chi_{xx} \quad (2.32)$$

Hence, the final expression for the susceptibility tensor is

$$\vec{\chi}_s = \begin{pmatrix} -\frac{\omega_{p,s}^2}{\omega^2 - \omega_{c,s}^2} & -i \frac{\omega_{c,s}}{\omega} \frac{\omega_{p,s}^2}{\omega^2 - \omega_{c,s}^2} & 0 \\ i \frac{\omega_{c,s}}{\omega} \frac{\omega_{p,s}^2}{\omega^2 - \omega_{c,s}^2} & -\frac{\omega_{p,s}^2}{\omega^2 - \omega_{c,s}^2} & 0 \\ 0 & 0 & -\frac{\omega_{p,s}^2}{\omega^2} \end{pmatrix} \quad (2.33)$$

The dielectric tensor can be formed

$$\vec{\epsilon} = \vec{I} + \sum_s \vec{\chi}_s \quad (2.34)$$

Where $\vec{\epsilon}$ is the dielectric tensor and can be written as [5]

$$\vec{\epsilon} = \begin{pmatrix} S & -iD & 0 \\ iD & S & 0 \\ 0 & 0 & P \end{pmatrix} \quad (2.35)$$

With Stix coefficients S, D and P are defined as

$$S = 1 - \sum_{j=i,e} \frac{\omega_{pj}^2}{\omega^2 - \omega_{cj}^2} \quad (2.36)$$

$$D = \sum_{j=i,e} \frac{\omega_{cj}}{\omega} \frac{\omega_{pj}^2}{\omega^2 - \omega_{cj}^2} \quad (2.37)$$

$$P = 1 - \sum_{j=i,e} \frac{\omega_{pj}^2}{\omega^2} \quad (2.38)$$

As we are searching for harmonic solutions of the type $B, E = B_0, E_0 e^{ikx - \omega t}$ the Maxwell's equations 2.11 and 2.12 can be rewritten as,

$$ik \times E = i\omega B \quad (2.39)$$

$$ik \times B = -i\omega\mu_0\epsilon_0 \vec{\epsilon} \cdot E \quad (2.40)$$

Taking again the curl of equation 2.15 and using equation 2.16,

$$\mathbf{k} \times (\mathbf{k} \times \mathbf{E}) = -\frac{\omega^2}{c^2} \vec{\epsilon} \cdot \mathbf{E} \quad (2.41)$$

Taking $n = \frac{ck}{\omega}$, where n is the refractive index of the anisotropic plasma medium, Equation 2.41 can be rewritten as

$$nn \cdot \mathbf{E} - n^2 \mathbf{E} + \vec{\epsilon} \cdot \mathbf{E} = 0 \quad (2.42)$$

The above equation can be written in a matrix form as

$$\begin{bmatrix} S - n_z^2 & -iD & n_x n_z \\ iD & S - n^2 & 0 \\ n_x n_z & 0 & P - n_x^2 \end{bmatrix} \cdot \begin{bmatrix} E_x \\ E_y \\ E_z \end{bmatrix} = 0 \quad (2.43)$$

$$\text{With } n_x = n \sin \theta$$

$$n_z = n \cos \theta$$

$$n^2 = n_x^2 + n_z^2$$

Equation 2.43 can now be written as

$$\begin{bmatrix} S - n^2 \cos^2 \theta & -iD & n^2 \sin \theta \cos \theta \\ iD & S - n^2 & 0 \\ n^2 \sin \theta \cos \theta & 0 & P - n^2 \sin^2 \theta \end{bmatrix} \cdot \begin{bmatrix} E_x \\ E_y \\ E_z \end{bmatrix} = 0 \quad (2.44)$$

The non-trivial solution of the above equation can be expressed as [5]

$$An^4 - Bn^2 + C = 0 \quad (2.45)$$

$$A = S \sin^2 \theta + P \cos^2 \theta \quad (2.46)$$

$$B = RL \sin^2 \theta + PS(1 + \cos^2 \theta) \quad (2.47)$$

$$C = PRL \quad (2.48)$$

$$R = S + D ; L = S - D \quad (2.49)$$

Since this is a quadratic equation in n^2 , there are always two solutions

$$n^2 = B \pm \sqrt{(B^2 - 4AC)/2A} \quad (2.50)$$

The solution with the larger phase velocity (smaller n^2) is called the fast wave, and the solution with the smaller phase velocity (larger n^2) is called the slow wave. When the solution is such that one of the roots $n^2 < 0$, then that wave is evanescent, it cannot propagate.

The dispersion relation can be put into another form,

$$\tan^2 \theta = \frac{-P(n^2 - R)(n^2 - L)}{(Sn^2 - RL)(n^2 - P)} \quad (2.51)$$

The dispersion relation for propagation at $\theta = 0$ and $\theta = \pi/2$ are quickly obtained as

$$\text{For } \theta = 0; P = 0 \text{ or } n^2 = R \text{ or } n^2 = L$$

$$\text{For } \theta = \pi/2; n^2 = \frac{RL}{S} \text{ or } n^2 = P$$

The most interesting features of the solution are resonances ($n^2 \rightarrow \infty$) and cut-offs ($n^2 \rightarrow 0$).

Perpendicular Propagation:

$$(k \perp B_0, \theta = \pi/2)$$

Within this work, waves propagating perpendicular to the direction of the magnetic field are not investigated experimentally. For completeness, however, perpendicular propagating waves are

introduced in brief. A more detailed analysis can be found in textbooks on plasma waves, e.g. Swanson [1989] or Stix [1992]. For perpendicular wave propagation, there are two possibilities:

1. Ordinary waves: ($n^2 - P = 0$)

The dispersion relation for the O-mode wave reads

$$k^2 c^2 = \omega^2 - \sum_s \omega_{p,s}^2 \quad (2.52)$$

The wave propagation is not affected by the magnetic field as the electric field vector is parallel to the axial magnetic field. The dispersion has real solutions (the wave propagates) above the cut-off $\omega > \omega_{p,s}$. As the dispersion depends on the plasma density only, O-waves can be used for plasma diagnostics, e.g. reflectometry and interferometry.

2. Extraordinary waves: ($Sn^2 - RL = 0$)

The dispersion of the X-mode wave is more complicated as neither the resonances nor the cut-offs can be seen straightforward

$$\frac{k^2 c^2}{\omega^2} = \frac{\left(1 - \sum_s \frac{\omega_{p,s}^2}{\omega(\omega + \omega_s \omega_{c,s})}\right) \left(1 - \sum_s \frac{\omega_{p,s}^2}{\omega(\omega - \omega_s \omega_{c,s})}\right)}{1 - \sum_s \frac{\omega_{p,s}^2}{\omega^2 - \omega_{c,e}^2}} \quad (2.53)$$

It propagates (has real solutions) in the two frequency regimes $\omega_L < \omega < \omega_{uh}$ and $\omega > \omega_R$. The two cut-off frequencies are defined by

$$\omega_{L,R} = \left[\left(\frac{\omega_{ce} + \omega_{ci}}{2} \right)^2 + \omega_{pe}^2 + \omega_{pi}^2 \right]^{1/2} \pm \frac{\omega_{ci} - \omega_{ce}}{2} \quad (2.54)$$

where the plus sign is attributed to ω_L and the minus sign to ω_R , respectively. The X-wave resonates at the upper and the lower hybrid frequency: $\omega_{UH}^2 = \omega_{ce}^2 + \omega_{pe}^2$ and $\omega_{LH}^{-2} = (\omega_{ce}\omega_{ci})^{-1} + (\omega_{pi}^2 + \omega_{ci}^2)^{-1}$.

They are called hybrid frequencies, because the wave resonates with a hybrid motion of the electrons and ions (ω_{LH}) and the hybrid electron motion determined by density and magnetic field (ω_{UH}).

Parallel Propagation:

$$(k \parallel B_0, \theta = 0)$$

For parallel propagation, $\theta = 0$. So Equation 2.44 can be written again as

$$\begin{bmatrix} S - n^2 & -iD & 0 \\ iD & S - n^2 & 0 \\ 0 & 0 & P \end{bmatrix} \cdot \begin{bmatrix} E_x \\ E_y \\ E_z \end{bmatrix} = 0 \quad (2.55)$$

The nontrivial solution is

$$[(S - n^2)^2 - D^2] P = 0 \quad (2.56)$$

Equation 2.56 has three solutions as described below

1. Plasma oscillation: $P = 0$

This is the simplest plasma motion which reads

$$\omega^2 = \sum_s \omega_{ps}^2 \quad (2.57)$$

This degenerate case is not a propagating wave as the group velocity is zero for all frequencies. It represents an oscillation at the plasma frequency. Usually, this frequency is the electron plasma frequency ω_{pe} as this term is by far the largest in the sum ($\omega_{pe} \gg \omega_{pi}$).

2. R-waves: $n^2 - R = 0$

The dispersion relation resulting from this root is

$$k^2 c^2 = \omega^2 - \sum_s \frac{\omega \omega_{p,s}^2}{\omega + \epsilon_s \omega_{c,s}} \quad (2.58)$$

There is one resonance at the electron cyclotron frequency $\omega_{c,e}$. This wave is right hand circular polarized and thus couples to the electron gyration at $\omega_{c,e}$. There is a cut-off at ω_R , but in contrast to the O-mode and the X-mode, there is as well a propagating low frequency wave $\omega < \omega_{c,e}$. This part of the R-wave is the only electromagnetic wave mode that propagates at low frequencies. It is called an electron whistler wave.

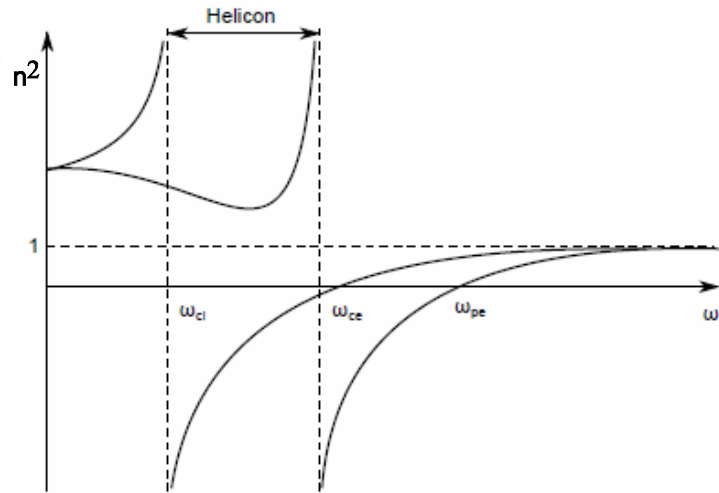


Figure 2.1 Dispersion of electromagnetic waves parallel to magnetic field showing the range of operation of Helicon waves in $n^2 - \omega$ diagram [7].

3. L-waves: $n^2 - L = 0$

The dispersion relation for the L-wave is

$$k^2 c^2 = \omega^2 - \sum_s \frac{\omega \omega_{p,s}^2}{\omega - \epsilon_s \omega_{c,s}} \quad (2.59)$$

The resonances are now at the cyclotron frequencies of the positive ion species in the plasma. The wave is left-hand circular polarized and couples to the ion gyration. There is a wave cut-off

at ω_L . For frequencies well above the ion cyclotron frequency, the magnetic field has no influence on the ion motion. Low frequency L waves are called ion whistler waves.

Propagation at Arbitrary Angles:

R-waves in unbounded plasmas do not necessarily have to propagate purely parallel to the ambient magnetic field. The angle between the wave vector k and the ambient magnetic field B_0 is called θ .

The dispersion relation Eq. 2.45 can alternatively expressed as Appleton-Hartree equation [1],

$$\mathbf{n}^2 = \mathbf{1} + \frac{2(A-B+C)}{B-2A \pm \sqrt{B^2-4AC}} \quad (2.60)$$

Neglecting collision and ion motions for finding out the right circularly polarized high frequency waves with quasi longitudinal approximation $\theta \approx 0$ and $\omega_{ci,pi} \ll \omega < \omega_{ce} \ll \omega_{pe}$, the dispersion relation has the following form

$$\mathbf{n}^2 = \mathbf{1} - \frac{\omega_{pe}^2}{\omega(\omega_{ce} \cos \theta - \omega)} \quad (2.61)$$

For the frequency range of interest, ($\omega_{ci,pi} \ll \omega < \omega_{ce} \ll \omega_{pe}$) and taking $n = \frac{ck}{\omega}$ and $n \cos \theta = \frac{ck_z}{\omega}$ the widely used helicon dispersion can be written as the dispersion relation becomes

$$\mathbf{n}^2 = \frac{k^2 c^2}{\omega^2} = \frac{\omega_{pe}^2}{\omega(\omega_{ce} \cos \theta - \omega)} \quad (2.62)$$

Rearranging this equation in terms of frequency we get,

$$\omega = \omega_{ce} \cos \theta \frac{k^2 c^2}{\omega_{pe}^2 + k^2 c^2} \quad (2.63)$$

Two approximations can be derived from here. First, for short wave lengths $k \gg \omega_{pe}/c$, writing $k^2 = k_{\parallel}^2 + k_{\perp}^2$ where k, k_{\parallel} and k_{\perp} are total, parallel and perpendicular wavenumbers, the above dispersion equation simplifies to

$$\omega = \omega_{ce} \frac{k_{\parallel}}{k} \quad (2.64)$$

These waves are quasi-electrostatic and strongly damped. In helicon research they are commonly referred to as slow mode waves or Trivelpiece-Gould modes. For long wave lengths $k \ll \omega_{pe}/c$ one obtains helicon waves and its dispersion relation becomes

$$\omega = \omega_{ce} \frac{k_{\parallel} k c^2}{\omega_{pe}^2} \quad (2.65)$$

These two waves merge for a particular magnetic field as shown by Shamrai and Taranov [8]. He finds a bi-quadratic equation which on neglecting collisions is as follows

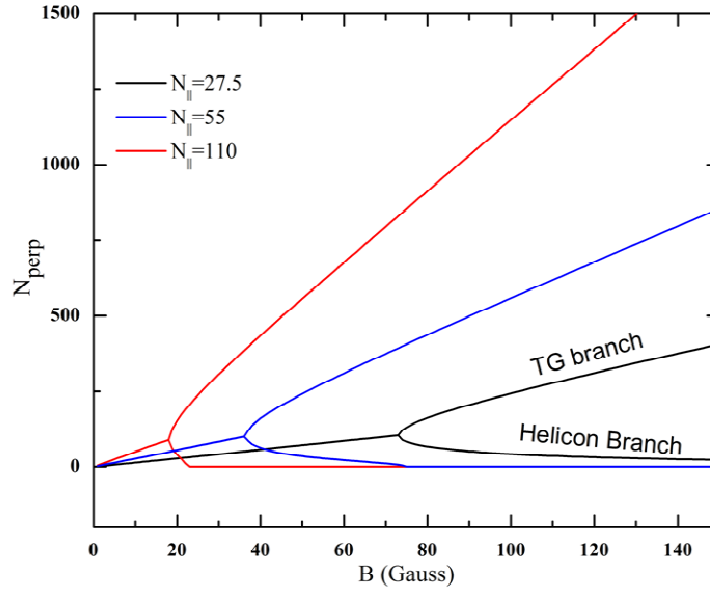


Figure 2.2 Coupling of Helicon and TG modes at low magnetic field for different N_{\parallel} at density $n_e = 10^{17} \text{m}^{-3}$ for $m = +1$ mode.

$$k_{\perp\pm}^2 = k_{\parallel}^2 \frac{1}{2\alpha^2\beta^2} (1 - 2\alpha - 2\alpha^2\beta^2 \pm \sqrt{1 - 4\alpha}) \quad (2.66)$$

$$\alpha = \frac{\omega_{pe}^2}{\omega_{ce}^2 N_{\parallel}^2}, \beta = \frac{\omega \omega_{ce} N_{\parallel}^2}{\omega_{pe}^2} \quad (2.67)$$

The slow wave with $k_{\perp} = k_{\perp+}$ corresponds to TG wave and the fast wave with $k_{\perp} = k_{\perp-}$ corresponds to the helicon wave. They merge when $\alpha = 1/4$. Figure 2.2 describes the two solutions in plasmas with density $n_e = 1 \times 10^{17} m^{-3}$ and for different parallel refractive indices.

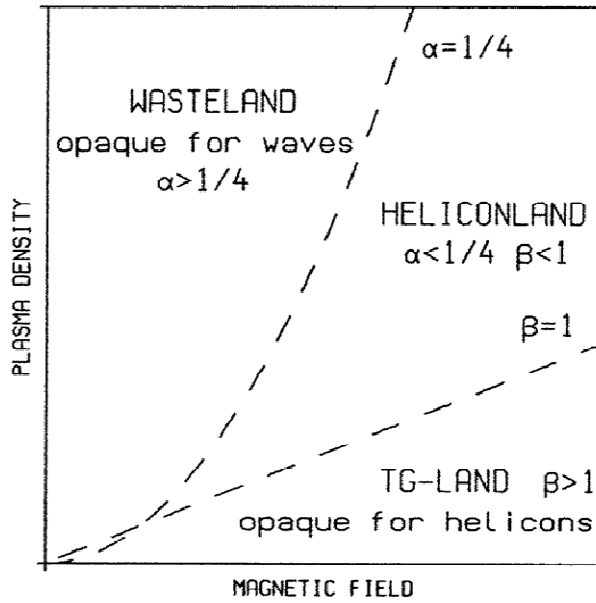


Figure 2.3 n - B diagram showing the parameter space of Helicon and TG modes [8].

At low magnetic fields the modes are indistinct and at higher magnetic fields they are very much apart in perpendicular wave numbers. The TG modes have very short wavelengths and are confined to the plasma boundary. Figure 2.3 shows the propagation regimes of TG and helicon modes including the cut-off conditions in the n - B parameter space [Shamrai et al 1996].

2.3 Oblique propagation and Resonance cone

The RCP dispersion can be written again as

$$n^2 = \frac{\omega_{pe}^2}{\omega(\omega_{ce} \cos \theta - \omega)}$$

Where θ is the angle between wave propagation direction and the magnetic field, $k_z = k \cos \theta$.

The refractive index has a resonance for [1]

$$\theta = \theta_{res} = \cos^{-1} \frac{\omega}{\omega_{ce}} \quad (2.68)$$

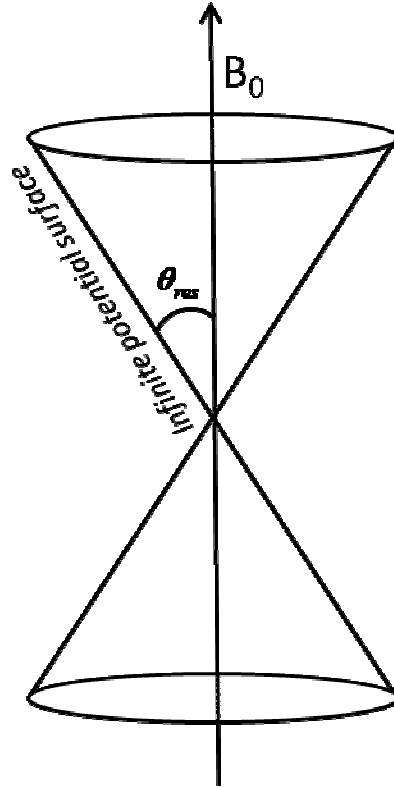


Figure 2.4 Resonance cone showing the infinite potential surface of a point source at cone apex.

and θ_{res} is known as the resonance cone angle. When a wave propagates at an angle $\theta = \theta_{res}$, the wave number becomes infinitely large. The potential of a point source at the cone apex is given by [1, 9-10]

$$\varphi(r, z) \approx \frac{q}{4\pi\epsilon_0 \left(\frac{r^2 + z^2}{S + P}\right)^{1/2}} \quad (2.69)$$

, where S and P are the Stix coefficients. r and z are the radial and axial directions of the cone and the potential diverges for resonance cone angle $\tan \theta_{res} = r/z = \pm\sqrt{-S/P}$. As the cold plasma in principle can have large wave numbers, the wave electric field increases near the resonance cone boundary [1, 11]. Thermal effects come into effect when wave number k becomes so large that the wave phase velocity becomes smaller than the thermal speed of the particles. Fisher and Gould first observed the resonance cones [9] and the thermal effects [10] where they have found that the potential near the resonance cone boundary is large but finite.

2.4 Helicon waves in a cylinder

So far, we have described plasma waves that propagate in an unbounded medium. Now we will address bounded helicon waves. In the previous section the dispersion relation is derived which has two solutions namely the TG mode and Helicon mode. There in equation 2.36, the values of the parallel and perpendicular wavenumbers are continuous as also evident from Figure 2.2. But when the wave is bounded in either a conducting or dielectric boundary we will see that the wave numbers are discrete and quantized. Taking ions immobile and neglecting collisions in a cold plasma the generalized Ohm's law (Equation 2.40) gives the current J for an applied electric and magnetic field.

$$\mathbf{E} = \frac{1}{qn_0} \mathbf{J} \times \mathbf{B}_0 + \frac{m}{q^2 n_0} \frac{\partial \mathbf{J}}{\partial t} \quad (2.70)$$

Taking the curl of the above equation, using the Maxwell's equation and looking for harmonic solutions in space and time

$$\mathbf{B} = \frac{kB_0}{qn_0\omega} \mathbf{J} - \frac{m_e}{q^2 n_0} \nabla \times \mathbf{J} \quad (2.71)$$

Ignoring the displacement current [2] and rearranging

$$\delta \nabla \times (\nabla \times \mathbf{B}) - k \nabla \times \mathbf{B} + \delta \mathbf{k}_s \mathbf{B} = \mathbf{0} \quad (2.72)$$

Where $\delta = \omega/\omega_{ce}$, and $k_s = \omega_{pe}/c$. Equation 2.40 can be factorized as

$$(\nabla \times -\mathbf{k}_{\perp+})(\nabla \times -\mathbf{k}_{\perp-})\mathbf{B} = \mathbf{0} \quad (2.73)$$

Here $k_{\perp+}$ and $k_{\perp-}$ are perpendicular wave numbers for a given axial wave number. The general solution is the sum of individual solutions [2]

$$\mathbf{B} = \mathbf{B}_+ + \mathbf{B}_- \quad (2.74)$$

where $\nabla \times \mathbf{B}_+ = \mathbf{k}_{\perp+}\mathbf{B}_+$ (2.75)

$$\nabla \times \mathbf{B}_- = \mathbf{k}_{\perp-}\mathbf{B}_- \quad (2.76)$$

The helicon dispersion relation can still be obtained from equation 2.40 by letting $\omega \ll \omega_{ce}$ i.e.

$$\nabla \times \mathbf{B} = \mathbf{k}_{\perp}\mathbf{B} \quad (2.77)$$

As wave magnetic field components are directly measurable quantities with a B-dot probe, a solution for them is sought. The general behavior of equations 2.75 and 2.76 can be equation 2.77. Taking the curl of this equation gives

$$\nabla^2 \mathbf{B} = k_{\perp}^2 \mathbf{B} \quad (2.78)$$

Now assuming a harmonic solution in a cylindrical coordinate system (r, θ, z) like $B, E = B_0, E_0 e^{i(m\theta + k_z z - \omega t)}$, the solution for z component of B is

$$\mathbf{B}_z = \mathbf{A}J_m(\mathbf{k}_{\perp}r) + \mathbf{B}K_m(\mathbf{k}_{\perp}r) \quad (2.79)$$

Where J_m is the Bessel function of first kind. A and B are arbitrary constants. K_m is Bessel function of second kind. $K_m(r)$ diverges at $r=0$ giving $B=0$.

So

$$B_z = AJ_m(k_{\perp}r) \quad (2.80)$$

Similarly the other components of B can be written as [Klozenberg 1968, Chen 1991]

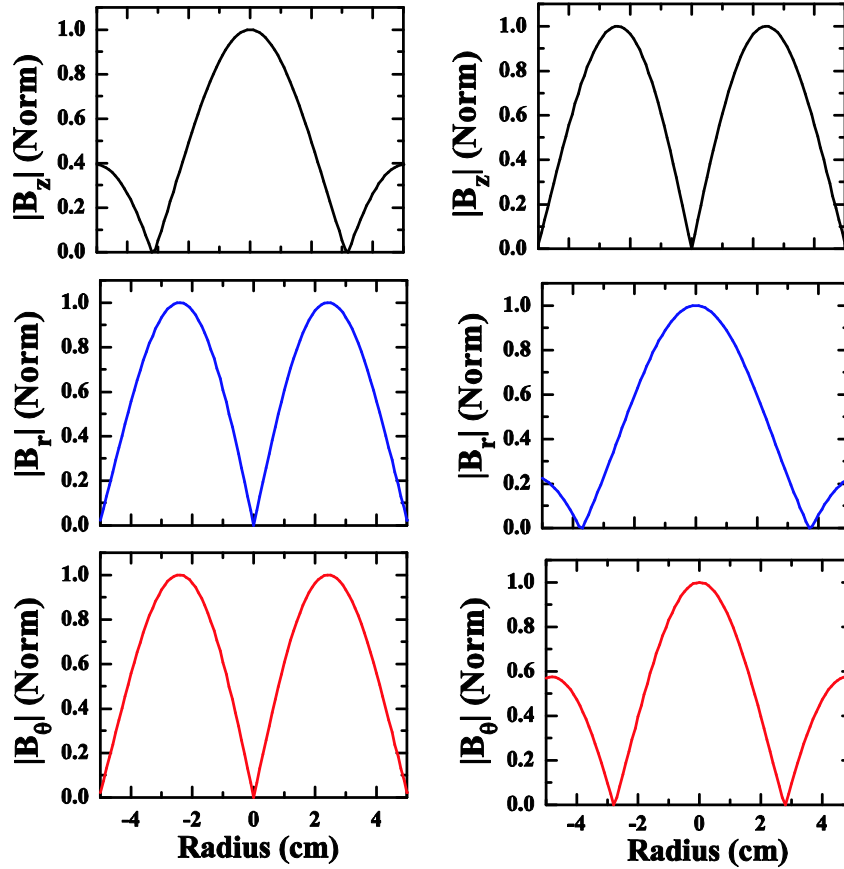


Figure 2.5 Mode structure of $m=0, +1$ modes in a plasma with cylindrical boundary.

$$B_r = \frac{iA}{2k_{\perp}} [(k + k_z)J_{m-1}(k_{\perp}r) + (k - k_z)J_{m+1}(k_{\perp}r)] \quad (2.81)$$

$$\mathbf{B}_\theta = -\frac{iA}{2k_\perp} [(\mathbf{k} + \mathbf{k}_z)J_{m-1}(k_\perp r) - (\mathbf{k} - \mathbf{k}_z)J_{m+1}(k_\perp r)] \quad (2.82)$$

And the electric field components are obtained using the Faraday's law by putting the B components.

$$\mathbf{E}_z = 0 \quad (2.83)$$

$$\mathbf{E}_r = \frac{\omega}{k} \mathbf{B}_\theta \quad (2.84)$$

$$\mathbf{E}_\theta = -\frac{\omega}{k} \mathbf{B}_r \quad (2.85)$$

The boundary condition is same for either a conducting or a dielectric boundary [12] requiring $B_r(r)|_{r=a} = 0$. This lead to the boundary condition as [12]

$$mk_z J_m(k_\perp a) + k k_z J'_m(k_\perp a) = 0 \quad (2.86)$$

Where the prime denotes first order derivative with respect to the radial coordinate. Equation 2.65 and the boundary condition equation 2.86 together can be used for a known density and magnetic field to find out the two unknowns as k_\perp and k_\parallel .

2.5 Helicon mode structure in non uniform radial density

All the above calculations for helicon dispersion and mode structure are calculated for a uniform radial density profile. The effects of realistic non-uniform density profile are on both dispersion and mode structures. Aliev and Kramer [13] have shown that for a parabolic radial density profile, the dispersion is $\omega \propto k^2$, compared to $\omega \propto k$. Though the theory suggests for a uniform plasma $\omega \propto k$, experiments by Degeling et al [14] have found a quadratic scaling of frequency with wave number. Results of effect of peaked density profiles show that $m = -1$ modes cannot propagate in a highly non-uniform plasma cylinder. So $m = +1$ modes can be used to produce less dense plasma with high radial uniformity and $m = -1$ modes can be used to produce sharper radial

profile with dense plasma at centre. M.P. Reilly [15] and Chen et al [16] have calculated the mode structures numerically for different radial density profiles and has found that the wave field profiles get more shrunken in radius with sharper density profiles.

2.6 Models of Helicon Power Deposition

Though rigorous theory and experiment has been performed in Helicon physics and helicon discharges, the high efficiency of the helicon waves is still under study. At least five different directions have been tried by many helicon physicists will be briefly outlined below.

Chen [12] has calculated the damping rate of Helicon waves through wave particle interaction (Landau damping) and has shown that the damping rates can explain the efficient ionization in helicon sources. Molvik [17] has used a high acceptance angle retarding field energy analyzer and observed electron beams in the helicon sources. These results are consistent with results by Ellingboe et al [1995] who have observed phased light emissions from the plasma. Later Blackwell and Chen [18] have shown that the number of fast electrons is very few to explain the Landau damping mechanism. An analytical calculation by Chen et al [19] further estimated the upper limit of Landau damping in a helicon discharge.

Shamrai et al. [8] have proposed that the efficiency of the absorption mechanism is not due to Landau damping, as proposed by Chen [12], but to coupling to quasioleostatic Trivelpiece-Gould modes, which are rapidly absorbed as they propagate inward from the radial boundary. Efficiency in power coupling to plasma by Trivelpiece-Gould modes is numerically shown to be higher than the helicon waves by Borg and Boswell [20], Arnush [2000], Shamrai and Taranov [8] and Shamrai and Shinohara [21]. Aliev and Kramer [22] have shown that for peaked radial density profile the mode conversion from the helicon to TG mode is possible at lower densities because of the modification of the wave mode structure by non-uniform radial density profiles. Direct measurement of TG modes is difficult because these modes are localized near the plasma boundary and also they have very short wavelengths in ~ 1 mm. However, Blackwell et al [23] have measured the high frequency current profile with \hat{j} probes to find evidence of TG modes in a low field helicon discharge but there is no direct measurement so far of these short waves.

Akhiezer et al [24] first theoretically proposed a non linear mechanism by which short scale ion acoustic turbulence excited through a kinetic parametric process causes strong absorption of helicon waves. Later Kramer et al [25] showed experimentally by cross correlation techniques using electric probes and microwave back-scattering that helicon wave decays into a TG waves travelling from boundary to inner plasma and ion acoustic fluctuations travelling from core to boundary. These ion acoustic fluctuations are correlated with the strong absorption of helicon waves. Lorentz et al [26] later found the threshold for parametric process and also the frequencies of pump and decay waves along with wave numbering parallel and perpendicular to magnetic field all obey the parametric decay process.

Degeling et al [14, 27] have shown both numerically and experimentally that the electrons in a Maxwellian distribution with velocities slower than the wave get trapped in the longitudinal component of the helicon wave electric field and are accelerated taking energy from the wave. It is shown in this work that electrons in a 3 eV Maxwellian distribution can have high enough energy to be near the maximum of Argon ionization cross section. The outcome of this model i.e. ionization pulses will travel away from the source at the wave phase velocity has been proved experimentally by Ellingboe et al [28] by measuring the Ar+ light emission pulses at RF period by time resolved optical emission spectroscopy within a tenth of RF period.

Briezman and Arifiev [29] have shown analytical calculations for non-axisymmetric modes ($|m| = 1$) for small longitudinal wave numbers with $\omega \propto k_z^2$ that radially localized surface wave type helicon modes which are decoupled from the TG modes can be excited in a radially non-uniform plasma, which can deposit energy through the process of wave particle interaction (Landau damping). With their lower wave frequency compared to normal helicons, the Landau damping rates are higher than normal helicons in uniform plasmas. Experimental radial density profile is used by Chen et al [30] to show RLH mode excitation and power deposition with frequencies close to the exciter frequency.

2.7 Mode Transitions in Helicon Discharge

Mode transitions are studied in RF capacitive, inductive and Helicon plasmas. In case of a RF capacitive plasma the discharge changes from a low density α discharge to a high density γ discharge by increasing the RF voltage [31-32]. It is shown that the transition happens when the

ionisation by the electrons emitted by secondary emissions is equal to the ionisation by the bulk electrons bouncing between the sheaths of the capacitive discharge plates.

In case of Inductive discharges the discharge is maintained by the induced electric fields produced by the antenna currents. This inductive electric fields drive plasma currents in order to oppose the magnetic fields produced by the antenna currents. At low density the plasma is maintained by capacitive electric fields as the skin depth is more so that the RF electric fields produced by the antenna high voltage can couple directly. But as the density is increased, the skin depth decreases and the electromagnetic fields decay exponentially within a very thin layer of plasma. This is the reason an inductive discharge is characterized by a hollow radial density profile. Also the RF electric field modulation of the plasma potential is much less compared to capacitive discharges. Capacitive and inductive discharges do not need an external magnetic field.

When an external magnetic field is applied to plasma, the dielectric of the plasma changes and can have normal modes which are of electromagnetic in nature. So, magnetized plasma allows certain frequencies depending upon parameters such as density and magnetic field for electromagnetic wave to penetrate to the core of the plasma. The electric field of these electromagnetic waves can deposit energy through either collisional or collisional processes. ECR and helicon sources are good example of wave sustained discharges but helicon can operate in all the three discharge regimes depending upon the density which can be increased either by RF power or magnetic field [33].

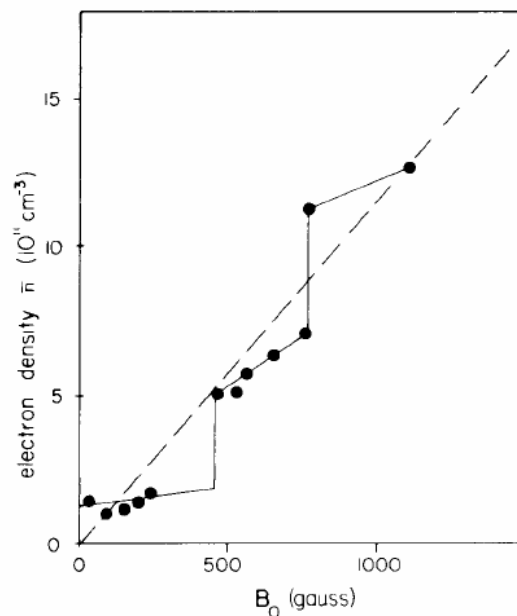


Figure 2.6 Mode transition in a helicon discharge by changing magnetic field [33].

2.8 Summary of the Chapter

Cold plasma dielectric tensor is derived from equation of motion and Maxwell's equation. Solutions for parallel to magnetic field propagation suggest longitudinal plasma oscillations along with transverse electron and ion cyclotron waves. Whistler dispersion relation and its bounded version as helicon wave dispersion relation are derived. Resonance cone propagation of right polarized waves is discussed in the context of quasiparallel wave propagation. Helicon wave field structure is calculated from generalized Ohm's law and Maxwell's equations. Finite electron mass effect is shown to give another solution as quasiolelectrostatic TG modes along with the normal quasiolelectromagnetic helicon modes. Helicon radial magnetic field profile for $m=0$ and $m=1$ modes are presented pictorially. Different coupling mechanisms to plasma by helicon waves are discussed. Mode transition in RF discharges is explained for capacitive, inductive and helicon discharges.

References

- [1] Paul Murray Bellan. (2006). *Fundamentals of plasma physics*. Cambridge University Press.
- [2] J. P. Klozenberg, B. McNamara, and P. C. Thonemann, "The dispersion and attenuation of helicon waves in a uniform cylindrical plasma," *Journal of Fluid Mechanics*, vol. 21, pp. 545-563, 1965.
- [3] Blevin, H. A., and P. J. Christiansen. "Helicon waves in a non-uniform plasma." *Plasma Physics* 10, no. 8 (1968): 799.
- [4] Ferrari, R. L., and J. P. Klozenberg. "The dispersion and attenuation of helicon waves in a cylindrical plasma-filled wave-guide." *Journal of Plasma Physics* 2, no. 02 (1968): 283-289.
- [5] T. H. Stix, *The Theory of Plasma Waves*: McGraw-Hill, 1962.
- [6] Swanson, D. G. "Plasma waves" *Academic Press, Boston, MA (USA), 1989*.
- [7] Boswell, Rod W., and Francis F. Chen. "Helicons-the early years." *Plasma Science, IEEE Transactions on* 25, no. 6 (1997): 1229-1244.
- [8] Shamrai, Konstantin P., and Vladimir B. Taranov. "Volume and surface rf power absorption in a helicon plasma source." *Plasma Sources Science and Technology* 5.3 (1996): 474.
- [9] Fisher, R. K., and Gould, R. W. (1969). Resonance cones in the field pattern of a short antenna in an anisotropic plasma. *Physical Review Letters*, 22(21), 1093.
- [10] Fisher, R. K., and Gould, R. W. (1971). Resonance cones in the field pattern of a radio frequency probe in a warm anisotropic plasma. *Physics of Fluids*, 14, 857.
- [11] Kuehl, H. H. (1974). Electric field and potential near the plasma resonance cone. *Physics of Fluids*, 17, 1275.
- [12] F. F. Chen, "Plasma Ionization by Helicon Waves," *Plasma Physics and Controlled Fusion*, vol. 33, no. 4, pp. 26, 1991.
- [13] Aliev, Yu M., and M. Kramer. "Effect of the plasma density gradient on helicon mode dispersion." *Physica Scripta* 79.3 (2009): 035502.
- [14] Degeling, A. W., C. O. Jung, R. W. Boswell, and A. R. Ellingboe. "Plasma production from helicon waves." *Physics of Plasmas* 3 (1996): 2788.
- [15] Reilly, Michael P. Thesis *Three Dimensional Imaging of Helicon Wave Fields via Magnetic Induction Probes* (2009).

- [16] Chen, Francis F., M. Johannes Hsieh, and Max Light. "Helicon waves in a non-uniform plasma." *Plasma Sources Science and Technology* 3, no. 1 (1994): 49.
- [17] Molvik, A. W., A. R. Ellingboe, and T. D. Rognlien. "Hot-electron production and wave structure in a helicon plasma source." *Physical Review Letters* 79.2 (1997): 233.
- [18] Blackwell, David D., and Francis F. Chen. "Time-resolved measurements of the electron energy distribution function in a helicon plasma." *Plasma Sources Science and Technology* 10.2 (2001): 226.
- [19] F. F. Chen, and D. D. Blackwell, "Upper Limit to Landau Damping in Helicon Discharges," *Physical Review Letters*, vol. 82, no. 13, pp. 2677, 1999.
- [20] Borg, G. G., and R. W. Boswell. "Power coupling to helicon and Trivelpiece–Gould modes in helicon sources." *Physics of Plasmas* 5 (1998): 564.
- [21] Shamrai, Konstantin P., and Shunjiro Shinohara. "Spectral and spatial characterization of a radio frequency power absorption in high pressure helicon plasmas." *Physics of Plasmas* 8 (2001): 4659.
- [22] Aliev, Yu M., and M. Krämer. "Mode conversion of nonaxisymmetric modes in strongly nonuniform helicon-sustained plasma." *Physics of Plasmas* 15 (2008): 104502.
- [23] Blackwell, D. D., T. G. Madziwa, D. Arnush, and F. F. Chen. "Evidence for Trivelpiece–Gould modes in a helicon discharge." *Physical review letters* 88, no. 14 (2002): 145002-145002.
- [24] Akhiezer, A. I., Mikhailenko, V. S., and Stepanov, K. N. (1998). Ion-sound parametric turbulence and anomalous electron heating with application to helicon plasma sources. *Physics Letters A*, 245(1), 117-122.
- [25] Krämer, M., Aliev, Y. M., Altukhov, A. B., Gurchenko, A. D., Gusakov, E. Z., and Niemi, K. (2007). Anomalous helicon wave absorption and parametric excitation of electrostatic fluctuations in a helicon-produced plasma. *Plasma Physics and Controlled Fusion*, 49(5A), A167.
- [26] Lorenz, B., Krämer, M., Selenin, V. L., and Aliev, Y. M. (2005). Excitation of short-scale fluctuations by parametric decay of helicon waves into ion–sound and Trivelpiece–Gould waves. *Plasma Sources Science and Technology*, 14(3), 623.
- [27] Degeling, A. W., and R. W. Boswell. "Modeling ionization by helicon waves." *Physics of Plasmas* 4 (1997): 2748.
- [28] Ellingboe, A. R., R. W. Boswell, J. P. Booth, and N. Sadeghi. "Electron beam pulses produced by helicon-wave excitation." *Physics of Plasmas* 2 (1995): 1807.
- [29] B. N. Breizman, and A. V. Arefiev, "Radially Localized Helicon Modes in Nonuniform Plasma," *Physical Review Letters*, vol. 84, no. 17, pp. 4, 2000.

- [30] Chen, Guangye, Alexey V. Arefiev, Roger D. Bengtson, Boris N. Breizman, Charles A. Lee, and Laxminarayan L. Raja. "Resonant power absorption in helicon plasma sources." *Physics of plasmas* 13 (2006): 123507.
- [31] Odrobina, I., and Kando, M. Discontinuous transitions between alpha and gamma regimes of rf capacitive discharge. *Plasma Sources Science and Technology*, 5, 517 (1996).
- [32] Moon, Se Youn, J. K. Rhee, Dan Bee Kim, and Wonho Choe. " α , γ , and normal, abnormal glow discharge modes in radio-frequency capacitively coupled discharges at atmospheric pressure." *Physics of Plasmas* 13 (2006): 033502.
- [33] Boswell, R. W. "Very efficient plasma generation by whistler waves near the lower hybrid frequency." *Plasma Physics and Controlled Fusion* 26.10 (1984): 1147.

Experimental Set up and Diagnostics

3.1 Introduction

The experimental works presented in this thesis are performed in a linear magnetized plasma device (Figure 3.1) produced by RF electric fields. The magnetic field is produced by a set of water cooled electromagnets arranged to give a uniform magnetic field in the source chamber. The RF antenna powered by a 2.5 kW RF generator along with an L-type matching network produces the plasma. The antenna is installed around a cylindrical glass tube connected to a cylindrical vessel made of SS304. This chapter describes the apparatus and diagnostics. The apparatus can be divided into three main sections: the vacuum system, the electromagnets and the RF system. The RF system consists of half helical helicon antenna, RF power source, matching network and RF shielding and grounding. Diagnostics used are various Langmuir probes for density, temperature and floating potential measurements, emissive probe for plasma potential measurement, magnetic probe for measuring wave field amplitude and phase, Rogowski for antenna current measurements.

3.2 Vacuum Vessel and Vacuum System

The total length of the experimental chamber is approximately 120 cm, which comprises of two linear chambers of cylindrical cross section of different radii, as shown in Figure 3.2. The first chamber, called the source chamber hereafter, measures 70 cm in length and is made up of borosilicate glass tube of 10 cm diameter with wall thickness of 0.4 cm. The RF antenna is installed around this cylindrical glass tube. One end of this glass tube is closed with an insulated end flange to make the plasma system current free and the other end is connected to a cylindrical diffusion chamber made up of stainless steel having an inner diameter of 21 cm and length of 50

cm. As the plasma diffuses to this chamber from the source chamber it is called the diffusion chamber. A stainless steel metal flange closes the other end of the diffusion chamber.

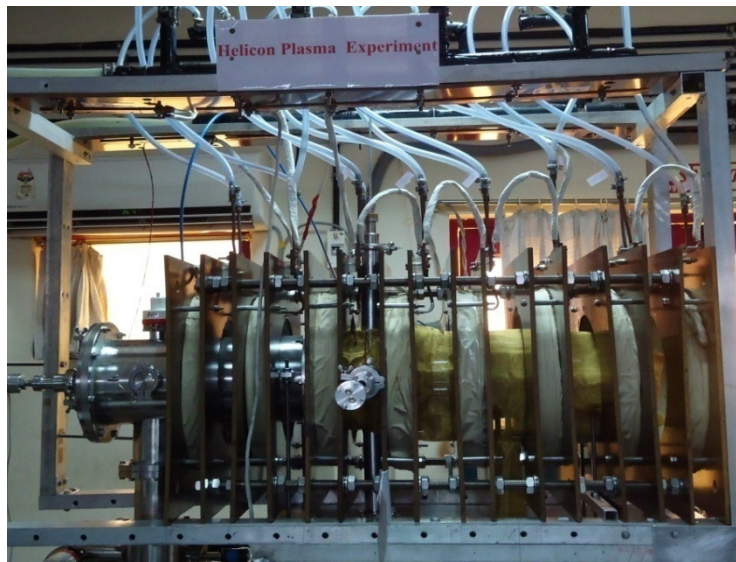


Figure 3.1 Picture of Helicon experimental Set up.

The plasma is produced in the source chamber and has four orthogonal diagnostic ports for diagnosing the source chamber plasma. The diffusion chamber has 15 radial ports on its periphery and three ports on the diffusion chamber end flange for various diagnostics.

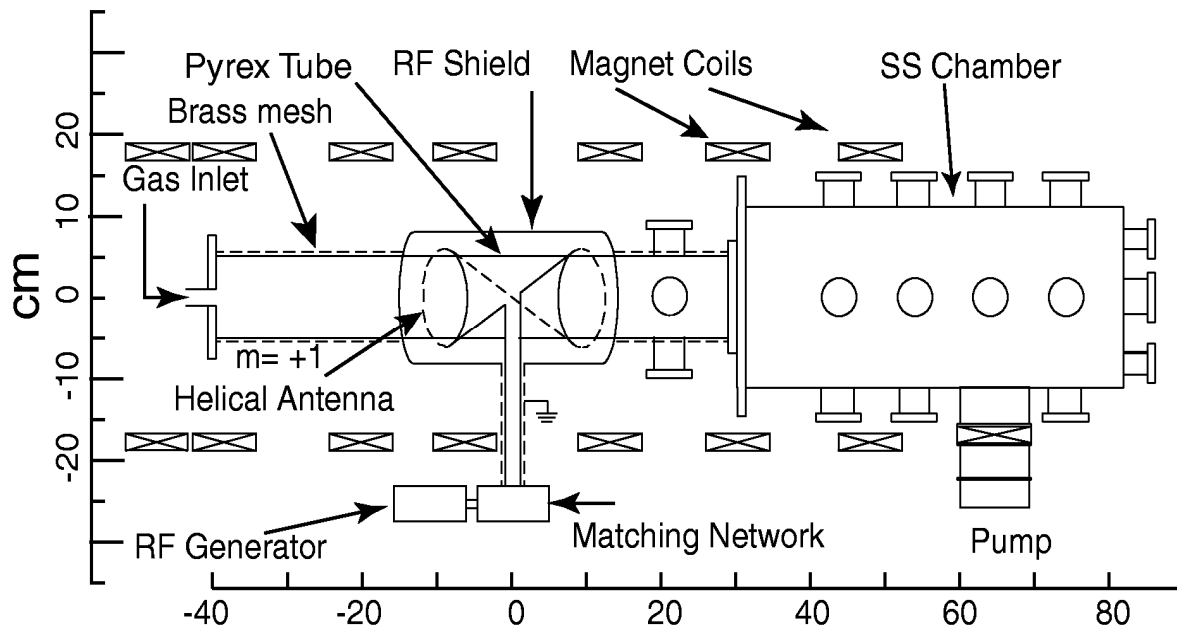


Figure 3.2 Schematic of the helicon experimental set up.

The vacuum chamber is Helium leak tested up to 1×10^{-7} mbar-liter/sec. A 1000 liter/s diffusion pump backed by a rotary pump is used to evacuate the system up to a minimum base pressure of 1×10^{-6} mbar. The pressure is measured in the diffusion chamber by an Alcatel Vacuum make AHC 2000, hot cathode-crystal combo gauge. The operational or fill-in pressure is varied from 1×10^{-4} mbar to 5×10^{-3} mbar. Gas is filled through a Pfeiffer make gas-dosing valve connected to the end flange of the source chamber, which allows fine changes in the system neutral gas pressure. Argon gas is used most of the times unless otherwise stated.

3.3 Electromagnets

The axial magnetic field is created by seven electromagnets made up of hollow copper pipes of 0.6 cm inner diameter and 0.8 cm outer diameter. The hollow pipes facilitate forced water flow to cool the electromagnets at high current for steady state operation. These tubes are wound over a PVC pipe of 33 cm outer diameter and with wall thickness 0.4 cm, which is supported on both sides by rectangular hylam blocks (60 cm x 60 cm) of 1.6 cm thickness. The inner diameter of each coil is 31.5 cm and the height and width are 6 cm each. Self-adhesive cotton tape of 500 micron thickness is used to achieve layer to layer insulation up to 1.5 kV. In each coil there are six layers each having six turns totaling 36 turns. Each magnet has a resistance of ~ 40 mili-Ohms. These magnets are then placed on an aluminum stand with proper mechanical support to withstand the electromagnetic forces acting on them. The placement of the magnets is shown in Figure 3.2. The magnets are aligned very carefully to make axis of magnets collinear with the vacuum vessel. A Sorensen make variable power supply rated 60 V, 167 A is used to power the electromagnets to achieve a maximum magnetic field of ~ 400 Gauss. Before mounting the electromagnets, each of them is separately tested for water flow, magnetic field and resistance. After assembling the magnets, a current of 52.5 Amp is passed through six magnets (as shown in Figure 3.2 excluding the seventh coil) connected in series and the magnetic field value on the axis of the chamber using is measured using a H.W. BELL Hall probe. The magnetic field is also simulated with EFFI code [1] by using the real coil dimensions such as average coil diameter, width, height and current density. Figure 3.3(a) shows the simulated and the measured axial magnetic field values along the axis of the chamber with six magnets. The measured magnetic field matches very well with the simulated values. To achieve different gradients in the axial direction we simulated the axial magnetic field profile with all the seven

magnets by varying the current in the seventh coil. Figure 3.3(b) clearly shows that several different gradients of magnetic field in the axial direction can be achieved in the machine varying the current in the seventh coil.

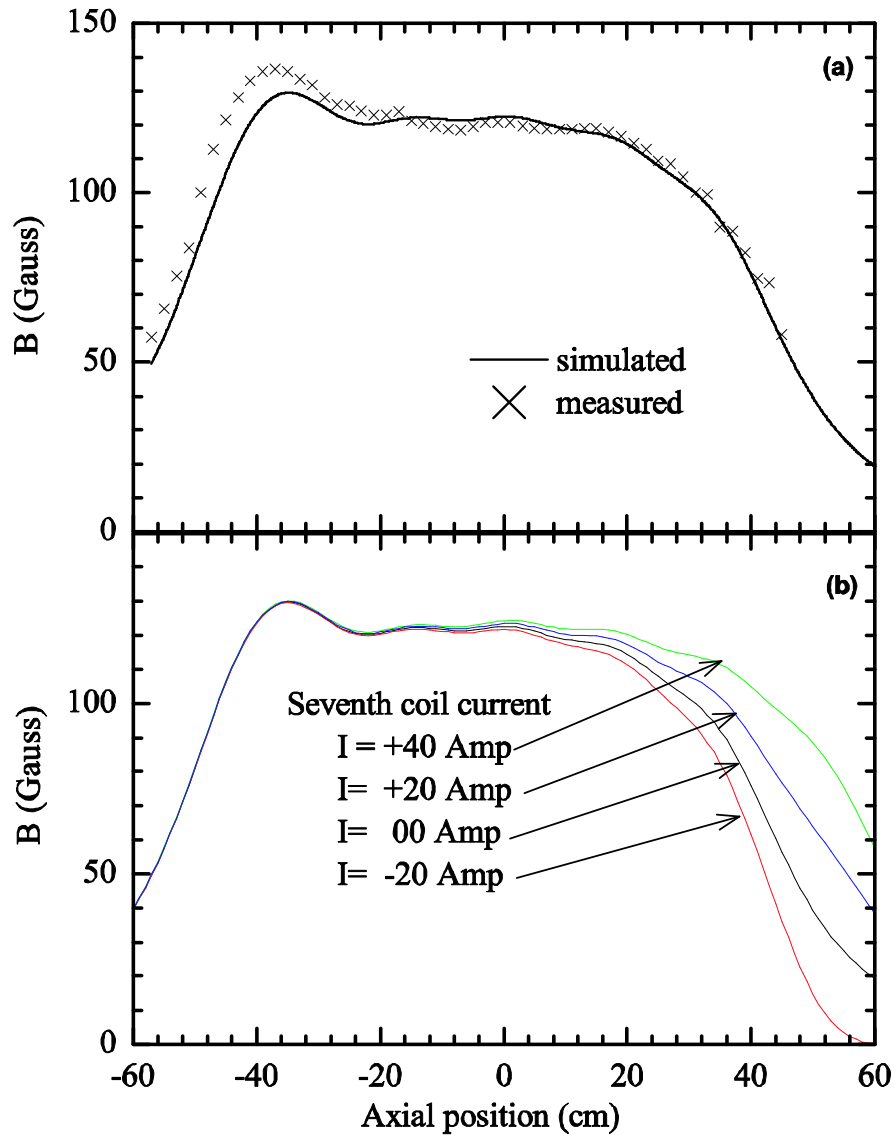


Figure 3.3 (a) Plot for magnetic field produced by 6 magnets at -47.8, -38.5, -20, -3.5, 13, 30 by passing a positive current of 52 Ampere and (b) additional variable current in the seventh coil at 47 cm to get a variable gradient.

Parameter (Unit)	Values for Argon gas
B (Gauss)	1-400
P_{neutral} (mbar)	$4 \times 10^{-3} - 1 \times 10^{-4}$
n (10^{11} cm^{-3})	0.1 - 5
T_e (eV)	3 - 8
λ_{Debye} (cm)	$1.8 \times 10^{-3} - 2.1 \times 10^{-2}$
r_e (cm)	0.01 - 10
r_i (cm)	1 - 460
f_{pe} (GHz)	0.87 – 6.28
f_{ce} (MHz)	2.8 – 1105
f_{ci} (kHz)	0.37 – 15
$f_{\text{e-n}}$ (kHz)	50 - 3267
$f_{\text{i-n}}$ (kHz)	0.466 - 30

Table 3.1 Parameter regime, length scales and time scales of the present helicon experiment.

3.4 Antenna and RF Matching Circuit

As the half wavelength antenna is shown to be more efficient [2] compared to the full wavelength antenna, we have designed and fabricated a half-wavelength helical $m = +1$ antenna with diameter of 12 cm and length of 18 cm. Picture of this antenna is shown in Figure 3.4. The antenna is connected to matching network through a shielded twin coaxial transmission line of diameter 3.5 cm. The helicon antenna is placed around the source (glass) chamber and RF shielding of the antenna is done by putting a 2 mm thick hollow coaxial copper cylinder of 20 cm

inner diameter and 25 cm length around it. The remaining part of the glass chamber is covered by two layers of brass mesh of 30% transparency. The full grounding and shielding scheme is elaborated in Figure 3.2. Proper RF shielding is ensured by measuring the radiation fields outside the antenna region by a Narda make field meter and is found to be less than 5 V/m in 1 meter radius from the antenna. A 13.56 MHz Advance Energy make MOSFET based RF amplifier is used to power the antenna. The amplifier has characteristic output impedance of 50 Ohm and it can supply RF power up to 2.5 kW with maximum reflection of 400 W. It contains an inbuilt power meter, which displays the forward and the reflected power.



Figure 3.4 Picture of the inside of the match box showing the variable Load and Tune Capacitors with auxiliary inductors.

The matching network used is a CESAR make 5 kW capacitive L-matching network designed for an inductive load [3]. The picture of the matching network is shown in Figure 3.4. There exist

two variable capacitors in the matching network, one is a load capacitor (C_L), which can be tuned from 20 to 1000 pF and another is a tune capacitor (C_T), which can be tuned from 5 to 500 pF.

3.4.1 The Antenna

Various antennas are used to produce helicon plasma [4]. A right half helical antenna is used for the present work. The helical antenna consists of two helical windings wound around the outside of the glass tube each azimuthally 180 degree displaced. Antenna is placed on two teflon spacers of about 3mm thick at the antenna ends fixed from the outside of the glass tube. The current in each winding is in the opposite direction to each other. This antenna is constructed with one length of copper plate with the two winding joined by a half loop at one end as shown in Figure 3.5. The helical antenna has a higher selectivity of parallel wavelength [5] than the double saddle coil [6] thus decreasing its useful wavelength range. For present experiment the length of the antenna chosen is 18 cm.



Figure 3.5 Picture of the half helical $m=+1$ antenna just before installation.

3.4.2 Matching Network

To ensure that the transmission line from the RF transmitter is terminated at its characteristic impedance the antenna is incorporated into an L-network, where the antenna predominantly behaves like an inductor as shown in Figure 3.5. When there is no plasma the resistance is the electrical resistance of the antenna. Once plasma is formed the resistance will increase. The output impedance (50Ω) of the RF source was matched to the impedance of antenna-plasma load for maximum power transfer. We used a commercial impedance matching network (AE, VM 5000 W) with a tuning unit. The tuning unit contains the matching components (variable capacitors and inductors), two dc motor servos, and RF sensors to provide feedback to the dc motor servos. L-type matching network is employed with two vacuum variable capacitors. Original capacitors initially provided by the vendor were not enough to match the impedance of the plasma under variety of experimental conditions. So we opted for a set of inductors in series with the capacitors and used different inductors as per experimental requirement. To have the confidence on the matching network a rough calculation has been made.

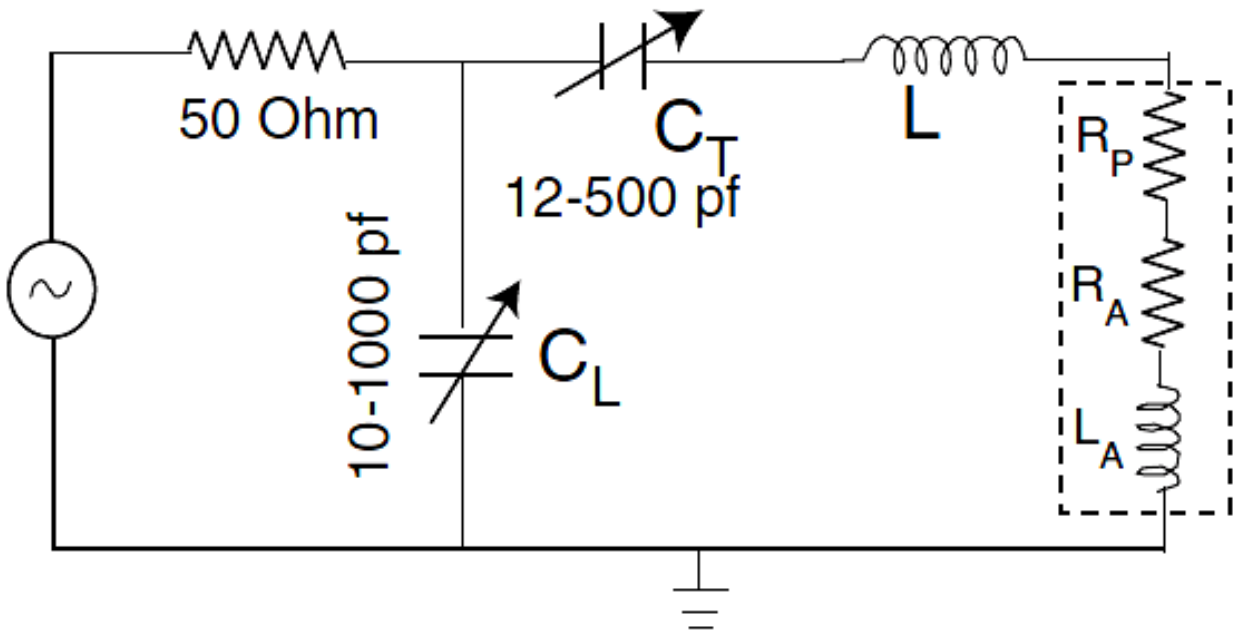


Figure 3.6 Schematic of the matching network attached to RF generator and a load composed of the antenna and plasma.

In Figure 3.6 we show the equivalent circuit of the L-type network is shown in which: L_A stands for the antenna inductance, resistance R_p is the electrical resistance of the antenna when the plasma is switched on, which increases when plasma is on. It is necessary to estimate the load and the tuning capacitance (C_L , C_T) for better designing of the L-network. Let us group L_A , R_p and C_T and call them the tune arm. Its impedance is

$$\mathbf{Z}_T = i\omega L_A + \frac{1}{i\omega C_T} + R_p \quad (3.1)$$

that can be written dividing real from imaginary part as

$$\mathbf{Z}_T = i\check{L} + R_p \quad (3.2)$$

$$\text{where, } \check{L} = \omega L_A - \frac{1}{\omega C_T} \quad (3.3)$$

Now let's assume that the tune capacitance does not completely cancel out the antenna inductance, and then the load capacitance can balance the net inductive impedance of the tune arm. The admittance (i.e. the inverse of the impedance) of the tune and load arm can be written as

$$\mathbf{Y}_T = \frac{R_p}{R_p^2 + \check{L}^2} - \frac{i\check{L}}{R_p^2 + \check{L}^2} \quad (3.4)$$

$$\mathbf{Y}_L = i\omega C_L \quad (3.5)$$

So that the total admittance Y of the L-network is given by

$$\mathbf{Y} = \mathbf{Y}_T + \mathbf{Y}_L \quad (3.6)$$

To find values of C_L and C_T , a resonance condition (i.e. along the tuning arm we only see real impedance) is imposed; then the total conductance (i.e. the real part of the admittance) will equal the inverse of the total line impedance Z_T , and the susceptance (i.e. the imaginary part of the admittance) of the two arms will cancel. These conditions give us, respectively, the following equations

$$\check{L}^2 = R_p(Z_T - R_p) \quad (3.7)$$

$$C_L = \frac{\check{L}}{R_p Z_T \omega} \quad (3.8)$$

For the antenna, plasma and transmission line we are using, it is possible to assume that $Z_T \gg R_p$ so that equation (3.7) gives

$$\check{L} = \sqrt{R_p Z_T} \quad (3.8)$$

Now combining equations (3.8) and (3.9) one can get the formula for the load capacitance

$$C_L = \frac{1}{\omega \sqrt{R_p Z_T}} \quad (3.10)$$

and substituting equation (3.9) into (3.3) the formula for the tune capacitance is

$$C_T = \frac{1}{\omega^2 L_A - \omega \sqrt{R_p Z_T}} \quad (3.11)$$

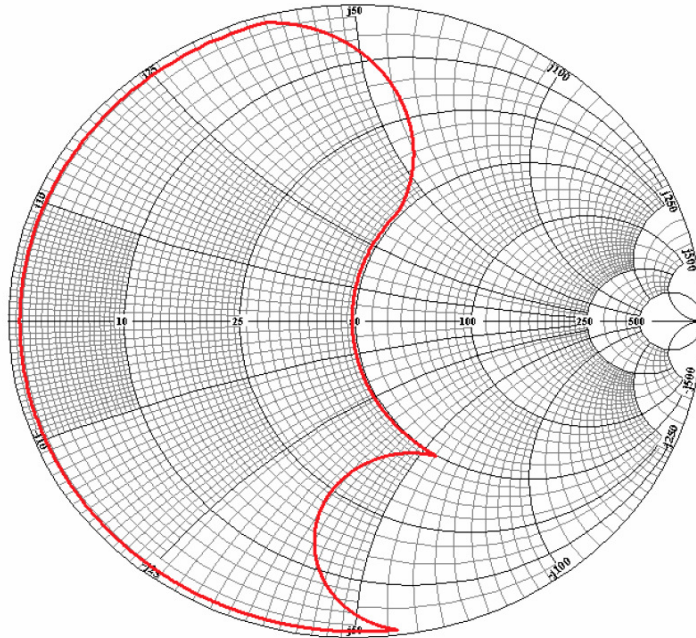


Figure 3.7 Smith Chart showing operational matching regimes of the current matching network attached to an inductive helicon antenna.

Taking a typical case with $L_A = 500 \text{ nH}$, $R_P \sim 1 \text{ Ohm}$, $Z_T = 50 \text{ Ohm}$ and $\omega = 85.2 \text{ MHz}$ and using Equations (3.10) and (3.11) we get: $C_L = 1650 \text{ pF}$ and $C_T = 330 \text{ pF}$. Two COMET make vacuum variable capacitors are used. By adding suitable inductors (water cooled) in series with the capacitors, the normal operation in a helicon regime of discharge requires values of C_L and C_T as $\sim 700 \text{ pF}$ and $\sim 100 \text{ pF}$ respectively. The matched region with these capacitors and inductors is shown by the region bordered with the red line in Figure 3.6. The load capacitor (C_L) can be tuned from 20 to 1000 pF and the tune capacitor (C_T) can be tuned from 5 to 500 pF so that zero reflection matching can be done for $R_P = 0.1 \text{ Ohm}$ to 2 Ohm. Both the capacitors are mounted inside the tuning box, which is made of silver coated copper, so that it acts as a Faraday cage. On the top side of the tuning box a fan is mounted to ensure cooling for the two capacitors. Measuring the power coupled into the plasma is very important for defining correctly the plasma parameters. The antenna radiation resistance is the principle measure of the efficiency of an antenna.

For a mismatched load both the voltage and current along with their phase measurement are necessary to estimate the power delivered to the load. However for a matched load with negligible reflection, antenna will see plasma as a resistive load only. To evaluate this load we assume that when plasma is on, the resistance of the antenna is given by the resistance of the antenna plus that of the plasma

$$R_T = R_A + R_P \quad (3.87)$$

The power dissipated by the antenna can be written as [7]

$$I_A^2 R_T = P_F - P_R \quad (3.13)$$

Measuring R_A without plasma we find, from the last two equations, a formula for R_P , which is the load of the antenna-plasma coupling

$$R_P = \frac{P_F - P_R}{I_A^2} - R_A \quad (3.14)$$

During measurements the power is monitored on the control panel of the RF generator. The matching network usually achieves reflections less than 1%.

3.5 Diagnostics

The RF produced plasma properties and plasma phenomena are characterized by different electric and magnetic probe diagnostics. Measurement principle, probe operation principle, design considerations of the probe, analysis methods and effect of different types of noise including the RF plasma potential fluctuations are discussed.

3.5.1 Single Langmuir Probe

Electric probes are one of the most widely used diagnostics used for basic characterization of the plasmas of widely ranging spatial and time scales. Though simple in construction and analysis for getting the plasma parameters, the techniques have evolved [8-15] a lot in the last century to characterize more and more complex phenomena. The theory is as old as the first electrical discharges. The simple theory was developed by Langmuir [8], which gives it the name. Langmuir probe theory attempts to explain the interaction of a metallic probe and plasma through a non-neutral region of charged particles called the sheath. A metallic probe is biased at different potentials and current is collected. This gives the current-Voltage (IV) characteristics of the Langmuir probe, where the drawn current is a non-linear function of the bias voltage. When a bias other than the space potential of the plasma is applied to the probe, a space charge sheath is formed around the probe surface to shield the electric field. So, the sheath limits the current to a space charge limited current thus by acting as a resistance. This dynamic resistance is called the sheath resistance and depends on the plasma parameters such as density, temperature and gas mass. The value of this sheath resistance in the electron collection regime is the ratio of electron current and temperature i.e. I_e/T_e and near the floating potential is the ratio of ion saturation current to electron temperature [16]. So,

$$R_s \propto n/\sqrt{T_e} \quad (3.15)$$

In experiments to measure the probe current, a shunt resistance R_m is normally used as a current sensor and the voltage drop across it is measured. This shunt resistance has to be chosen

carefully as it becomes a part of the Langmuir probe circuit. In low temperature and low density plasmas this resistance cannot be very small as then the current signal will be comparable to the noise level of a practical LP circuit. At the same time to quantify the response of plasma, all the probe bias voltage should drop in the sheath for which the shunt resistance should not be large enough that a significant portion of the bias voltage drops across R_m only.

In plasma, the electron flux onto a plasma exposed electrically floating probe is more than that of ions because of mainly two reasons. First, the electrons are lighter than ions and secondly, random thermal velocity is higher for electrons compared to more or less cold ions. So for a floating object, the more mobile electrons impinge first. As the probe is electrically floating, the probe gets charged to a negative potential such that the electrons are repelled and ions are collected. The potential of the probe settles to a negative potential w.r.t. the plasma potential such that the fluxes of electron and ion are equal. This equilibrium potential is called the floating potential of the probe. There are two ways in which the probe current can be made zero or negligible and the floating potential can be measured. This is done either by changing the bias to collect negligible current in which case the measuring resistance is much less than sheath resistance or by removing the bias and making the measuring resistance much higher than the sheath resistance such that the probe collects a negligible current.

When a probe is biased negative w.r.t. the floating potential an ion rich sheath is formed. Normally for bias voltages less than four times electron temperature (in volts) less than the floating potential in Maxwellian plasma, almost all the electrons are repelled and the collected current in the probe is Bohm current due to ions. This current is called the ion saturation current.

When the probe bias is equal to the space potential of the plasma, then virtually there is no sheath around the probe as there is no electric field to be shielded. So, all the electrons in the Maxwellian distribution are collected randomly. This is the maximum electron current and is known as the electron saturation current to a probe.

When a probe is biased with a potential less than the plasma potential, electrons are repelled as per their energy. One can scan the entire energy distribution of the electrons just by varying the probe bias w.r.t the plasma potential. As the bias approaches the floating potential, only tail electrons in the Maxwellian distribution are collected by the probe and so the current

decreases. As we will see in the subsequent sections, the current collected in the region between the plasma and floating potential of the I-V characteristics, has a slope from which electron temperature can be derived.

The saturations mentioned in the last section are seldom obtained. Ideally the saturations are obtained for the extreme positive and negative bias values of the I-V characteristics. But when the bias is increased, the sheath edge extends more into the plasma to accommodate higher electric fields, so that the sheath or collection area increases and so is the probe current. For thick sheaths, where sheath thickness is more than the probe radius, saturation current is independent of the bias voltage for planar probes where as saturation current in spherical probes varies as proportion to bias voltage and in cylindrical probes the saturation current varies as square root of bias voltage [8]. Recent work by Sheridan [17-18] has estimated probe area correction factors while estimating density from ion saturation current. The sheath thickness can be approximated from the following expression [18-19]:

$$\frac{s}{\lambda_{de}} = \left(\frac{4\sqrt{2}}{9} \right)^{\frac{1}{2}} \left(\frac{eV_0}{kT_e} \right)^{\frac{3}{4}} \quad (3.16)$$

Where, s is the sheath thickness and V_0 is the voltage drop in the sheath.

The Langmuir probe theory for magnetized plasmas is discussed by Demidov et al [20] and Hutchinson [21]. These theories provide an equilibrium solution for the portion of the IV characteristic where the probe potential is less than the plasma potential so that always an ion sheath is formed around the probe. The electrons are electrostatically repulsed by the sheath electric field, and are modeled as a Maxwell-Boltzmann velocity distribution modified by the Boltzmann factor. The total current from the plasma to the probe $I(V_p)$ as a function of bias voltage V_p in a plasma with plasma potential V_s is then sum of the electron current and the ion current,

$$I(V_p) = n_{\infty} e A_p \left(\frac{T_e}{m_i} \right)^{1/2} \left[\frac{1}{2} \left(\frac{2m_i}{\pi m_e} \right)^{1/2} \exp\left(\frac{eV_s - V_p}{T_e} \right) - \frac{A_s}{A_p} \exp\left(\frac{1}{2} \right) \right] \quad (3.17)$$

The first term is the contribution from the electrons and the second term from the ions. Here n_{∞} is the density of unperturbed plasma away from the probe surface, A_p is the probe surface area, e

is the electronic charge, m_i is ion mass, m_e is the electron mass, T_e is electron temperature, A_s is the sheath surface area. A probe diameter can always be chosen such that the radius of the probe is much larger than the sheath thickness so that the ratio $\frac{A_s}{A_p}$ is nearly unity. This is called the planar sheath approximation. Differentiating the probe current w.r.t. the probe bias,

$$\frac{dI}{dV} = \frac{e}{T_e} (I - I_s) + \frac{dI_s}{dV} \quad (3. 18)$$

Where I_s is the ion saturation current given by

$$I_s = \exp\left(\frac{1}{2}\right) n_\infty e A_p \left(\frac{T_e}{m_i}\right)^{\frac{1}{2}} \quad (3. 19)$$

Assuming, $dI_s/dV \ll dI/dV$, the electron temperature is determined from

$$T_e = e \frac{(I - I_s)}{dI/dV} \quad (3. 20)$$

Relation between Plasma potential and Floating Potential:

As for the reason described earlier for not getting saturation in a cylindrical probe and also for high density plasmas like helicon sources one needs to collect a large amount of current to get the plasma potential, the floating potential where a very less current is collected can give an estimate of the plasma potential. The floating potential is defined as the potential at which the probe current goes to zero. The ion flux Γ_i to a probe at a potential less than plasma potential is given by

$$\Gamma_i = \frac{1}{4} n_s \left(\frac{kT_e}{M}\right)^{\frac{1}{2}} \quad (3. 21)$$

The electron flux Γ_e at a bias equal to the floating potential is given by

$$\Gamma_e = \frac{1}{4} n_s \left(\frac{8kT_e}{\pi m}\right)^{\frac{1}{2}} \exp\left(\frac{eV_f}{kT_e}\right) \quad (3. 22)$$

Equating both the fluxes

$$\left(\frac{kT_e}{M}\right)^{\frac{1}{2}} = \left(\frac{8kT_e}{\pi m}\right)^{\frac{1}{2}} \exp\left(\frac{eV_f}{kT_e}\right) \quad (3.23)$$

And taking logarithm of both sides we get,

$$V_f = \frac{1}{2} \frac{kT_e}{e} \ln\left(\frac{2\pi m}{M}\right) \quad (3.24)$$

This is the potential attained by a probe w.r.t. the plasma potential when exposed to plasma and drawing no current. As the ions are heavier than electrons, a floating probe will always be charged negative w.r.t. the plasma potential.

For Argon gas used in our experiment $V_f \approx -4.7T_e$. Additional $-0.5T_e$ drop in the presheath to satisfy the Bohm criterion, the plasma potential can be expressed for argon gas as $V_p \approx V_f + 5.2T_e$.

Effect of Magnetic field on Langmuir Probe data analysis:

When a probe is used in plasma with an external magnetic field, the probe current to the plasma depends on the magnetization of the charged particles. The probe radius has to be carefully chosen to consider the effect of magnetic field. There are three cases to be considered. Low magnetic fields: Both electrons and ions have the larmour radius larger than probe radius. Here the theory of probe collection in unmagnetized case is still applicable. In the intermediate magnetic fields, the electron larmour radius is smaller than the probe radius but not the ion larmour radius. In this case the electron current collection in the surface perpendicular to the magnetic field is reduced. So the ratio of electron and ion saturation current is decreased. We worked in this regime of magnetic fields. As we are calculating the density from ion saturation current, the results are unaffected by magnetic field. In case very high magnetic field, both electron and ion have larmour radius smaller than the probe dimension such that the all the saturation currents are affected.

Sheath Ionization and its signature:

A sheath becomes collisional if the electron-neutral collision length can be accommodated inside the sheath width. This in our system can happen for a low density high pressure plasma discharge conditions. When a bias more than the plasma potential is applied, the electrons before being collected can do an ionizing collision. The ionization leads a secondary plasma formation near the sheath.

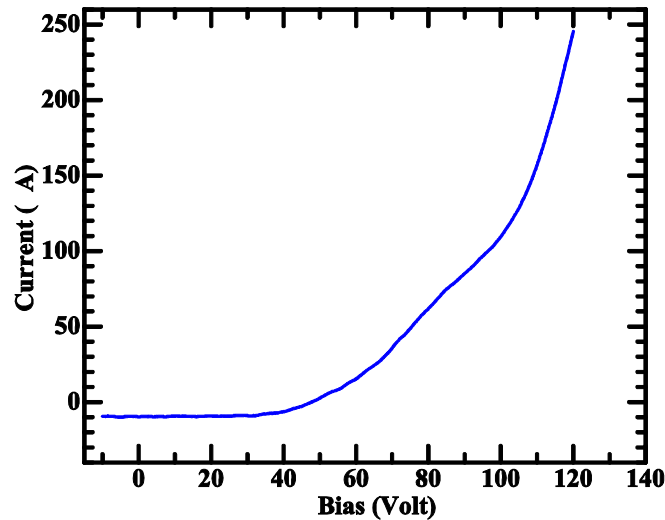


Figure 3.8 Typical IV characteristics of Langmuir probe with sheath ionization.

This secondary plasma is sometimes called as an anode double layer and its existence solely depends on a critical current which in turn depends on the electron number density (which is more near plasma potential), gas species, collision cross-section and neutral gas pressure. The IV characteristics instead of being saturated, has a sudden rise in current for incremental increase of the probe bias above plasma potential. A typical IV characteristics obtained at high pressure (8×10^{-2} mbar) is shown in Figure 3.8.

Probe cleaning:

The probe if not a clean surface can lead to many problems including erroneous/irreproducible IV characteristics, degassing, secondary emission etc which will ultimately lead to irreproducible data. Impurities on the probe surface can be cleaned by heating the surface. This is done by keeping the probe in electron saturation mode for longer times. As

the magnitude of electron current is more, this will heat the probe surface through Joule heating and the surface gets cleaned. Some impurities can stick to the surface of the probe which can be cleaned by bombarding ions on to the probe by keeping the probe in the ion saturation regime. The ions hit the surface and clean it by sputtering the probe surface.

Probe, probe holder, and shaft Size limitations:

The planar sheath approximation has the basic assumption that the sheath thickness is smaller than the probe radius. When the sheath thickness is high, large currents can now flow, the sheath resistance decreases. . The frequency response ($\propto 1/R_s C_s$) of a Langmuir probe is inversely proportional to the sheath resistance. So when the sheath resistance decreases with bigger probe size, the small fluctuations get amplified and affect the DC characteristics. Also a bigger probe reduces the space resolution. They can also disturb the plasma by taking a large amount of current. When you have a bigger probe holder which is most of the time an insulator, it can disturb the plasma electron energy distribution (EEDF). If the rate of loss of high energetic plasma electrons to the probe holder or shaft is more than the rate of replenishment of these fast electrons by thermalization processes in the plasma, the EEDF will be significantly affected. The probe shaft is generally a grounded metallic body which can significantly disturb either by taking current from the plasma or by disturbing any potential structure if at all to be studied.

Design:

The probe tip is made of 0.5 mm cylindrical tungsten wire with a plasma exposed length of 3 mm. The probe tip is silver brazed with a copper cable which is connected to a coaxial cable for signal transfer. The probe tip is inside a ceramic bid and the bid is connected to a machinable ceramic holder. The probe holder is connected to a SS 304 metallic probe shaft which has vacuum compatible connection at the other end for both vacuum and electrical integrity. The probe shaft is housed in a Wilson vacuum feedthru for linear and rotational motion without breaking the vacuum. A floating source of ± 150 V made of batteries in series is used to bias a high power amplifier (PA-85) which amplifies a triangular ramp signal of ± 5 V produced by a signal generator at a frequency of 1 Hz. This time varying signal is applied to the probe through a coaxial cable. A shunt resistance of 1 kOhm is used to measure the probe current. The output

voltage across the measuring resistance is obtained in the oscilloscope through a unity gain optical isolation amplifier. The schematic of the measurement circuit is shown in Figure 3.9.

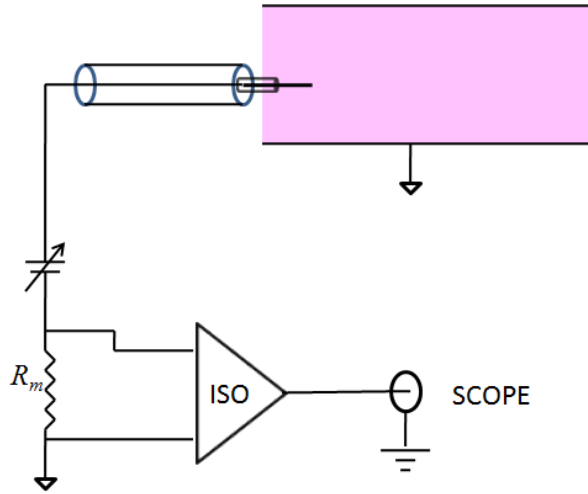


Figure 3.9 Schematic of SLP measurement circuit.

Capacitive Pick-Up limits sweep frequency:

The cable capacitance used to give a variable bias to the probe or RFEA limits the frequency of the ramp. The representative electrical circuit is shown in Figure 3.10. The sweeping voltage acts as a source which drives a displacement current in the current measurement circuit and as the measuring resistance is in series of the source, a voltage drop corresponding to the differentiated input signal is obtained and it is expected that this signal in all the experimental conditions be less than the original conduction current.

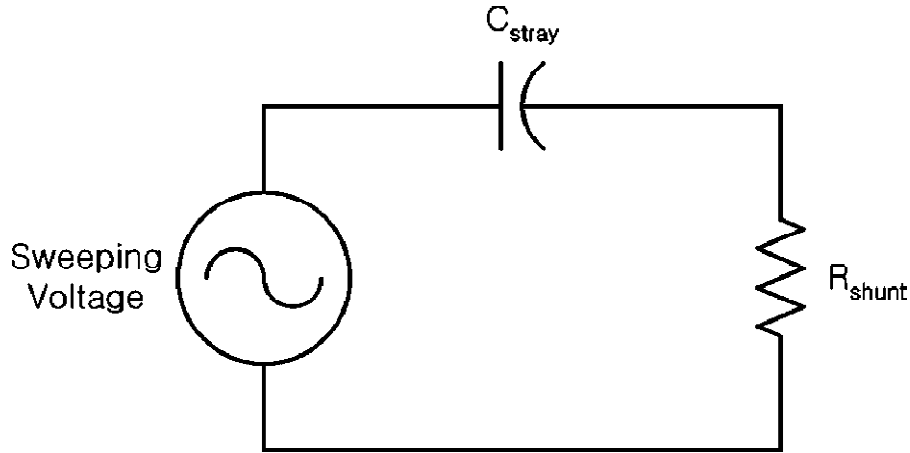


Figure 3.10 Equivalent electrical circuit of a Langmuir probe for time varying bias and current measurements.

The output voltage measured across the measuring resistance when there is no plasma is solely because of the displacement current generated through the stray capacitance of the cable used. So the voltage drop across the measuring resistance is

$$V_0 = I_d \times R \quad (3.25)$$

The displacement current can be written as

$$I_d = \epsilon_0 A \frac{\partial E}{\partial t} = \frac{\epsilon_0 A}{d} \frac{\partial V}{\partial t} \quad (3.26)$$

Taking V as a sinusoidally varying voltage signal with frequency ω ,

$$I_d = C\omega V \quad (3.27)$$

So the amplitude of voltage drop in the measuring will be

$$V_0 = I_d \times R = RC\omega V \quad (3.28)$$

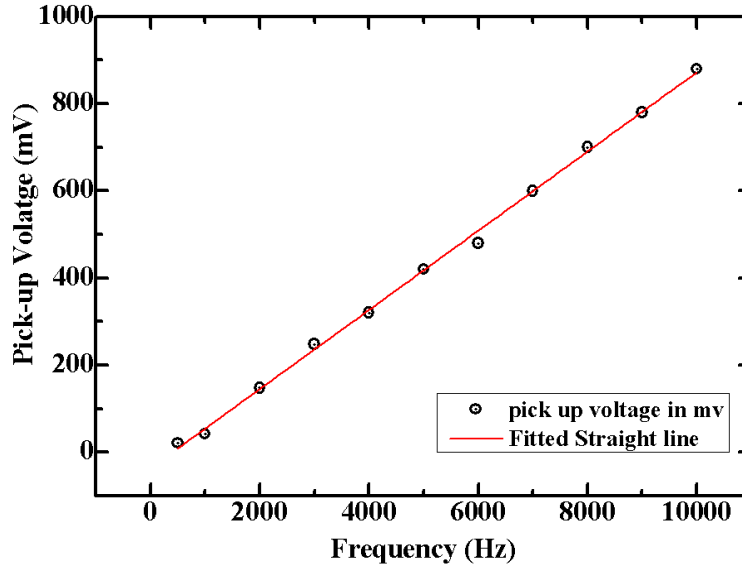


Figure 3.11 Voltage drop across a measuring resistance in the absence of plasma for different bias frequencies applied to Langmuir probe through a RG 58 coaxial cable of 2 meter length showing the limitations of bias frequency.

Using a triangular sweep of $70 V_{pk-pk}$, a resistance of 1 k-Ohm and an RG-58 cable of nearly 2 meters, the output voltage across the measuring resistance is plotted with triangular sweep frequency and is shown in Figure 3.11. It is seen from experiment and calculations; the output voltage is proportional to frequency. The output characteristic has a form of a square wave as it should be a differential form of the input signal. This kind of output characteristics in a signal confirms it to be of capacitive pick up. It should be noted that for low density plasmas, one need to take care of this sweep frequency, where the generated displacement current can be of the order of the ion saturation currents.

3.5.2 Wall Probe

When a material body is inserted inside an electron-ion plasma, the floating body is negatively charged by the electrons. This negative potential is known as the floating potential of the material and it accelerates the less mobile ions so that the total current to the floating object is zero. This floating potential depends on electron temperature and electron to ion mass ratio and is expressed as (Equation 3.24)

$$V_f = \frac{1}{2} \frac{kT_e}{e} \ln \left(\frac{2\pi m}{M} \right),$$

Where, k , T_e , m and M are the Boltzmann's constant, electron temperature, electron mass and ion mass respectively. As $m \ll M$, V_f is always negative with respect to the plasma potential.

When a high frequency voltage is applied by a metallic antenna on the outer wall of a dielectric glass tube, a potential is induced in the inner wall of the glass tube through the capacitance of the glass which is exposed to the plasma. The plasma electrons respond quickly compared to the heavier ions. This creates an imbalance in the currents flowing to the dielectric body and the electrons have to charge the body to a negative potential such that the electron and ion currents are equal to maintain the floatingness of the dielectric glass wall. This can also be understood as the rectification of the RF potential by the sheath which has a nonlinear IV characteristic. For a dielectric wall this process was first explained by Kino and Butler [22]. Figure 3.12 shows how a sheath generates a DC potential and subsequently charges the wall.

This potential is sum of the floating potential of a DC plasma system as described earlier and another potential because of additional different response of electrons and ions to the high frequency oscillating electric field. This potential is known as the DC self bias and the total potential is expressed as per Chabert [23] as

$$V_{RF} = \frac{kT_e}{e} \left[\frac{1}{2} \ln \left(\frac{2\pi m}{M} \right) - \ln I_0 \left(\frac{eV_1}{kT_e} \right) \right] \quad (3. 29)$$

Where I_0 is the zero-order modified Bessel function and for sufficiently low RF applied voltages compared to temperature, its value tends to unity, so that the contribution to floating potential from the RF can be neglected.

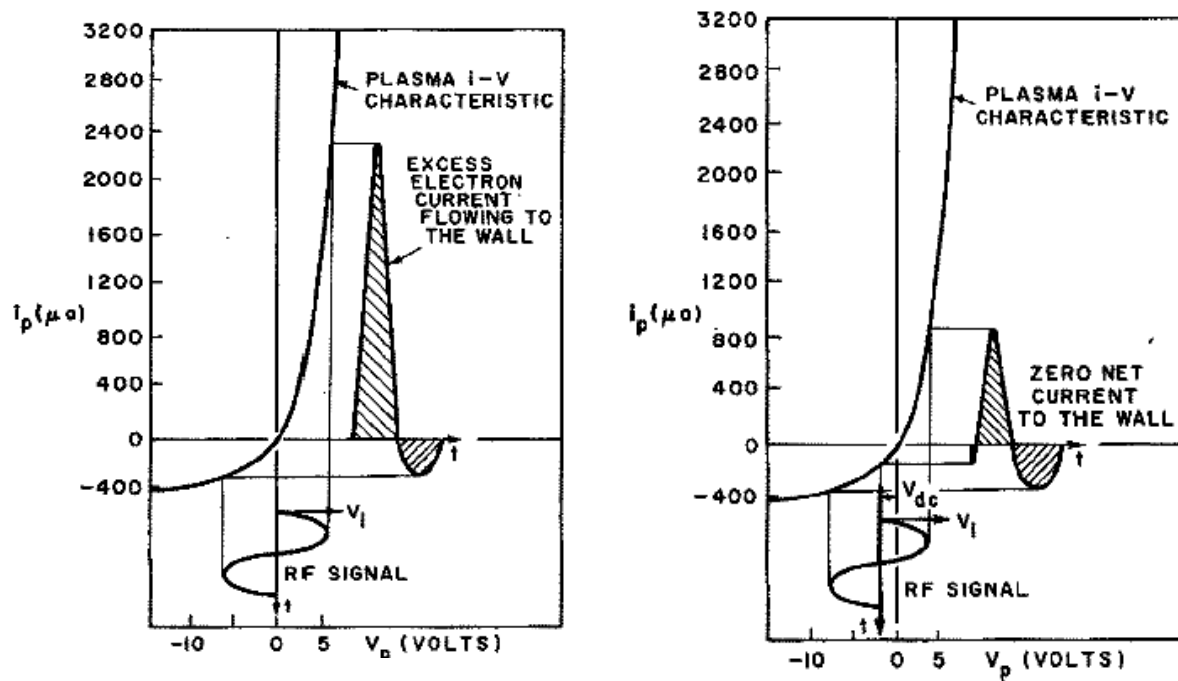


Figure 3.12. (a) Instantaneous flow of excess electrons to the wall in response to an RF voltage in an RF cycle. (b) Subsequent decrease in the average value of induced voltage i.e. floating potential of the wall [22].

The DC self bias is measured using a different Langmuir probe as shown schematically in Figure 3.13. This consists of a molybdenum planar probe tip of 5mm diameter. This is connected to a ceramic probe holder which is subsequently connected to an L-shaped probe shaft.

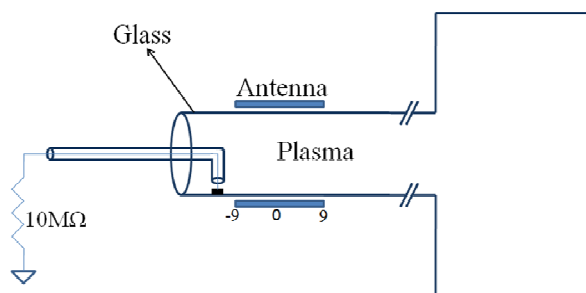


Figure 3.13 Schematic of the wall probe measurement arrangement.

An RG-178 coaxial cable is used to take the voltage output. The probe measures the floating potential while sliding on the glass surface very close only to ensure that the wall potential is as close as to the probe potential. The voltage drop is measured across a high impedance of 10 M-Ohm. Aanesland et al [24] have used this static method to measure the wall potential in helicon plasma. The floating potential can also be measured by a dynamic method, changing the bias on the probe and finding the bias at which the current to the probe changes sign. The picture of the wall probe attached to the source end flange is shown in Figure 3.14.



Figure 3.14 Picture of the wall probe for DC bias measurement.

3.5.3 RF Compensated Probe

Apart from applied bias, probe diameter and ion mass the current collected by a Langmuir probe depends on density, temperature and plasma potential. So any fluctuation in the later stated quantities will change the I-V characteristics of the Langmuir probe. The Langmuir probe has a non-linear IV characteristic which rectifies any harmonic fluctuations superposed on it. The probe has finite capacitance which limits it to respond to low frequencies only. Garscadden [25] has calculated the effects of these fluctuations on probe characteristics. In this thesis only the effect of space potential oscillations will be discussed for their predominance over

the other oscillations. For presence of space potential oscillations of amplitude V_{rf} , the instantaneous electron current to the probe can be written as [25],

$$i = \frac{1}{4}nev_{th}A \exp\left(\frac{V_s - V_p + V_{rf} \sin \omega t}{T_e}\right) \quad (3.30)$$

Where n is the electron density, e is the electronic charge, v_{th} is the mean velocity of electrons, A is the probe area, V_s is the DC plasma potential, V_p is the probe bias, V_{rf} is the amplitude of RF plasma potential oscillations, T_e is electron temperature and ω is the RF frequency at which plasma potential is oscillating.

As the probe can see only the average electron current, the time average over a full cycle of RF time period gives

$$\langle i \rangle = \frac{1}{T} \int_0^T \frac{1}{4}nev_{th}A \exp\left(\frac{e(V_s - V_p + V_{rf} \sin \omega t)}{T_e}\right) dt \quad (3.31)$$

As we know

$$\frac{1}{T} \int_0^T \exp(a \sin \omega t) dt = I_0(a) \quad (3.32)$$

Where $I_0(a)$ is the zero-order modified Bessel function with argument a and for $a = 0$, its value tends to unity.

Therefore the average electron current collected by the probe can be expressed as

$$\langle i \rangle = \frac{1}{4}ev_{th}A \exp\left(\frac{V_s - V_p}{T_e}\right) I_0\left(\frac{eV_{rf}}{T_e}\right) \quad (3.33)$$

Taking the logarithm of the average current

$$\ln \langle i \rangle = \frac{e(V_s - V_p)}{T_e} + \ln\left(\frac{1}{4}ev_{th}A\right) + \ln\left[I_0\left(\frac{eV_{rf}}{T_e}\right)\right] \quad (3.34)$$

Where the first two terms on the RHS are same as the DC case, the third term is the vertical shift of the IV characteristics for which temperature estimation will be erroneous. The horizontal DC shift in the floating potential ΔV_f is obtained by flux balance of electrons and ions in the presence of RF oscillations [23]

$$\Delta V_f = T_e \ln \left[I_0 \left(\frac{eV_{rf}}{T_e} \right) \right] \quad (3.35)$$

Compensation techniques:

The techniques for using a Langmuir probe in RF environment will be discussed as it has evolved in the years. Chen [26] increased the ramp frequency up to 1 MHz range. All the other methods can be broadly divided into two parts: active compensation and passive compensation.

Active Compensation:

Braithwaite [27] applied the attenuated and phase shifted voltage of the powered electrode of a capacitive discharge to the Langmuir probe. Anartone [28] fed the probe tip with an RF signal from outside and varied the phase and amplitude of the outside signal of same frequency till the maximum positive floating potential is reached. This above method is called the active compensation. Because the sheath has a finite capacitance, higher harmonics of the RF signal from plasma can be generated and the probe needs to be fed with harmonic frequencies and also the probe needs to be compensated for every change in the plasma conditions which may be tedious.

Passive Compensation:

Cantin and Gangne [29] used a unity gain amplifier and fed the RF voltage oscillations on a floating electrode to the probe. But the amplifier has a voltage limitation of 9 volt peak-to-peak. The other method known as the passive compensation method was introduced by Paranjpe et al [30] who used a copper rod unexposed to the plasma to couple the RF signal to the current measuring probe exposed to the plasma. Sudit and Chen [16] used a reference electrode exposed to the plasma having area larger than the probe area and used a coupling capacitor to couple the

RF fluctuations to the probe. They have used inductors as RF chokes which offer high impedance to the RF signals at fundamental and higher harmonics. As the compensating electrode is kept near to the probe, the compensation need not be changed every time.

Design:

Two single Langmuir probes are used out of which one is compensated and the other is an uncompensated only for comparison. The picture of the probes is shown in Figure 3.15. The uncompensated probe is same as described in the last section. The tungsten probe tips are covered with thin ceramic pipe of 0.7 mm diameter and length 10 mm leaving an exposed tip of 3 mm length and 0.5 mm diameter for both the probes.



Figure 3.15 Picture of the RF compensated probe along with an uncompensated probe.

A winding of 30 turns of 125 micron tungsten filament is done over the ceramic pipe whose one end is connected to one end of a ceramic capacitor of 10 nF capacitance which is kept inside the hollow ceramic probe holder.

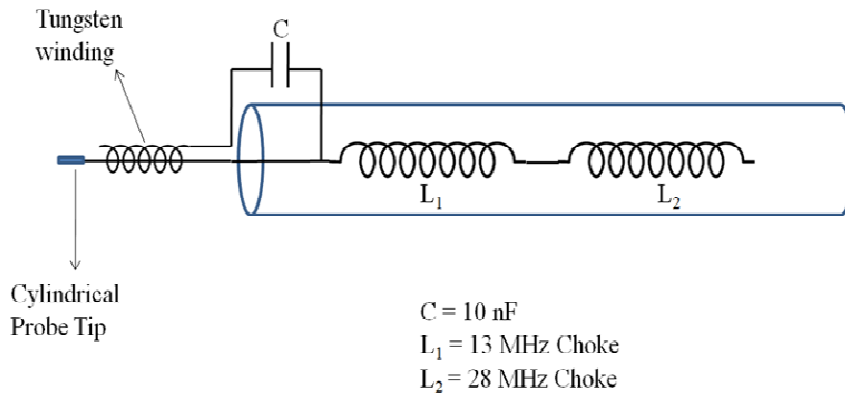


Figure 3.16 Schematic of the RF compensated probe along showing the compensating winding, coupling capacitor and the self resonating RF chokes.

The other end of the capacitor is connected to the probe tip from inside the probe shaft. The probe length after the capacitor connection towards the measurement circuit is connected in series with two self resonating inductors which act as chokes for RF frequencies of 13.56 MHz and 27.12 MHz as shown in Figure 3.16.

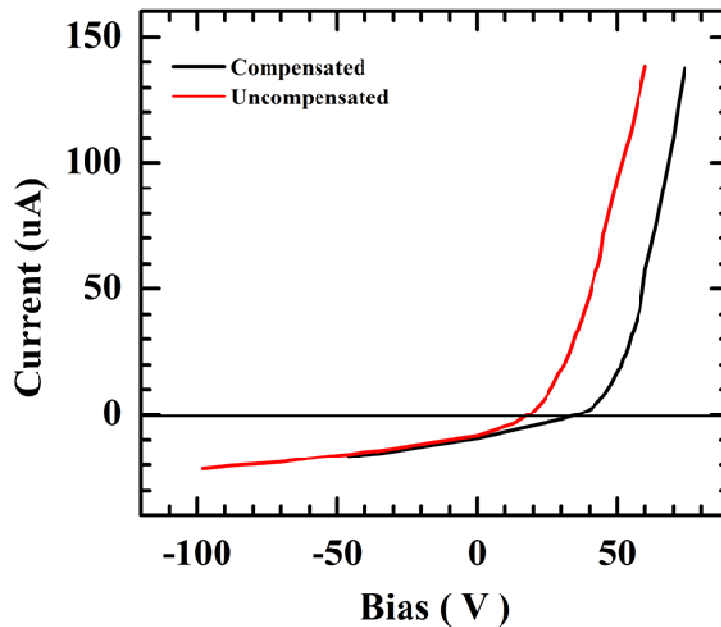


Figure 3.17 Comparison of IV characteristics of compensated and uncompensated Langmuir probe.

The current signals from the plasma are carried by RG 174 coaxial cables which are connected to Vacuum BNCs at the end of the flange connected to a vacuum feed-through. The IV

characteristics obtained at 250W RF power, 8×10^{-4} mbar and 100 G magnetic field are shown in Figure 3.17 which shows a change in floating potential of ~ 15 V and the temperature obtained are ~ 3.1 eV for uncompensated and ~ 2.9 eV for compensated probe.

3.5.4 Double Langmuir Probe

Though single Langmuir probes suffice as an electrostatic probe diagnostics in most of the cases to determine density and temperature, they have certain limitations in specific plasmas and plasma conditions. Single Langmuir probes always take the reference of the vessel wall which in turn is in contact with the bulk plasma. This vacuum wall references are not available in the case the plasma is produced in a dielectric chamber and also in electrodeless discharges. Another limitation comes from the amount of probe current that is drawn to characterize the plasma. In dilute, after glow and decaying plasmas where the probe current can be a significant part of the discharge current, the probe may disturb the plasma. This is because of the larger surface area of the vacuum vessel sheath. To get rid of these above stated problems Johnson and Malter [31] have proposed a double Langmuir probe procedure in which another probe is placed nearby to act as a reference and becomes the return path for the probe current. As this floating probe draws a maximum current equal to the ion saturation current it can be used in dilute plasmas.

Principle of operation:

The basic theory of operation can be understood from the electrical circuit diagram as shown in Figure 3.18. When a bias is applied between the two probes, the probes collect current but as the system is floating the currents to the probes are equal and opposite.

Let's say, after a voltage V is applied to the probes, the two floating probes P_1 and P_2 attain potentials of ϕ_1 and ϕ_2 respectively.

Therefore

$$V = \phi_2 - \phi_1 \quad (3.36)$$

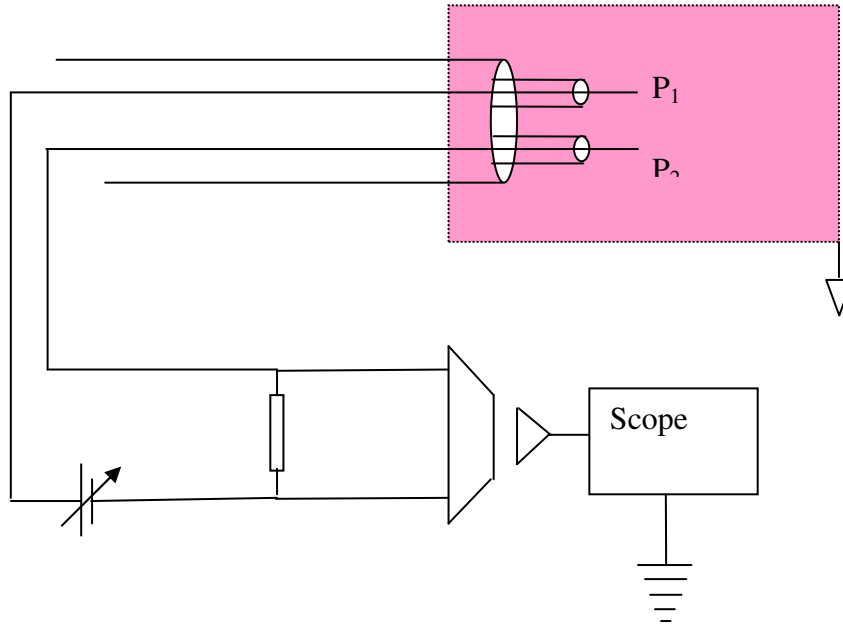


Figure 3.18 Schematics of Double Langmuir probe measurement circuit.

Let the plasma potential be ϕ_p . The current in P1 of area A_1 be I_1 and in P2 of area A_2 be I_2 is sum of the respective electron and ion currents.

$$I_2 = -\frac{eA_2n_0\bar{v}_e}{4} \exp\left(e\frac{\phi_2 - \phi_p}{T_e}\right) + n_s e u_B A_2 \quad (3.37)$$

Rearranging,

$$-\frac{n_0\bar{v}_e}{4} \exp\left(\frac{-e\phi_p}{T_e}\right) = \left(\frac{I_2}{eA_2} - n_s u_B\right) \exp\left(\frac{-e\phi_2}{T_e}\right) \quad (3.38)$$

Similarly the current in P1 can be expressed in terms of plasma potential as

$$-\frac{n_0\bar{v}_e}{4} \exp\left(\frac{-e\phi_p}{T_e}\right) = \left(\frac{I_1}{eA_1} - n_s u_B\right) \exp\left(\frac{-e\phi_1}{T_e}\right) \quad (3.39)$$

So,

$$\left(\frac{I_2}{eA_2} - n_s u_B\right) \exp\left(\frac{-e\phi_2}{T_e}\right) = \left(\frac{I_1}{eA_1} - n_s u_B\right) \exp\left(\frac{-e\phi_1}{T_e}\right) \quad (3.40)$$

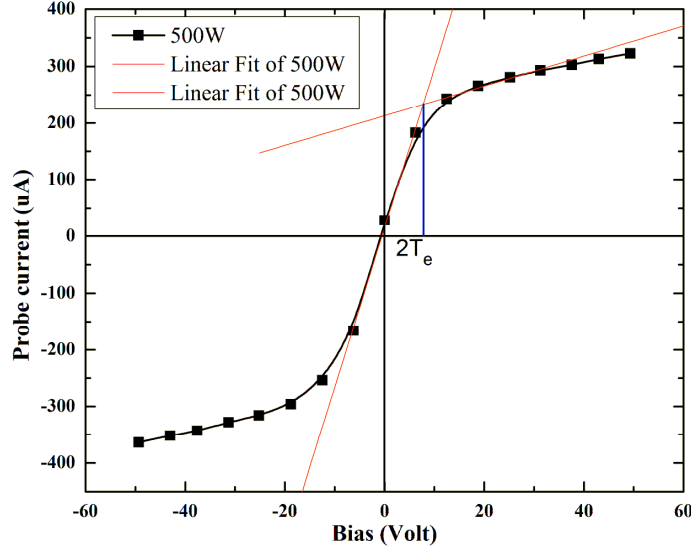


Figure 3.19 Determination of temperature from double probe IV characteristics.

As to the floating probe the total current is zero, so the current in each probe is $I = I_1 = -I_2$.

So, replacing the currents and using Equation 3.40,

$$I \left(1 + \frac{A_1}{A_2} \exp\left(\frac{-eV}{T_e}\right) \right) = n_s u_B e A_1 \left(1 - \exp\left(\frac{-eV}{T_e}\right) \right) \quad (3.41)$$

$$I = n_s u_B e A_1 \left[\exp\left(\frac{eV}{T_e}\right) - 1 \right] \left[\exp\left(\frac{eV}{T_e}\right) + \frac{A_1}{A_2} \right]^{-1} \quad (3.42)$$

For a symmetrical double probe with $A_1 = A_2$, the current in each probe is [using the identity for $\tanh(ax)$],

$$I = I_{sat} \tanh\left[\frac{eV}{2kT_e}\right] \quad (3.43)$$

Where the ion saturation current $I_{sat} = n_s u_B e A$. Taking the slope near $V = 0$ as shown in Figure 3.19.

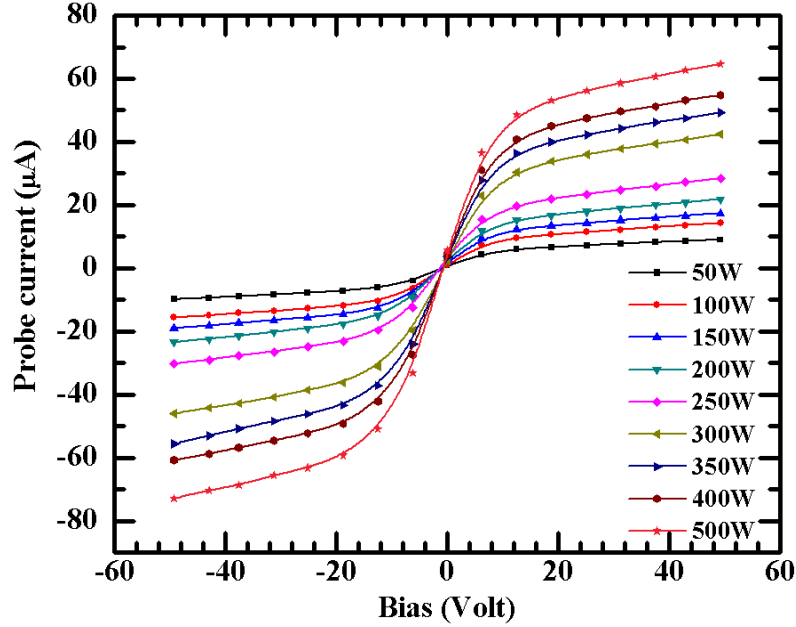


Figure 3.20 Double Probe characteristics measured at $z=22$ cm for different RF for powers 50-500 W with 4×10^{-3} mbar pressure and 55 Gauss magnetic field.

$$\left. \frac{dI}{dV} \right|_{V=0} = \frac{I_{sat}}{V_b} = \left[I_{sat} \frac{e}{2kT_e} \operatorname{sech}^2 \left(\frac{eV}{2kT_e} \right) \right]_{V=0} = I_{sat} \times \frac{e}{2kT_e} \quad (3.44)$$

$$V_b = \frac{2kT_e}{e} \quad (3.45)$$

$\tanh ax$ has slope of a for $x = 0$, we can calculate the temperature by just finding the slope of the line passing through the origin of IV characteristics as shown in Figure 3.19. The double probe characteristics measured at 4×10^{-3} mbar and 55 Gauss for powers 50-500 W are shown in Figure 3.20.

Design:

The double probe is made of two identical tungsten probe tips of 0.5 mm diameter and 3 mm exposed length. The bias is given by a floating power supply and the current flowing through a series measuring resistance gives a voltage drop. This voltage is measured by an oscilloscope through a unit optical isolation amplifier. The schematic of the measurement circuit is shown in Figure 3.18.

3.5.5 Triple Langmuir Probe

Single Langmuir probe is widely used as a probe diagnostics for measurement of density and temperature in plasmas. A metallic probe exposed to the plasma is biased w.r.t. the vessel reference and the current collected is passed through a measuring resistance. The voltage drop across the resistance is used to calculate the collected current. The probe current Vs bias voltage gives the I-V characteristics of the probe. Temperature is deduced from the slope of the electron collecting region of the probe characteristics. Density is obtained from the measured ion saturation current and the deduced electron temperature. The first and foremost stringent requirement is that the measurement needs a good reference of an appreciable area. Second, SLP draws a large amount of current in the electron collection regime, which may be a part of the discharge current in some plasma systems like afterglow plasma. Third, the amount of bias applied even in case of a low temperature plasma can be very high when the plasma potential (or floating potential) is of very high magnitude (either positive or negative). High bias voltages often put a larger demand on the current measurement circuit. The above mentioned problems are overcome by using a double Langmuir probe which does not need a reference and uses one of the probe tips as a reference and also it draws a maximum current of ion saturation current. The other problem involved in SLP which is not overcome by a DLP is the tedious data analysis, which also cannot give the instantaneous values of temperature and density in case of time varying plasma. If a high frequency bias is given, capacitive pick up as shown in Figure 3.11, can generate noise currents comparable to ion saturation currents. This noise current produces a voltage drop which may be comparable to the fluctuation (time varying parameters) signals.

To overcome all the previously mentioned shortcomings in SLP and DLP, a third probe is used with a DLP. The third probe in addition to DLP constitutes the triple Langmuir probe (TLP). As in DLP one of the probes collects ion current while the other collects the electron current, here in

TLP also one probe collects electron current equivalent of the ion saturation current collected by a second probe with a third probe kept floating. The potential difference between the floating reference probe and the electron current collecting probe is a measure of temperature if the later collects an amount of electron current equal to the ion saturation current. The probe circuit consisting of the reference probe and ion saturation collecting probe can accommodate a series resistance across which the voltage can be measured to deduce ion saturation current in the circuit. This ion saturation current along with the temperature obtained gives the density. As the potential difference between floating probe and electron collecting probe is proportional to electron temperature, instantaneous temperature fluctuations can be obtained using a TLP.

Working Principle:

In its simplest form [32-33] the triple-probe method employs three separate Langmuir probes of identical shape and dimension placed a small distance apart and individually biased to three different potentials (Figure 3.21) The probe potentials are less than the plasma potential so that negatively biased sheaths exist around each probe. The spacing between probes must be large enough to adequately shield them from one another. The current to each probe is the sum of the ion saturation current and the electron current. By combining these conditions with the current density equations, the triple-probe equations are derived. As all probe potentials are less than the plasma potential, an ion sheath is formed around all the three probes. One of the assumptions is that all the probes see the same plasma so that different characteristics do not exist for different probes.

A triple Langmuir probe (TLP) [32] to get the instantaneous density and temperature is used. If the potential of the three probes P₁, P₂ and P₃ are respectively V₁, V₂ and V₃ as shown in Figure 3.22, we can define the following potentials and currents [33]

$$V_{d2} = V_2 - V_1 \tag{3.46}$$

$$V_{d3} = V_3 - V_1 \tag{3.47}$$

$$I_1 = I_2 + I_3 \tag{3.48}$$

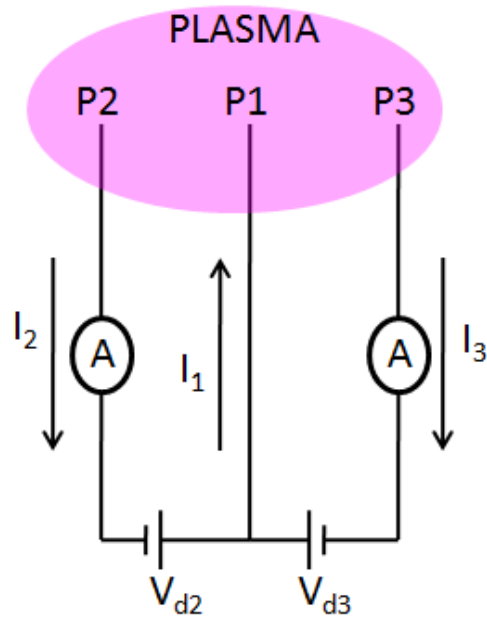


Figure 3.21 Schematics of the triple Langmuir probe circuit

The Currents as shown in Figure 3.22 to all the three probes are I_1 , I_2 and I_3 respectively and can be written as

$$-I_1 = -I_{esat} \exp\left(-\frac{-eV_1}{T_e}\right) + I_+ \quad (3.49)$$

$$-I_2 = -I_{esat} \exp\left(-\frac{-eV_2}{T_e}\right) + I_+ \quad (3.50)$$

$$-I_3 = -I_{esat} \exp\left(-\frac{-eV_3}{T_e}\right) + I_+ \quad (3.51)$$

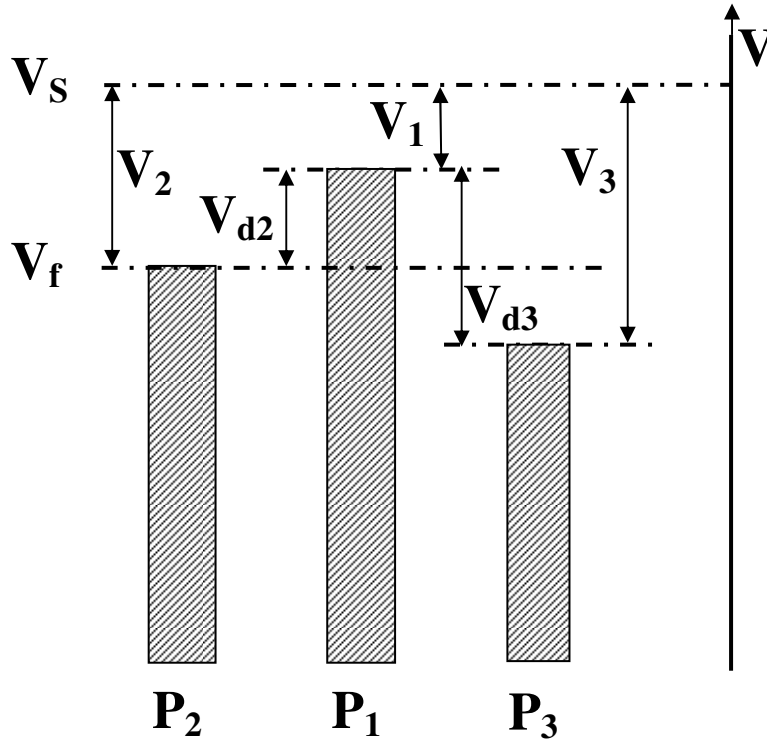


Figure 3.22 Potential diagram of TLP.

Where I_+ is the ion saturation current which is the same for all the three probes if they are of equal area. I_{esat} is the electron saturation current and T_e is the electron temperature in eV.

If we keep our second probe P_2 floating as shown in Figure 3.23 then $I_2 = 0$ and $I_1 = I_3$ by Equation 3.48. Now we measure V_{d2} and this way the density and temperature is calculated. For the floating measurements using TLP by optical isolation of which input reference is P_2 and output reference is data acquisition system.

$$\frac{I_1 + I_2}{I_1 + I_3} = \frac{1 - \exp\left(\frac{-eV_{d2}}{T_e}\right)}{1 - \exp\left(\frac{-eV_{d3}}{T_e}\right)} \quad (3.52)$$

In our system we have kept probe P_2 as floating so there is no current flowing in P_2 , so that $I_2 = 0$ and we measure only the differential voltage between P_1 and P_2 which is V_{d2} .

$$I_1 = I_3 \text{ as } I_2 = 0 \quad (3.53)$$

So the new set of relations for deducing temperature and density will be

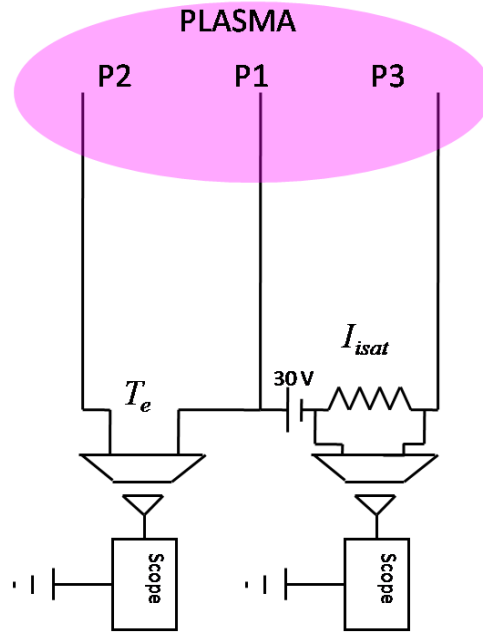


Figure 3.23 Modified circuit of TLP with optical isolation for instantaneous display of ion saturation current and temperature.

$$\frac{1}{2} = \frac{1 - \exp\left(\frac{-eV_{d2}}{T_e}\right)}{1 - \exp\left(\frac{-eV_{d3}}{T_e}\right)} \quad (3.54)$$

$$I_+ = I_1 \frac{1 + \exp\left(\frac{-eV_{d3}}{T_e}\right)}{1 - \exp\left(\frac{-eV_{d3}}{T_e}\right)} \quad (3.55)$$

In the case, $eV_{d3} \gg 2T_e$, the expression for temperature is $T_e = 1.44V_{d2}$. This value of temperature when used in ion saturation current expression gives density. We have given a

floating bias of 30 V which is more than twice of every temperature range in our experiment. For ion saturation current, $I_+ \approx I_1$ for $eV_{d3} \gg 2T_e$.

Design:

Three probes of 0.5 mm diameter and 3 mm length are used as probe tips. All the connections are made with RG 174 coaxial cables. Two optical isolation amplifiers are used to isolate the measurement reference (P_1) and the acquisition circuit reference (scope) for ion saturation and floating voltage measurements. These amplifiers have bandwidth of 250 kHz. Low pass filters (mini-circuits make low pass filters) have been used to filter out RF interference if any.

3.5.6 Emissive Probe

Plasma potential and its fluctuations are important parameters that can characterize electric fields and their fluctuations inside plasma. Using a cold probe we have seen in section 3.5.1 that, plasma potential can be estimated from the floating potential when you have the information of the electron temperature. But the estimation of electron temperature is often tedious. Also in the presence of electron beams or drifted electrons floating potential cannot give correct values of plasma potential. So, hot probes are often used to find the plasma potential. The hot or emissive probe works on the principle that the emitted electrons compensate for the ion sheath for probe biases below the plasma potential, so that the floating potential of the hot probe is always near the plasma potential (no ion sheath) for high enough emission irrespective of presence of fast or drifted electrons.

Working Principle:

The current in I-V characteristics has components from the collected current and emitted current. Neglecting the space charge effects, the emitted current can be expressed as [34]:

$$I_{em}(V_b) = \begin{cases} I_{em0} \exp[-e(V_b - V_p)/T_w] f(V_b - V_p), & V_b \geq V_p \\ I_{em0} & , V_b \leq V_p \end{cases} \quad (3. 56)$$

Where V_b is the probe bias, V_p is the plasma potential, T_w is the wire temperature, $f(V_b - V_p)$ accounts for orbital angular momentum of emitted electrons (depends on the wire radius and the dimensions of the sheath separating the wire from the virtual anode formed by the plasma). Here I_{em0} is the temperature limited emission current given by the Richardson-Dushman equation expressed as

$$I_{em0} = AT_w^2 S \exp\left(\frac{e\phi_w}{T_w}\right), \quad (3.57)$$

Where A is the Richardson's constant, ϕ_w is the work function of the wire material, S is the surface area of the wire. In case of emission of the filament inside the plasma, the emitted current is constant for bias less than plasma potential because the emitted electrons do not see any retarding potential (neglecting space charge effects). So the emitted electrons behave like collection of ions by the probe, so that the overall current is replenished by these emitted electrons below the plasma potential. When a bias above plasma potential is applied, the electrons feel a retarding force for the plasma acts like a cathode and the emission current decreases rapidly. As the emitted electrons are in equilibrium with a temperature of the order of the probe temperature which is of the order of few tenth of eV, the transition region of constant emission to almost no emission is very sharp.

The collected current is the current collected by a cold Langmuir probe and can be expressed as

$$I_e(V_b) = \begin{cases} I_{e0} \exp[e(V_b - V_p)/T_e] , & V_b \leq V_p, \\ I_{e0} f'(V_b - V_p) & , V_b \geq V_p. \end{cases} \quad (3.58)$$

Where, I_{e0} is the electron saturation current, T_e is the electron temperature in eV and $f'(V_b - V_p)$ accounts for the orbital angular momentum of collected electrons. When the bias is very

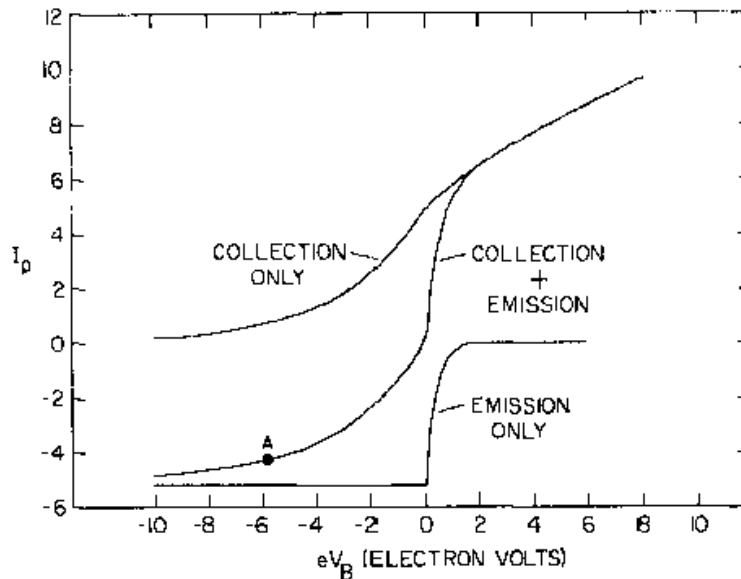


Figure 3.24 IV characteristics of an emissive probe showing the bias dependence contributions from emission current and collection current [35].

negative w.r.t. plasma potential, the probe collects ion saturation current and then when the bias is increased the probe starts collecting electrons and all the electrons are collected near plasma potential and the collected current ideally becomes constant near or above the plasma potential.

Methods of Emissive Probe:

Floating potential method:

The floating potential of a sufficiently heated emissive probe is close to the local plasma potential, and this is the most widely used method for plasma potential determination and the most convenient method [36]. When a probe emits thermionically, the sheath potential drop in front of the emissive probe decrease for the emitted electron currents compensate for the ion currents. When the probe is strongly heated such that there is no sheath in front of the probe, the floating potential of the probe approaches the plasma potential. As can be seen from the figure the saturated floating potential of the probe is close to the plasma potential. When measuring floating potential we are using a high series resistance which will have a load line almost parallel

to the voltage axis of figure 3.25. This load line intercepts the probe IV characteristics of each curve near the floating potential i.e. current to the probe is almost zero. As the heating current increases the incremental shift in floating potential decreases and saturates for high enough heating current. This saturation floating potential corresponds to the plasma potential.

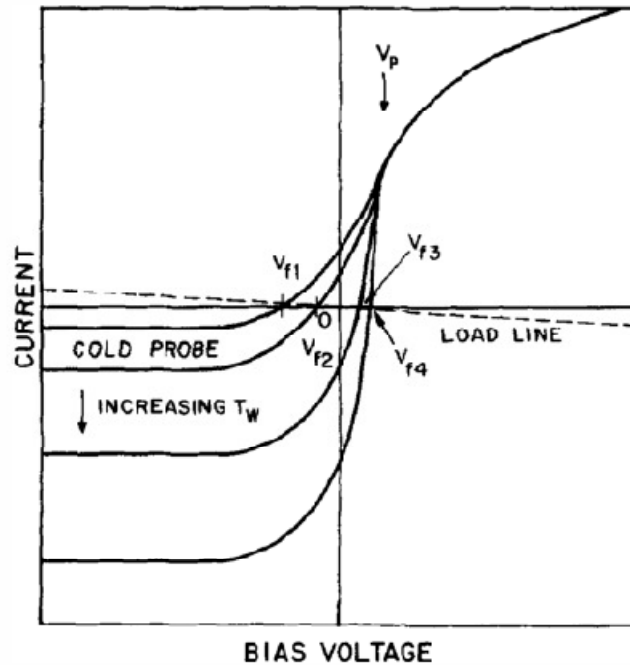


Figure 3.25 Plasma potential determination by floating potential method where an emitting probe's floating potential approaches the local plasma potential for strong emission [37].

Inflection point method:

For an emissive probe when the bias is less than the plasma potential, the current in the probe circuit is because of both emission and collection currents. When the bias is near or more than plasma potential, the current to the probe is changes as the total current is now only the collection current with no emitted electrons are accepted by the plasma. So the differentiated IV characteristic of an emissive probe shows a peak at the plasma potential [35]. This is illustrated in Figure 3.26.

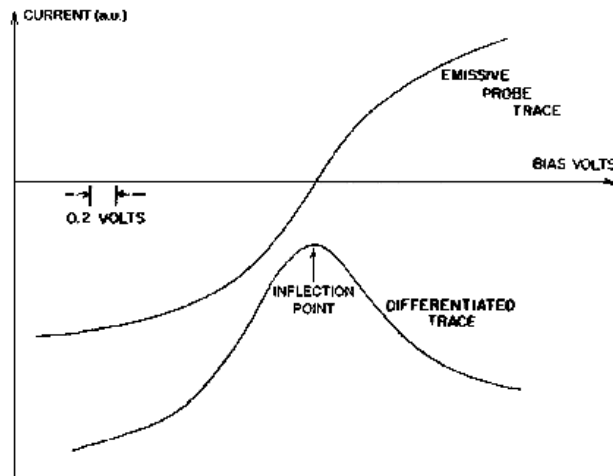


Figure 3.26 Plasma potential determination by inflection point method, where the differentiated IV characteristic of a partially emitting hot probe has an inflection point near the plasma potential [35].

Separation point method:

The potential at which characteristics of a cold probe and strongly emitting probe start to deviate is known as the plasma potential [38-39] as shown in Figure 3.27. But to ensure that the probe is strongly emitting, the electron saturation current of the cold probe must be equal to that of the ion saturation current of a strongly emitting probe. But as in many cases, either because of RF field effects or geometry effects we do not get the electron saturation, this method has shortcomings of space charge effects as one would work in a strong emission conditions.

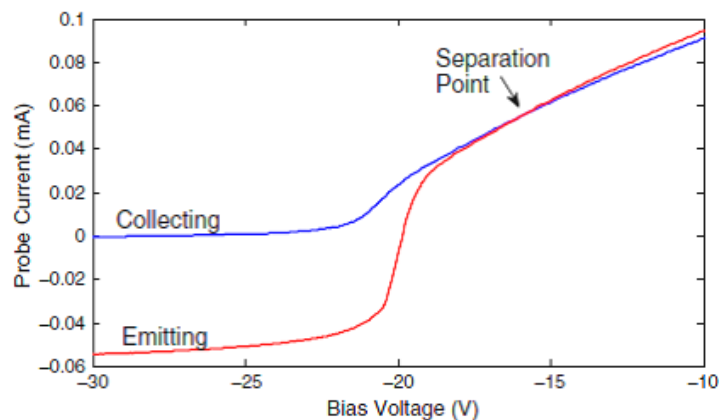


Figure 3.27 Plasma potential determination by separation point method where the IV characteristics of cold and hot probes separate from each other.

Effect of space charge limited emission:

When the emission current is less such that the floating potential of the emissive probe is less than the plasma potential, an ion sheath is formed around the emissive probe. The emitted electrons thus see a monotonic potential and get accelerated to the plasma. But when the emission current is increased a condition comes when there is no sheath around the probe. Further increasing the emission, the emitted electrons make a virtual cathode which can send back all or part of the emitted electrons back to the probe [40]. This is called the space charge limited emission and observed for high emission currents. This is a drawback of floating potential method of plasma potential determination using emissive probe. One can always check for the space charge effect by increasing the emission current to a level where the floating potential value saturates but does not decrease upon increasing heating current. That's why in floating potential method very high heating currents are not used. The inflection point method has overcome this problem as the plasma potential can be determined for low heating currents without strong emission.

Ye and Takamura [40] have done the analytical calculations including the space charge effect and found a relation between the floating potential and plasma potential as

$$V_f = V_p + \alpha \left(\frac{T_e}{e} \right) \quad (3.59)$$

, where α has the value of -0.95, -0.99 and -1.01 respectively for hydrogen, helium and argon.

Effect of RF potential fluctuations:

When the plasma potential oscillates with a frequency such that the emissive probe cannot follow the potential fluctuations, then the average current collected by an emissive probe has two slopes. In case of inflection point method when the emission current is low, $\frac{d(I)}{dV}$ has two peaks for potential fluctuations more than electron temperature with the two peaks corresponding to the minimum and maximum value of the RF amplitude [41-42]. The value of the plasma potential then is given by the average value of these two peaks. In the case of floating potential method however with strong emission, the value of plasma potential obtained so remains unaffected.

Effect of Magnetic field:

When the probe radius is larger than the electron larmour radius, the electrons that leave the surface of the filament can come back to the filament so that a space charge region will be formed. When the filament arch surface is perpendicular to the magnetic field a JXB force acts on the filament and there is a chance that it may get deformed or broken [36]. But as we are using a thin filament of 0.125 mm for which the current requirement for strong emission is less all the two problems discussed above can be neglected for the magnetic fields used in this thesis.

Measurement accuracy and errors:

The plasma potential obtained using an emissive probe is accurate up to potential equivalent of probe temperature T_w/e . In floating potential method the probe potential is measured with a high series impedance when the emission is strong for which a finite current passes through the filament. Therefore a finite voltage $2\Delta V$ drops across the filament. This voltage has to be subtracted to find the real floating potential. But for that it is necessary to know out of two legs to which the measuring circuit is connected. Marvlag et al [43] have shown that when emission current is equal to the electron saturation current (or for strong emission)

$$V_s = V_f \pm \Delta V \quad (3. 60)$$

Where the sign depends on which leg is connected to the measurement circuit.

Design:

The loop of the emissive probe is made of tungsten filament of 0.125 mm. The length of the filament is 10 mm and diameter of the loop is ~ 3 mm. The tungsten loop is inserted inside a twin bore ceramic tube of 2.5 mm outer diameter (Figure 3.28). The electrical connections are made by spiraling the tungsten filament's extended length over small copper strands. Tungsten wires 0.5 mm diameter and 6 mm length are used to fill the gaps inside which also act to decrease the filament heat load.

The copper strands used to wrap the filament are then soldered with the current carrying copper wires and the wires are taken outside using vacuum BNCs. The heating current required for 0.125 mm diameter tungsten wire is in between 2.5-3 Ampere which is supplied by an Aplab

floating power supply. The floating potential of the probe is measured by a 10 M-ohm impedance in the case of the floating potential method. The variation of floating potential with heating current is shown in Figure 3.29.

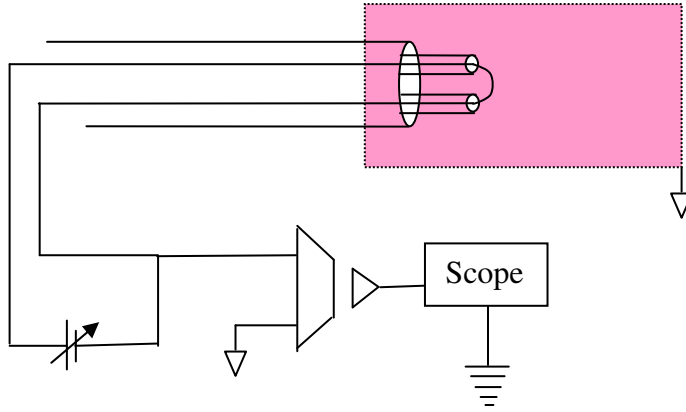


Figure 3.28 Schematic of the emissive probe for measurement of plasma potential with floating potential method.

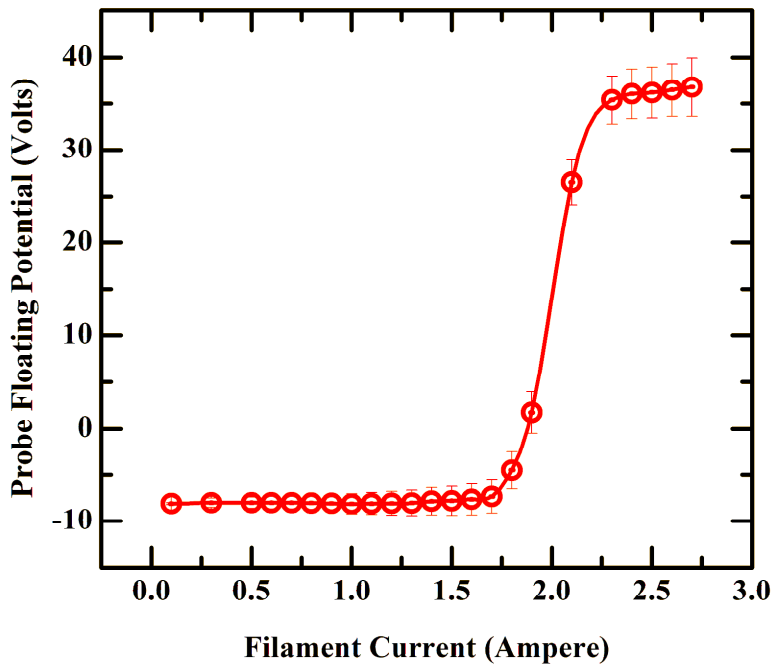


Figure 3.29 Floating potential variation of emissive probe with filament heating current in plasma measured at $z=50$ cm for 200 G source magnetic field, 100 W RF power and 2×10^{-4} mbar pressure

3.5.7 B-dot Probe

B-dot probes are widely used to measure magnetic field fluctuations in plasmas [44-51]. Multiple loop B-dot probes are often used to increase the output signal strength. However, in case of RF plasma, significant oscillating potential differences [47] can be present between a magnetic probe and plasma (and antenna). A magnetic probe can couple capacitively to these oscillating potentials in the plasma or antenna. This pick up signal depends on the potential amplitude, the capacitance between the probe and plasma and the terminating resistance. Often a 50 Ohm terminating resistance is used to reduce the electrostatic pick up. But sometimes this is not enough at least when the wave field amplitudes are small. To get rid of this capacitive pick up some techniques like hybrid combiners or baluns are often used. Another method, that has an inherent capacitive pick up rejection can be used is a single loop B-dot probe made of a co-axial cable as shown in Figure 3.31. The use of this kind of probe is limited to higher frequencies though.

Single loop B-dot probes are used to characterize the mode structure of helicon waves [4] and to measure the parallel wave length of the helicon waves. The magnitudes of perpendicular wave magnetic field components are measured to characterize and confirm $m=+1$ helicon modes. Two probes are used to measure helicon wave axial wavelength. This is done by taking one probe as reference probe and its phase as the reference for phase measurement. The other probe is translated axially and the phase variation along axis is noted. The slope of the phase variation is used to estimate the wavelength or the wave number of the helicon wave.

Working principle:

Whenever a time varying magnetic flux cuts a surface of a conducting loop, a voltage is induce in the ends of the loop. As per faraday's law

$$\nabla \times \vec{E} = -\frac{\partial \vec{B}}{\partial t} \quad (3. 61)$$

Integrating over the surface area of the coil and taking sinusoidal variations of fields,

$$\int (\nabla \times \vec{E}) \cdot dA \hat{n} = - \int \omega \vec{B} \cdot dA \hat{n} \quad (3. 62)$$

Where dA is the differential area and \hat{n} is vector normal to the plane of the coil. Using Stoke's theorem

$$\oint \vec{E} \cdot d\vec{l} = -\omega \vec{B} \cdot A \hat{n} \quad (3.63)$$

Where A is the total area of the coil and dl is a differential line segment along the perimeter of the loop. This gives the induced voltage in the loop which can be expressed as

$$V_{loop} = \omega NBA \cos \theta \quad (3.64)$$



Figure 3.30 Picture of the single loop B-dot probe made of a coaxial cable.

For we are interested only fluctuations in the 13.56 MHz, we have used a single loop B-dot probe, which reduces the parasitic capacitance and the inductance and gives enough signal to noise ratio. The area of the coil is 10 mm^2 and the radius of the loop is 3 mm. It is made up of a RG174 coaxial cable of 1.8 mm diameter. At one end the cable is looped and after the loop the centre conductor is connected to the nearest shielding of the loop as shown in Figure 3.30. Electrostatic pick up is reduced in this design. The probes are checked for electrostatic pick up noise by rotating the probe 180 degree. The results for measurement of amplitude of helicon wave axial component B_z for 300W RF power, 2×10^{-3} mbar and 30 G magnetic field using this probe inserted from a radial port at $z=22$ cm is shown in Figure 3.31. The probe axis when rotated by 180 degree shows a phase variation of 180 degree and also the signal amplitude is same as 0 degree as expected for a voltage output induced in the probe due to magnetic field oscillations only. This confirms the inherent capacitive pick up rejection of this single loop

coaxial B-dot probe. The shielding helps in two ways. One it forms a part of the loop and at the same time acts as shield for electrostatic signals inside the plasma, which are because of the high RF voltage fluctuations of the plasma potential. Also the low frequency signals in kHz range of frequencies cannot induce enough voltage more than the noise level of the probe to get detected.

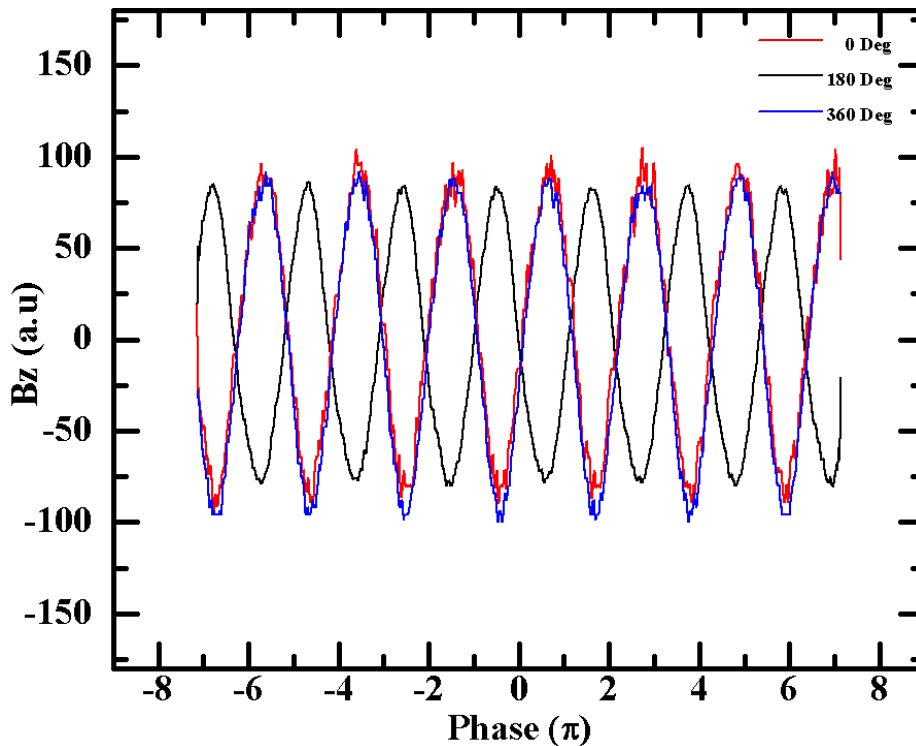


Figure 3.31 The graphs showing the inherent electrostatic pick up rejection by use of a single loop b-dot probe. The probe output for 0 deg (red), 180 deg (black) and 360 deg (blue) showing the capacitive pick up is negligible.

3.5.8 Antenna-Plasma Load Measurements

A rogowski or RF current probe (CT) is used to measure the antenna RF current flowing in the antenna circuit. The antenna current is a measure of antenna-plasma resistance and RF power transfer efficiency in any RF plasma system when the reflected power is negligible when compared to the forward power. A Pearson 410 [ref] rogowski is inserted around the antenna transmission line leg just after the match box. This rogowski has the high frequency 3 dB point at 20 MHz, a peak current value of 5 kA and peak RMS current value of 50 A. The output of this CT has a calibration factor or sensitivity of 0.1 V/A. The CT has a BNC output which is

connected to a 50 Ohm BNC and subsequently the output is monitored with a digital oscilloscope of 1 M-ohm input impedance which necessitates a termination of 50 Ohm before connecting to the oscilloscope. Using the above mentioned calibration factor the output voltage is noted and later converted to current values. Having the knowledge of the values of forward power P_{for} , reflected power P_{ref} , the RMS current value the total antenna resistance can be written as for reflections $<1\%$ as [7]

$$R_{tot} = \frac{P_{for} - P_{ref}}{I_{RMS}^2} \quad (3.65)$$

Here R_{tot} is the sum of the antenna vacuum resistance R_A and the antenna-plasma resistance R_P . The antenna vacuum resistance is calculated by powering the antenna without plasma and noting down the RMS value of antenna current. This vacuum current is used to drive the antenna resistance which is actually the sum of skin resistances (of antenna, transmission line, and match box inductors), contact resistances of all the frictional electrical connections and eddy current losses. Once R_A is known, the plasma resistance R_P is calculated by subtracting the value of R_A from R_{tot} which is obtained in the presence of the plasma. R_P is the sum of all the plasma processes leading to heating, ionization and maintaining the plasma thus is a sum of all the capacitive, inductive and wave coupling depending upon the discharge conditions. The power transfer efficiency η is the ratio of absorbed power P_{abs} and the total supplied RF power P_{tot} and is expressed as follows

$$\eta = \frac{P_{abs}}{P_{tot}} = \frac{R_P}{R_P + R_A} \quad (3.66)$$

The efficiency and plasma resistance both increase when the discharge transitions from a capacitive to inductive to Helicon wave mode.

3.6 Summary of Chapter 3

A linear helicon plasma device with controllable magnetic field gradient is designed and developed. Vacuum levels of 1×10^{-6} mbar are achieved. RF matching is done using an L-type matching network with less than 1 % reflection. Various probes with their electronics are designed, developed and tested in plasma with low level of noise. Working principles of all the probes are discussed.

References

- [1] S. J. Sackett, EFFI Code (Lawrence Livermore National Laboratory, California, (1978).
- [2] Porte, L., S. M. Yun, D. Arnush, and F. F. Chen. "Superiority of half-wavelength helicon antennae." *Plasma Sources Science and Technology* 12, no. 2 (2003): 287.
- [3] Chen, Francis F. "Capacitor tuning circuits for inductive loads." *UCLA Report* (1992).
- [4] Light, Max, and Francis F. Chen. "Helicon wave excitation with helical antennas." *Physics of Plasmas* 2 (1995): 1084.
- [5] Kamenski, I. V., and G. G. Borg. "An evaluation of different antenna designs for helicon wave excitation in a cylindrical plasma source." *Physics of Plasmas* 3 (1996): 4396.
- [6] Boswell, Rod W., and Francis F. Chen. "Helicons-the early years." *Plasma Science, IEEE Transactions on* 25, no. 6 (1997): 1229-1244.
- [7] Lafleur, T., C. Charles, and R. W. Boswell. "Characterization of a helicon plasma source in low diverging magnetic fields." *Journal of Physics D: Applied Physics* 44, no. 5 (2011): 055202.
- [8] Mott-Smith, H. M., & Langmuir, I. (1926). The theory of collectors in gaseous discharges. *Physical Review*, 28(4), 727.
- [9] F. F. Chen, in *Plasma Diagnostic Techniques*, ed. by R. H. Huddlestone and S. L. Leonard (Academic Press, New York, 1965)
- [10] L. Schott, in *Plasma Diagnostics*, ed. by W. Lochte-Holtgreven (John Wiley, New York, 1968)
- [11] I. H. Hutchinson, *Principles of Plasma Diagnostics*, (Cambridge University Press, 1987)
- [12] N. Hershkowitz, How Langmuir Probes Work, in *Plasma Diagnostics, Discharge Parameters and Chemistry*, ed. by O. Auciello and D.L. Flamm (Academic Press, 1989)
- [13] Demidov, V. I., Ratynskaia, S. V., & Rypdal, K. (2002). Electric probes for plasmas: The link between theory and instrument. *Review of scientific instruments*, 73(10), 3409-3439.
- [14] N. A. Krall and A. W. Trivelpiece, *Principles of Plasma Physics*, (San Francisco Press, 1986)
- [15] J. C. Sprott, *Electrostatic Probe Techniques*, PLP 88, University of Wisconsin, Madison (1966)
- [16] Sudit, I. D., & Chen, F. F. (1994). RF compensated probes for high-density discharges. *Plasma Sources Science and Technology*, 3(2), 162.
- [17] Sheridan, T. E. "How big is a small Langmuir probe?." *Physics of Plasmas* 7 (2000): 3084.
- [18] Sheridan, T. E. "The plasma sheath around large discs and ion collection by planar Langmuir probes." *Journal of Physics D: Applied Physics* 43, no. 10 (2010): 105204.

- [19] Lee, Dongsoo, and Noah Hershkowitz. "Ion collection by planar Langmuir probes: Sheridan's model and its verification." *Physics of plasmas* 14 (2007): 033507.
- [20] Demidov, V. I., Svetlana V. Ratynskaia, and K. Rypdal. "Electric probes for plasmas: The link between theory and instrument." *Review of scientific instruments* 73, no. 10 (2002): 3409-3439.
- [21] Hutchinson, Ian H. "A fluid theory of ion collection by probes in strong magnetic fields with plasma flow." *Physics of Fluids* 30 (1987): 3777.
- [22] Butler, H. S., and G. S. Kino. "Plasma Sheath Formation by Radio-Frequency Fields." *Physics of Fluids* 6 (1963): 1346.
- [23] Chabert, Pascal, Nicholas Braithwaite, and Nicholas St J. Braithwaite. *Physics of Radio-Frequency Plasmas*. Cambridge University Press, 2011.
- [24] Aanesland, A., Charles, C., Boswell, R. W., & Fredriksen, Å, Sputtering effects in a helicon plasma with an additional immersed antenna. *Plasma Sources Science and Technology*, 12, 85 (2003).
- [25] Garscadden, Alan, and Karl George Emeléus. "Notes on the effect of noise on Langmuir probe characteristics." *Proceedings of the Physical Society* 79, no. 3 (1962): 535.
- [26] Chen, Francis F. "Double-Probe Method for Unstable Plasmas." *Review of Scientific Instruments* 35, no. 9 (1964): 1208-1212.
- [27] Braithwaite, N. St J., N. M. P. Benjamin, and J. E. Allen. "An electrostatic probe technique for RF plasma." *Journal of Physics E: Scientific Instruments* 20, no. 8 (1987): 1046.
- [28] Annaratone, B. M., and N. St J. Braithwaite. "A comparison of a passive (filtered) and an active (driven) probe for RF plasma diagnostics." *Measurement Science and Technology* 2, no. 8 (1991): 795.
- [29] Cantin, A., and R. R. J. Gagne. "Pressure dependence of electron temperature using rf-floated electrostatic probes in rf plasmas." *Applied Physics Letters* 30, no. 7 (1977): 316-319.
- [30] Paranjpe, Ajit P., James P. McVittie, and Sidney A. Self. "A tuned Langmuir probe for measurements in rf glow discharges." *Journal of Applied Physics* 67, no. 11 (1990): 6718-6727.
- [31] Johnson, E. O., & Malter, L. A floating double probe method for measurements in gas discharges. *Physical Review*, **80**, 58 (1950).
- [32] Chen, S. L., & Sekiguchi, T. (1965). Instantaneous Direct-Display System of Plasma Parameters by Means of Triple Probe. *Journal of Applied Physics*, 36(8), 2363-2375.
- [33] Ji, H., H. Toyama, K. Yamagishi, S. Shinohara, A. Fujisawa, and K. Miyamoto. "Probe measurements in the REPUTE-1 reversed field pinch." *Review of scientific instruments* 62, no. 10 (1991): 2326-2337.

- [34] Langmuir, Irving, and Karl T. Compton. "Electrical discharges in gases part II. Fundamental phenomena in electrical discharges." *Reviews of modern physics* 3, no. 2 (1931): 191.
- [35] Smith, J. R., Noah Hershkowitz, and P. Coakley. "Inflection-point method of interpreting emissive probe characteristics." *Review of Scientific Instruments* 50, no. 2 (1979): 210-218.
- [36] Kemp, Robert F., and J. M. Sellen. "Plasma potential measurements by electron emissive probes." *Review of Scientific Instruments* 37, no. 4 (1966): 455-461.
- [37] Makowski, M. A., and G. A. Emmert. "New method to measure plasma potential with emissive probes." *Review of Scientific Instruments* 54, no. 7 (1983): 830-836.
- [38] Chen F. F. *Plasma Diagnostic Techniques* ed. R H Huddlestone and S L Leonard (New York; Academic Press, 1965) p. 113.
- [39] C R Hoffmann and D J Lees "A differential method of measuring plasma potential" *Plasma Physics* 13 pg. 689 (1971)
- [40] Ye, M. Y., and S. Takamura. "Effect of space-charge limited emission on measurements of plasma potential using emissive probes." *Physics of Plasmas* 7 (2000): 3457.
- [41] Lho, T., N. Hershkowitz, and G. H. Kim. "Effect of harmonic rf fields on the emissive probe characteristics." *Review of Scientific Instruments* 71, no. 2 (2000): 403-405.
- [42] Wang, E. Y., N. Hershkowitz, T. Intrator, and C. Forest. "Techniques for using emitting probes for potential measurement in rf plasmas." *Review of scientific instruments* 57, no. 10 (1986): 2425-2431.
- [43] Mravlag, E., and P. Krumm. "Space potential measurements with a continuously emitting probe." *Review of Scientific Instruments* 61, no. 8 (1990): 2164-2170.
- [44] R. H. Lovberg, in *Plasma Diagnostic Techniques*, edited by Richard H. Huddlestone and Stanley L. Leonard (Academic, New York, 1965), Chap. 3.
- [45] W. Böttcher, in *Plasma Diagnostics*, edited by W. Lochte-Holtgreven (North Holland, Amsterdam, 1968), Chap. 10.
- [46] Awasthi, L. M., S. K. Mattoo, R. Jha, R. Singh, and P. K. Kaw. "Study of electromagnetic fluctuations in high beta plasma of a large linear device." *Physics of Plasmas* 17 (2010): 042109.
- [47] Reilly, Michael P., William Lewis, and George H. Miley. "Magnetic field probes for use in radio frequency plasma." *Review of Scientific Instruments* 80, no. 5 (2009): 053508-053508.
- [48] Everson, E. T., P. Pribyl, C. G. Constantin, A. Zylstra, D. Schaeffer, N. L. Kugland, and C. Niemann. "Design, construction, and calibration of a three-axis, high-frequency magnetic probe (B-dot probe) as a diagnostic for exploding plasmas." *Review of Scientific Instruments* 80 (2009): 113505.
- [49] Franck, Christian M., Olaf Grulke, and Thomas Klinger. "Magnetic fluctuation probe design and capacitive pickup rejection." *Review of scientific instruments* 73, no. 11 (2002): 3768-3771.

[50] Eom, G. S., G. C. Kwon, I. D. Bae, G. Cho, and W. Choe. "Heterodyne wave number measurement using a double B-dot probe." *Review of Scientific Instruments* 72, no. 1 (2001): 410-412.

[51] Loewenhardt, P. K., B. D. Blackwell, and Beichao Zhang. "A simple miniature magnetic probe with inherent electrostatic rejection." *Review of scientific instruments* 64, no. 11 (1993): 3334-3335.

[52] <http://www.pearsonelectronics.com/pdf/410.pdf>

Helicon Characterization

Helicon mode characterization and initial plasma experiments performed in the newly built diverging magnetic field helicon experiment described in Chapter 3 will be presented in this chapter. Radio frequency (RF) plasma is produced in the experimental set up with all the vacuum systems, electromagnets, RF circuitry and diagnostics which are tested individually. Helicon mode is identified at low magnetic fields (<200 Gauss) by observing the mode transitions of a helicon discharge, radial density profiles and wave field measurements. Initial physics experiments to observe current free double layers are discussed. The chapter will describe antenna efficiency measurements, discharge mode transitions, mode structure at low magnetic field and CFDL observation.

4.1 Antenna Efficiency

The half helical $m = +1$ antenna is designed for two purposes, one for RF plasma production and the other is helicon wave excitation with the later dependent on the density produced by the former through the helicon dispersion relation for a certain ambient magnetic field. So it is necessary to find out the efficiency of the antenna and its associated circuitry to deliver significant power to the plasma. The power transfer efficiency The RF power transfer efficiency has been calculated to estimate the RF power absorption in the plasma, using the relation [1-2]

$$\eta = \frac{R_p}{R_p + R_A} \quad (4.1)$$

Where η is the power transfer efficiency, R_p is the plasma resistance and R_{ant} is the vacuum resistance. The equivalent circuit of the antenna (Figure 3.3) is composed of an effective inductance, L_A , a circuit resistance, R_A , which includes all Ohmic and contact resistances, and

any eddy current losses relevant to the antenna, transmission line and the matching network. The plasma resistance, R_p includes all power losses attributed to the plasma, including power losses due to capacitive, inductive and wave coupling. Since the total reactance of the combination of antenna and plasma is matched under every measurement condition and the observed reflected power is $< 1\%$, total input power from the RF generator must be dissipated in the combined antenna-plasma system. The total current in the antenna is related to the total effective antenna loading resistance, $R_{eff} = R_A + R_p$, and the net power flow to the antenna is given by [2]

$$P_F - P_R = I_{rms}^2 R_{eff} \quad (4.2)$$

Where P_F and P_R are the forward and reflected powers respectively and $I_{rms} = I_{rf}/\sqrt{2}$ with I_{rf} is the amplitude of the sinusoidally varying current measured by a RF current probe coaxially held around the reference leg of the transmission line. The external circuit resistance R_A is estimated by measuring the antenna current in the absence of plasma.

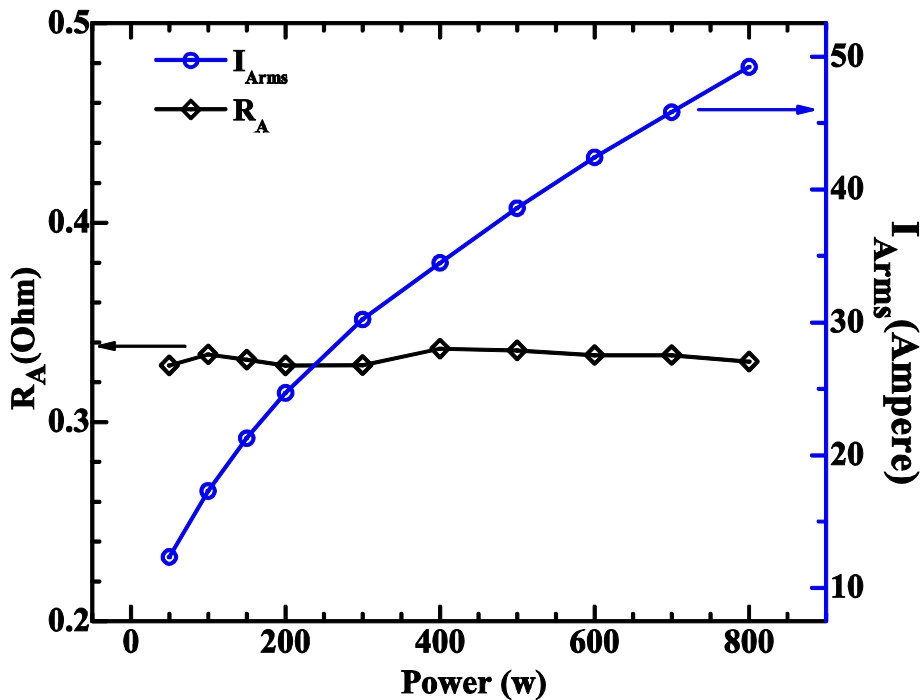


Figure 4.1 Variation of antenna RMS current and antenna resistance with RF power in vacuum at 5×10^{-5} mbar.

Figure 4.1 shows the variation of antenna current in vacuum with RF power at 5×10^{-5} mbar. The estimated value of the antenna resistance R_A is ≈ 0.34 Ohm. In this case all of the input power is dissipated in the matching network-antenna system. Figure 4.2 (a) shows the variation of antenna current, I_{rms} , with input power in the presence of plasma. Using the known power output from the generator (calibrated with a 50 Ohm resistive load) and measured reflected power, the plasma resistance is calculated from Equation 4.2. The variation of plasma resistance with input power at constant gas fill-in pressure of 2×10^{-3} mbar and a constant magnetic field of 100 Gauss near source is shown in Figure 4.2 (b). It can be clearly seen from Figure 4.2 (b) that at low input power, the plasma resistance remains low (≈ 0.16 Ohm) before increasing to around 0.8 Ohm above 500 W of input power. Figure 4.2 (b) also reveals that the value of plasma resistance does not change monotonically but exhibits jumps at specific values of input power.

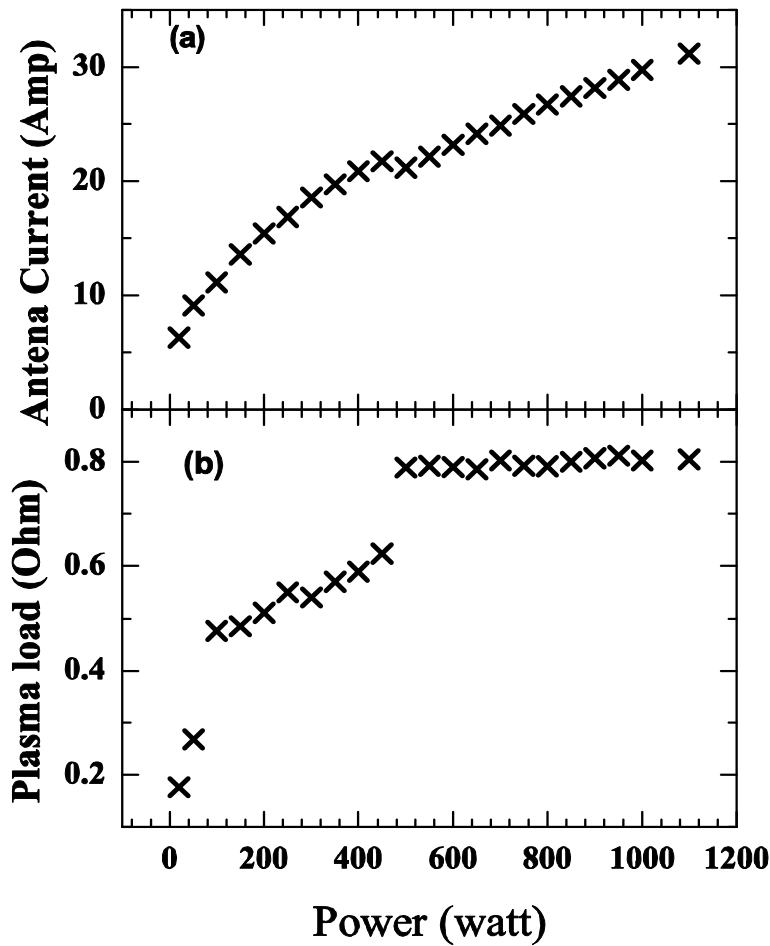


Figure 4.2 (a) Antenna current and (b) estimated antenna-plasma resistance variation with RF power at 2×10^{-3} mbar Ar and 100 G magnetic field measured at $Z=22$ cm.

These jumps in plasma resistance at around 40 W and 450 W of input power are indicative of transitions from capacitive to inductive mode and inductive to helicon mode respectively, which will be discussed elaborately in the next section. After determining the plasma resistance, the power transfer efficiency η has been calculated. For low input powers (< 50 W), the power transfer efficiency is less than 30% and it rises up to 75% for input power of > 1200 W which is typical for a helicon discharge [1].

4.2 Discharge mode transitions

As discussed in Chapter 2, the discharge mode transitions are observed in all RF discharges. In helicon literature [3] the modes are named E, H or W depending on the dominant electric field responsible for maintain the discharge is of capacitive, inductive or wave origin respectively. EHW mode transitions in helicon discharges are observed by changing source parameters either of RF power [1, 3-4] and ambient magnetic field [5]. These transitions are observed by monitoring the density [3-6], Q-factor of matching circuit [6], plasma potential [7] or antenna plasma resistance [8]. In this thesis mode transitions are studied by increasing the RF power at 110 G magnetic field with four different argon neutral pressures (3×10^{-4} mbar, 6×10^{-4} mbar, 9×10^{-4} mbar and 40×10^{-4} mbar) and measuring density in the upstream region at $z = 22$ cm along with load capacitance values of matching network for zero RF power reflection. The helicon dispersion (Equation 2.x) suggests transition to helicon mode at lower density i.e. lower RF power for a lesser ambient magnetic field.

Figure 4.3 (a) shows the variation of plasma density with RF power as measured by a triple Langmuir probe at $z = 22$ cm. At 3×10^{-4} mbar (lowest pressure) the transition from capacitive to inductive discharge though possible in the applied RF power range, the transition to helicon sustained discharge is not visible. But in all the other three higher pressures clear transitions to helicon discharge are possible. As per the design of the matching network [Chapter 3] $C_L \propto 1/\sqrt{R_p}$, the value of the load capacitor gives an indirect feedback of the antenna-plasma resistance. So the C_L values are noted and their variations with RF power are plotted in Figure 4.3 (b). As evident from the figure, the transitions in density values of Figure 4.3 (a) are magnified in C_L plots with clear and distinct transitions well visible. The reason for antenna-plasma resistance or C_L value to be more sensitive to external plasma parameters is because it represents

a macroscopic change of the discharge in total corresponding to antenna plasma resistance whereas the density measurement using Langmuir probe is a single point local microscopic sampling. For the lowest pressure there is only one transition (E-H) but for all other higher pressures there are two transitions (E-H and H-W). The transitions to helicon mode from an inductive mode happened at a lower RF power for a higher pressure. Another observation from this study is that the slope of density variation is different in all the sustained modes indicating different mechanisms of sustaining the discharge.

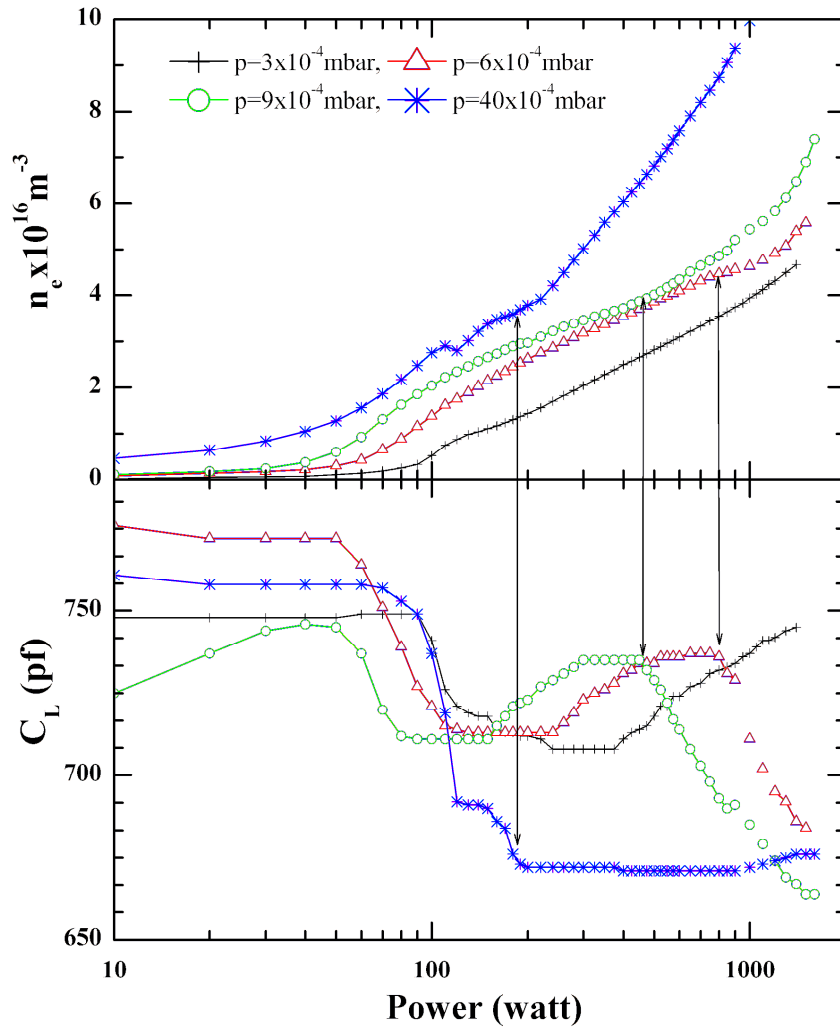


Figure 4.3 Mode transitions observed at 100 Gauss for different Argon pressures. Transitions are observed (a) in density variation with power at $z=20$ cm and (b) in load capacitor values of the matching network.

However, from all these above-mentioned observations we can conclude that at low powers (< 50 W) the plasma discharges are capacitive in nature i.e. the power is coupled to the plasma capacitively. As we increased the input power > 50 W up to < 500 W, the power is coupled to the plasma inductively and higher densities compared to the capacitive mode are observed. At higher powers (> 500W), the power coupling to the plasma happens due to the direct coupling of antenna fields to helicon wave fields as the density rises more sharply compared to the inductive mode.

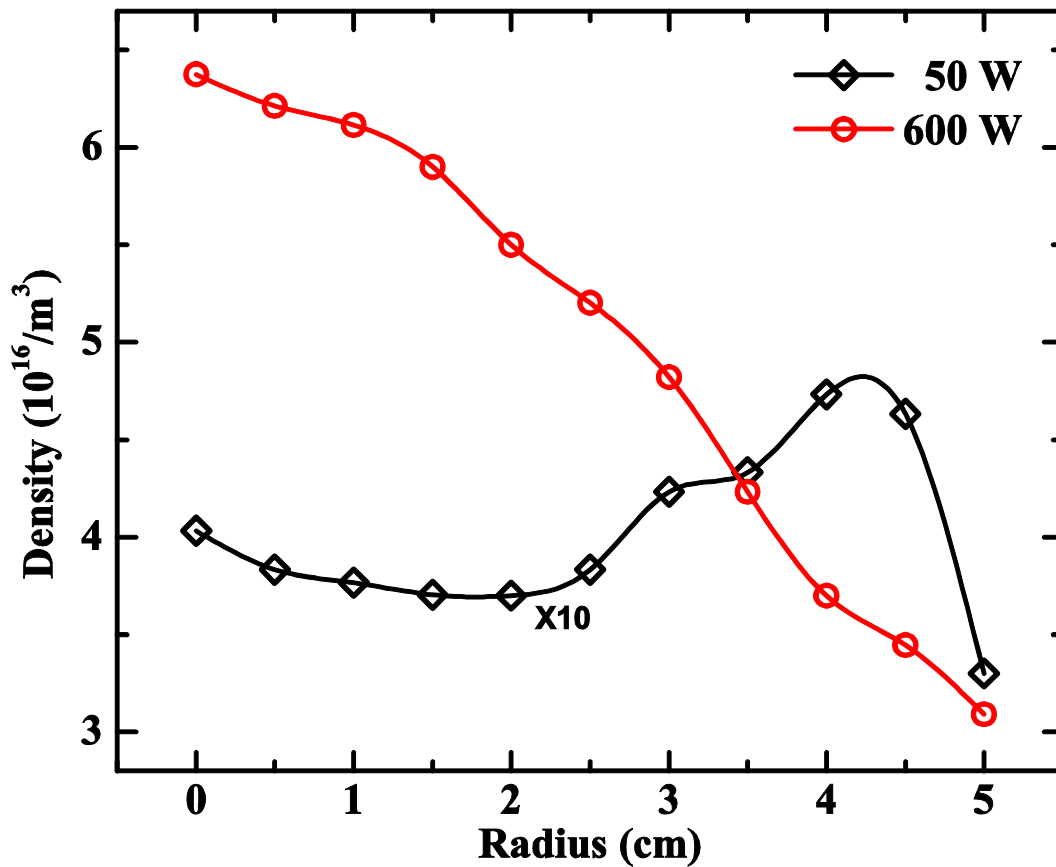


Figure 4.4 Radial density profile for two different RF powers (50W and 600W) at pressure $\sim 2 \times 10^{-3}$ mbar and magnetic field ~ 100 G measured at Z=22 cm.

The existence of inductive and helicon modes are further supported by the measurement of density profile at 22 cm away from the source as it is expected that for an inductive mode the power deposition will be away from the center and near the boundary unlike the helicon mode in which maximum power is deposited away from the radial boundary of the discharge [4, 9-10].

At low input power ($\sim 50 - 500$ W), radial profile of electron density remains hollow (Figure 4.4), a signature of inductive mode discharge. However, at higher input power (>500 W) peaked radial profile of density is observed (Figure 4.4), indicating the existence of helicon mode in the plasma.

4.3 Mode structure at Low magnetic field

Excitation of helicon $m = +1$ mode is confirmed by measuring the axial component of wave magnetic field along the radius. Figure 4.x shows the variation B_z amplitude normalized to unity, measured with a single loop B-dot probe at $z = 22$ cm with 300 W RF power and 2×10^{-3} mbar pressure. Along with are shown theoretical $m = +1$ curves of B_z of helicon waves in a cylindrical boundary [24] with a perpendicular wave number of 76 m^{-1} .

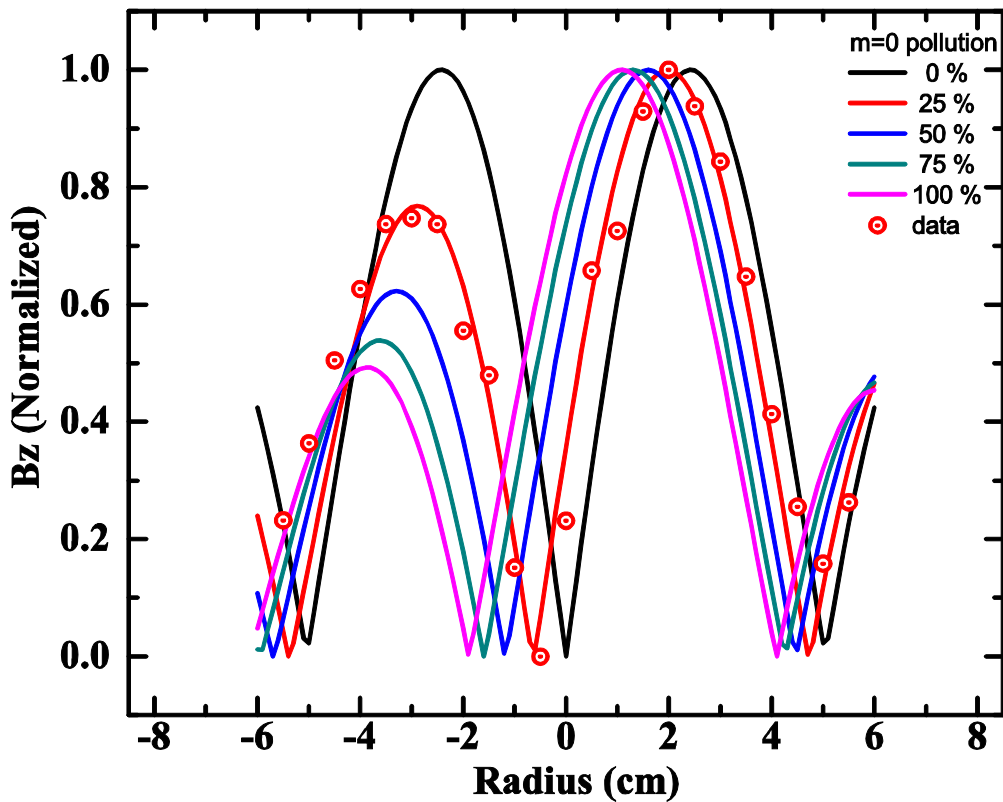


Figure 4.5 Radial variation measured B_z (circles) at 30 G, 300W and 2×10^{-3} mbar. The solid lines are theoretical curves of pure $m = +1$ mode along with mixed modes with 25%, 50%, 75% and 100% additional $m = 0$ mode content. All values are normalized to 1.

The variations are asymmetric with respect to the origin and also the minimum on axis is shifted to negative radius values. These kinds of variations at low magnetic field have been reported earlier [11-13]. The reason for $m = 0$ antenna field structure is not clear.

To see the effect of pollution, theoretical B_z radial profiles are plotted in Figure 4.5 for a mixed mode with 100% $m = +1$ mode content in addition to a variable % of $m = 0$ mode. $m = +1$ is basically a $J_1(k_{\perp}r)$ function which is asymmetric in radius (argument) for a given value of k_{\perp} .

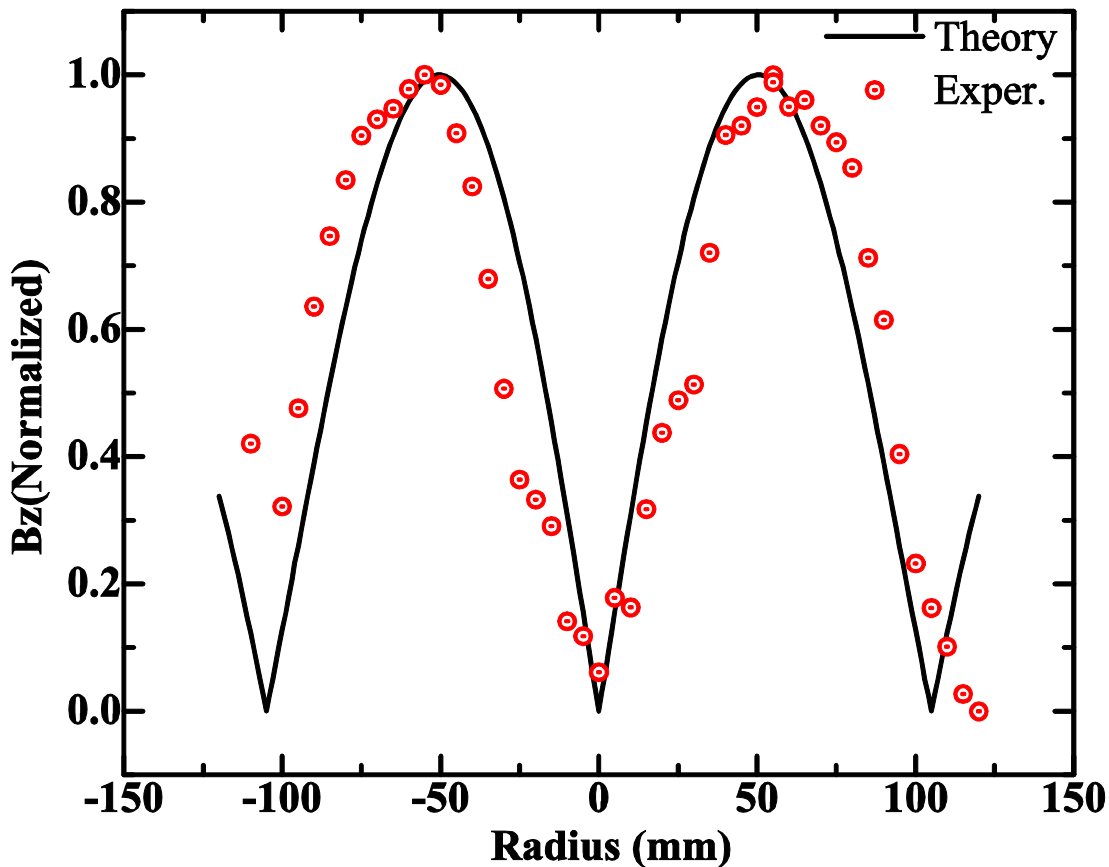


Figure 4.6 Radial variation of B_z amplitude in normalized units for 300W RF power, 30 G and Argon neutral pressure of 2×10^{-3} mbar measured at $Z=40$ cm.

But as we measure the peak-to-peak values we cannot distinguish the positive and negative amplitudes. Whereas, $m = 0$ mode is symmetric with respect to the argument of the Bessel component it consists of. So on one side of radial variation has values decreased and the other

side the values are increased, the total radial variation which on normalization gives an asymmetrical behavior.

Though it is expected that the induced fields (or antenna fields) will die down in a thin skin depth, the application of magnetic field has already been proposed by Chen [14] to increase the skin depth giving rise to an anomalous skin depth.

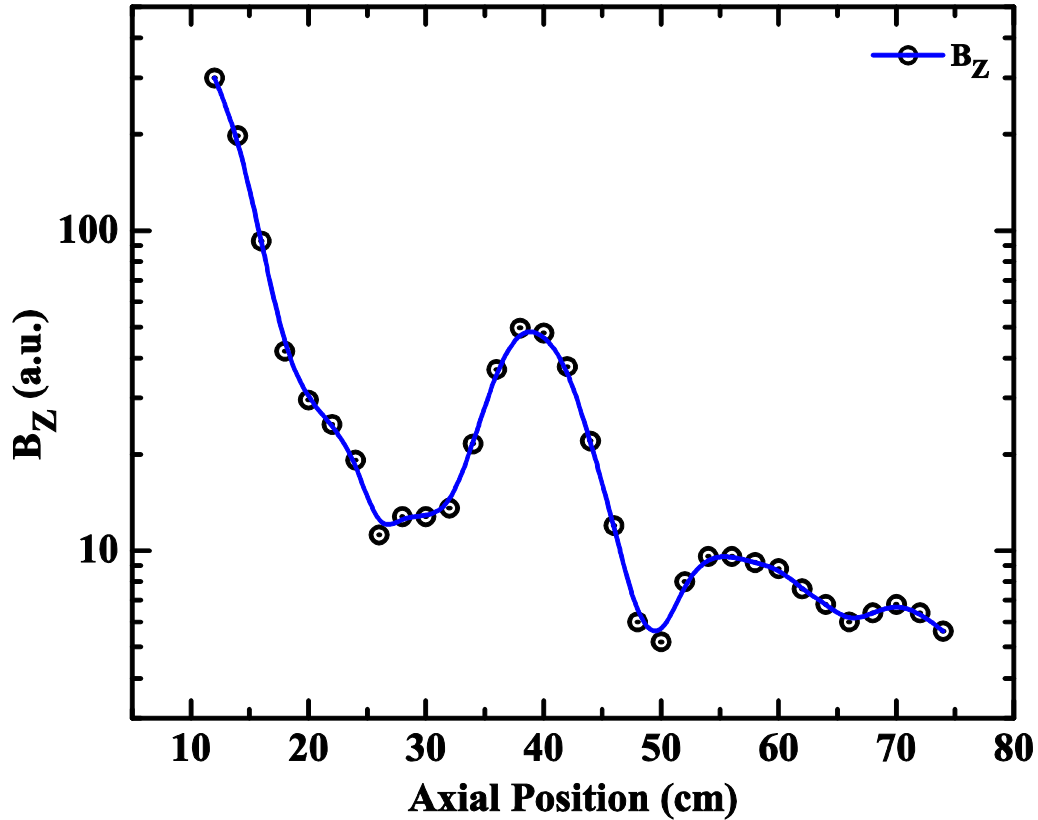


Figure 4.7 Variation of axial magnetic field of Helicon wave along the axis for 600 W RF power at pressure $\sim 2 \times 10^{-3}$ mbar and magnetic field ~ 100 Gauss.

Figure 4.5 shows that a pollution of $\sim 25\%$ $m = 0$ mode is there. To confirm that the antenna fields are causing the asymmetric radial variation, B_z in the downstream plasma is measured at $z=40$ cm. Figure 4.6 shows a radial profile which is symmetric which confirms that $m = 0$ mode pollution is negligible. So, the mode structure measured near the antenna shows $m = +1$ mode

excitation with pollution from $m = 0$ mode with a pure $m = +1$ mode downstream of the source.

The existence of helicon wave in the plasma at higher input powers (>500 W) is further substantiated by the measurement of axial profile of wave magnetic field using a single loop B-dot probe as shown in Figure 4.7 for 600 W RF power and a pressure of 2×10^{-3} mbar with 100 Gauss magnetic field. From the slope of the axial phase variation of the wave magnetic field, the wavelength was calculated ~ 22 cm in the source region and ~ 19.5 cm in the diffusion region using the phase axial slope as shown from Figure 4.8.

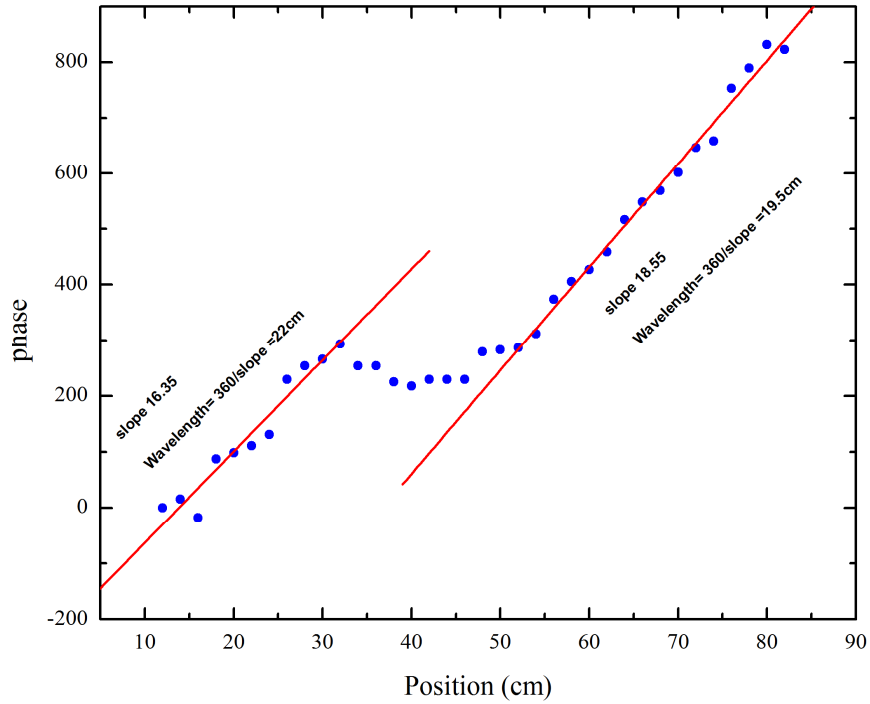


Figure 4.8 Axial variation of helicon wave phase measured at $r=0$ with a single loop B-dot probe at $\sim 2 \times 10^{-3}$ mbar, 300W and 100 G magnetic field.

4.4 Axial density profile

One of the primary aims of this thesis is study of CFDL. CFDL in a helicon discharge are typically performed in an expanding geometry and an expanding magnetic field with 100's of Gauss in the source chamber and 10's of Gauss in the diffusion chamber [15-19]. The combined

effect of both geometry and magnetic field expansion sets up a density gradient in the axial direction which gives rise to an ambipolar potential drop. This potential drop evolves into a free standing often stable potential structure as the neutral pressure is reduced. An experiment is performed to look for density gradients set up in the axial direction at 2×10^{-3} mbar and 110 Gauss magnetic field near the antenna. Figure 4.8 shows axial variation of density measured by a double Langmuir probe for three different powers at $r = 0$.

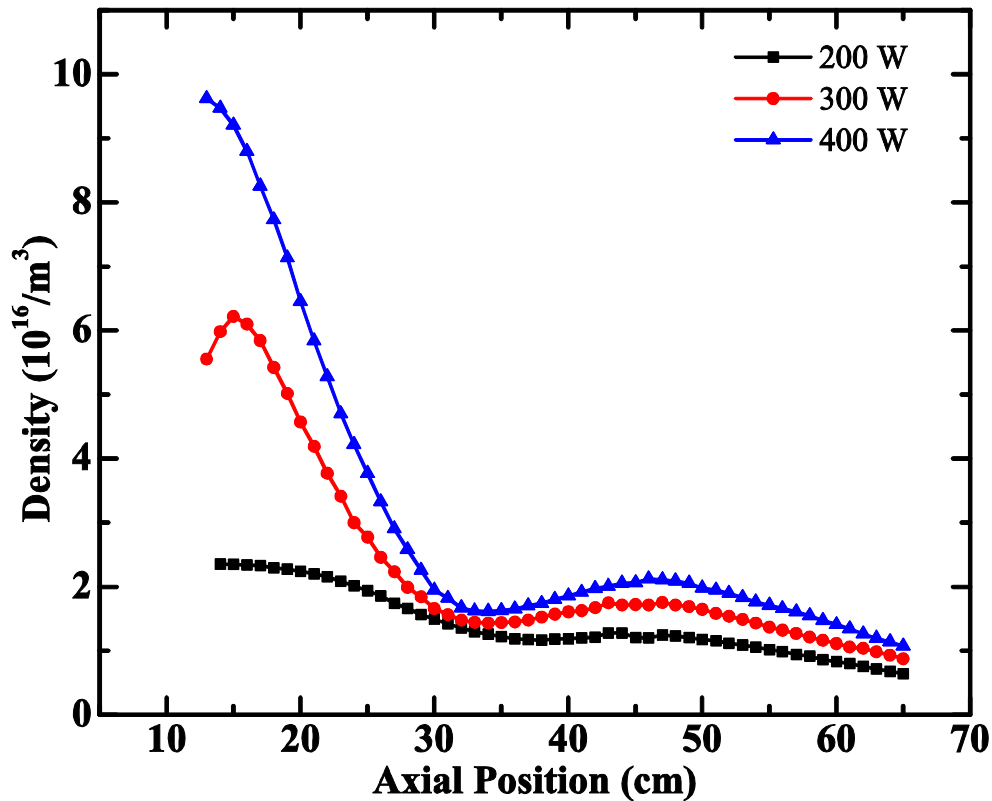


Figure 4.9 Axial variation of density measured at $r=0$ for three powers 200W, 300W and 400W, source magnetic field of 100 G and 2×10^{-3} mbar Ar pressure.

Upstream-to-downstream density ratios of ~ 2.7 , 5.3 and 8.8 are obtained for RF input power of 200 W, 300 W and 400 W respectively. The variation of upstream and downstream densities shows that the maximum power deposition is happening near the source only. But one of the interesting features is a hump in the density near axial locations of $z = 35-55$ cm in the diffusion chamber, the hump getting peaked for higher RF powers. Though the occurrence of downstream density peaks much away from the antenna are reported in high power and high magnetic field

experiments [20-22], these downstream density peaks which are observed here at low magnetic field low RF power are not reported so far. Thorough investigation of these downstream density peaks will be discussed in Chapter 5.

4.5 Observation of Current free double layer

CFDL formation in the expanding helicon plasma is studied at 600W RF power, 280 G magnetic field and Argon neutral pressure of 1.2×10^{-4} mbar. On axis plasma potential is measured along the axial direction with a saturated emissive probe in floating potential method (discussed in chapter 3) by passing a filament current of 2.7 Ampere in a 0.125 mm tungsten filament. The variation of plasma potential and density are shown in Figure 4.3 (a) and (b) respectively. The axial magnetic field profile used for this experiment is shown in Figure 3.3.

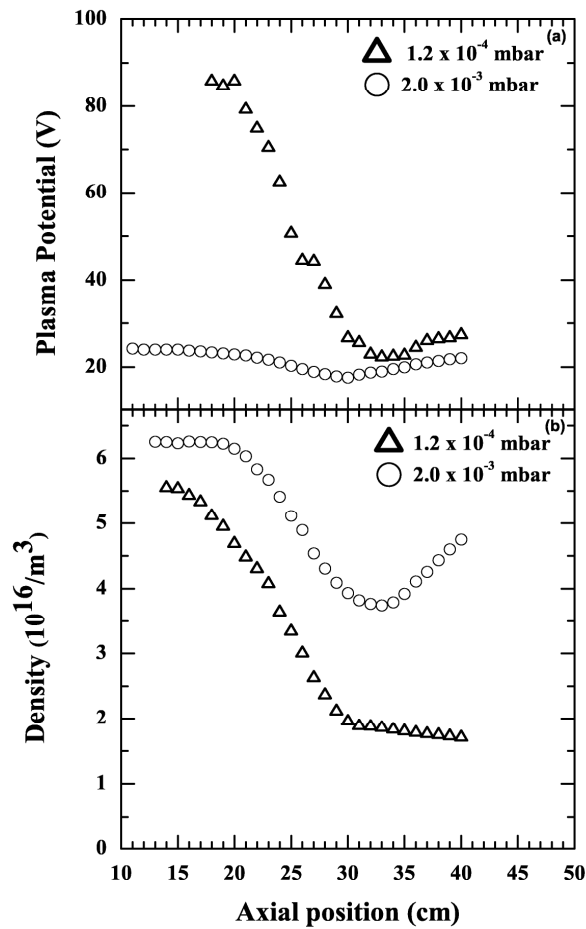


Figure 4.10 Axial variations of (a) plasma potential and (b) plasma density at 2×10^{-3} mbar and 1.2×10^{-4} mbar of Argon with RF power of 600W and 280 G magnetic field in source.

Plasma expansion leads to a density fall with upstream and downstream densities of $5.5 \times 10^{16}/\text{m}^3$ and $1.7 \times 10^{16}/\text{m}^3$ respectively with a nearly equal temperature of $T_e \sim 6$ eV in the potential fall region. The axial density is measured by a double probe and electron temperature is measured by a RF compensated Langmuir probe. For this expansion to be a Boltzmann expansion which relates upstream (n_0, V_0) and downstream (n_z, V_z) densities and plasma potentials by $V_z - V_0 = -T_e (\text{eV}) \times \ln(n_z/n_0)$ [15, 17, 23], the maximum drop should be ~ 7.5 V. This observation plasma potential drop of ~ 50 V in bulk plasma is more than the local T_e can be termed as a CFDL as it cannot be explained through a simple Boltzmann plasma expansion. The average thickness of the CFDL is $\sim 1000 \lambda_D$ taking into consideration of upstream and downstream plasma density and electron temperature.

Measurement of density and plasma potential at a higher pressure of 2×10^{-3} mbar is presented in Figure 4.3 (a) and (b) respectively where a potential drop of ~ 6 V is observed which is of the order of the local electron temperature of ~ 5 eV and for this the expected plasma potential drop due to a Boltzmann plasma expansion is ~ 4.4 V.

So, we have observed a CFDL in the source chamber plasma before the geometrical expansion into the diffusion chamber with a potential drop $\phi_{DL} \approx 8T_e$ and thickness of $\sim 1000 \lambda_D$ which form at low pressure and are not observed at higher pressure. Though this kind of CFDL with thickness > 50 - $100 \lambda_D$ are observed in few recent experiments [15-16], there are experiments with observation of sharp CFDL with thickness $< 100 \lambda_D$ [17-19]. Further studies on sharp CFDL formation and the effect of magnetic field gradient will be presented in Chapter 6.

4.6 Summary of Chapter 4

Antenna resistance is measured without plasma. Helicon antenna efficiency is shown to increase with RF power in the presence of plasma. Discharge mode transitions are observed at different pressures. At lower pressure the transitions are obtained at higher RF powers for a constant magnetic field. Radial density profiles are shown to confirm the inductive and helicon modes. Helicon wave excitation with half helical $m = +1$ mode is confirmed by measuring the radial variation of the axial component of magnetic field. Additionally, the mode is shown to be

polluted by the antenna fields near the antenna and pure away from the antenna in the diffusion chamber. Axial variation of the phase of the helicon wave gives a wave length of 22 cm in the source and 19.5 cm in the diffusion chamber. Axial density profiles in a diverging magnetic field configurations shows upstream-to-downstream density ratios of ~ 2.7 , 5.3 and 8.8 are obtained for RF input power of 200 W, 300 W and 400 W respectively. Downstream density peaks are observed in the diffusion chamber which gives indication of helicon power deposition away from the antenna. Current free double layer is observed at low pressures with a potential drop of $\sim 8 kT_e/e$ and thickness of $\sim 1000 \lambda_D$. The double layer vanished at higher pressure with the potential drop of the order of T_e and can be explained through a simple Boltzmann expansion. The DL is formed inside the source chamber and in the bulk of the plasma aligned to magnetic field.

References

- [1] Chi, Kyeong-Koo, T. E. Sheridan, and R. W. Boswell. "Resonant cavity modes of a bounded helicon discharge." *Plasma Sources Science and Technology* 8, no. 3 (1999): 421.
- [2] Lafleur, T., C. Charles, and R. W. Boswell. "Characterization of a helicon plasma source in low diverging magnetic fields." *Journal of Physics D: Applied Physics* 44.5 (2011): 055202.
- [3] Ellingboe, A. R., and R. W. Boswell. "Capacitive, inductive and helicon-wave modes of operation of a helicon plasma source." *Physics of Plasmas* 3 (1996): 2797.
- [4] Franck, Christian M., Olaf Grulke, and Thomas Klinger. "Mode transitions in helicon discharges." *Physics of Plasmas* 10 (2003): 323.
- [5] Boswell, R. W. "Very efficient plasma generation by whistler waves near the lower hybrid frequency." *Plasma Physics and Controlled Fusion* 26.10 (1984): 1147.
- [6] Perry, A. J., D. Vender, and R. W. Boswell. "The application of the helicon source to plasma processing." *Journal of Vacuum Science & Technology B: Microelectronics and Nanometer Structures* 9, no. 2 (1991): 310-317.
- [7] Perry, Andrew, Garrard Conway, Rod Boswell, and Harold Persing. "Modulated plasma potentials and cross field diffusion in a Helicon plasma." *Physics of Plasmas* 9 (2002): 3171.
- [8] Chi, Kyeong-Koo, T. E. Sheridan, and R. W. Boswell. "Resonant cavity modes of a bounded helicon discharge." *Plasma Sources Science and Technology* 8, no. 3 (1999): 421.
- [9] Degeling, A. W., C. O. Jung, R. W. Boswell, and A. R. Ellingboe. "Plasma production from helicon waves." *Physics of Plasmas* 3 (1996): 2788.
- [10] Yun, Seokmin, Suwon Cho, George Tynan, and Hongyoung Chang. "Density enhancement near lower hybrid resonance layer in $m=0$ helicon wave plasmas." *Physics of Plasmas* 8 (2001): 358.
- [11] Sato, Genta, Wataru Oohara, and Rikizo Hatakeyama. "Experimental evidence of $m=-1$ helicon wave cutoff in plasmas." *Journal of the Physical Society of Japan* 75.4 (2006): 3501.
- [12] Chi, Kyeong-Koo, T. E. Sheridan, and R. W. Boswell. "Resonant cavity modes of a bounded helicon discharge." *Plasma Sources Science and Technology* 8.3 (1999): 421.
- [13] Lafleur, T., C. Charles, and R. W. Boswell. "Plasma control by modification of helicon wave propagation in low magnetic fields." *Physics of Plasmas* 17 (2010): 073508.
- [14] Chen, Francis F. "Collisional, magnetic, and nonlinear skin effect in radio-frequency plasmas." *Physics of Plasmas* 8 (2001): 3008.
- [15] Charles, Christine, and Rod Boswell. "Current-free double-layer formation in a high-density helicon discharge." *Applied Physics Letters* 82, no. 9 (2003): 1356-1358.

- [16] Sutherland, Orson, Christine Charles, N. Plihon, and R. W. Boswell. "Experimental evidence of a double layer in a large volume helicon reactor." *Physical review letters* 95, no. 20 (2005): 205002.
- [17] Takahashi, K., K. Oguni, H. Yamada, and T. Fujiwara. "Ion acceleration in a solenoid-free plasma expanded by permanent magnets." *Physics of Plasmas* 15 (2008): 084501.
- [18] Hairapetian, G., and R. L. Stenzel. "Expansion of a two-electron-population plasma into vacuum." *Physical review letters* 61, no. 14 (1988): 1607.
- [19] Sun, Xuan, Amy M. Keesee, Costel Biloiu, Earl E. Scime, Albert Meige, Christine Charles, and Rod W. Boswell. "Observations of ion-beam formation in a current-free double layer." *Physical review letters* 95, no. 2 (2005): 025004.
- [20] Chen, Francis F., Isaac D. Sudit, and Max Light. "Downstream physics of the helicon discharge." *Plasma Sources Science and Technology* 5.2 (1996): 173.
- [21] Chen, Francis F. "Physics of helicon discharges." *Physics of Plasmas* 3 (1996): 1783.
- [22] Sudit, Isaac D., and Francis F. Chen. "Discharge equilibrium of a helicon plasma." *Plasma Sources Science and Technology* 5.1 (1996): 43.
- [23] Wiebold, Matt, Yung-Ta Sung, and John E. Scharer. "Experimental observation of ion beams in the Madison Helicon eXperiment." *Physics of Plasmas* 18 (2011): 063501.
- [24] Chen, Francis F. "Plasma ionization by helicon waves." *Plasma Physics and Controlled Fusion* 33.4 (1991): 339.

Low Magnetic Field Helicon Studies

5.1 Introduction

A Helicon source operates in the frequency range between ion cyclotron and electron cyclotron frequencies usually with magnetic field of few hundreds of Gauss to few kilo Gauss. Appearance of helicon mode is generally identified by mode transitions which involves a transition from a capacitive to inductive to wave sustained discharge [1]. The transitions are can be observed from the step like transitions in measured plasma density and antenna-plasma coupling, obtained by increasing power at fixed magnetic field (B) of few hundred Gauss or vice versa. At high magnetic fields (>100 Gauss) it is observed that the density increases with applied magnetic field when in helicon mode as per the dispersion relation. However, previous studies have shown that at low magnetic fields of less than 100 Gauss, plasma density peaks at some specific magnetic fields, generally between 20 Gauss to 50 Gauss in different experiments using 13.56 MHz RF system [2-9]. Unlike usual helicon discharge mode transitions (see Chapter 2 and 4) at high magnetic fields (few hundred Gauss), the observance of density peaks at low magnetic fields seems to be a resonance phenomenon.

Chen [3] first reported this low magnetic peak in 2 cm diameter helicon discharge using 1600 W RF power where the density peak was observed at ~ 50 G with peak density of $6 \times 10^{18} m^{-3}$ an increase of nearly 40% from the no field case. Many other experiments subsequently reported similar observations of a density peak at magnetic fields between 10-50 G. Degeling et al [2] have observed density peak (Figure 5.1) around 50G for RF powers in 500-2000 W in a 18 cm diameter source using single loop antenna at 13.56 MHz. Wang et al have shown that the a higher magnetic field is required for the density peak to occur for a plasma

formed using higher ion mass or a higher source frequency. He measured the plasma resistance and has shown that the plasma resistance is well correlated with the density variations.

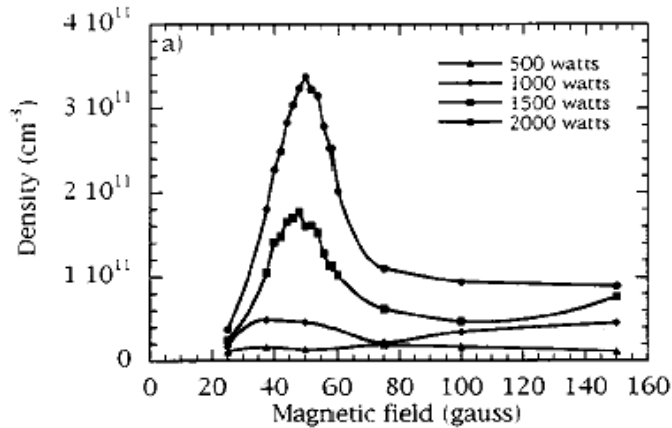


Figure 5.8 Density variation with applied magnetic field in the WOMBAT experiment. Degeling et al [2].

An experiment by Eom [10] has shown that for a high frequency RF discharge operating at 98 MHz, the peak occurs at 140 G. Recently Lafleur et al [9] have done extensive experiments in a diverging magnetic field helicon experiment and shown that the density can increase by an order from the no field case. Their density variations were well correlated with the measured variations of antenna-plasma radiation resistance and Q-value of the RF circuit for different RF powers and pressures in a helicon discharge produced by a double-saddle coil antenna.

Very few explanations are available for the observed density peak at low magnetic fields. Degeling et al [2] and Lafleur et al [9] interpreted this by invoking wave particle trapping; however the dependence of the trapping on magnetic field is not clear. Lafleur et al have also mentioned of a direct transition from a capacitive discharge at no applied magnetic field to a helicon discharge at the peak magnetic field (where the density peaks). But it is not clear why the discharge is not maintained for magnetic fields higher than the peak magnetic field and transits back to a capacitive discharge. Chen [11] suggested through the HELIC code results for a loop ($m = 0$) antenna that the density peak at low magnetic field is due to the constructive interference between $m = +1$ mode propagating along the magnetic field and the $m = +1$ mode generated due the source end wall reflection of $m = -1$ mode propagating opposite to the magnetic field

direction. The axial power absorption was shown to be in the near field of the antenna and the radial power absorption was near the plasma boundary. This radial boundary power absorption was shown to be due to TG modes. Again, it is not clear why the reflection occurs only at certain low magnetic fields and why similar density peak is not observed for high magnetic fields. Shamrai and Taranov [12] analytically derived the wave dispersion relation for waves propagating parallel to the magnetic field in a bounded plasma medium taking into account the finite mass of electrons. They found that the wave dispersion relation has two modes, one helicon (fast) and other is TG (slow) mode. Furthermore, they have predicted the possibility of mode conversion from helicon to TG mode in helicon plasmas. These two modes are well separated at higher magnetic field (> 200 Gauss for 13.56 MHz); however at low magnetic fields (< 100 Gauss for 13.56 MHz) they get coupled naturally under some typical conditions. Later Cho [13] studied the dispersion characteristics of the radial eigenmodes and resistive loading of helicon plasmas to explain the occurrence of the density peak at low magnetic fields. He concluded that in case of helical antenna the occurrence of density peaks are due to TG-helicon mode coupling at specific low magnetic fields where the perpendicular wave numbers of the helicon and TG modes are equal. Though TG modes are detected indirectly by Blackwell et al [14], their direct absorption has not been measured.

Most of the works at low magnetic field helicon discharges have shown a density peak away from the ECR magnetic field ~ 5 G for 13.56 MHz source frequency. In this thesis for the first time experimental observation of two density peaks (excluding the ECR peak) are reported in a helicon discharge carried out in low magnetic field (< 100 Gauss). The occurrence of density peaks is explained with the help of resonance of obliquely propagating right circular polarized electromagnetic (helicon) wave. These results are discussed in section 5.2. Plasma density and visible light intensity are measured on both sides of the antenna along with the antenna plasma resistance to look for the role of $m = -1$ modes. The observations and explanations are discussed in Section 5.3 in the light of polarization reversal of $m = \pm 1$ modes. Some of the high uniform magnetic field helicon discharge experiments have shown the peaking in axial density away from the helicon antenna. But with a low diverging magnetic field downstream density peaks have been observed nearly two wavelengths away from the antenna centre. This results on downstream density peaking are discussed in Section 5.4 for different RF power and neutral gas pressure. Though all the experiments of low field density peak are done earlier by many authors

in uniform magnetic fields the recent results by Lafleur et al [9] shows that for a single coil near the antenna the density rises nearly ten times. So, the density peaking phenomena along with the antenna-plasma coupling is studied for four different magnetic field topologies near the antenna and will be discussed in Section 5.5.

5.2 Multiple Density Peaks

After achieving a base pressure of $\sim 1 \times 10^{-6} \text{ mbar}$ in the system, argon gas is fed into the system at different pressures to produce plasma by powering the helicon antenna. The plasma density is measured using a double Langmuir probe placed in the source chamber 20 cm away from antenna centre towards the diffusion chamber. Figure 5.2 shows variation of measured axial plasma electron density at $z = 22 \text{ cm}$ with applied magnetic field near the antenna in the source chamber for different RF power and pressure. As the magnetic field is slowly increased from 0 G, the density also increases and goes through the ECR point around 5 G. Beyond the ECR point density continues to increase monotonically till 25 G to 30 G before falling sharply to half of its peak value near 40 G. However, increasing the magnetic field above 40 G, the density again increases and attains a peak around 50 G. It is clear from the figure that the magnitude of the main density peak at $\sim 25 \text{ G}$ increases with both pressure and power. Density rises approximately three times from $6 \times 10^{16} \text{ m}^{-3}$ to a peak value of $\sim 2 \times 10^{17} \text{ m}^{-3}$ at higher pressures ($\sim 2 \times 10^{-3} \text{ mbar}$). Whereas, at lower pressure of $\sim 0.4 \times 10^{-3} \text{ mbar}$, density only rises to $\sim 40\%$ of its initial value. The second peak is much clearly visible at low fill-in pressures. Figure 5.2 further shows that the main density peak always occurs at magnetic field values between 20 G to 30 G with the peak shifting towards the higher magnetic fields for higher power and pressure much like other reported results at low magnetic fields [7,9]. This kind of resonance density peaking with magnetic field seems likely to be the result of wave coupling rather than transitions of EHW type.

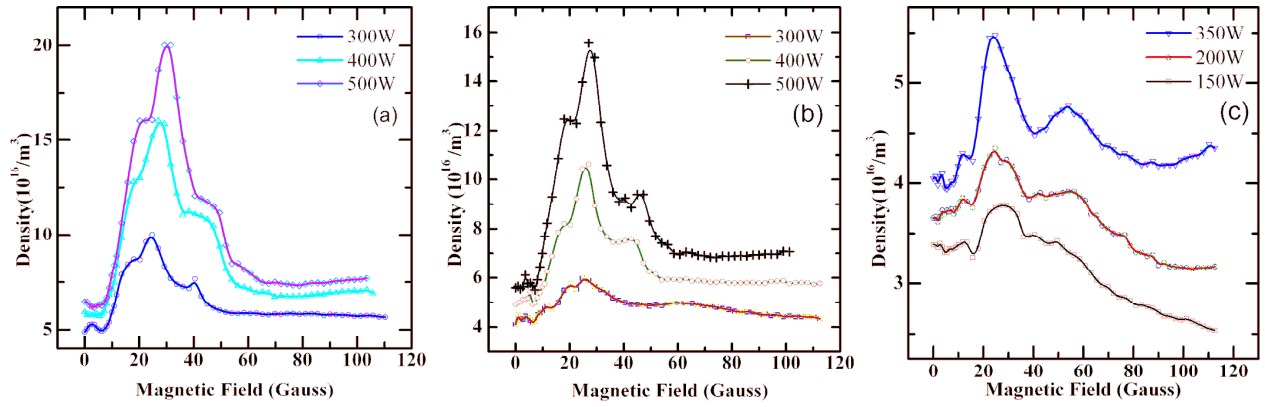


Figure 5.2 Plasma density on axis at $z = 20$ cm versus magnetic field. (a) 300, 400, and 500 W RF power, $p = 2 \times 10^{-3}$ mbar, (b) 300, 400, and 500 W RF power, $p = 0.8 \times 10^{-3}$ mbar, and (c) 100, 200, and 350 W RF power, $p = 0.4 \times 10^{-3}$ mbar.

Figure 5.3 shows the variation of matching network C_L values for corresponding values of RF power, fill-in pressure and magnetic field for which density is measured (Figure 5.2). The C_L values, as mentioned in Chapter 3 are measure of the antenna-plasma coupling (R_p) through the relation $C_L \propto 1/\sqrt{R_p}$. So a dip in C_L value is indicative of a peak in R_p . Multiple R_p peaks in magnetic fields can be deciphered from the C_L variations shown in the above figure consistent with the corresponding density variations except at low RF power and low fill-in pressures.

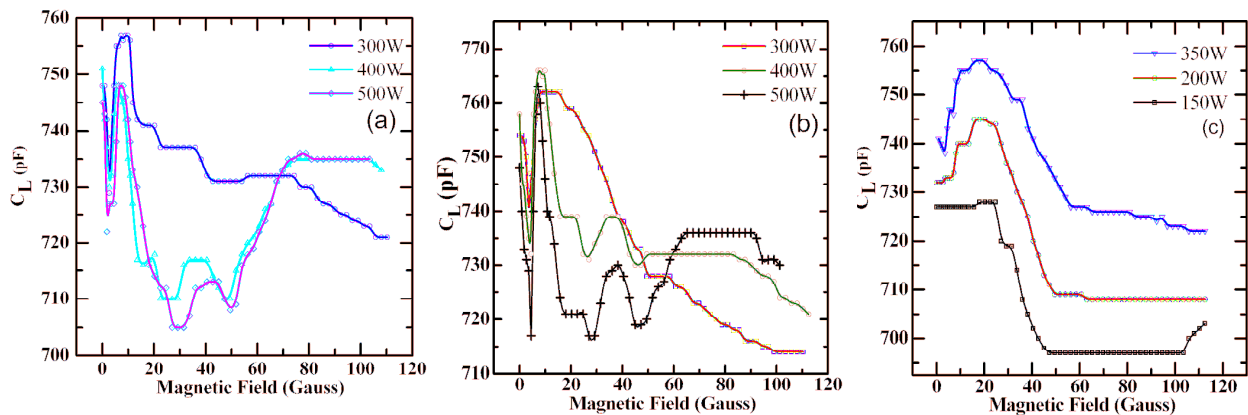


Figure 5.3 C_L values of the matching network at $z = 20$ cm versus magnetic field. (a) 300, 400, and 500 W RF power, $p = 2 \times 10^{-3}$ mbar, (b) 300, 400, and 500 W RF power, $p = 0.8 \times 10^{-3}$ mbar, and (c) 100, 200, and 350 W RF power, $p = 0.4 \times 10^{-3}$ mbar.

It should be noted that at low densities, the changes in R_P are very less beyond the first peak, so that the changes in C_L are not resolvable through the previously mentioned inverse square-root dependence on R_P . Another feature to be noted is that though C_L variations have appreciable dips around 5 G for almost all the plots, the density variations do not show significant density peaks.

The existence of the helicon wave is established in our experiment by measuring the amplitude and phase of the axial wave magnetic field, B_z using a single loop B-dot probe. In Figure 5.6 magnitude of axial wave magnetic field along the z-axis is plotted for two different magnetic fields (25 G and 50 G) where the 1st and 2nd density peaks are observed. The measurements are done by positioning the magnetic probe 10 cm downstream from the antenna and moving it along the z-axis for discharges with argon fill-in pressure of 0.4×10^{-3} mbar and 350 W RF power. As seen from figure 5.4, a hump in B_z around 20-40 cm has been observed, which is because of beating between the fundamental and higher order radial modes as established earlier [15-16]. The time difference between the reference probe and scanning probe gives the phase and the phase variation as a function of distance is plotted in Figure 5.5 for $B = 25$ and 50 G.

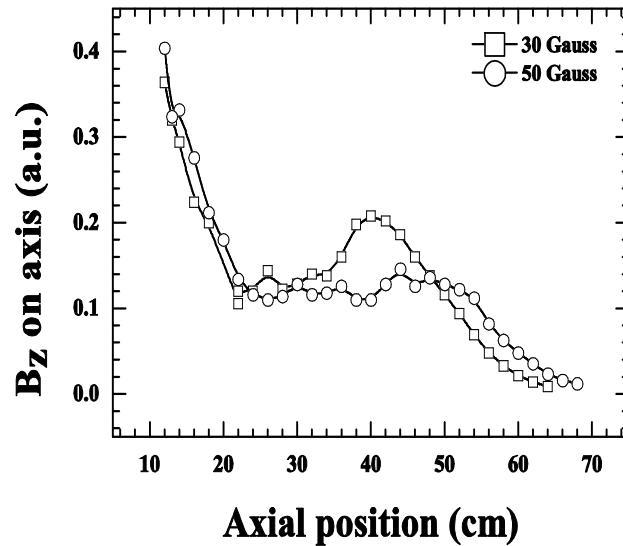


Figure 5.4 Axial profile of the axial component of the wave magnetic field at two different (30 and 50 G) ambient magnetic fields.

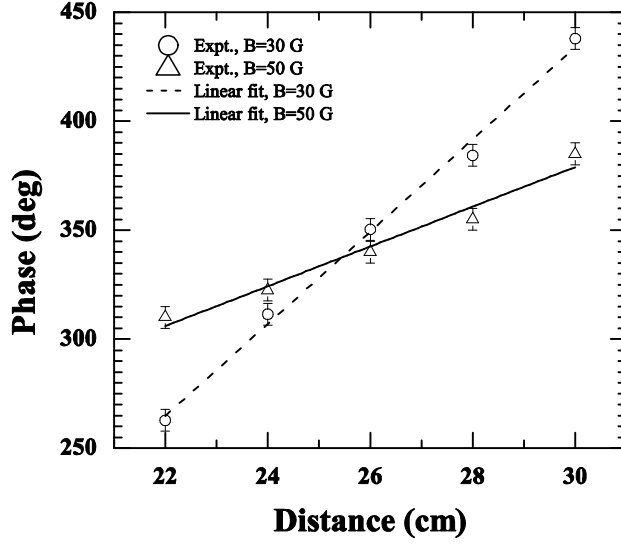


Figure 5.5 Variation of phase with distance for $p = 0.4 \times 10^{-3}$ mbar, RF power 350 W. $B = 30$ G (open circle) and $B = 50$ G (open diamond).

The effective travelling wavelength is calculated from the slope of the fitted straight lines to the experimental data using the expression $\lambda_{\parallel} = 360(d\phi/dz)^{-1}$, where z is the axial distance and ϕ is the phase. Parallel wavelengths for $B = 25$ G and 50 G come out to be ~ 18 cm and 40 cm respectively. Corresponding parallel wavenumbers are $k_{\parallel} = 34$ m $^{-1}$ and $k_{\parallel} = 15.7$ m $^{-1}$ and parallel refractive indices (n_{\parallel}) are 123 and 55 respectively.

Investigating the experimental results further, we revisited the wave properties of helicon plasma. The relevant mode in helicon regime is the R-wave with $\omega \ll \omega_{ce}$ also known as the whistler wave. Bounded whistler waves are referred as helicon waves. The dispersion relation for R-wave in cold magnetized plasma can be rewritten as follows (Equation 2.61):

$$n^2 = \frac{c^2 k^2}{\omega^2} = 1 - \frac{\omega_{pe}^2}{\omega(\omega + i\nu - \omega_{ce} \cos\theta)} \quad (5.1)$$

Where n is the index of refraction, $k^2 = k_{\parallel}^2 + k_{\perp}^2$, $\cos\theta = k_{\parallel}/k$ with k , k_{\parallel} and k_{\perp} are respectively total, parallel and perpendicular wavenumbers. ω , ω_{pe} and ω_{ce} are respectively the wave, electron plasma and electron cyclotron frequencies, ν is the electron collision frequency and c is the velocity of light. In the frequency range, $\omega_{ci} \ll \omega \leq \omega_{ce} \ll \omega_{pe}$, the dispersion relation becomes

$$\frac{c^2 k^2}{\omega^2} = \frac{\omega_{pe}^2}{\omega(\omega_{ce} \cos\theta - \omega - i\nu)} \quad (5.2)$$

This equation has two solutions for k . Since in helicon antenna produced plasma parallel wavenumber k_{\parallel} is set by antenna so it may be wiser to consider rewriting the dispersion relation in terms of k_{\perp} following Shamrai and Taranov [12]

$$k_{\perp\pm}^2 = k_{\parallel}^2 \frac{1}{2\alpha^2 \beta^2} (1 - 2\alpha - 2\alpha^2 \beta^2 \pm \sqrt{1 - 4\alpha}) \quad (5.3)$$

Where,

$$\alpha = \frac{\omega_{pe}^2}{\omega_{ce}^2 n_{\parallel}^2}, \quad \beta = \frac{\omega \omega_{ce} n_{\parallel}^2}{\omega_{pe}^2}$$

The above equation shows that there are two values of k_{\perp} related to slow and fast wave. $k_{\perp+}$ corresponds to TG perpendicular wave number and $k_{\perp-}$ corresponds to helicon perpendicular wave number. It is seen from equation 5.3 that necessary condition of propagation of both the waves is $\alpha < 1/4$ i.e., $\omega_{pe}^2 < \omega_{max}^2 = (1/4)\omega_{ce}^2 n_{\parallel}^2$ considering collisionless wave propagation. In addition to this, the bracketed term in right hand side of Equation 5.3 should be positive for helicon wave to propagate. This happens when $\beta < 1$ or $\omega_{pe}^2 > \omega_{min}^2 = \omega \omega_{ce} n_{\parallel}^2$. Hence, helicon wave propagates radially outward from higher to lower density with $\beta \ll 1$ and $\alpha = 1/4$ are the lower and higher cut-off conditions for helicon respectively. For plasmas with a radial non-uniformity, helicon mode propagates in the interior of plasma where $\alpha < 1/4$ and

$\beta < 1$. It then stops propagating beyond $\beta \approx 1$. TG mode propagates in the outer plasma where $\alpha < 1/4$ and $\beta > 1$ and stops propagating in the interior where, $\alpha < 1/4$ and $\beta < 1$.

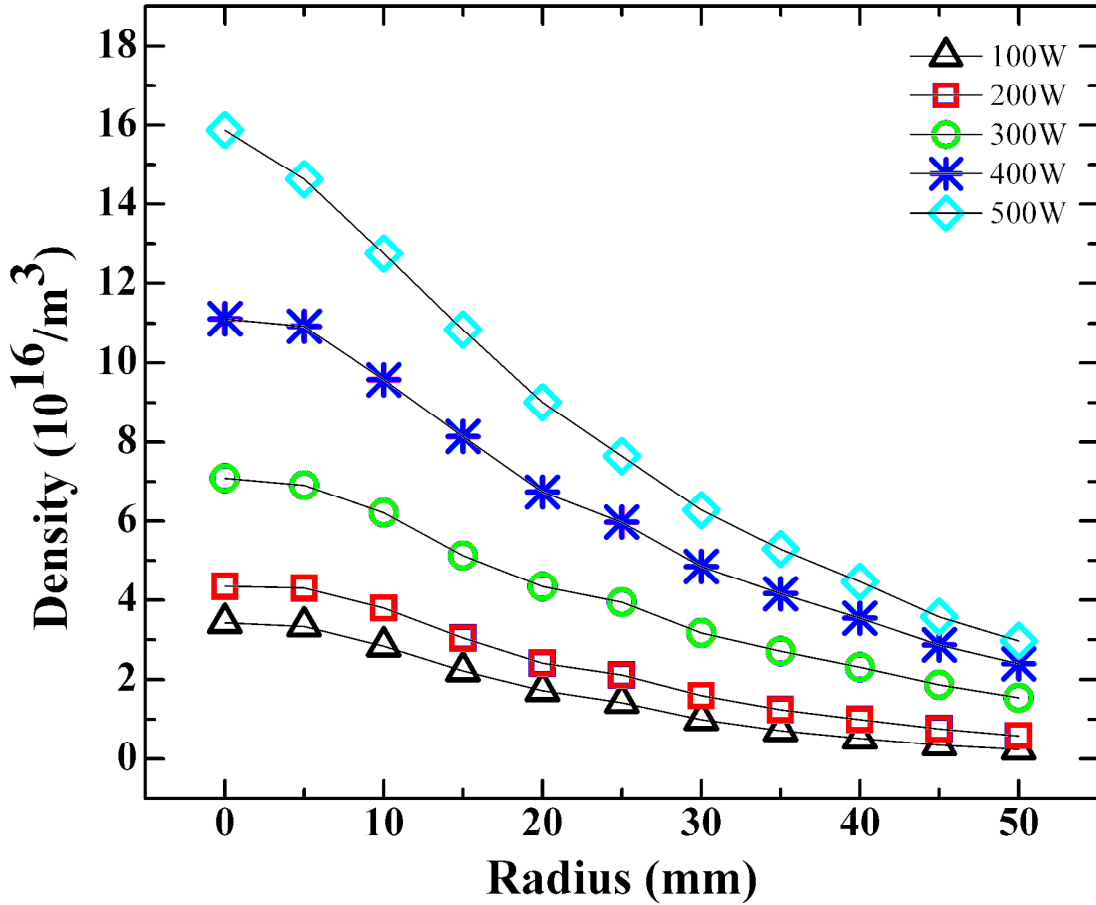


Figure 5.6 radial density profile for different powers measured at $z=20$ cm for 30 G magnetic field and 2×10^{-3} mbar

Helicon mode and TG mode are well separated at higher magnetic fields. There is a natural mode confluence at critical magnetic field corresponding to $\alpha = 1/4$ and $\beta \approx 1$ ($k_{\perp+} = k_{\perp-}$). In the present experiment, for $B = 25$ G and measured $n_{\parallel} = 123$, $\alpha = 1/4$ corresponds to a density $\sim 2.3 \times 10^{17} m^{-3}$ which is higher than the maximum density achieved in the system even for high pressure (2×10^{-3} mbar). For lower pressures, the experimental density at the critical magnetic

field is even lower. This means $\alpha=1/4$ natural mode confluence point (high density cut-off for helicon) does not exist in the system and hence TG-helicon coupling does not seem to explain the observed density peaks in our experiment. Further the measured radial density profiles at $z = 22$ for different RF powers and fill-in pressure of 8×10^{-4} mbar as shown in Figure 5.6 does not show any localized power absorption at the plasma boundary as observed in HELIC code simulations by Chen [11].

The experimental evidence of presence of radial modes illustrates the possibility of obliquely propagating helicon modes. Taking the mass of the electron $m_e = 0$, the boundary condition for helicon wave propagation gives the perpendicular wavenumbers for cylindrical plasma which can be obtained by the zeros of the Bessel component of wave magnetic fields. For the first and the second zeros of first order Bessel function (J_1), $k_{\perp 1}$ and $k_{\perp 2}$ are given by $3.83/a$ and $7.02/a$ respectively where a is the effective plasma radius. Taking $a = 5$ cm in our case, we get $k_{\perp 1} \sim 76$ m^{-1} and $k_{\perp 2} \sim 140$ m^{-1} . Similar values of k_{\perp} are reported in similar experimental setup and conditions by Lafleur et al [9, 17]. Once the k_{\parallel} and k_{\perp} are known, the angle of propagation can be found from the expression $\cos\theta = k_{\parallel}/k = k_{\parallel}/\sqrt{k_{\parallel}^2 + k_{\perp}^2}$. To understand the relation between the angle of propagation and critical magnetic field where density peaks let us look into the resonance cone behaviour of obliquely propagating helicon wave. For obliquely propagating R-wave, the cold plasma dispersion relation following Stix's notation can be written as

$$\tan^2\theta = -\frac{P(n^2-R)(n^2-L)}{S(n^2-RL)(n^2-P)} \quad (5.4)$$

Where n is the refractive index and coefficients P , R , L and S are given in reference 18.

At resonance, ($n^2 \rightarrow \infty$), this requires,

$$\tan^2\theta_{res} = -\frac{P}{S} \quad (5.5)$$

This equation defines the resonant angle θ_{res} for given plasma parameters. It means the wave ceases to propagate when its wave vector coincides with θ_{res} . However, it propagates within a cone (called resonance cone) $0 < \theta < \theta_{res}$ as discussed in Chapter 2 (section 2.3). In the limit, $\omega_{ci} \ll \omega < \omega_{ce} < \omega_{pe}$,

$$\tan^2 \theta_{res} = \frac{\omega_{ce}^2}{\omega^2} - 1 \quad \text{and therefore } \cos \theta_{res} = \frac{\omega}{\omega_{ce}} \quad (5.6)$$

The resonance cone angle from the above equation comes out to be $\theta_{res} = 78.9^\circ$ and 84.5° taking the experimental values of magnetic field values of $B = 25$ G and 50 G respectively at which the density peaks. Calculated wave propagation angle values of $\theta = 76.2^\circ$ from measured wavenumbers, k_{\parallel} and k_{\perp} , considering measured 1st axial mode ($k_{\parallel 1} = 34 \text{ m}^{-1}$) and estimated 2nd radial mode ($k_{\perp 2} = 140 \text{ m}^{-1}$) and $\theta = 83.6^\circ$ considering measured 2nd axial mode ($k_{\parallel 2} = 17.5 \text{ m}^{-1}$) and estimated 2nd radial mode $k_{\perp 2} = 140 \text{ m}^{-1}$, using the relation $\cos \theta = k_{\parallel} / k = k_{\parallel} / \sqrt{k_{\parallel}^2 + k_{\perp}^2}$ match quite well with the values estimated from Equation 5.6. This analogy clearly indicates that when the helicon wave propagates near resonance cone angle, the density peaks in our system.

Strong absorption of helicon wave correlated with the excitation of convective electrostatic fluctuations with frequency > 100 kHz for magnetic fields > 100 G are reported in many experiments [18-22]. In search of a possible secondary wave generation near $B = 25$ and 50 G, we measured the floating potential fluctuations using a double probe and observed a very systematic variation of floating potential fluctuations, whose spectra have a broad maximum around 10 to 20 kHz near these magnetic fields. Analytical works by Arnush et al [23], Boswell [24] and Boswell et al [25] suggested that for oblique wave propagation near resonance cone the wave can have large spatial gradients of electric field which can trap and amplify a non-convective ion acoustic wave in the low frequency range. Figure 5.7 shows the variation of floating potential fluctuation amplitude with applied magnetic field for three different powers at pressure $p = 0.8 \times 10^{-3} \text{ mbar}$. It is very clear from the figure that the fluctuation increases significantly at those magnetic fields where the density peaks are observed.

Therefore, oblique helicon wave propagation along the resonance cone boundary in this experiment seems to be generating a non-convective electrostatic wave, which is transferring the energy to the plasma from helicon waves creating density peaks at specific magnetic fields and hence describes the dependence of density peaking at those specific magnetic fields.

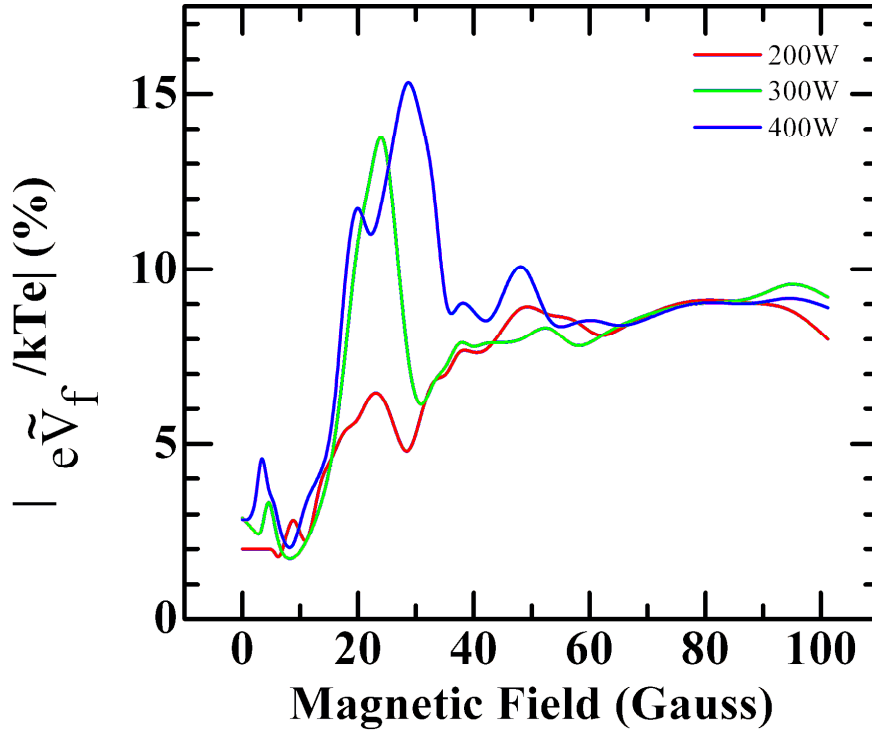


Figure 5.7 Floating potential fluctuation amplitude variation with magnetic field measured for RF powers of 200 W, 300 W and 400 W with argon fill in pressure of 0.8×10^{-3} mbar.

Further, the observed dependency of density peak occurrences at specific magnetic fields on source frequency with similar conditions of RF power, neutral pressure, source tube radius and antenna in reference 7 (Figure 6) can easily be explained using our model as keeping the RF power, neutral pressure, source tube radius and antenna same, the ratio of k_{\parallel}/k remains constant, and to satisfy the resonance cone propagation condition expressed in Equation 5.6, the density peak should occur at higher magnetic fields for a higher source frequency.

5.3 Polarization reversal and asymmetric density peaking

Lot of studies has been carried out to understand the density peak at low B away from ECR point in helicon plasmas. One of the interesting observations of last section (Figure 5.2 and Figure 5.3) is that the capacitance values have large dips around 5 Gauss but the density plots do not show peaks ~ 5 Gauss. As mentioned earlier, the C_L values are measure of plasma resistance and show the macroscopic behavior of the plasma. The source frequency of 13.56 MHz corresponds to the electron cyclotron resonance (ECR) for magnetic field ~ 5 Gauss. The observation of non-absorption of ECR wave is anti-intuitive. One of the possible reasons may be polarization reversal. The electromagnetic wave propagating along the direction of magnetic field is a right hand polarized wave (RHPW) and that propagating in a direction opposite to magnetic field is left hand polarized wave (LHPW). The polarization of the launched mode is maintained only at the axis and the boundary condition ($E_\theta = 0$) for a bounded wave needs the wave to have a linear polarization. This process is shown theoretically and experimentally for microwave frequencies for electron cyclotron waves that an LHPW can have its polarization reversed to an RHPW or vice versa in bounded plasmas.

However, not much literature is available for the process of polarization reversal in range of radio frequencies. As it is a well-known fact that the right polarized wave should be absorbed near the ECR point, however, the small or nonexistent density peak near ECR point observed in the previous helicon experiments warrants detailed studies. Lafleur et al [9] reported that the peaking phenomenon is magnetic field direction independent. Parametric studies are carried out by changing both the magnetic field magnitude and direction at different powers and pressures. The magnetic field direction along the positive z-axis is referred to as “normal B direction” and “ $m = \pm 1$ sides” is referred to the sides towards which the conventional $m = \pm 1$ helicon modes propagate (Figure 5.8).

The plasma density is measured by a movable double Langmuir probe (DP) and an RF compensated Langmuir probe, which is also used for temperature measurement. Two collimated optical probes (lens-fiber combination) are used to collect the visible light from the same locations that of the Langmuir probes and transmitted to photodiodes through optical fibers and subsequently converted to voltage signals by current to voltage converters. A Pearson make

Rogowski coil (sensitivity = 0.1V/Amp up to 50 MHz) is used to measure the RF current in the antenna near the reference leg of the transmission line. The reflected power P_R is always less than 1% (0-2 W for all experiments) of the forward power P_F .

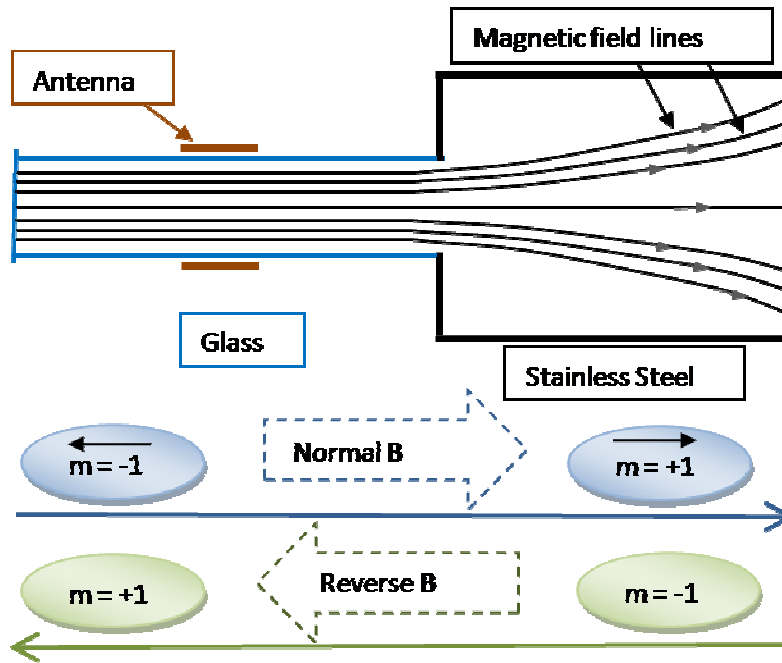


Figure 5.8 $m=|l|$ propagation direction for normal and reverse field directions shown schematically.

Experiments are done by keeping the magnetic field direction along the positive z-axis (normal B direction), i.e., towards the diffusion chamber. Since the antenna is a right helical antenna, the conventional $m = +1$ mode propagates towards the diffusion chamber in this case. Figure 5.9 shows the variation of plasma density and light emission with magnetic field at $z = \pm 18 \text{ cm}$ in the plasma produced with fill in pressure of $\sim 1.4 \times 10^{-3} \text{ mbar}$ and RF power of 500 W. A significant electron density peak has been observed in the diffusion side i.e., in the “ $m = +1$ side”, at an applied magnetic field value of $\sim 30 \text{ G}$ (Figure 5.9 (a)). On the “ $m = -1$ side” i.e.,

towards the source end plate side, density peaks are distinctively different compared to the “m = +1 side” both in terms of magnitude and required magnetic fields as shown in Figure 5.9 (b).

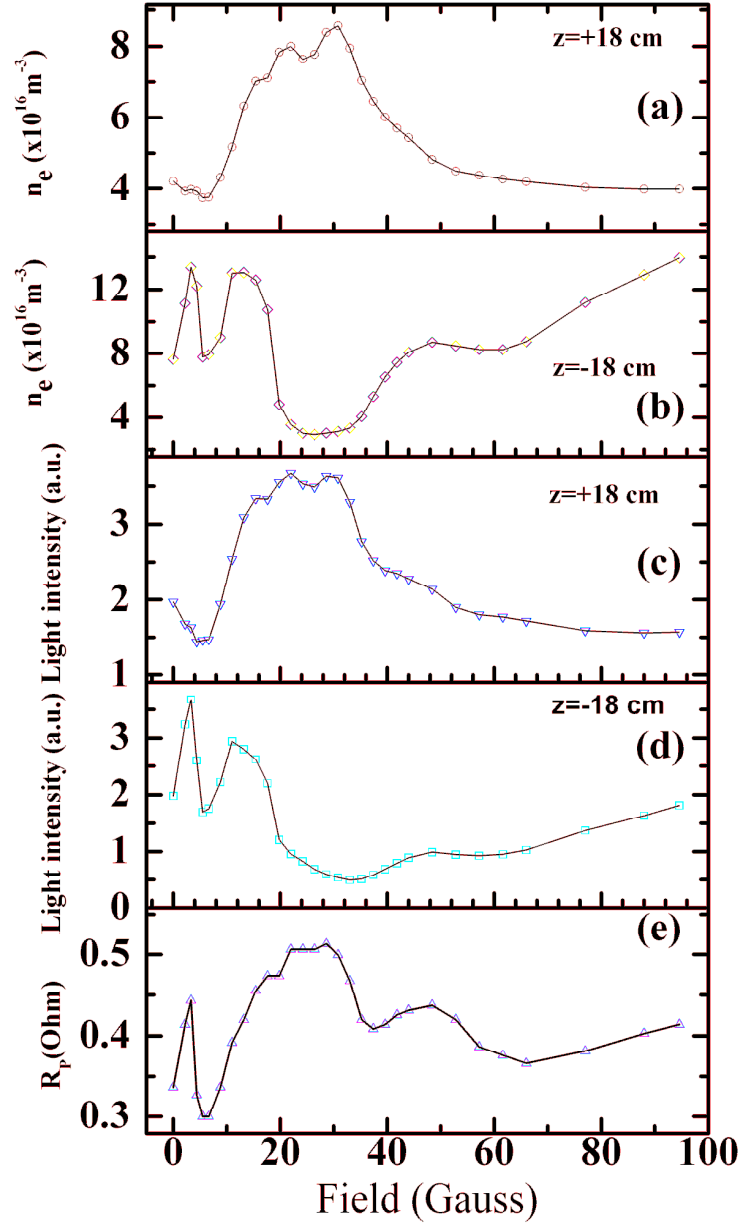


Figure 5.9 Variation of electron density (n_e), visible light intensity (I_{vis}) and antenna plasma resistance (R_p) with magnetic field for 500 W at pressure $1.4 \times 10^{-3} \text{ mbar}$. (a) n_e at +18 cm, (b) n_e at -18 cm, (c) I_{vis} at +18 cm, (d) I_{vis} at -18 cm and (e) R_p

In contrast to the “ $m = +1$ side” a very prominent density peak has been observed at 5 G which corresponds to the electron cyclotron peak. Another peak in density has been observed around 12 G and a tiny hump in density around 50 G. In this “ $m = -1$ side”, not only the density peak around 30 G is absent, a decrease in density has been observed at this magnetic field. Further, the magnitude of density peak on “ $m = -1$ side” around 12 G is almost 1.5 times higher than the density peak observed at ~ 30 G in the “ $m = +1$ side”. The density data on either side is further substantiated by recording the collimated total light emission from $z = \pm 18\text{cm}$ as shown in Figure 5.9(c) and 5.9(d). The light intensity variations closely follow the ion saturation current variations on the respective sides for all RF powers and this non-intrusive method removes any doubt regarding contamination of results due to the disturbances created by the Langmuir probes.

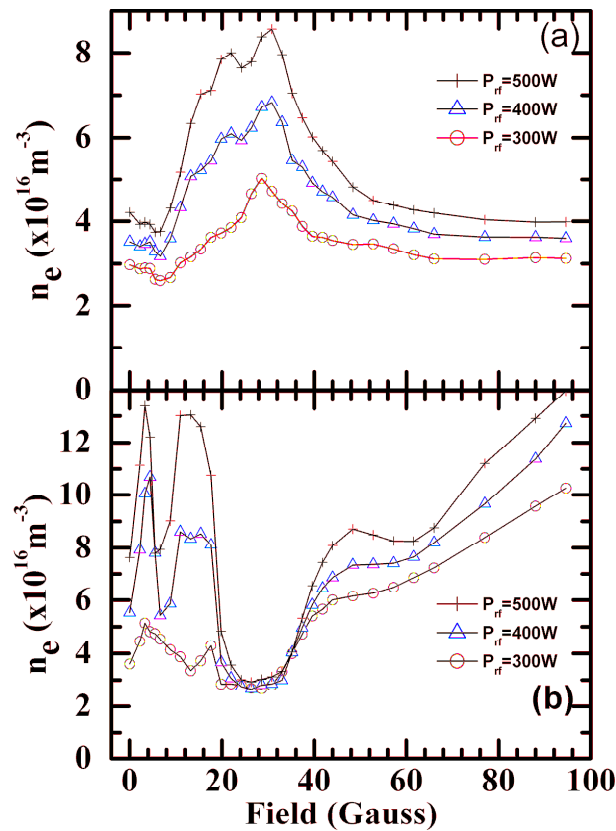


Figure 5.10 Variation of electron density (n_e) with magnetic field for 300, 400 and 500 W at pressure 1.4×10^{-3} mbar. (a) n_e at $+18 \text{ cm}$ and (b) n_e at -18 cm .

The characteristics behavior of density in the “ $m = +1$ side” with the magnetic field direction towards the same side, shows features similar to those described in Section 5.2. The variation of

antenna plasma resistance, R_p with the applied magnetic field is shown in Figure 5.9 (e). The measurement clearly shows that the variation of R_p does not follow the plasma density or total light emission measured at either side of the antenna. However, the sum of variations of plasma density or total light emission from both sides of the antenna matches quite well with R_p . This is quite expected, as R_p is the macroscopic response of the plasma produced on both sides of the antenna. So, the discrepancy observed in last section about the C_L dips and no-occurrence of 5 G ECR peak on $m = +1$ side is understood now.

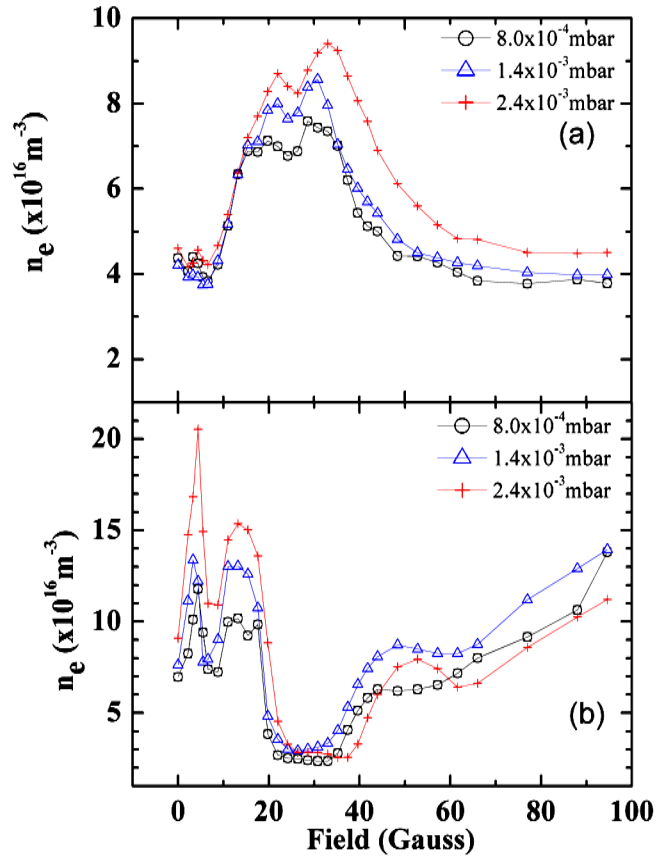


Figure 5.11 Variation of electron density (n_e) with magnetic field for 500 W at pressures 8×10^{-4} , 1.4×10^{-3} and 2.4×10^{-3} mbar. (a) n_e at +18 cm, (b) n_e at -18 cm.

In order to establish the results further, the experiments are repeated for three different values of fill in pressures as well as for three different values of input powers. The density and total light

emissions variations with magnetic field for different powers and pressures are plotted in Figure 5.10 and Figure 5.11 respectively.

The magnitude of density peaks at 12 G and 50 G in the $m = -1$ side for normal B operation increases with increasing power (Figure 5.10) while little variations of other peaks are observed. Increasing the fill in pressure further from $1.4 \times 10^{-3} \text{ mbar}$ and keeping the input power constant at 500 W the density peak at $\sim 5 \text{ G}$ dominates over peak at 12 G in magnitude in the “ $m = -1$ side” for normal B operation.

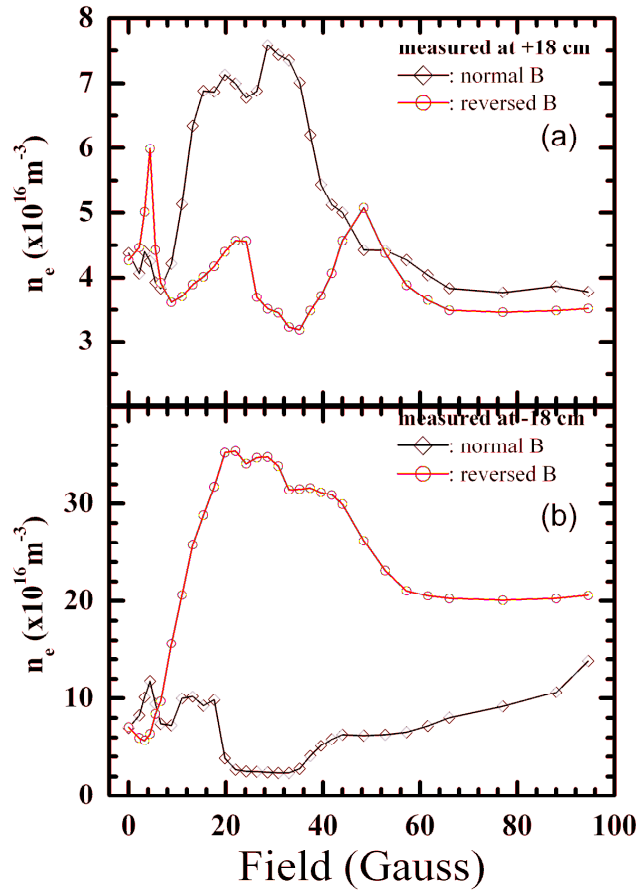


Figure 5.12 Variation of electron density (n_e) with magnetic field for 500 W at pressure $1.4 \times 10^{-3} \text{ mbar}$. (a) “normal B” and (b) “reverse B”. n_e at +18 cm, (b) n_e at -18 cm. Inset of (a) at +18 cm “normal B” (open triangle) and “reverse B” (+).

Reversing the magnetic field direction symmetrically reverses all the density peak observations. The plasma density measured on both sides of the antenna is plotted in Figure 5.12. The figure

clearly shows that the density peak at ~ 30 G is now observed on the other side of the antenna (towards the end plate) as the conventional “ $m = +1$ ” mode now lies in this direction after changing the magnetic field direction. Similarly the prominent density peak at ~ 5 G is observed at positive z direction (towards diffusion chamber) as the “ $m = -1$ ” mode now lies on this side.

By changing the magnetic field direction we notice that the density signal by the probe positioned at $+18$ cm for normal B is very similar to density signal by the probe positioned at -18 cm for reverse B. This clearly indicates density peaking is a mode activity. To establish this fact, the radial profile of axial component of wave magnetic field is measured at 12 G and 30 G magnetic fields for both normal and reverse magnetic field directions at $z = +18$ cm. The profiles are shown in Figure 5.13.

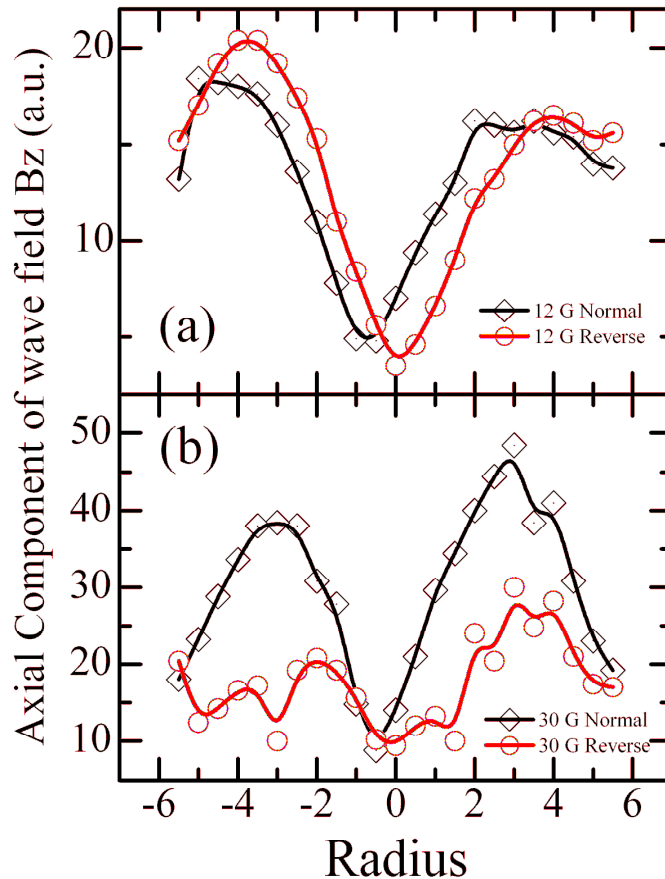


Figure 5.13 Radial variations of axial wave field component of helicon waves measured at $z = +18$ cm for both directions of magnetic field at (a) 12 G, “normal B” (open diamond) and “reverse B” (open circle) (b) 30 G, “normal B” (open diamond) and “reverse B” (open circle).) RF power is 500 W and pressure 1.4×10^{-3} mbar.

It is very clear from the figure that in both configuration of magnetic fields, the helicon wave exists in our system and have the characteristics of $|m| = 1$. Further, the observations of wave fields for both configurations of magnetic field measured at one side of the antenna ascertain the existence of the wave fields on both sides of antenna in case of the magnetic field being applied in any one direction. The simultaneous measurement of wave field on both sides of the antenna is not possible due to the availability of radial port only on one side of the antenna.

Measurements of plasma density on both sides of the antenna by varying the applied magnetic field in the low magnetic field regime have revealed two important observations, which to best of our knowledge are never reported before. First the observation of a strong density peak near ECR point on “m = -1 side”, which should be more pronounced conventionally on “m = +1” side where it is almost nonexistent. Second, the observance of many density peaks other than at ECR point on both side of antenna occurring at different applied magnetic fields. On “m = +1 side” a peak is visible at 30 G whereas on “m = -1 side” an additional peak is visible at 12 G but the 30 G peak is absent.

Multiple density peaks observed in the m = +1 side for both the normal and reversed magnetic field directions can be understood through oblique cyclotron resonance of helicon waves when propagating in the resonance cone boundary. In the present experiment, $k_{\parallel} \approx 34 \text{ m}^{-1}$ has been estimated from the slope of axial variation of phase of B_z , shown in Figure 5.5 obtained using magnetic probes and the plasma radius of 5 cm sets the 1st perpendicular wave number $k_{\perp 1} \sim 76 \text{ m}^{-1}$ and second perpendicular wave number $k_{\perp 2} \sim 140 \text{ m}^{-1}$. This corresponds to $\cos\theta = 1/2.2$ with $k_{\perp 1}$ and $\cos\theta = 1/4.2$ with $k_{\perp 2}$. Hence the first resonance should occur approximately at B ~ 11 G and second resonance at B ~ 22 G. These values of magnetic field are quite close to the ones for which the density peaks are observed on m = +1 side for both the normal and reversed magnetic field directions. This analysis suggests that resonating obliquely propagating helicon waves are responsible for the observed density peaks on m = +1 side for both the normal and reversed magnetic field directions. The detailed mechanism of observed density peaks due to the oblique propagation of helicon waves along the resonance cone boundary can be explained as in Section 5.2.

As the wave absorption profile is affected by the wave polarization profile, the observed density peaks in the $m = -1$ side cannot be directly described by the resonance phenomena because it is a very well known that the right handedly polarized wave (RHPW) can only be absorbed via resonating with electrons while a left handedly polarized wave (LHPW) is not related to ECR []. However, the wave absorption is quite possible on the $m = -1$ side, if the polarization reversal occurs for the LHPW into RHPW. It has been observed both theoretically [26] and experimentally [27-28] that in bounded plasma, polarization of a RHPW or LHPW is strictly maintained at the axis, but polarization can be reversed at some or many radial locations, where LHPW becomes RHPW and RHPW becomes LHPW. In bounded plasma with cylindrical boundary, the electromagnetic wave has radius dependent perpendicular electric field components $E_r(r)$, $E_z(r)$, and $E_\theta(r)$, which decide the wave polarization. The polarization index S can be expressed [26] in terms of the perpendicular wave electric components as

$$S = \frac{|E_r + iE_\theta|}{|E_r - iE_\theta|} \quad (5.7)$$

For $0 < S < 1$ the wave is right polarized and for $1 < S < \infty$ the wave is left polarized. $S = 0$, $S = 1$ and $S = \infty$ correspond to right circular, linear and left circular polarization. Depending on the plasma parameters and their radial variation the polarization can change from LHPW to RHPW or *vice versa*. The weak density peak near ECR point on the “ $m = +1$ ” side may be due to conversion of RHPW into LHPW. The reason for much higher densities observed for the reversed $m = -1$ mode compared with the reversed $m = +1$ mode as shown in Figure 5.12 is not fully understood and is under investigation. The density mismatch on either side may be related to polarization reversal radius where an RHPW is polarization-reversed to LHPW or vice versa.

5.4 Downstream Density Peak

Another type of density peak has also been observed by Chen et al [29] and Tysk et al [30]. While measuring axial density along the axis they reported/observed a downstream density peak far away from the antenna for a uniform magnetic field. This phenomenon has been explained as a consequence of decay in electron temperature away from the source [31]. They explained at this location “the ionization rate is low and the diffusion rate is large, so that

production and loss mechanisms would not be expected to produce a peak”. However, performing an energy balance, they were able to show a density rise due to temperature decay. Additionally, since nearly all power is absorbed in the near field antenna region of the helicon discharge the density peak was not due to any significant wave absorption downstream [31]. Another group to have observed this effect is Tysk et al [30] but little is mentioned regarding the observation. In both the observation the magnetic field at the location of density peak is almost same as that near the antenna.

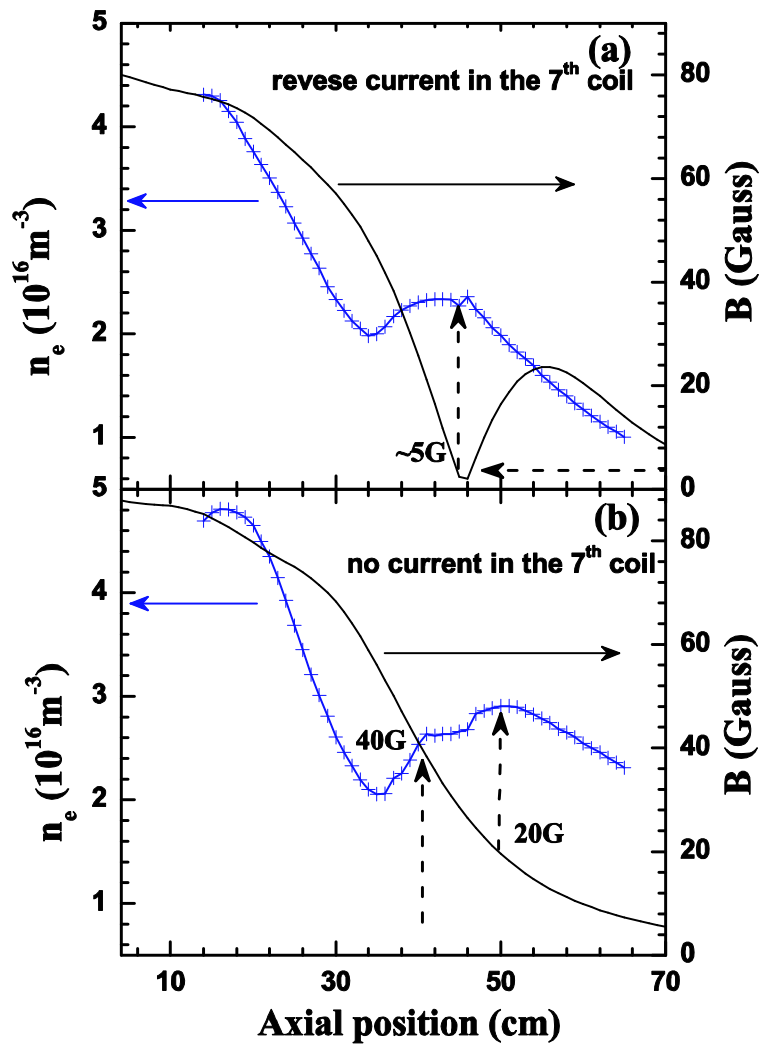


Figure 5.14: Axial variation of density and magnetic field, $p=4 \times 10^{-4}$ mbar, power=400W, (a) Reverse current in 7th coil & (b) no current in 7th coil.

In the present experiment, density measurement shows usual density peak when magnetic field is varied. In addition, for constant but axially non-uniform magnetic field axial density scan shows density peak at a particular axial location away from the antenna in the expansion chamber. Axial components of wave magnetic field reveals that for 88 G source magnetic field no helicon wave propagation in the source region whereas in the downstream where magnetic field is less than 40 G or so wave propagates giving rise to a density peak in the downstream.

The magnetic field in the source region is kept at around 88 G and it starts falling from $z \sim 15$ cm to the end of the expansion chamber where magnetic field is ~ 7 G. Density is measured axially. In the downstream when the magnetic field is decreasing an axial peak in density is observed. A typical trace is shown in figure 5.x.b for pressure $p = 4 \times 10^{-4}$ mbar and at RF power of 400 W for a source magnetic field around 88 G. Magnetic field is decreasing away from the source. As density was scanned axially density decreases from source region as expected. However, further down axially it is noticed that density again increases before it finally goes down. Position of this density peak corresponds to a position where magnetic field is approximately 20 G at $z = 50$ cm. Chen [31] explained this downstream density peak phenomenon by particle and power balance in the downstream region. However in the present case, the magnetic field is decreasing downstream. This kind of density behavior indicates local deposition of power around $z = 50$ cm. This is more apparent when the magnetic field gradient is made sharper by passing same amount of opposite current in 7th coil. This brings the ECR location (5G) inside the expansion chamber. Fig 5.14 shows the density and magnetic field traces for two different magnetic field gradients. Fig 5.14 (b) shows the traces when there is no current in the 7th coil, i.e., ECR location (5G is almost at the end of the expansion chamber. Density trace shows a peak at $z = 50$ cm where magnetic field is around 20 G. Later, same amount of current is passed in 7th coil but in the opposite direction. This is shown in Fig 5.14 (a). Density traces shows a peak at $z = 44$ cm where magnetic field is around 5 G. Cyclotron frequency corresponding to 5 G is 14 MHz and applied rf frequency is 13.56 MHz. Hence, the local density peak is attributed to cyclotron resonance.

To understand this downstream peak further, wave propagation of helicon wave was studied experimentally. RF power and pressure were kept constant at 400 W and 4×10^{-4} mbar respectively while the magnetic field (with six coils) at the source was maintained around 88 G. The phase of B_z was measured using a fixed reference probe positioned near the antenna edge at

20 cm downstream from the antenna centre and oriented to measure B_z . The radial position of the scanning probe was placed in the centre at the same axial location as the reference probe to begin with. It was then moved axially by 1 or 2 cm toward expansion chamber. Signals from the scanning probe were plotted with respect to fixed probe for phase shift measurement. Measured time difference between the fixed probe and scanning probe was translated to the phase variation with distance. This is plotted in figure 5.15. Straight line fitting of the curves gives us effective travelling wavelength calculated from the slope using the expression $\lambda = 360(d\phi/dz)^{-1}$, where z is the axial distance and ϕ is the phase. From Figure 5.15 it is seen that phase is nearly constant up to $z \sim 42$ cm showing no propagating wave. Beyond $z = 42$ cm phase is changing. Corresponding wavelength and parallel wave number (k_{\parallel}) become ~ 35 cm and 17.94 m^{-1} respectively.

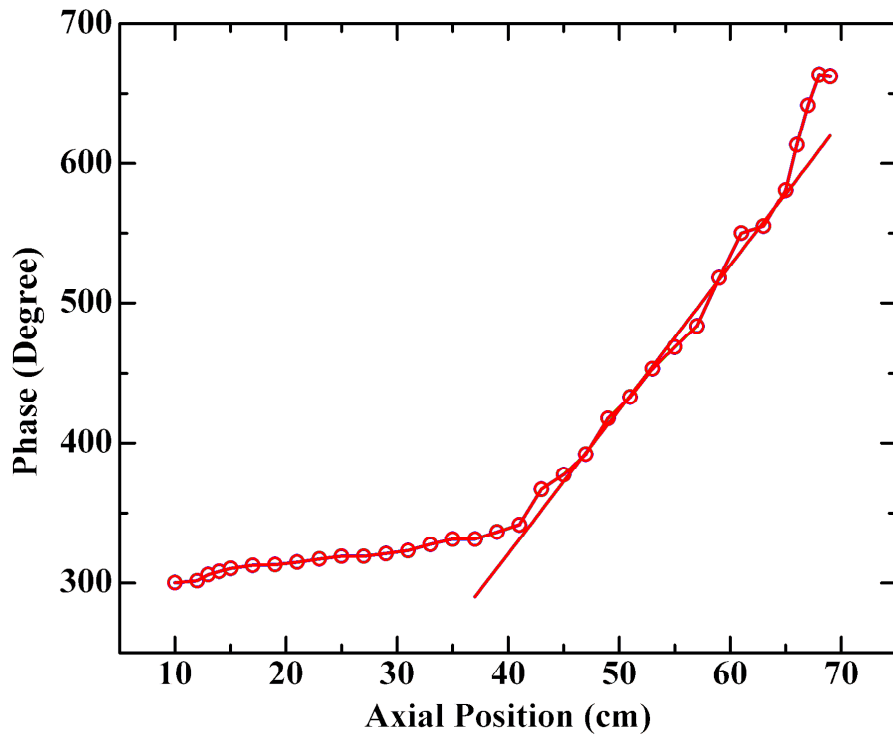


Figure 5.15 Variation of helicon B_z phase along axis for 88 G source magnetic field, 300W RF power and 8×10^{-4} mbar neutral pressure.

This means wave is propagating with parallel wave number of 17.94 m^{-1} . Density rise from this points till $z = 50$ cm is because of resonance of helicon wave propagation at an oblique angle. This has been explained earlier in Section 5.2. Measured parallel wave number (k_{\parallel}) is 17.4 m^{-1} . The

perpendicular wave number (k_{\perp}) for cylindrical plasma, was calculated from the zero of the Bessel functions. For the second zero root of 1st order Bessel function (J_1), k_{\perp} is given by $7.02/a$ where a is effective plasma radius in the diffusion chamber. Taking $a = 10.5$ cm we get $k_{\perp} = 66.8 \text{ m}^{-1}$. Hence, $\cos\theta = k_{\parallel}/k = 0.26$. So, from the resonance condition, $\omega - \omega_{ce}\cos\theta = 0$, we find $B \sim 18.5$ Gauss which is close to the experimentally observed magnetic field ($B=20$ Gauss) near the density peak. Hence, local deposition of power by obliquely propagating helicon wave is producing the axial density peak.

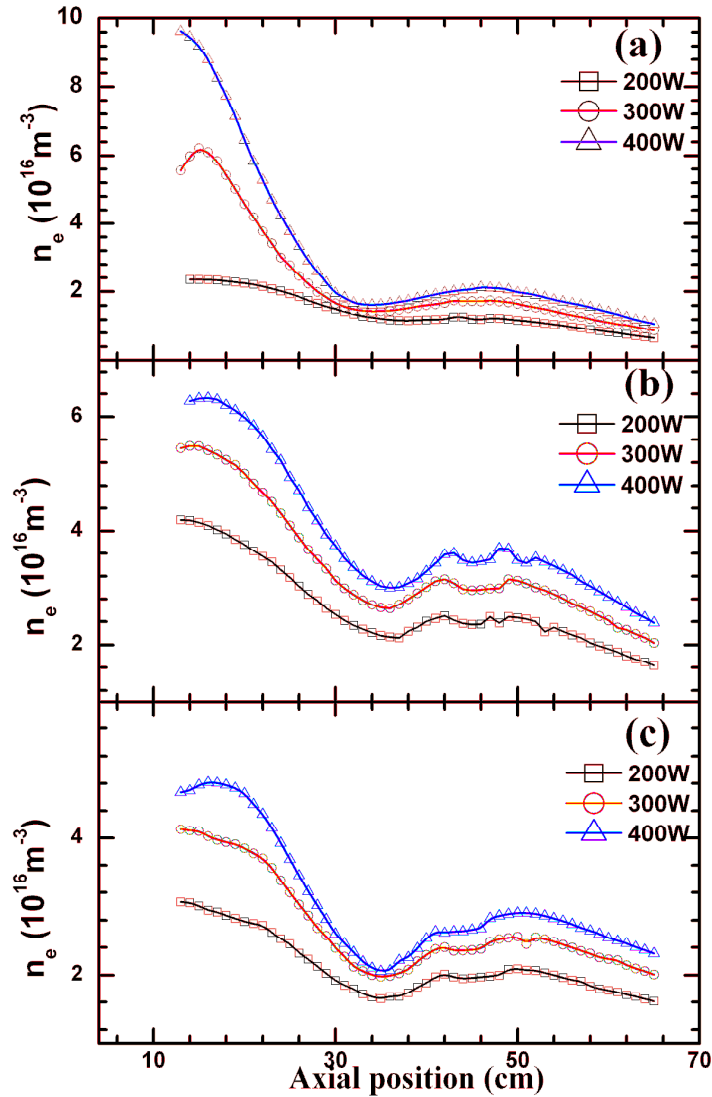


Figure 5.16 Axial variation of density for 200W, 300W and 400W at there argon neutral pressures of (a) 2×10^{-3} mbar, (b) 8×10^{-4} mbar & (c) 4×10^{-4} mbar. Magnetic field at antenna centre is 88 G.

Parametric studies were carried out at different pressures for different powers. Axial density is measured at different pressures and powers and plotted in figure 5.16. Magnetic field is also plotted in the same figure. For, high pressure, $p=4 \times 10^{-3}$ mbar density peak is at $z=46$ cm where B is around 25G. Keeping pressure same peak decreases with power. As lower pressures, $p = 8 \times 10^{-4}$ mbar or $p = 4 \times 10^{-4}$ mbar, there are two humps in density trace, one is at $B=20$ G and other being at $B=40$ G. The higher magnetic field hump may be because of higher k_{\perp} (lower wavelength).

5.5 Efficient Low Field Helicon Source

Helicon waves propagating near the electron cyclotron resonance cone angle boundary can excite electrostatic fluctuations which subsequently can dump energy in the plasma. This process is described in Section 5.2 and is shown to be responsible for peaking in density as well as antenna plasma coupling in low field helicon discharges, where the helicon wave propagates at a resonance cone angle with respect to the applied magnetic field. Though much of the experiments to study the low field helicon discharges have used a uniform magnetic field, recently Lafleur et al [9] using a diverging magnetic field near the antenna have obtained a ten fold increase in density from the density at no magnetic field. Also reported in this work is that using another coil (described as exhaust coil in their report), the density did not rise as much compared to the single coil. The source coil current was varied by keeping the current in the exhaust coil constant at one of the values between 0-5 A in 1 A steps. As for 1 A current in the exhaust coil current, the density value must have decreased as with the case with only source coil. Now, on top of this any current in the source coil will increase the magnetic field near the antenna and the densities will follow the only source coil case after 1 A if the coils are taken as identical as is the case.

When we have a magnetic field which is uniform near the antenna, as per section 5.2 the oblique cyclotron resonance for a single mode will happen at a particular magnetic field. But in case of a diverging magnetic field near the antenna, all the radial and axial modes in the system will have resonance due to the availability of different magnetic fields. So it seems that magnetic field profile near the antenna dictates the density peaking phenomena. To see the effect of magnetic field gradient near the antenna we have used 4 different magnetic field configurations with

completely uniform magnetic field near the antenna to the most diverging field one can obtain with a single coil.

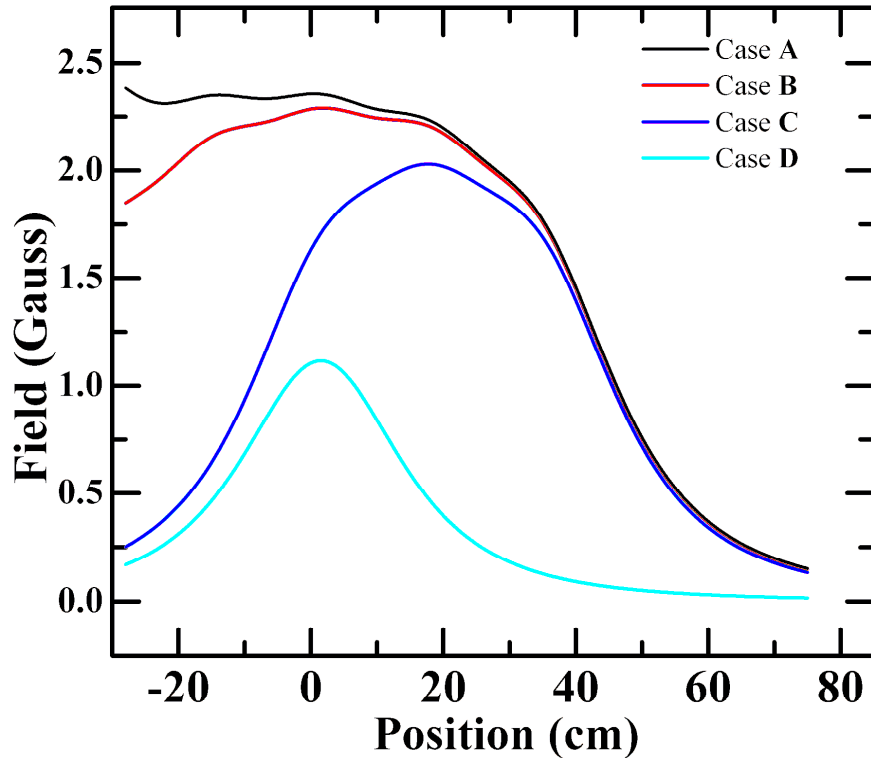


Figure 5.17 Axial variation of magnetic field for Cases A-D when 1 A current is passed in the coil(s).

Figure 5.17 shows axial variation of magnetic field when 1A current is passed for four different magnetic field topologies used. The left most coil as shown in the experimental set up (Figure 3.2) is the first coil and the right most coil is the seventh coil. Case A corresponds to a magnetic field profile when 1 A current is passed through 6 coils as is the case described in Section 5.3 and 5.4. Case B magnetic field is produced by taking out the first coil and keeping the other 5. Case C magnetic field is obtained by removing the first and second coils from left and keeping only 4 coils. Case D magnetic field corresponds to 1 A current in fourth coil by removing the first, second, third, fifth and sixth coils.

Double Langmuir probe is placed at $z = \pm 18 \text{ cm}$ from the antenna axial centre to measure the ion saturation current. Both the probes have probe tips of 0.5 mm diameter tungsten wires and are of length 3 mm. Electron temperature is measured by a RF compensated probe +18 cm away from the antenna centre. A rogowski coil is used to measure the RF current in the antenna near the reference leg of the antenna from which the power transfer efficiency, $\eta = R_P / (R_P + R_A)$ is calculated.

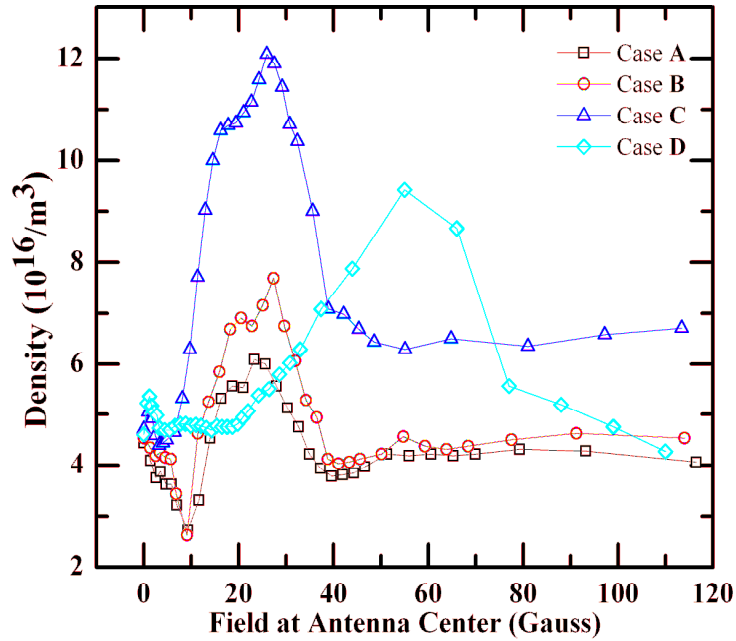


Figure 5.18 variation of density at $z = +18 \text{ cm}$ with applied magnetic field at antenna centre for Cases A-D. RF power is 300W and pressure $8 \times 10^{-4} \text{ mbar}$.

Figure 5.18 shows the variation of density measured at $z = +18 \text{ cm}$ for all the cases outlined above. As for density peaks studied so far, here also for $m=+1$ side the ECR peak is very small or non-existent. Density peaked around 30 G for Case A, B and C. For the most non-uniform case D, the density peaked $\sim 50 \text{ G}$. As the coils are removed or field non-uniformity is increased from Case A-case C, density at $\sim 30 \text{ G}$ increased but for Case D the density decreases as compared to Case C. As the probe is kept at $z = +18 \text{ cm}$, for case D the magnetic field decreases rapidly and the measured density becomes less in the diverging field region. Also on the $m=+1$ side, the volume of the plasma is more than $m=-1$ side, so the particle loss on $m=+1$ side will be more.

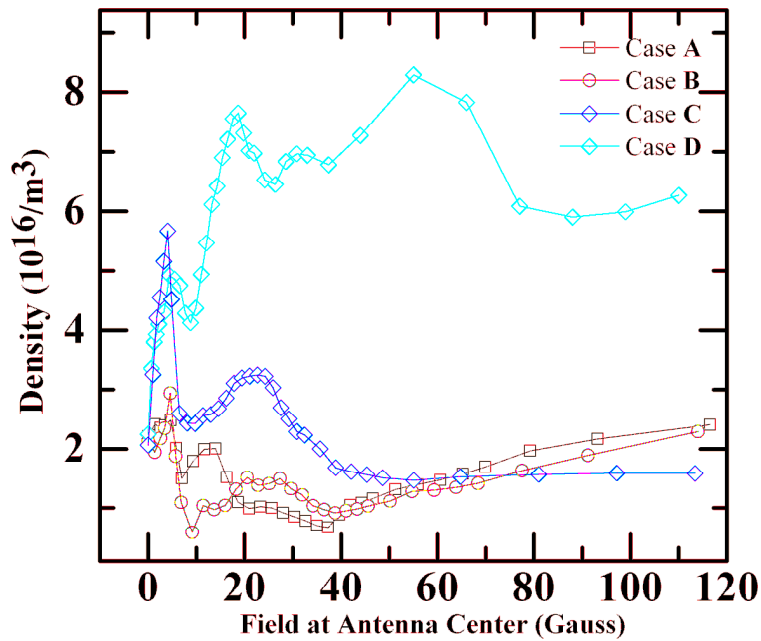


Figure 5.19 variation of density at $z = -18$ cm with applied magnetic field at antenna centre for Cases A-D. RF power is 300W and pressure 8×10^{-4} mbar.

Density variations on $m = -1$ side are shown in Figure 5.19 for the different magnetic field cases A-D. The ECR peak around 5 G is well visible this side as it is described in Section 5.2. The 12 G peak which is described in Section 5.2 is present for Case A. For case B-D, there is another peak in between 20-25 G. For case D, the density at each magnetic field increases and there is a peak around 50 G.

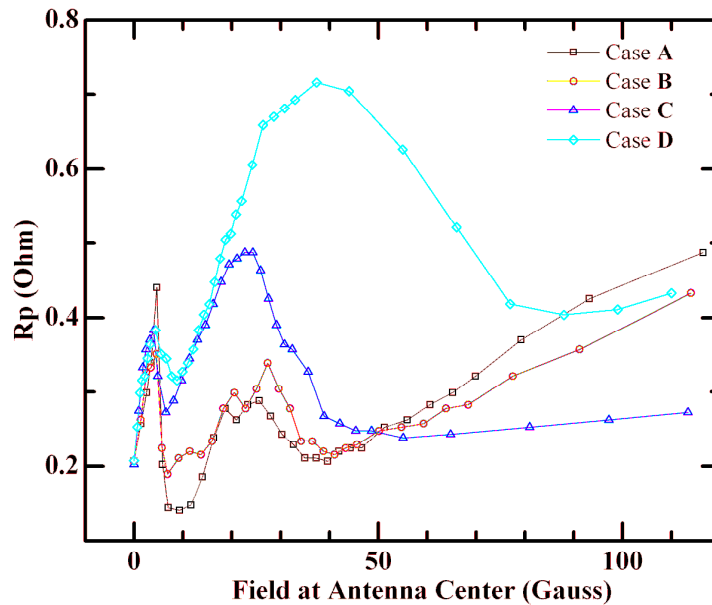


Figure 5.20 Variation of density at $z = -18$ cm with applied magnetic field at antenna centre for Cases A-D. RF power is 300W and pressure 8×10^{-4} mbar

The calculated plasma resistance is shown in figure 5.20 for all the four cases. For every case the plasma resistance has a peak ~ 5 G corresponding to the electron cyclotron resonance absorption. For nearly uniform magnetic field cases (Case A, B and C), the plasma resistance peaked ~ 30 G. For the single coil case D, the plasma resistance is highest and occurs ~ 50 G. As it was discussed in Section 5.2, the plasma resistance explains the behavior on both sides of the antenna. This behavior of density rise on both sides of antenna is different from Lafleur et al [9] as in their case the plasma boundary on the $m = -1$ side is just 5 cm from the antenna and they have measured the density in the centre of the antenna.

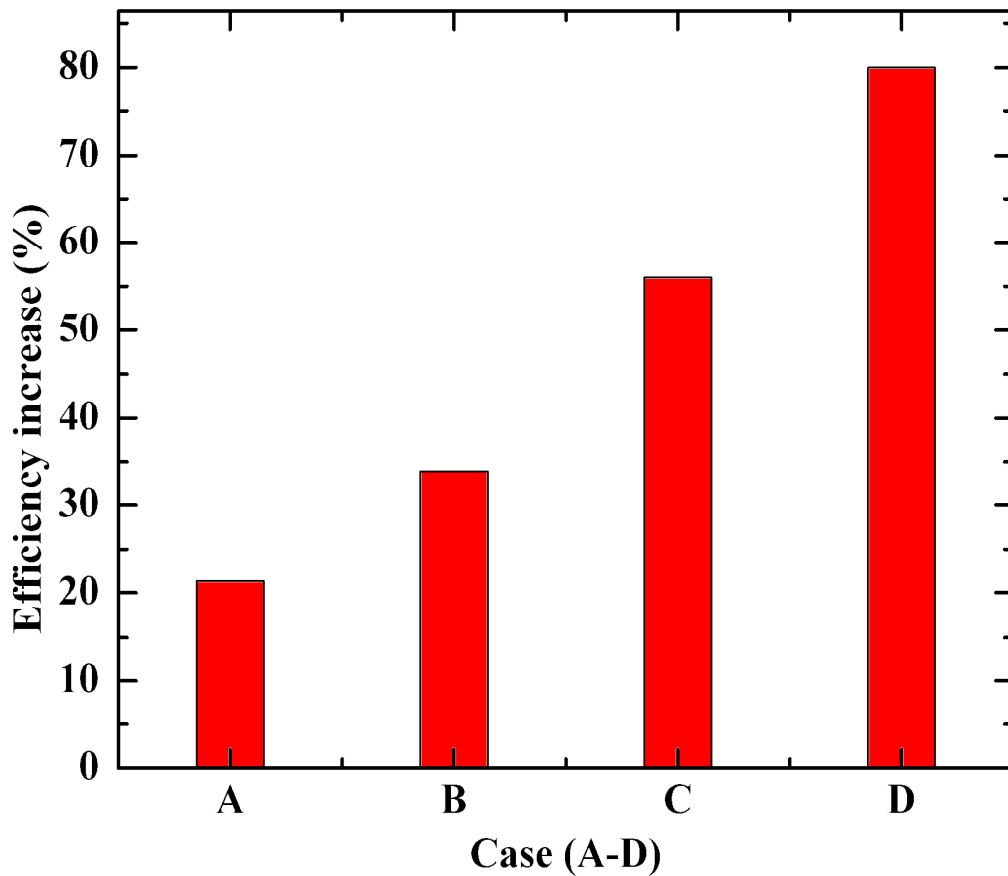


Figure 5.21 Increase in efficiency from the zero field case to the efficiency at the density peak for the four field topologies shown in Figure 5.20.

The efficiency of the antenna is calculated using Equation 3.66. For the most uniform magnetic field case (case A) the increase in efficiency of antenna plasma coupling from the zero field to the peak magnetic field is nearly 21%, where as for the most non-uniform case the increase is ~ 80% (Figure 5.21). As low field helicon sources are proposed recently for space propulsion [32], using a diverging magnetic field near the antenna is well suited.

5.6 Conclusions

Multiple density peaks are observed for the first time in a helicon experiment operated at low magnetic fields. The density peaks are shown to be observed near the resonance cone angles of obliquely propagating helicon waves. Resonance cone propagation leading to excitation of electrostatic fluctuations are confirmed, the amplitude of fluctuations being large at the magnetic fields where the propagation angle coincides with the resonance cone angle. Energy transfer from helicon waves to these fluctuations which deposit energy in the plasma is proposed to explain the density peaks. This proposition helps in explaining the results of Wang et al where the density peaks are observed at higher magnetic fields for higher source frequencies which is required to satisfy the resonance condition. Measurement of density, visible light intensity and antenna plasma resistance at low magnetic field (< 100 G) clearly shows density peaking phenomena on both sides of the antenna at different applied magnetic fields. The density peak observed at the electron cyclotron resonance point around 5 G, where the cyclotron frequency is close to the source frequency of 13.56 MHz, always has higher magnitude in the “ $m = -1$ side”, compared to $m = +1$ side. This is explained by the polarization reversal of LHPW to RHPW. The reason behind non-occurrence of 30 G peak on “ $m = -1$ side” is not clear. The wave field measurements have shown that $|m| = 1$ character is present near all the peaks. The antenna dumps power on both sides simultaneously as the plasma resistance behavior can only be explained when taking into account of the variations on both sides of the antenna. With a source magnetic field of 88 G, density peaks are observed far away from source in the diffusion chamber near locations close to having fields around 30 G. Phase measurements in the axial direction show propagating and non-propagating regions. In the diffusion chamber the density peak is explained by oblique resonance as explained in Section 5.2 by considering the measured parallel wave number and estimated perpendicular wave number. Four different field topologies near the antenna is used to look for effect of magnetic field gradient. It is shown that for the

availability of different magnetic fields near the antenna, the density on both sides along with the antenna-plasma coupling increases which is proposed to be through a multimode oblique resonance.

References

- [1] Boswell, R. W. "Plasma production using a standing helicon wave." *Physics Letters A* 33, no. 7 (1970): 457-458.
- [2] Degeling, A. W., C. O. Jung, R. W. Boswell, and A. R. Ellingboe. "Plasma production from helicon waves." *Physics of Plasmas* 3 (1996): 2788.
- [3] Chen, F. F., X. Jiang, J. D. Evans, G. Tynan, and D. Arnush. "Low-field helicon discharges." *Plasma Physics and Controlled Fusion* 39, no. 5A (1997): A411.
- [4] Lho, Taihyeop, Noah Hershkowitz, J. Miller, W. Steer, and Gon-Ho Kim. "Azimuthally symmetric pseudosurface and helicon wave propagation in an inductively coupled plasma at low magnetic field." *Physics of Plasmas* 5 (1998): 3135.
- [5] Wang, S. J., J. G. Kwak, C. B. Kim, and S. K. Kim. "Observation of enhanced negative hydrogen ion production in weakly magnetized RF plasma." *Physics Letters A* 313, no. 4 (2003): 278-283.
- [6] Sato, G., W. Oohara, and R. Hatakeyama. "Efficient plasma source providing pronounced density peaks in the range of very low magnetic fields." *Applied physics letters* 85, no. 18 (2004): 4007-4009.
- [7] Wang, S. J., Jong-Gu Kwak, S. K. Kim, and Suwon Cho. "Experimental study on the density peaking of an RF plasma at a low magnetic field." *Journal of Korean Physical Society* 51 (2007): 989.
- [8] Sato, G., W. Oohara, and R. Hatakeyama. "Experimental characterization of a density peak at low magnetic fields in a helicon plasma source." *Plasma Sources Science and Technology* 16, no. 4 (2007): 734.
- [9] Lafleur, T., C. Charles, and R. W. Boswell. "Characterization of a helicon plasma source in low diverging magnetic fields." *Journal of Physics D: Applied Physics* 44, no. 5 (2011): 055202.
- [10] Eom, G. S., Junghee Kim, and Wonho Choe. "Wave mode conversion and mode transition in very high radio frequency helicon plasma." *Physics of plasmas* 13 (2006): 073505.
- [11] Chen, Francis F. "The low-field density peak in helicon discharges." *Physics of Plasmas* 10 (2003): 2586.
- [12] Shamrai, Konstantin P., and Vladimir B. Taranov. "Volume and surface rf power absorption in a helicon plasma source." *Plasma Sources Science and Technology* 5, no. 3 (1996): 474.
- [13] Cho, Suwon. "The resistance peak of helicon plasmas at low magnetic fields." *Physics of plasmas* 13 (2006): 033504
- [14] Blackwell, D. D., T. G. Madziwa, D. Arnush, and F. F. Chen. "Evidence for Trivelpiece-Gould modes in a helicon discharge." *Physical review letters* 88, no. 14 (2002): 145002-145002.

- [15] Light, Max, Isaac D. Sudit, Francis F. Chen, and Donald Arnush. "Axial propagation of helicon waves." *Physics of Plasmas* 2 (1995): 4094.
- [16] Sakawa, Y., N. Koshikawa, and T. Shoji. "A higher-order radial mode of helicon waves." *Plasma Sources Science and Technology* 6, no. 1 (1997): 96.
- [17] Lafleur, T., C. Charles, and R. W. Boswell. "Plasma control by modification of helicon wave propagation in low magnetic fields." *Physics of Plasmas* 17 (2010): 073508.
- [18] Akhiezer, A. I., Mikhailenko, V. S., and Stepanov, K. N. (1998). Ion-sound parametric turbulence and anomalous electron heating with application to helicon plasma sources. *Physics Letters A*, 245(1), 117-122.
- [19] Kline, J. L., and E. E. Scime. "Parametric decay instabilities in the HELIX helicon plasma source." *Physics of Plasmas* 10 (2003): 135.
- [20] Corr, C. S., N. Plihon, P. Chabert, O. Sutherland, and R. W. Boswell. "Spatially limited ion acoustic wave activity in low-pressure helicon discharges." *Physics of plasmas* 11 (2004): 4596.
- [21] Virko, V. F., G. S. Kirichenko, and K. P. Shamrai. "Parametric ion-acoustic turbulence in a helicon discharge." *Plasma Sources Science and Technology* 12, no. 2 (2003): 217.
- [22] Krämer, M., Aliev, Y. M., Altukhov, A. B., Gurchenko, A. D., Gusakov, E. Z., and Niemi, K. (2007). Anomalous helicon wave absorption and parametric excitation of electrostatic fluctuations in a helicon-produced plasma. *Plasma Physics and Controlled Fusion*, 49(5A), A167.
- [23] Arnush, Donald, and Charles F. Kennel. "Refraction by the electromagnetic pump of parametrically generated electrostatic waves." *Physical Review Letters* 30, no. 13 (1973): 597.
- [24] Boswell, R. W. "Non-convective parametric instability associated with whistler wave resonance cone." *Physics Letters A* 55, no. 2 (1975): 93-94.
- [25] Boswell, R. W., and M. J. Giles. "Trapping of decay waves in whistler resonance cones." *Phys. Rev. Lett.:(United States)* 36, no. 19 (1976).
- [26] Ganguli, A., M. K. Akhtar, and R. D. Tarey. "Theory of high-frequency guided waves in a plasma-loaded waveguide." *Physics of Plasmas* 5 (1998): 1178.
- [27] Ganguli, A., M. K. Akhtar, R. D. Tarey, and R. K. Jarwal. "Absorption of left-polarized microwaves in electron cyclotron resonance plasmas." *Physics letters A* 250, no. 1 (1998): 137-143.
- [28] Takahashi, K., T. Kaneko, and R. Hatakeyama. "Polarization-reversal-induced damping of left-hand polarized wave on electron cyclotron resonance." *Physical review letters* 94, no. 21 (2005): 215001.
- [29] Chen, Francis F., Isaac D. Sudit, and Max Light. "Downstream physics of the helicon discharge." *Plasma Sources Science and Technology* 5, no. 2 (1996): 173.

[30] Tysk, Shane M., C. Mark Denning, John E. Scharer, and Kamran Akhtar. "Optical, wave measurements, and modeling of helicon plasmas for a wide range of magnetic fields." *Physics of Plasmas* 11 (2004): 878.

[31] Sudit, Isaac D., and Francis F. Chen. "Discharge equilibrium of a helicon plasma." *Plasma Sources Science and Technology* 5. (1996): 43.

[32] Chen, Francis F. "Permanent magnet helicon source for ion propulsion." *Plasma Science, IEEE Transactions on* 36, no. 5 (2008): 2095-2110.

Current Free Double Layer

6.1 Introduction

Monotonic potentials form in the boundary of a plasma vessel or any material inserted in plasma and these potential structures are known as sheaths. Double layers (DL) or double sheaths are potentials formed in the bulk of the plasma. Normally DLs are formed in the interface of two different plasmas and need a current to maintain this potential. Current free double layers are potential structures formed self consistently in a current less plasma. Recently many experiments reported observations of DLs in current-less systems. Most of the works on current free double layer (CFDL) are reported in low pressure geometrically expanding helicon plasma systems with a diverging magnetic field. Still many experiments are going on to find out the formation mechanism of CFDLs as well as to find out the role of different external parameters like neutral pressure [1], antenna frequency [2], magnetic field [1, 3-4] as well as the strength and location of magnetic field gradient [5-8]. Electric fields can be created in the bulk of geometrically expanding plasmas with or without diverging magnetic fields either by the normal Boltzmann plasma expansion [8-10] or by DL like self consistent potential structures [1-8]. Ambipolar plasma expansion and subsequent potential formation is discussed in Section 6.2 followed by an introduction to double layers in Section 6.3. A DL normally needs finite relative ion-electron drifts or a current to be sustained [39]. Current free plasmas can also sustain potential structures in an expanding geometry. These CFDLs are explained in Section 6.4 along with recent experimental and conceptual developments in CFDLs produced in low pressure helicon discharges. One of the common features of helicon CFDL experiments is a dielectric source tube around which a helical antenna is wrapped to produce plasma. It is believed that finite amount of charging of this dielectric wall is necessary to form a CFDL [37-38]. In RF discharges a floating object can acquire a negative potential known as the DC-self bias. In this

thesis work a borosilicate glass source tube is used and its charging dependence on various external parameters like RF power, gas mass, gas pressure and magnetic field is studied and the results are described in Section 6.5. Role of magnetic field gradient and the location of maximum field gradient are studied in a low pressure and low power RF plasma and the results are presented in Section 6.6.

6.2 Boltzmann Plasma Expansion

For Maxwellian electrons in a plasma, electron temperature, density and plasma potential are related. Plasma density decreases when relatively denser plasma expands from the source region of a discharge to a vacuum chamber with area larger than the source. This density decreases creates a potential fall away from the source.

Consider a plasma source where density near source as n_0 and plasma potential $V = 0$ and take two points A and B away from the source. The potential and temperature are respectively V_A and T_{eA} at location A. Density n_{zA} for a Maxwellian plasma electrons at A can be expressed as

$$n_{zA} = n_0 \exp(-V_A/T_{eA}) \quad (6.88)$$

Similarly for a location B, if the potential and temperature are respectively V_B and T_{eB} then density n_{zB} for a Maxwellian plasma electrons there can be expressed as

$$n_{zB} = n_0 \exp(-V_B/T_{eB}) \quad (6.89)$$

From the above two equations we can have

$$\ln\left(\frac{n_{zA}}{n_{zB}}\right) = \frac{V_B}{T_{eB}} - \frac{V_A}{T_{eA}} \quad (6.90)$$

So if the temperature at location A and B are equal with $T_{eA} = T_{eB} = T_e$ then the potential difference $V_B - V_A = \nabla V$ between location B and A can be written as

$$\nabla V = -T_e \ln\left(\frac{n_{zA}}{n_{zB}}\right) \quad (6.91)$$

So if $n_{zA} > n_{zB}$ i.e. if the density drops from location A to location B then a potential drop will be created as per Equation 6.4.

When a plasma expands in a diverging magnetic field, the magnetized electrons will follow the field lines and flow in a larger area. When the magnetic field strength decreases, the flux tube area increases. If the magnetic flux tube area and field strength at $x = 0$ are A_0, B_0 and at x are A_x, B_x [Figure 6.1] then

$$\mathbf{A}_0 \mathbf{B}_0 = \mathbf{A}_x \mathbf{B}_x \quad (6.92)$$

As the magnetic field diverges, the plasma density decreases and the density n_0 at $x = 0$ is related to density n at x by

$$\frac{n}{n_0} = \frac{B}{B_0} = \frac{A_0}{A} \quad (6.93)$$

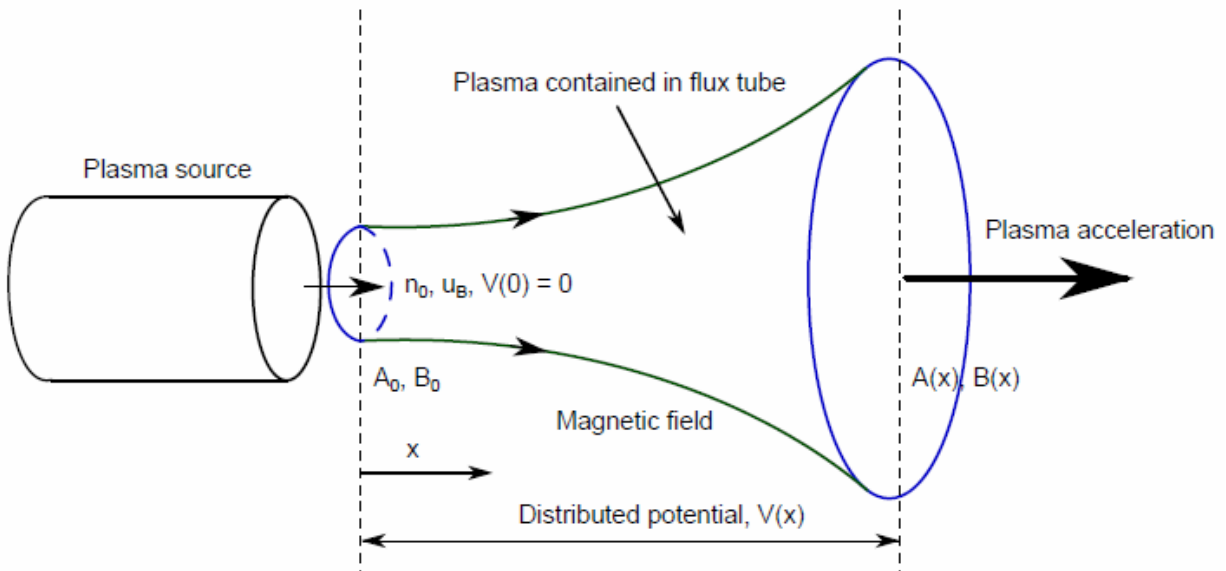


Figure 6.1 Ambipolar plasma expansion in diverging magnetic field [12].

Assuming ions entering the location $x = 0$ at Bohm velocity u_B , the ion continuity equation will be

$$n(x)u(x)A(x) = n_0u_BA_0 \quad (6.94)$$

, where $u(x)$ is the velocity at x . The ion velocity can be found from the energy conservation equation as

$$\frac{1}{2}Mu^2(x) = \frac{1}{2}Mu_B^2 + qV(x) \quad (6.95)$$

Thus when the plasma expands, density decreases and a potential $V(x)$ is set up which accelerates the ions. This kind of ambipolar plasma expansion with or without a diverging magnetic field is reported by many authors in RF discharges. Lafleur et al [8] have reported ion acceleration over a length of 15 cm with ion beam energy of 18 eV in an expanding low pressure ($\approx 4.3 \times 10^{-4}$ mbar, Argon) helicon plasma source at low magnetic fields of ~ 20 G using a retarding field energy analyzer (RFEA). Corr et al [9] have observed ion beams with energy ~ 50 eV in a geometrically expanding capacitive discharge. Longmier et al [10] have observed ambipolar ion acceleration over a length of 10^4 - 10^5 Debye lengths with ion speeds four times ion sound speed at 30 kW RF power and 1.7 kG magnetic field in low argon pressures of $\approx 2.6 \times 10^{-5}$ mbar.

6.3 Double Layer

A double layer (DL) in its simplest form is a sandwich of two oppositely charged space charge layers. It is different from the normal sheath as the DL forms in the bulk of the plasma where as the former forms on boundary of any material inserted into the plasma or on the boundary of the vessel containing the plasma. A typical potential, electric field and space charge density profile of DL in a plasma is given in Figure 6.2. Though the total charge of the DL is zero, quasi-neutrality is violated inside the DL. A DL can have extended pre-sheaths on both sides much like a sheath to match the conditions of the quasi-neutral plasma on either side.

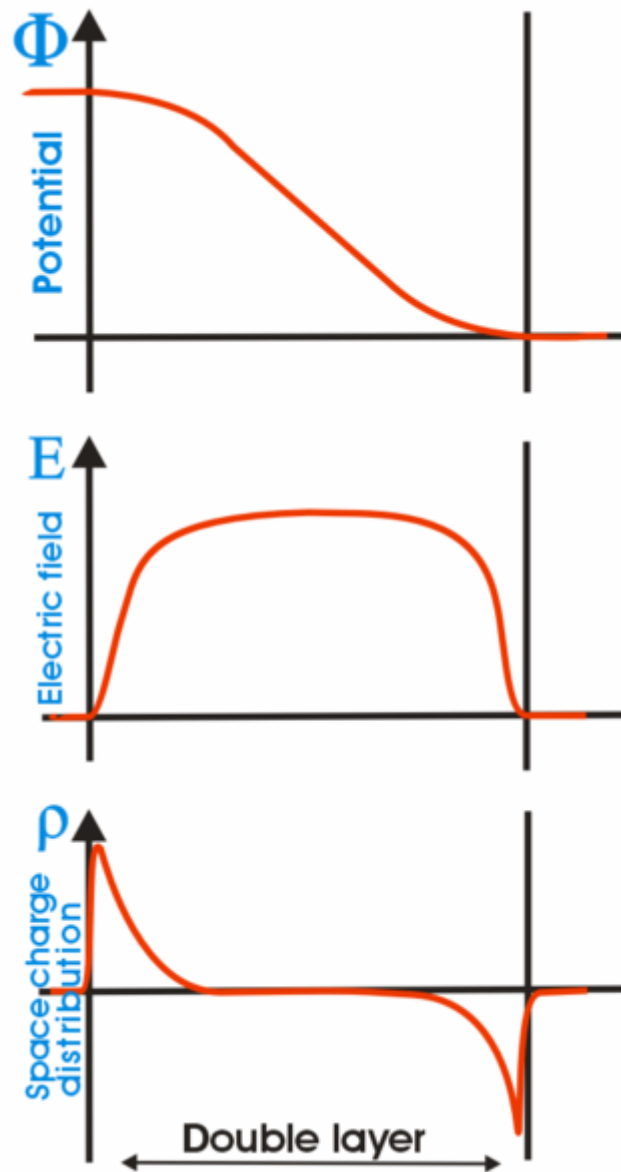


Figure 6.2 Electric potential, electric field and space charge distribution inside a double layer [13].

The potential drop inside the DL can be as large as 2000 times [14-15] the electron temperature (in Volts) to an order of electron temperature [16] with the former known as the strong DLs and the latter as the weak DLs. There are DLs which can have drops even less than electron temperature which are known as the ion acoustic type DLs (IADL). Chan et al. [16] reported the

first laboratory evidence of such structures. The existence of IADLs was confirmed by experiments by Sekar and Saxena [17] in 1985. The formation of strong double layer requires the existence of four distinct groups of particles namely trapped and accelerated electrons and ions as shown in Figure 6.3, while weak double layers may be constructed with only three out of these four groups. DLs can be stationary [1-8] or propagating [18-19]. They are formed in both electropositive [1-8] and electronegative [20] plasmas.

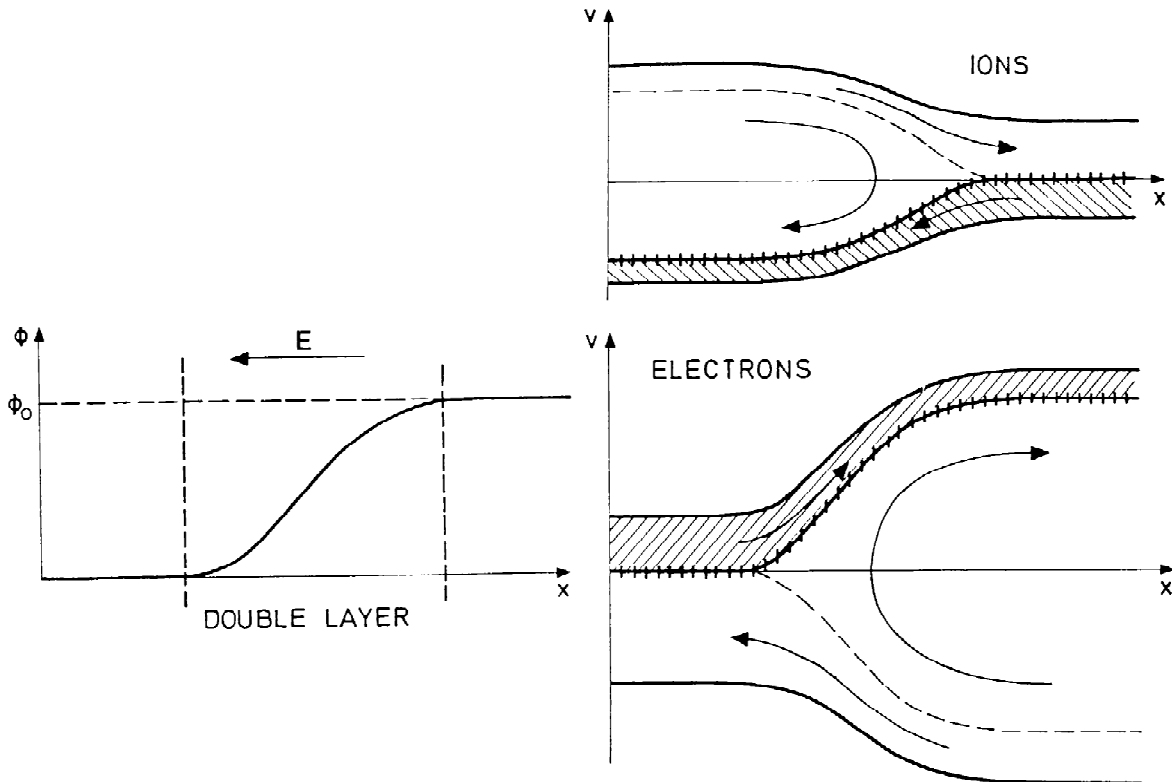


Figure 6.3 Potential distribution $\Phi(x)$, and the ion and electron phase space distributions across a DL with potential drop Φ_0 (and the corresponding internal electric field \mathbf{E}). The hatched areas indicate accelerated populations. The reflection of ions and electrons within the separatrices (symmetrically placed broken and barred curves) are indicated by the arrows symbolizing velocity reversal. Ions or electrons with energy larger than Φ_0 (with very large initial velocity) are not reflected but can pass through the DL, as indicated [21].

Electric fields inside the plasma are often interesting as they can be used as source of thrust for space propulsion [22-23] and also accelerated ions can be used to functionalize materials [24] of interest to semiconductor industry. As a source for charged particle acceleration, they are believed to explain some important astrophysical phenomena like aurora formation [25]. Alfvén [25], suggested that a DL present in the magnetosphere can accelerate electrons to earth's upper atmosphere which leads to the precipitation and the subsequent observation of aurora. With rocket-borne detectors McIlwain [26], found the presence of mono energetic electrons which suggested electrostatic acceleration. Later Satellite observations by Forrest Mozer [27] in the magnetosphere have revealed electrostatic shocks aligned to magnetic field. It is recently proposed that double layers may play a significant role in supplying and accelerating plasma in magnetic coronal funnels [28].

6.4 Current Free Double layer

Perkins and Sun [29] analytically suggested that current free plasmas can sustain a potential drop in a diverging magnetic field by solving the Vlasov equation. Hatakeyama et al. [30] observed the first experimental CFDL by mixing two plasmas of unequal electron temperature in a triple plasma device. Hairapetian and Stenzel [31] created two-electron temperature plasma and then allowed its expansion. Adjusting the individual temperatures of the two groups of electrons they have observed CFDL formation.

6.4.1 Helicon CFDL experiments

Charles and Boswell [11] observed the first helicon CFDL in which they have measured a sharp potential drop of 45 V in $\sim 50 \lambda_D$ along the magnetic field. The experiment was performed at 250 W RF power and a pressure of 0.4 mTorr with 130 G magnetic field in the source chamber which decreased to few tens of Gauss in the diffusion chamber. The experimental set up, the axial potential profile and axial density profile are shown in Figure 6.4. Argon and Hydrogen plasmas were used for CFDL formation and ion beams accelerated in the CFDL are observed in the downstream by a retarding field energy analyzer [32]. The formation of double layers in current-free plasmas and associated ion beams were confirmed by similar experiments [1-5, 7, 33-35].

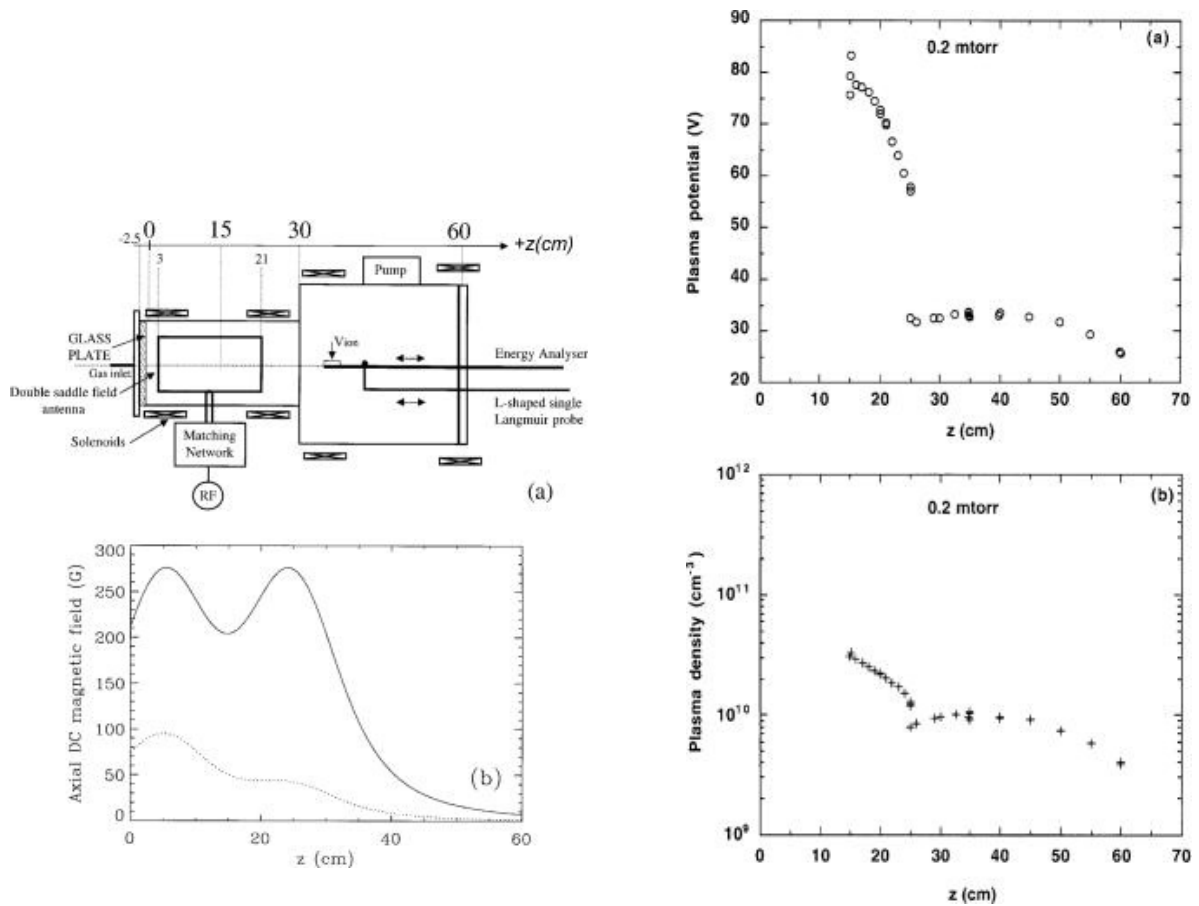


Figure 6.4 Chi-Kung source, axial applied magnetic field, measured axial plasma potential and density at 250 W RF power, 0.2 mTorr and 130 G at source [11].

Charles and Boswell [36] also did the time evolution study of the CFDL formation and found that the current-free double layer was formed in the first 100 μs of the discharge. Charles [37] also showed that CFDL formation was accompanied by negative charging of the source walls. Meige et al [38] in 1D PIC simulations have shown that finite amount of source wall charging is necessary for CFDL formation.

6.4.2 Helicon CFDL Models

After the observation of CFDL in helicon plasmas, many models have tried to explain the observations of CFDL formation in low pressure helicon discharges by taking various groups of

trapped and free electron distributions. A current driven DL is modelled using four groups of particles as free and trapped electron and ions [39].

Taking a Maxwellian upstream electron population, with no additional energetic electron population Chen [40] considered a Boltzmann plasma expansion in the diverging magnetic field. As the plasma expands in a diverging magnetic field, the density and plasma potential fall according to Boltzmann expansion. For a potential drop of $0.5 kT_e/e$, the ions get accelerated and attain the Bohm velocity after which their density decrease is slower than that of electrons. So the plasma expansion is considered to be a simple Boltzmann expansion until the point where quasi-neutrality breaks down ($n = n_0 e^{-1/2}$) and the double layer forms. The double layer potential is self-consistently set such that equal electron and ion fluxes can flow across it, and it is therefore current free. As to a floating material inside plasma the ion and electron fluxes are equal, this double layer structure thus evolved is current free in nature. For Argon plasma a CFDL drop of $\sim 5.2 kT_e/e$ was proposed. This model does not take into account the collisions and also cannot explain the 165 eV ion beams observed by Weibold et al [35] for a 14 eV plasma.

Lieberman et al [41] in a diffusive model used a group of fast electrons being accelerated by the CFDL towards upstream plasma along with the four group of particles needed for a current driven DL. These fast electrons will get reflected from the source end wall sheath to ensure that the DL formed is current free. As the source diameter is less than the diffusion chamber diameter in all the CFDL experiments, the loss of electrons in the upstream will be higher upstream. This electron loss is compensated by the extra accelerated group of particle travelling towards the source from the diffusion by increasing the ionization in the source region. Their explanations can explain the pressure dependency of CFDL strength observed in the experiments. For very low neutral pressure where collisions are sparse, additional ionization in the source cannot happen and the CFDL vanishes and for higher pressures there is no longer a need for ionization by the energetic electrons and the double layer vanishes. But so far in experiments these fast electrons are not observed though there is experimental evidence that the source ionization increases [2] with CFDL formation.

Ahedo et al [42] used a Bi-Maxwellian electron distribution and shown that for collisionless plasma, the ratio of hot electron density and temperature to Maxwellian electron density and temperature plays a role in CFDL formation.

Takahashi et al [43] measured the electron energy distribution in an expanding low pressure helicon discharge. In the upstream they found a Bi-Maxwellian distribution with free and trapped electrons. The break energy of the distribution upstream was found to be the CFDL potential drop so that the hotter population escapes the source. The temperature of the trapped electron was higher than the free electrons as the trapped electron stay for longer time being trapped in the wall sheath and the CFDL potential. The fast electrons stay considerably for a lesser time in the source. The faster electrons which go to the right side grounded wall sheath get reflected and then again get accelerated when they enter the upstream. So a single source of Bi-Maxwellian electrons can sustain the CFDL. In the downstream they have observed only the hotter population which has escaped from the source.

6.4.3 Helicon CFDL instabilities

Observation of two different types of low frequency instabilities are reported in helicon CFDL experiments. Aanesland et al [1] have observed an instability in the frequency range of 10-20 kHz concurrent with the CFDL in a low pressure helicon discharge. Electrons accelerated from the downstream plasma through CFDL were believed to excite an ionization instability in the upstream plasma. They have done a theoretical calculation for excitation of ionization instability by an electron beam in the low pressure upstream plasma and found the dispersion of the ionization instability and its growth rate. The theoretically calculated pressure dependency of the ionization instability frequency matched quite well with the experimental data.

Thakur et al [2] reported observation of ion acoustic instability of 17.5 kHz, that is excited when the source frequency is below 12 MHz. For frequencies between 12-15 MHz stable CFDL formations was reported along with increase in signal-to-noise ratio in all electrostatic probes, upstream plasma density and velocity of ions downstream. For low RF frequencies the coupling to plasma is shown for their system to be better, so that a strong CFDL tries to form but that results in formation of high energy beams through acceleration in the high potential drop which were proposed to drive the ion acoustic velocity. They proposed that this electrostatic instability will self limit the formation of strong CFDL formation.

The above mentioned results are different from each other as in case of Aanesland et al [1] the instability is concurrent with the CFDL where as for Thakur et al [2] the CFDL formed only after the ion acoustic instability got suppressed at higher source frequencies.

6.4.4 Effect of Magnetic field Strength and Gradient

Charles and Boswell [3] studied the role of magnetic field on CFDL formation. By increasing the magnetic field they have observed ion beam formation in downstream plasma for a critical magnetic field of 50 G in the source. The source potential and density increased simultaneously at 50 G but in the downstream plasma the effect was little. Ion magnetization at 50 G is attributed to this transition from an expanding plasma to a plasma containing a CFDL. When the ion is magnetized the ion loss to the radial wall decreases and amounted to the density rise. Similar results were obtained by Takahashi et al [4] in EMPI source have shown that for two different dielectric source tubes of radii of 3.25 cm and 2.3 cm, the CFDL is formed for 125 G and 195 G respectively the values of these magnetic fields also are the magnetic fields where the ions got magnetized.

Though the observation of the CFDL were reported by many authors, the location of the CFDL with respect to the geometrical expansion point and also with respect to the maximum magnetic field gradient location was not clear. The role of magnetic field gradient and its location was studied by Sutherland et al [7], Byhring et al [5] and Schroder et al [6]. Sutherland et al. [7] showed that the double-layer strength could be scaled by a factor of at least 2 in a bigger system and that the double layer presumably forms in the vicinity of maximal gradient of the magnetic field. Byhring et al [5] changed the magnetic field gradient by using an extra coil in which the current is passed in the same direction as the other coils. So by increasing the current in their last coil they could decrease the magnetic field gradient which location was much inside the source plasma. They have found that CFDL only formed for up to 8 A in the last coil which was confirmed by RFEA measurements. For their case CFDL formed 6 cm downstream of the geometrical expansion location. A study on independent effects of geometric expansion, magnetic field and field gradient along with its location are studied by Schroder et al [6] in VINETA device. For magnetic field gradient location coinciding with the geometric expansion they have found the CFDL strength is highest. For low magnetic fields the CFDL formed nearer to the diameter change location but for higher magnetic field the DL was pushed to the downstream plasma. They have also reported that for the geometric expansion location nearer to the source stronger potential drops are formed.

6.5 Study of Dielectric Wall Charging

Current free double layers (CFDL) are observed [11] in diverging magnetic field low pressure helicon experiments with an RF antenna wrapped around a cylindrical source tube made of dielectric material and it is believed [37-38] that dielectric glass wall charging lifts the plasma potential in the source chamber of this kind of discharges. Meige et al [38] have done 1D simulation and found that finite wall charging is necessary for the CFDL formation and it may be noted that this can be a reason that no CFDL formation is reported so far without use of dielectric source tubes. The plasma potential of the source region of helicon CFDL experiment depends on the loss rate of electrons and ions whereas the flux of ions to the dielectric wall determines the wall potential.

When a material body is inserted inside an electron-ion plasma, the floating body is negatively charged by the electrons. This negative potential is known as the floating potential (V_f) of the material and it accelerates the less mobile ions near the wall so that the total current to the floating object is zero. This floating potential depends on electron temperature and electron to ion mass ratio and is expressed as $V_f = (kT_e/2e)[\ln(2\pi m/M)]$, where k , T_e , m and M are the Boltzmann's constant, electron temperature, electron mass and ion mass respectively. As $m \ll M$, V_f is always negative with respect to the plasma potential.

When a high frequency electric field is applied to a floating dielectric which is exposed to the plasma, the plasma electrons respond quickly compared to the heavier ions. This creates an imbalance in the currents flowing to the dielectric body and the electrons have to charge the body to a negative potential such that the heavier ions are accelerated resulting in a flux balance of electrons and ions. Emeleus and Garscadden [44] have shown this DC voltage generation as process of rectification by a non-linear sheath in response to harmonic oscillation of RF voltage. Butler and Kino [45] have given a detailed theory of this sheath rectification process for an antenna outside a glass vessel which acts as a capacitance along with measurement of the DC bias voltage inside a glass wall surface exposed to the plasma. This potential is sum of the floating potential of a DC plasma system as described earlier and another additional potential because of difference in response of electrons and ions to the high frequency oscillating electric

field. This potential is known as the DC self bias and the total potential is expressed as per Chabert [46] as

$$V_{RF} = \frac{kT_e}{e} \left[\frac{1}{2} \ln \left(\frac{2\pi m}{M} \right) - \ln I_0 \left(\frac{eV_1}{kT_e} \right) \right]$$

Where I_0 is the zero order modified Bessel function and V_1 is the RF voltage induced in the inner wall exposed to plasma through the capacitance of the dielectric wall. A parametric study of wall potential in the source region of a low pressure helicon discharge is performed with variation in RF power, neutral gas fill-in pressure, gas mass and magnetic field. Wall probe inserted from the source end flange as shown Figure 3.13 is used to measure the floating potential in a static method as used by Aanesland et al [5] by touching the probe tip to the wall. The molybdenum tip of the wall probe is 3 mm in diameter and its planar surface touches the glass wall curved surface while moving axially. DC floating potential is measured using a high impedance of 10 M Ohm.

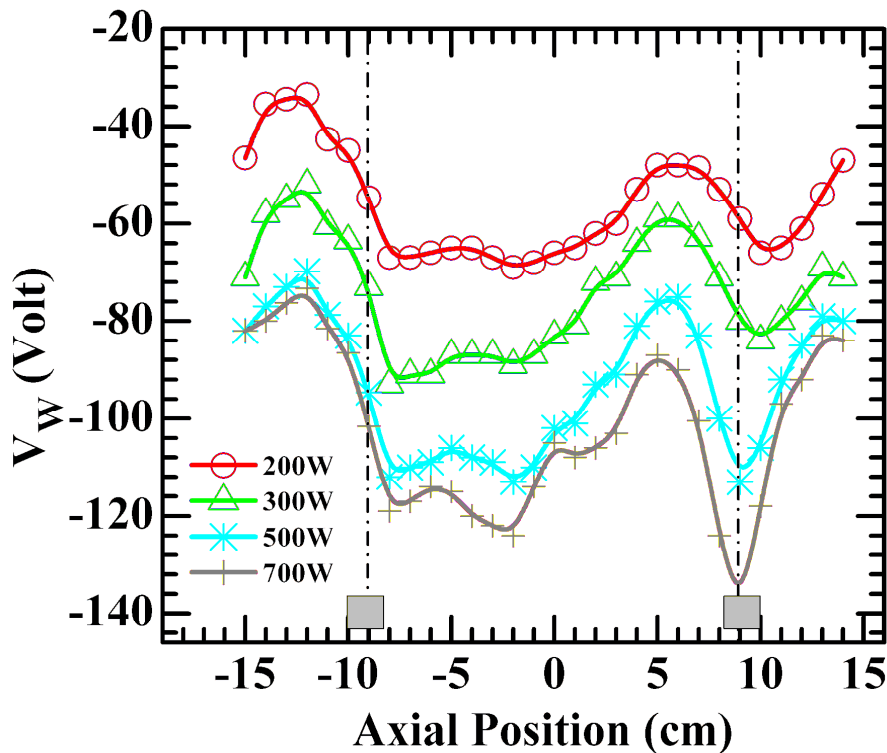


Figure 6.5 Axial variation of DC bias potential for different RF powers at Argon fill-in pressure of 4×10^{-4} mbar. the shaded region are the antenna circular ring positions.

Figure 6.5 shows the variation of DC bias voltage with RF power at 200 G and 4×10^{-4} mbar of Argon neutral pressure. The axial locations close to the antenna straps have higher wall potential and near the ring connected to the live side of the matching network wall charging is high, the behaviour being more pronounced for higher RF powers. Figure 6.6 shows the variation of wall potential at $z = +9$ cm (near the antenna ring) with RF power at 4×10^{-4} mbar. As increasing the RF power increases the RF voltage on the antenna, according to Equation 1, the DC bias increases.

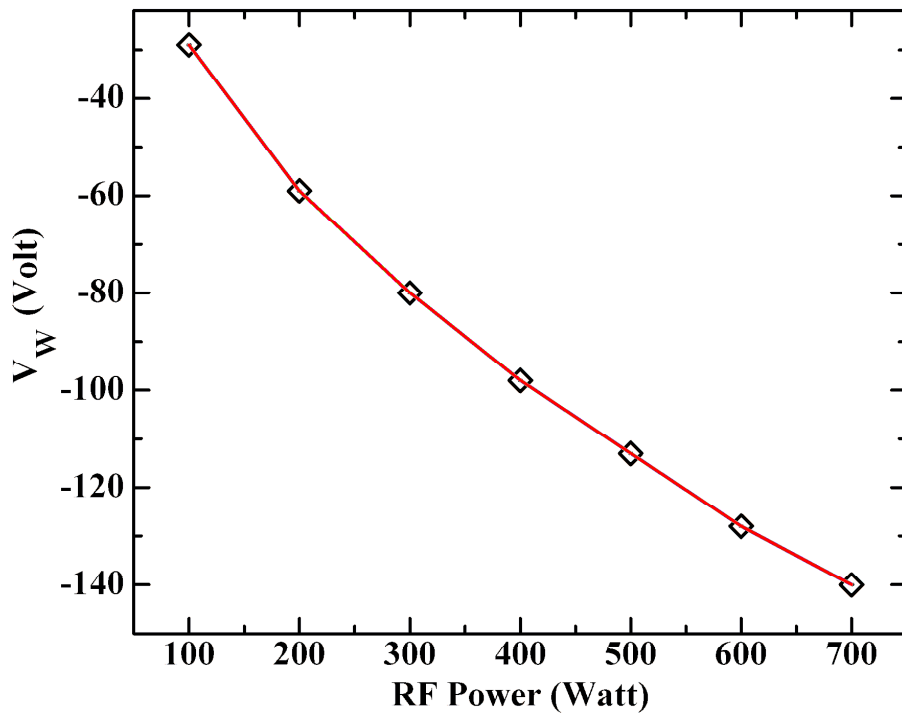


Figure 6.6 Variation of DC bias potential with power near antenna ring at $z = +9$ cm at Argon pressure of 4×10^{-4} mbar.

To see the effect of neutral gas pressure in detail, DC bias is measured near both the antenna rings at $z = +9$ cm and $z = -9$ cm for different pressure at 300 W RF power and is shown in Figure 6.7. The DC bias increases as the pressure is decreased from 4×10^{-3} mbar at a magnetic field of 200 G and for pressures less than 6×10^{-4} mbar it again starts to decrease. It

may be noted that the flux of ions reaching the wall decides the wall potential. For higher pressures the ion flux to the wall is higher as the ionization as well as diffusion of ions to the wall is high. As the pressure is decreased the collision length as well as the ionization decreases leading to a lesser flux to the wall which in turn requires increased wall charging. The observed variation of wall charging with pressures less than 6×10^{-4} mbar is not expected and cannot be explained.

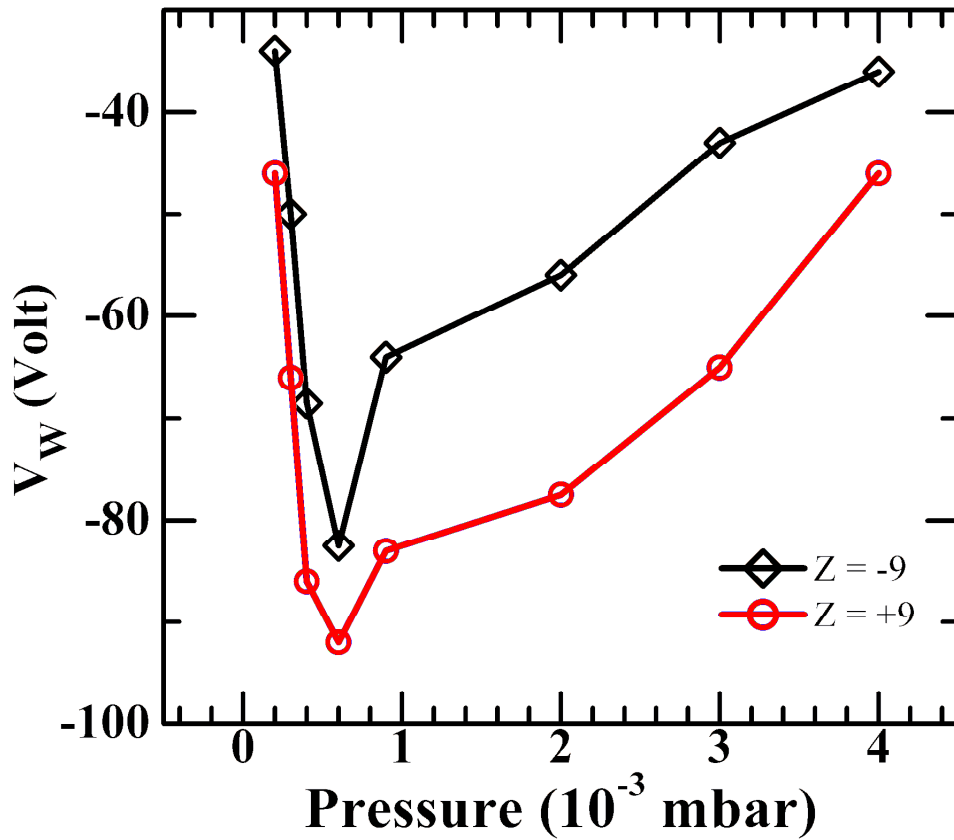


Figure 6.7 Variation of DC bias potential with neutral pressure of Argon at RF power of 300 W and magnetic field 200 G.

As the DC bias is produced because of less ion flux to the wall and as the ion flux depends on the ion magnetization, effect of magnetic field has been studied by varying the source applied magnetic field at 4×10^{-4} mbar and measuring the wall potential near the right ring of antenna at $z = +9$ cm for different gases. The variation of wall potential with applied magnetic field for helium, argon and krypton gas is shown in Figure 6.8. When the ions are not

magnetized the flux of the ions to the wall is more. As the magnetic field is increased the larmour radius decreases and the ion loss to the wall decreases linearly with the applied magnetic field till the larmour radius is equal to the source radius of ~5 cm with a flux which is ion mass dependent.

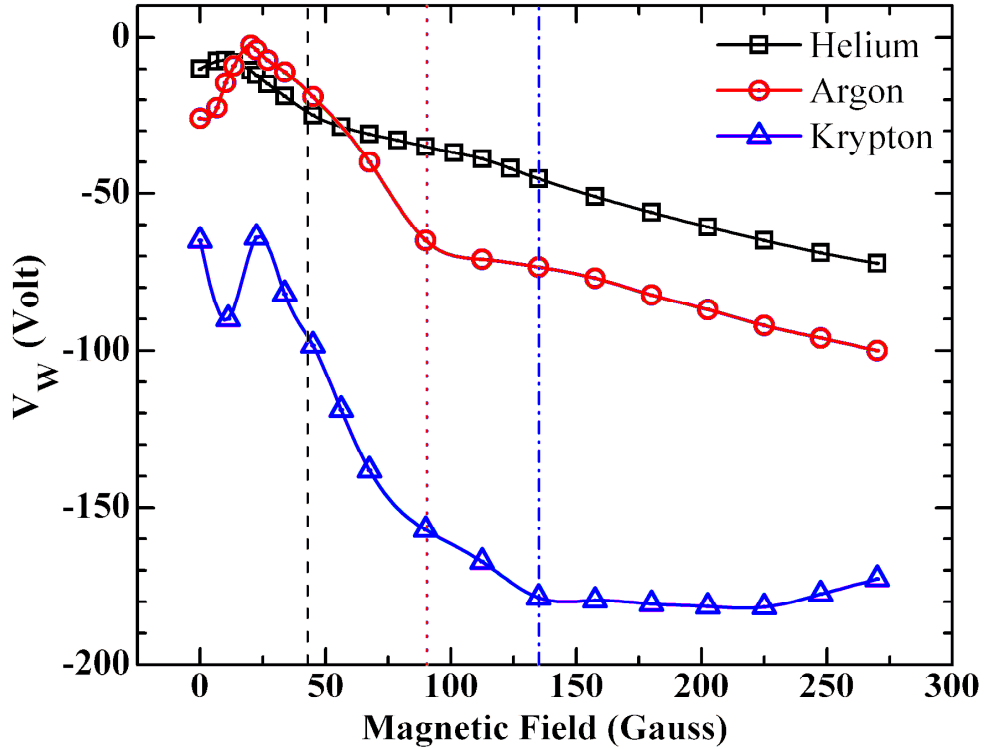


Figure 6.8 Variation of DC bias potential with magnetic field for three different gases: Helium, Argon and Krypton at magnetic field of 200G and neutral gas pressure of 4×10^{-4} mbar.

As the ion larmour radius becomes smaller than the source radius of 5 cm for further increase in magnetic field, ions and electrons both are magnetized and the ion loss is dependent on the electron loss. So when the ion larmour radius becomes comparable to the source radius, the ion loss rate changes to give an inflection point in wall potential magnetic field variation for the magnetic field required for ion magnetization. By taking an ion temperature $T_i \sim 0.2$ eV [48], the calculated thermal velocities for helium, argon and krypton using $v_{th,i} = \sqrt{8kT_i/\pi M}$ are $3.45 \times 10^3 m/s$, $1.1 \times 10^3 m/s$ and $0.76 \times 10^3 m/s$ respectively. The magnetic field so required for magnetization of helium, argon and helium are 30 G, 95 G and 137 G respectively

compared to magnetic fields at the respective inflection points of 42 G, 91 G and 135 G in Figure 6.8.

6.6 Experimental Observations of multiple CFDL

In current driven double layers (CDDL) the potential structure is obtained by forcing two plasmas with different properties like plasma potential, temperature or velocity distribution to mix. They need an external current to sustain the electric field in the DL. Anode double layer (ADL) is a CDDL in collisional plasma (high neutral pressure) where potential structure forms on a positively biased electrode in contact with plasma. So the ADL is formed between the newly formed plasma (with high plasma potential) around or near the electrode and the pre-existing plasma (lower plasma potential). The potential drop is nearly the ionization potential of the gas used. In the presence of an ADL if the potential of the anode is increased, multiple double layers are reported.

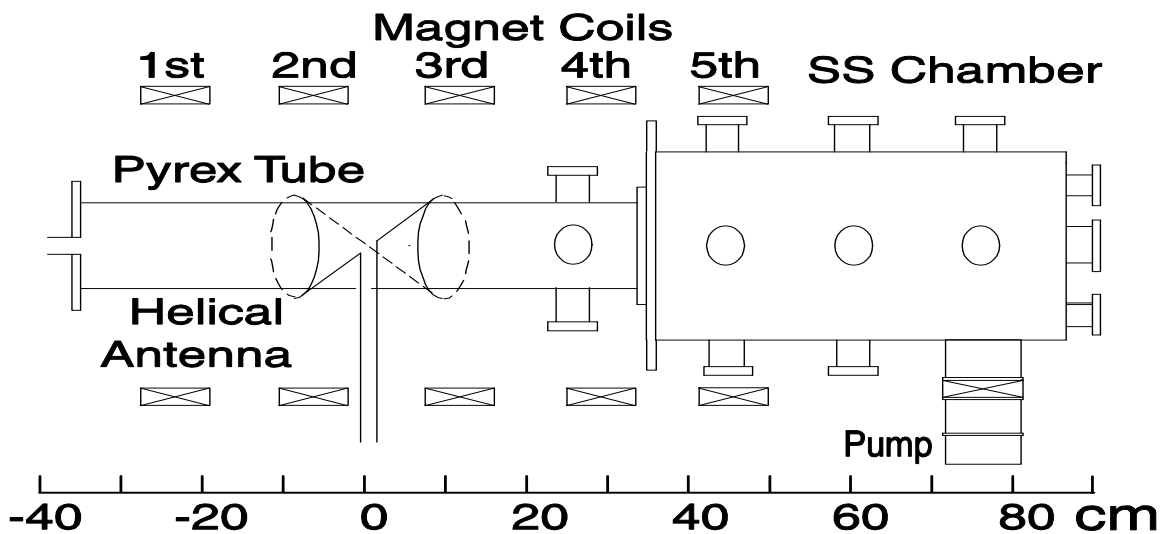


Figure 6.9 Experimental set up with new coil positions to study the role of magnetic field gradient on CFDL formation.

Stronger potential drops in CFDLs are proposed to be limited by beam driven instabilities [2]. Increasing source magnetic field, the CFDL strength was shown to saturate for higher magnetic fields when ions are magnetized [3-4]. Decreasing the neutral pressure though the strength of DL

increases, the DL vanishes for very low pressures [1]. As a CFDL is fundamentally current-less, parameters important to increasing the source plasma potential in a controlled manner without disturbing the plasma matching conditions are unknown. Instability free strong and stable CFDLs are need of space plasma thrusters employing helicon sources.

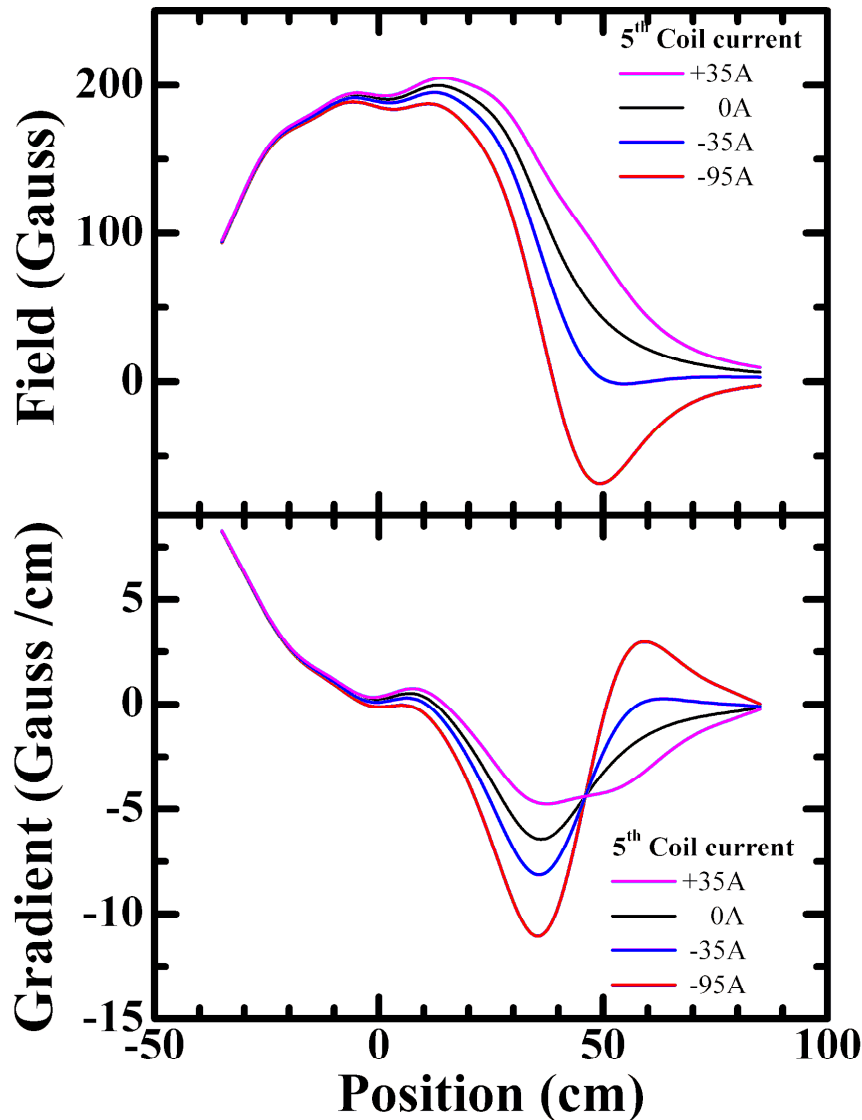


Figure 6.9 Axial component of dc magnetic field and (c) its gradient for different coil current. 4 coils are placed at -24.5 cm, -6.5 cm, 12.5 cm, and 28 cm with +95 A. 5th coil is placed at 46 cm and given currents are +35 A, 0 A, -35 A, and -95 A.

A new magnetic field configuration is used to study the role of magnetic field gradient on CFDL formation and structure. Five coils located at $z = -24.5$ cm, -6.5 cm, 12.5 cm, 28 cm, and 46 cm, are used to produce axial magnetic field in source and expansion chambers (Figure 6.9). While a single power supply is used to power Coils I-IV in series, an independent power supply feeds the current I_v to the Coil V. Thus by keeping current I_i - I_{iv} in coils I-IV fixed, the current I_v can be varied to achieve different gradients near the interface and the field configuration in expansion chamber. Plots of axial magnetic field and Magnetic field gradient for a fixed current of $+95$ A in Coils I-IV and different values of I_v (from 0 A to -95 A; negative sign implying a current direction opposite to that in Coils I-IV), are shown in Figure 6.10.

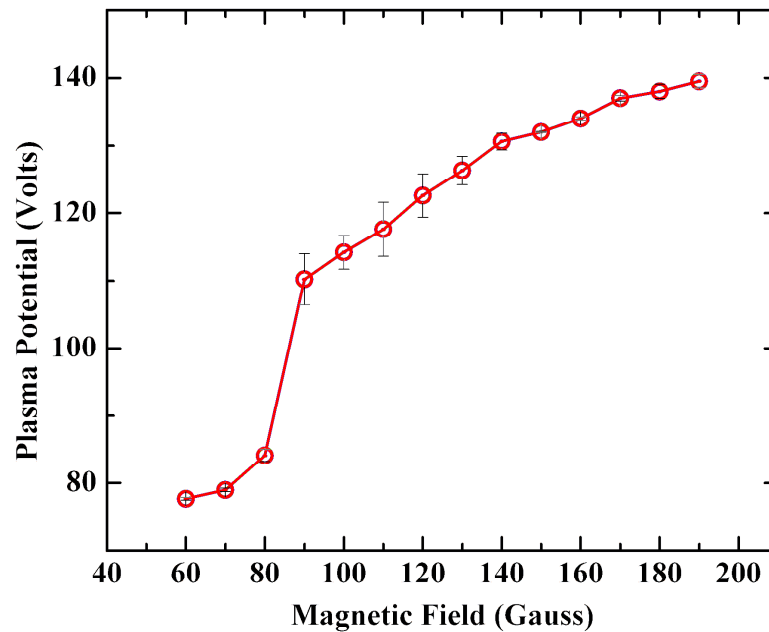


Figure 6.11 Plasma potential variation on axis measured at $z=18$ cm with source magnetic field for 100 W RF power and 2×10^{-4} mbar Argon pressure.

Plasma is produced with Argon gas introduced in the expansion chamber using a mass flow controller and pressure is maintained at $\sim 2 \times 10^{-4}$ mbar. RF power of 100 W is applied to the Helicon antenna with reflected power $<2\%$. With $I_v = 0$ A, plasma potential variation with magnetic field produced by only four coils is shown in Figure 6.11. For magnetic field ~ 90 G in the source chamber, a jump in plasma potential is evident and for magnetic field values more than 90 G, the change in plasma potential is very less. Charles and Boswell [3] have already

shown that the source plasma potential increases for a magnetic field value at which the ions are magnetized. With an ion temperature of 0.2 eV [48], the experimental value is quiet close to the calculated value for an ion to magnetize in a $\sim 5\text{cm}$ plasma radius source.

To see the effect of magnetic field gradient plasma potentials are measured using an emissive probe, as a function of I_v at $z= 18\text{ cm}$ (inside the source) at the axis and are shown in Figure 6.12. It is seen that the plasma potential, on the axis, increases initially as I_v is changed from 0 to $I_v = -35\text{ A}$. Further change of I_v results in decrease of this potential till $I_v= -50\text{ A}$. Finally, for larger negative values of I_v , plasma potential starts increasing again and continues rising and saturates near $I_v = -95\text{ A}$. It may be noted that the magnetic field in the source region does not change significantly as I_v is changed from 0A to -95A . The gradient at the interface, however, changes from 4.7 Gauss/cm to 11 Gauss/cm .

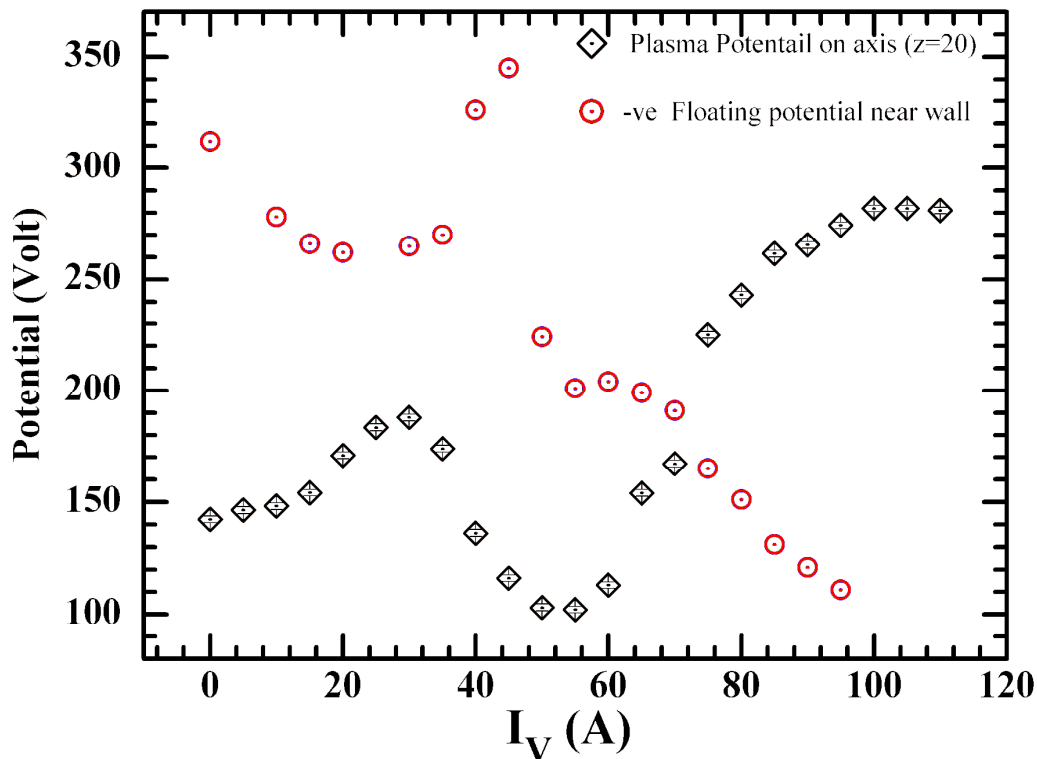


Figure 6.10 Variation of floating potential near the wall and plasma potential at the axis measured at $z=20\text{ cm}$ in the source chamber with the last coil negative current. Current in four other coils are 95 A each. RF power 100 W , pressure $2 \times 10^{-4}\text{ mbar}$.

To understand the reason for plasma potential increase in source chamber for increase in magnetic field gradient scale length near the throat, floating potential (Figure 6.12) near the source tube wall, and Plasma densities, at edge as well on the axis are measured in the source chamber at $z = 17\text{cm}$ (Figure 6.13) as a function of I_V .

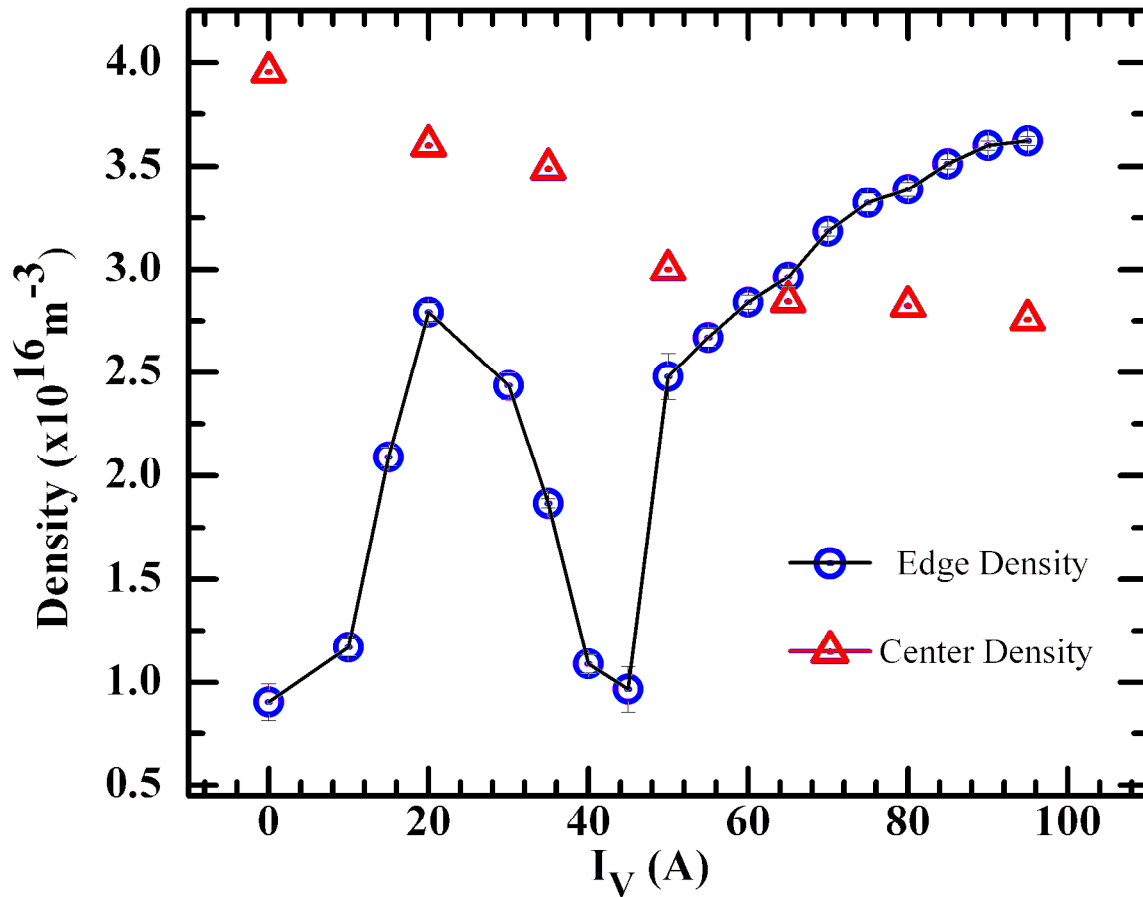


Figure 6.11 Variation of edge and central current density in the source chamber with the last coil negative current. Current in four other coils are 95 A each. Rf power 100 W, pressure 2×10^{-4} mbar.

Edge density is observed to increase, as I_V is made more negative, whereas, there is marginal change in central density. This means there is an extra source of ionization at the edge. Electrons are lost to the wall by two mechanisms. One is through ambipolar diffusion in presence of the radial electric and the other one is the motion along the magnetic field line which cut the dielectric wall. The increasing negative current I_V increases the divergence of magnetic field lines

at the interface and more field lines pass through the wall of the insulated source chamber. This will lead to trapping of the magnetized electrons reaching the dielectric wall, as proposed by Takahashi et al. [49]. The electrons bounce back and forth between the field lines cutting the source tube wall on one side and the sheath on the insulated end plate of the source chamber on the other side. This back and forth motion of electrons, causes additional local ionization. The area of the shell of the terminated field lines not going to expansion chamber increases as I_v becomes more negative. As edge density increases/decreases wall charging should decrease/increase. This should lead to lower/higher floating potential near the wall. This is evident from the floating potential measurement near the source chamber wall (Figure 6.12). As the edge density increases floating potential decreases. Additional ionization near the edge leads to reduction in the radial loss of ions and hence electrons from the bulk plasma. Now to maintain electron energy balance, the plasma potential in the source has to increase to facilitate more axial electron loss and thus compensate less electron loss in the radial direction. The decrease of this plasma potential between $I_v = -35A$ and $-50A$ is a new feature which may be due to very strong divergence of field lines near the interface. In addition to strong gradients and divergence, as discussed below, an axial null and a radial cusp gets formed for negative values of I_v . The positions of the null and cusp are within the expansion chamber for $I_v \gtrsim -50A$. The increase in the potential, for $I_v \gtrsim -50A$ may be the effect of presence of the null and the cusp in expansion chamber.

Further studies were made by scanning plasma potential axially for different I_v . Figure 6.14 shows the axial plasma potential variation for 95A current in the first four coils and $I_v = +35 A, 0A, -35A$ and $-95A$. For $I_v = +35 A$, the plasma potential is constant from $z=15-20$ cm and falls smoothly, from $\sim 100V$ to $\sim 50V$ over a distance of ~ 8 cm remaining constant at $50V$ beyond $z=28$ cm and thus indicating the presence of a broad CFDL. Upstream plasma density and temperature are $\sim 3 \times 10^{16} \text{ cm}^{-3}$ and ~ 6 eV respectively. This corresponds to a Debye length (λ_D) of 0.1 mm and therefore a CFDL with potential drop of $\sim 8 kT_e/e$ and width $\sim 800 \lambda_D$ is formed.

For $I_v = 0A$, the plasma potential structure evolves to a narrower DL structure. A constant potential of $150V$ up to $z=20$ cm, is followed by a sharp fall to $100V$, within ~ 4 cm and a further slower fall to $\sim 50V$ at $z= 34$ cm, beyond which the potential remains constant at $50V$. Upstream density and temperature at the axis remains same. The potential in the region of $z=20-34$ cm,

thus, exhibits a knee like structure, with total drop of 100V, the drop in within first 4 cm ($\sim 400\lambda_D$) being $\sim 50V$.

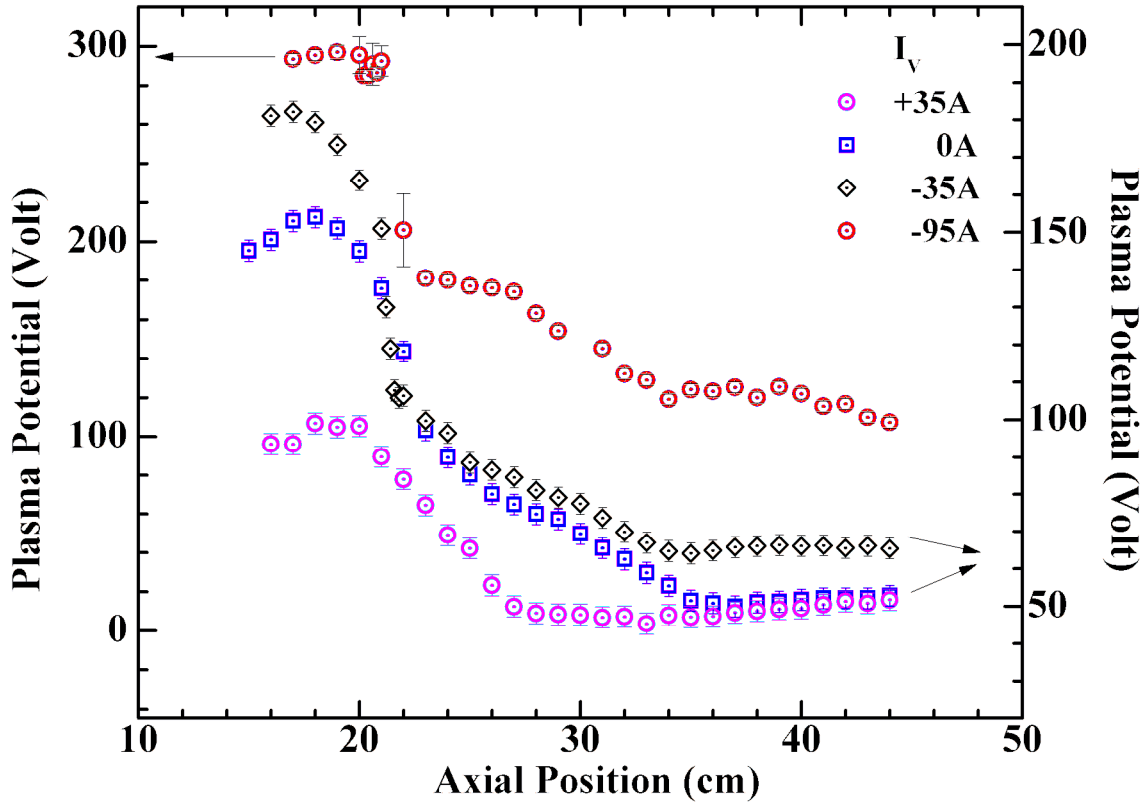


Figure 6.12 Variation of plasma potential along the axis of the device for different current in the last coil; circle -95 Amp, square -35 Amp, Triangle 0 Amp and star =35 Amp. Current in other four coils placed at 30.5 cm, 18 cm, 10.6 cm, 3cm are +95 Amps each.

As I_v is changed further to -35A, the potential in the region $z=15-20$ cm rises to 156V and drops within ~ 4 cm to 100V followed by a slower drop to 54V from $z=24$ cm to $z=34$ cm, beyond which it becomes constant at $\sim 54V$. The knee like feature seen in case of $I_v = 0A$ becomes more prominent in this case with an initial drop of $\sim 56V$ in $\sim 4cm$ ($\sim 400\lambda_D$) followed by further fall of $\sim 46V$ over ~ 10 cm.

Finally, as I_v is changed to -95A, instead of the knee like structure seen in above two cases, a multiple DL structure is seen. The potential between $z=15-20$ cm now goes up to 300V and this

is followed by a sharp fall (~ 1.8 cm) to 180V at $z \sim 22$ cm. This is designated as 1st DL with drop of 120 volts within ~ 1.8 cm ($\sim 180 \lambda_D$). The potential remains nearly constant at 180V till $z \sim 27$ beyond which the potential drops to ~ 120 V within ~ 7 cm. This drop of potential by ~ 60 V within ~ 7 cm is designated as 2nd DL. Beyond $z=34$ cm the potential remains nearly constant at 120V till $z \sim 40$ cm and a slower drop is observed beyond ~ 40 cm. So a sharp DL (~ 120 V; ~ 1.8 cm) is observed which is followed by a shallower DL (~ 60 V; ~ 7 cm) for this value of I_v . As there is a quasi-neutral region exists in between the two DLs, the total structure formed in this case is termed as a multiple CFDL structure.

A sharp drop of potential in first three cases as well as 1st DL in last case, are located well within the source chamber around $z \sim 20$ cm; the 2nd DL in last case and the knee like structure observed in cases of $I_v = 0$ and -35 V, are all located closer to the interface, but still within the source chamber. In all cases, the potential between, $z=15-20$ cm, rises sharply as I_v is changed from $+35$ A through 0 A to negative values (consistent with observations presented in Figure 6.12), while the potentials in the expansion chamber beyond $z=35$ cm, for all these cases, also increase but not as strongly as within the source chamber.

The observed increase in the strength of CFDL may be due to increasing field gradient at the interface and increasing divergence of field lines, as discussed above. Besides increasing the magnetic field gradient, the negative I_v also changes the configuration of the magnetic field in expansion chamber such that an axial null and radial cusp are formed in expansion region, the location of which depends upon the relative strength of I_v and current in Coils I-IV. Magnetic field maps are generated for different I_v values to identify the location of the null and strength of the cusp. It may be noted that the increase in the axial potential in source region ($z=18$ cm; Figure 6.12) described earlier, for increasing negative I_v , occurs till the null point is outside the expansion chamber (for negative values of the null is outside the system till $I_v \sim -35$ A). When the null and cusp are, however, inside the expansion chamber, the cusp geometry results in the improved confinement in the axial direction. This improved confinement, and hence reduced axial loss, forces plasma potential to decrease in the source chamber. Higher the I_v , better is the cusp confinement till the null comes close to the interface. The plasma potential in source region, thus, decreases continuously till $I_v \sim -50$ Amp, when null is located at $z \sim 40$ cm. As the null approaches the source chamber more and more field lines cut the source tube wall resulting in

increased particle loss along the field lines to the source chamber wall. This leads to more electrons to bouncing back and forth between the end wall sheath and sheath near the inner wall of the source following the magnetic field lines which intersect the source tube wall, leading to higher edge density as observed. So there are two processes involved. One is reduced loss in axial direction due to the magnetic cusp and the other is reduced loss in the perpendicular direction because of increase in number of lines intersecting the source wall, which subsequently leads to edge ionization. Under this situation the plasma potential in the source chamber has to go up to increase the loss and maintain electron energy balance. Thus stronger DL is observed as the null moves closure to interface and in the process the cusp becomes stronger.

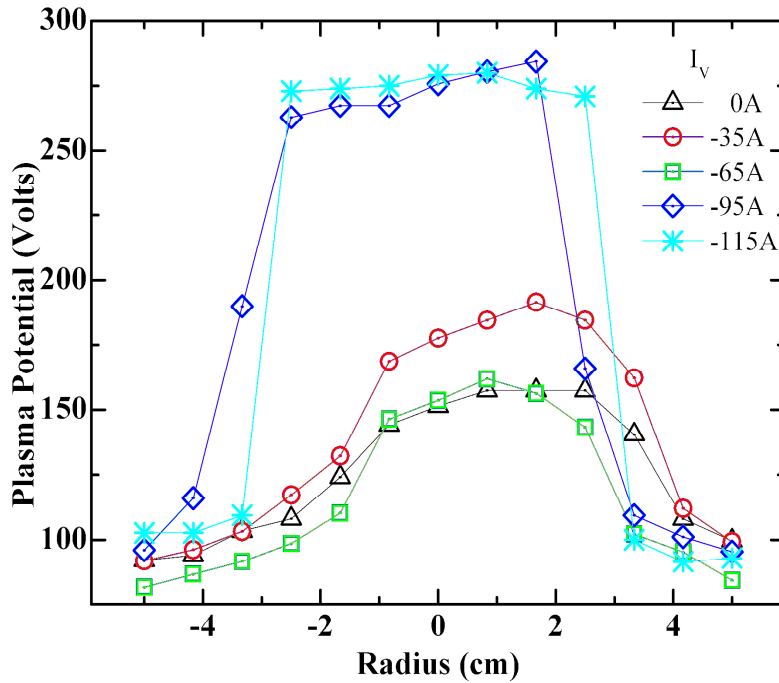


Figure 6.15 Radial variation of plasma potential with I_v measured at $z=18$ cm with an L-shaped emissive probe for 100W RF power and 2×10^{-4} mbar Argon pressure.

The saturation in the source plasma potential with I_v can be understood looking at the radial plasma potential profile shown in Figure 6.15, measured at $z=18$ cm using an L-shaped emissive probe. With the increase in source plasma potential, the radial electric field increases and enhances the radial loss of ions to the wall, so that the process of increasing the plasma potential by increasing magnetic field gradient is limited. The loss of more ions for higher values of I_v is

also evident from the measured lower values of wall potential (Figure 6.12) and higher values of edge density (Figure 6.13).

Diverging field with strong magnetic field gradient at the interface, results in the formation of strong CFDL (50-100V corresponding to 8-16 kT_e/e with widths $\sim 180-400\lambda_D$) in source region. Change of I_v from positive values through 0A to negative values increases the strength of CFDL and at $I_v = -95A$, a multiple CFDL is formed, with 2nd DL located in source chamber close to the interface in the region of strong field gradient. For negative I_v values, an axial null and an asymmetric radial cusp is formed which move closer to the interface with the cusp becoming stronger for larger values of negative I_v . The change of trapped and free particle populations in source and expansion chamber, due to the presence of the null and the cusp, may be responsible for the observed features. Even though the exact role of null and cusp geometry near the interface is not clear, it is clear from the experimental observation that it is possible to have a control on the strength of the DL by changing magnetic field gradient.

6.7 Summary of Chapter 6

Double layers and Current free double layers are discussed with emphasis on helicon CFDLs. Effect of neutral pressure, magnetic field, RF frequency, and magnetic field gradient on CFDLs are discussed. Wall charging is studied to see the effect of RF power, neutral gas pressure, ion mass and magnetic field. Ion magnetization is shown to play role in wall charging and also on source plasma potential. Observations of multiple CFDLs by changing the magnetic field gradient near the throat of an expanding helicon source are discussed and the results are explained on the basis of ion loss to wall as well as cusp field formation near throat. This process seems to be limited by the radial electric fields produced concurrent with higher source plasma potentials which will increase the radial loss of ions to the wall.

References

- [1] Aanesland, A., M. A. Lieberman, C. Charles, and R. W. Boswell. "Experiments and theory of an upstream ionization instability excited by an accelerated electron beam through a current-free double layer." *Physics of plasmas* 13 (2006): 122101.
- [2] Thakur, Saikat Chakraborty, Alex Hansen, and Earl E. Scime. "Threshold for formation of a stable double layer in an expanding helicon plasma." *Plasma Sources Science and Technology* 19, no. 2 (2010): 025008.
- [3] Charles, C., and R. W. Boswell. "The magnetic-field-induced transition from an expanding plasma to a double layer containing expanding plasma." *Applied Physics Letters* 91, no. 20 (2007): 201505-201505.
- [4] Takahashi, K., Charles, C., Boswell, R. W., and Fujiwara, T. (2010). Double-layer ion acceleration triggered by ion magnetization in expanding radiofrequency plasma sources. *Applied Physics Letters*, 97(14), 141503-141503.
- [5] Byhring, H. S., C. Charles, Å. Fredriksen, and R. W. Boswell. "Double layer in an expanding plasma: Simultaneous upstream and downstream measurements." *Physics of plasmas* 15 (2008): 102113.
- [6] Schröder, T., O. Grulke, and T. Klinger. "The influence of magnetic-field gradients and boundaries on double-layer formation in capacitively coupled plasmas." *Euro physics Letters* 97, no. 6 (2012): 65002.
- [7] Sutherland, O., Charles, C., Plihon, N., and Boswell, R. W. (2005). Experimental evidence of a double layer in a large volume helicon reactor. *Physical review letters*, 95(20), 205002.
- [8] Lafleur, T., C. Charles, and R. W. Boswell. "Ion beam formation in a very low magnetic field expanding helicon discharge." *Physics of Plasmas* 17 (2010): 043505.
- [9] Corr, C. S., J. Zanger, R. W. Boswell, and C. Charles. "Ion beam formation in a low-pressure geometrically expanding argon plasma." *Applied Physics Letters* 91, no. 24 (2007): 241501-241501.
- [10] Longmier, Benjamin W., Edgar A. Bering III, Mark D. Carter, Leonard D. Cassady, William J. Chancery, Franklin R. Chang Díaz, Tim W. Glover et al. "Ambipolar ion acceleration in an expanding magnetic nozzle." *Plasma Sources Science and Technology* 20, no. 1 (2011): 015007.
- [11] Charles, C., & Boswell, R. (2003). Current-free double-layer formation in a high-density helicon discharge. *Applied Physics Letters*, 82(9), 1356-1358.
- [12] Lafleur, Trevor Alain. "Helicon Wave Propagation in Low Diverging Magnetic Fields." Thesis, Australian National University (2011).
- [13] L. P. Block. A double layer review. *Astrophysics and Space Science*, 55:59–83, 1978.

- [14] N. Sato, R. Htakeyama, S. Iizuka, and K. Saeki. Ultrastrong stationary double layers in a nondischarge magnetoplasma. *Physical Review Letters*, 46(20): 1330–1333, 1981.
- [15] T. Sato and H. Okuda. Ion-acoustic double layers. *Physical Review Letters*, 44 (11):740–743, 1980.
- [16] Chan, Chung, M. H. Cho, Noah Hershkowitz, and Tom Intrator. "Laboratory Evidence for Ion-Acoustic—Type Double Layers." *Physical Review Letters* 52, no. 20 (1984): 1782.
- [17] A. N. Sekar and Y. C. Saxena. Development of ion-acoustic double layers through ion-acoustic fluctuations. *Plasma Physics and Controlled Fusion*, 27:181–191, Feb. 1985.
- [18] Plihon, N., C. S. Corr, P. Chabert, and J-L. Raimbault. "Periodic formation and propagation of double layers in the expanding chamber of an inductive discharge operating in Ar/SF6 mixtures." *Journal of Applied Physics* 98 (2005): 023306.
- [19] Meige, Albert, Nicolas Plihon, G. J. M. Hagelaar, J-P. Boeuf, Pascal Chabert, and R. W. Boswell. "Propagating double layers in electronegative plasmas." *Physics of plasmas* 14 (2007): 053508.
- [20] N. Plihon, C. S. Corr, and P. Chabert. Double layer formation in the expanding region of an inductively coupled electronegative plasma. *Applied Physics Letters*, 86(091501), 2005
- [21] M. A. Raadu and J. J. Rasmussen. Dynamical aspects of electrostatic double layers. *Astrophysics and Space Science*, 144:43–71, 1988.
- [22] F. N. Gesto, B. D. Blackwell, C. Charles, and R. W. Boswell. Ion detachment in the helicon double-layer thruster exhaust beam. *Journal of Propulsion and Power*, 22(1), 2006.
- [23] West, Michael D., Christine Charles, and Rod W. Boswell. "Testing a helicon double layer thruster immersed in a space-simulation chamber." *Journal of Propulsion and Power* 24, no. 1 (2008): 134-141.
- [24] C. Charles. Large area generation of supersonic ion beams; application to surface functionalisation. In Proceedings of the 6th international conference on reactive plasmas and 23rd symposium on plasma processing, 2006.
- [25] H. Alfvén. On the theory of magnetic storms and aurorae. *Tellus*, 10(1):104–116, 1958.
- [26] McIlwain, Carl E. "Direct measurement of particles producing visible auroras." *Journal of Geophysical Research* 65, no. 9 (1960): 2727-2747.
- [27] F. S. Mozer, C. W. Carlson, M. K. Hudson, R. B. Torbert, B. Parady, J. Yatteau, and M. C. Kelley. Observations of paired electrostatic shocks in the polar magnetosphere. *Physical Review Letters*, 38:292–295, Feb. 1977.
- [28] Boswell, Roderick W., Eckart Marsch, and Christine Charles. "The current-free electric double layer in a coronal magnetic funnel." *The Astrophysical Journal Letters* 640, no. 2 (2006): L199.

- [29] Perkins, Francis W., and Y. C. Sun. "Double layers without current." *Physical Review Letters* 46 (1981): 115-118.
- [30] Hatakeyama, R., Y. Suzuki, and N. Sato. "Formation of electrostatic potential barrier between different plasmas." *Physical Review Letters* 50, no. 16 (1983): 1203.
- [31] Hairapetian, G., and R. L. Stenzel. "Observation of a stationary, current-free double layer in a plasma." *Physical review letters* 65, no. 2 (1990): 175.
- [32] Charles, C. "Hydrogen ion beam generated by a current-free double layer in a helicon plasma." *Applied physics letters* 84, no. 3 (2004): 332-334.
- [33] Cohen, Samuel Alan, N. S. Siefert, S. Stange, R. F. Boivin, E. E. Scime, and F. M. Levinton. "Ion acceleration in plasmas emerging from a helicon-heated magnetic-mirror device." *Physics of Plasmas* 10 (2003): 2593.
- [34] Sun, Xuan, Amy M. Keesee, Costel Biloiu, Earl E. Scime, Albert Meige, Christine Charles, and Rod W. Boswell. "Observations of ion-beam formation in a current-free double layer." *Physical review letters* 95, no. 2 (2005): 025004.
- [35] Wiebold, Matt, Yung-Ta Sung, and John E. Scharer. "Experimental observation of ion beams in the Madison Helicon eXperiment." *Physics of Plasmas* 18 (2011): 063501.
- [36] Charles, C., and R. W. Boswell. "Time development of a current-free double-layer." *Physics of plasmas* 11 (2004): 3808.
- [37] C. Charles. High source potential upstream of a current-free electric double layer. *Physics of Plasmas*, 12(044508), 2005.
- [38] Albert Meige, Numerical modeling of low-pressure plasmas: applications to electric double layers, Thesis, Australian National University (2006).
- [39] Andrews, J. G., and J. E. Allen. "Theory of a double sheath between two plasmas." *Proceedings of the Royal Society of London. A. Mathematical and Physical Sciences* 320, no. 1543 (1971): 459-472.
- [40] Chen, Francis F. "Physical mechanism of current-free double layers." *Physics of plasmas* 13 (2006): 034502.
- [41] Lieberman, M. A., C. Charles, and R. W. Boswell. "A theory for formation of a low pressure, current-free double layer." *Journal of Physics D: Applied Physics* 39, no. 15 (2006): 3294.
- [42] Ahedo, Eduardo, and Manuel Martínez Sánchez. "Theory of a Stationary Current-Free Double Layer in a Collisionless Plasma." *Physical review letters* 103, no. 13 (2009): 135002.
- [43] Takahashi, Kazunori, Christine Charles, Rod W. Boswell, and Tamiya Fujiwara. "Electron Energy Distribution of a Current-Free Double Layer: Druyvesteyn Theory and Experiments." *Physical Review Letters* 107, no. 3 (2011): 035002.

- [44] Garscadden, Alan, and Karl George Emeléus. "Notes on the effect of noise on Langmuir probe characteristics." *Proceedings of the Physical Society* 79, no. 3 (1962): 535.
- [45] Butler, H. S., and G. S. Kino. "Plasma Sheath Formation by Radio-Frequency Fields." *Physics of Fluids* 6 (1963): 1346.
- [46] Chabert, Pascal, Nicholas Braithwaite, and Nicholas St J. Braithwaite. *Physics of Radio-Frequency Plasmas*. Cambridge University Press, 2011.
- [47] Aanesland, A., Charles, C., Boswell, R. W., & Fredriksen, Å, Sputtering effects in a helicon plasma with an additional immersed antenna. *Plasma Sources Science and Technology*, 12, 85 (2003).
- [48] Keesee, Amy M., Earl E. Scime, Christine Charles, Albert Meige, and Rod Boswell. "The ion velocity distribution function in a current-free double layer." *Physics of plasmas* 12 (2005): 093502.
- [49] Takahashi, Kazunori, Christine Charles, Rod Boswell, and Rikizo Hatakeyama. "Radial characterization of the electron energy distribution in a helicon source terminated by a double layer." *Physics of plasmas* 15 (2008): 074505.

Conclusion and Future Work

7.1 Conclusion

A geometrically expanding linear helicon plasma device with a diverging magnetic field is built from scratch. Vacuum levels of 2×10^{-6} mbar are achieved. RF matching is done using an L-type matching network with less than 1 % reflection. Various probes with their electronics are designed, developed and tested in plasma taking into consideration of electrical noise. Antenna vacuum resistance is measured without plasma. Helicon antenna efficiency is shown to increase with RF power in the presence of plasma from ~34 % at low powers to ~70% at high powers.

Discharge mode transitions are observed at different pressures by varying the RF power at fixed magnetic field of 110 G. At lower pressure the transitions are obtained at higher RF powers for a constant static magnetic field. Measured radial density profiles confirm the inductive discharge at low RF power and helicon modes at high RF power. Helicon wave excitation with half helical $m = +1$ mode is confirmed by measuring the radial variation of the axial component of magnetic field. Additionally, the mode is shown to be polluted by the antenna fields near the antenna and pure away from the antenna in the diffusion chamber for low magnetic fields. Axial variation of the phase of the helicon wave gives a wave length of 22 cm in the source region.

Axial density profiles in a diverging magnetic field configurations shows upstream-to-downstream density ratios of ~ 2.7, 5.3 and 8.8 are obtained for RF input power of 200 W, 300 W and 400 W respectively at 2×10^{-3} mbar. Current free double layer is observed at low pressures of 1.2×10^{-4} mbar and 600 W RF power with a potential drop of ~ 8 kT_e/e and thickness of ~ 1000 λ_D . The double layer vanished at higher pressure with the potential drop of the order of kT_e/e which can be explained through a simple Boltzmann expansion. The DL is formed inside the source chamber and in the bulk of the plasma aligned to ambient magnetic field.

Multiple density peaks are observed for the first time in a helicon experiment operated at low magnetic fields. The density peaks are shown to be observed near the resonance cone angles of obliquely propagating helicon waves. Resonance cone propagation leading to excitation of electrostatic fluctuations are confirmed, the amplitude of fluctuations being large at the magnetic fields where the propagation angle coincides with the resonance cone angle. A mechanism of energy transfer from helicon waves to these electrostatic fluctuations which can deposit energy in the plasma is proposed to explain the density peaks. This proposition helps in explaining the results of Wang et al [] where the density peaks are observed at higher magnetic fields for higher source frequencies. Measurement of density, visible light intensity and antenna plasma resistance at low magnetic field (< 100 G) clearly shows density peaking phenomena on both sides of the antenna at different applied magnetic fields. The density peak observed at the electron cyclotron resonance point around 5 G, where the cyclotron frequency is close to the source frequency of 13.56 MHz, always has higher magnitude in the “ $m = -1$ side”, compared to $m = +1$ side. This is explained by the polarization reversal of LHPW to RHPW. The reason behind non-occurrence of 30 G peak on “ $m = -1$ side” is not clear. The wave field measurements have shown that $|m| = 1$ character is present near all the peaks. The antenna dumps power on both sides simultaneously as the plasma resistance behavior can only be explained when taking into account of the variations on both sides of the antenna. Density peaks are observed far away from source in the diffusion chamber near locations close to having fields around 20 G with source magnetic fields of 88 G. Phase measurements in the axial direction show propagating and non-propagating regions. The observations are explained on the basis of resonance cone propagation leading to density rise. Four different field topologies near the antenna is used to look for effect of magnetic field gradient. It is shown that for the availability of different magnetic fields near the antenna, the density on both sides along with the antenna-plasma coupling increases which is proposed to be through a multimode oblique resonance. Antenna efficiency increased 80% (for single) of its value without magnetic field for the most diverging magnetic field near antenna case.

Study of wall charging is described in the experimental set up for different RF power, neutral gas pressure and ion mass along with effect of magnetic field. Ion magnetization is shown to play role in wall charging and the rate of increase of wall charging decreases thereafter. Multiple CFDLs are observed changing the magnetic field gradient near the throat of the expanding helicon source. When the magnetic field gradient is increased, more number of magnetic field

line cross the dielectric glass wall. This leads to edge ionization by trapped magnetized electrons. This edge ionization by electron trapping is explained to decrease the perpendicular ion loss to the wall from the bulk of source plasma. This is confirmed by wall potential measurements. To maintain the electron energy balance, the source plasma potential increases and an axial electric field is set to enhance particle loss in parallel to magnetic field direction till there is a cusp inside the diffusion chamber. After a cusp is formed for negative currents in the last coil > 35 A, axial loss is reduced and the plasma potential decreases in the source chamber. For higher magnetic field gradients with negative current > 50 A, the ionization near wall becomes strong and perpendicular ion loss is decreased, which forces an increase in the source plasma potential. This leads to formation of multiple CFDL.

7.2 Future Work

Sharpness of EHW transitions needs to be studied in detail at higher magnetic fields. A balance transmission line using a balanced-to-unbalance transformer needs to be used for less radiation levels at higher RF powers. Variable frequency RF generator can be used to further study resonance cone propagation as the resonance condition says low B peak will be obtained at a higher magnetic field for a higher source frequency. Detailed studies on nature of electrostatic fluctuations should be carried out to understand the exact mechanism of power deposition. Wave polarization can be measured on both side of the antenna to find the polarization reversal radius and how this radius depends on radial density gradients. Cusps of higher strengths near the geometrical expansion should be studied to know the role of cusp in electron trapping. Cusps inside source can be used to increase the radial loss of ions which can in principle increase the source plasma potential.

High radial electric fields produced in case of strong CFDLs. The role of these electric fields in ion loss to the wall and the subsequent effects like rotational instability needs to be studied. Diverging B-field along with the cusp seems potentially strong candidate for future helicon double layer thruster.